Scuola Normale Superiore di Pisa

Classe di Scienze

Corso di Perfezionamento in Fisica

New precise measurements of the ratio of leptonic decays of K^+ and K^- mesons

Supervisor
Prof. Italo MANNELLI

Candidate
Luca FIORINI

PhD Thesis

Pisa

Winter 2005

Overview

The present PhD thesis concludes an experimental work of three years in the field of particle physics under the supervision of Prof. I. Mannelli.
This work has been developed within the NA48/2 international collaboration and is part of the research of the collaboration, which, recently, terminated its second year of data taking at the SPS CERN site. The plan of the paper is the following:
In the first Chapter an introduction to the relevant topics will be presented; in the second Chapter the theoretical motivation and the presently published experimental results will be briefly exposed; Chapter 3 will present the NA48/2 experimental apparatus, while Chapter 4 will focus on the methods employed in order to achieve the goals of the measurement; starting from Chapter 5 the details of the analysis will be presented. The final Chapter will conclude the thesis comparing the results obtained by the candidate with the theoretical predictions and the experimental results presently available.

Contents

Chapter 1

Introduction

In the field of high energy particle physics, experiments on Kaon systems have represented an important source of information on the fundamental interactions of Nature.
Since the discovery of K mesons in 1949 [1], the study of their properties has stimulated many remarkable ideas. Apart from the evident importance that Kaons had in the hypothesis of the existence of the *'strangeness'* quantum number proposed by Gell-Mann [2] and Pais [3], the famous $\theta - \tau$ puzzle had a relevant role in the innovative hypothesis formulated by Lee and Yang in 1956 [6] of Parity (P) violation in weak interactions. In the following years Kaon phenomenology gave important hints toward the unification of weak interactions for strange and non strange particles proposed by Cabibbo [7]. That unification was a success, and nowadays its elegant extension to all the three families of quarks explains the presently known flavor structure of quarks.
The study of Kaons decays had also a primary role in the investigation of the fundamental symmetry of Nature. In 1955, Gell-Mann and Pais [4] concluded that the neutral Kaon states of definite mass and lifetime were not the strangeness eigenstates $|K^0>$ and $|\overline{K^0}>$, but

$$|K_1> \equiv \frac{|K^0> + |\overline{K^0}>}{\sqrt{2}} \ , \qquad |K_2> \equiv \frac{|K^0> - |\overline{K^0}>}{\sqrt{2}}$$

where $K_1 \to 2\pi$ was permitted, while $K_2 \to 2\pi$ was not allowed, implying a much longer lifetime for K_2 particle. The discovery of the neutral Kaon with long life time (K_L)[5] and the explanation of the original Gell-Mann and Pais argument in terms of CP invariance were the basis for a new theory of weak interactions. The outstanding discovery in 1964 of the unexpected CP violating $K_L \to \pi\pi$

decay mode [8], determined a revolution in the way of thinking symmetries in Nature. Fundamental interactions, that up to then were thought to be invariant under time reversal (T) symmetry[1], were discovered to have a privileged time direction. This fact, that in 1967 Sakharov connected with the matter-antimatter abundance asymmetry in the Universe, remained as an unique property of the neutral Kaon system until recent years, linking in a deep way Kaon physics with the research on symmetry properties of the fundamental laws of particle interactions.

An important contribution to Kaon physics in recent times has been given by the NA48 experiment, that a few years ago published its final result on the precise measurement of $\mathfrak{Re}(\frac{\epsilon'}{\epsilon})$ [11] related to the direct CP violation component of the $K_L \to 2\pi$ decay. The experiment research program didn't finish with the most precise $\mathfrak{Re}(\frac{\epsilon'}{\epsilon})$ measurement ever performed, but it was extended to investigate the rare decays of the K_S particle during the year 2002 (under the name of NA48/1) and, presently, to the search of the CP violation and the study of rare decays of the $K^{\pm}$ system (under the name NA48/2).

NA48/2 can be considered from several points of view as a new experiment as it implements a completely new beam line, new detectors and a new methodology of analysis. It is in the framework of this experiment that the study presented in this thesis has been developed.

Its main focus is on the measurement of the ratio of the leptonic decays of the Kaon:

$$R \;=\; \frac{K^{\pm} \to e^{\pm}\nu(\gamma)}{K^{\pm} \to \mu^{\pm}\nu(\gamma)}$$

This measurement is itself an important direct test of the V-A structure and lepton universality incorporated in the electroweak interactions model.

The result obtained is compatible with the theoretical expectation at the level of precision improved by a factor 2 relative to the previous world average.

[1] CP violation implies T violation via the CPT theorem. CPT theorem, elaborated in 1954 [9] [10], relies on very general assumptions of relativistic field theory (causality and locality) and explains the observed equality between particle and antiparticle masses, magnetic moments and absolute value of charge.

Chapter 2

Physical motivations

2.1 NA48/2 Research Program

Since the discovery of the CP violation in the $K_L - K_S$ mixing during the sixties, the neutral Kaons system, has been studied extensively by theoreticians and experimentalists. Despite the fact that, in principle, direct CP violation can be observed in the $K^+ - K^-$ system, none of the experiments performed till now has succeed to detect it. After the successful precise measurement of the direct CP violation component in the $K_L \to 2\pi$ decay and one year of extensive studies of the K_S rare decays by NA48/1, the NA48 collaboration has started a new challenging study of the charged Kaon system.
The main objective of the experiment is the measurement of the ratio

$$A_g = (g^+ - g^-)/(g^+ + g^-),$$

where g^+ and g^- are the slope parameters describing, respectively, the linear dependence of the K^+ and K^- decay probabilities as a function of the u kinematic variable of the Dalitz plots in the $K^\pm \to \pi^\pm\pi^+\pi^-$. The u variable is related to the energy (E^*_π) of the *odd* pion (the pion having the sign opposite to the one of the decaying Kaon) in the Kaon center of mass system as follows:

$$u = (2M_K/m^2) \cdot (M_K/3 - E^*_\pi),$$

where M_K and m are the Kaon and pion mass, respectively. The experiment is designed to reach a sensitivity, limited by statistics rather than systematics, of $\sim 10^{-4}$ in the measurement of such direct CP-violating asymmetry.
Similarly the collaboration is involved in the measurement of the asymmetry of

the Dalitz plot between K^+ and K^- in the $K^\pm \to \pi^\pm\pi^0\pi^0$ decay. The study of this decay can also allow the measurement of the $a_0^0 - a_2^0$ scattering length as recently pointed out by Cabibbo [12]. Another goal of the experiment is the study of the form factors of the $K^\pm \to \pi^+\pi^- e^\pm\nu$ decay (also called K_{e4}), with statistics high enough ($\sim 10^6$ K_{e4}) to allow to measure the $\pi\pi$ scattering length parameter a_0^0 with an accuracy better than 1%. This measurement is related to to the size of the $q\overline{q}$ condensate of the QCD vacuum postulated in Chiral Perturbation Theory (χPT).
Many others rare decays are also studied, like:

$K^\pm \to \pi^\pm\pi^0\gamma$,
$K^\pm \to \pi^\pm\gamma\gamma$
$K^\pm \to \pi^\pm\pi^0\gamma\gamma$,
$K^\pm \to \pi^\pm\pi^0 l^+l^-$,
$K^\pm \to \pi^\pm l^+l^-$,
$K^\pm \to l^\pm\nu l^+l^-$

to test χPT predictions and also leptonic and semileptonic decays of the $K^\pm$, like:

$K^\pm \to e^\pm\nu_e$ (called K_{e2})
$K^\pm \to \mu^\pm\nu_\mu$ (called $K_{\mu 2}$)
$K^\pm \to \pi^0 e^\pm\nu_e$ (called K_{e3})
$K^\pm \to \pi^0\mu^\pm\nu_\mu$ (called $K_{\mu 3}$)

that allow the measurement of V_{us} element of the CKM mixing matrix, the testing of V-A structure of weak interactions and of lepton universality.

2.2 Lepton Universality

Lepton Universality describes the fact that, apart the mass, the three lepton families $\binom{\nu_e}{l_e^-}$, $\binom{\nu_\mu}{l_\mu^-}$ and $\binom{\nu_\tau}{l_\tau^-}$ have identical properties. This property is directly related to the structure of the fundamental fermion fields. Testing this universality might unveil the dynamics generating the observed fermionic structure.
The Standard Model gauge theory is based on the symmetry group $SU(3)_C \otimes SU(2)_L \otimes U(1)_Y$ describing strong, weak and electromagnetic interactions and it

assumes an universal structure for coupling of leptons and quarks to γ, W and Z bosons. No one questions today the universality of the coupling of the leptons to the photon, which is the fascinating universality of the electric charge. This property is indeed embedded in the QED theory which, however, is not related at all with the existence or the structure of leptons and quark families. Therefore, when electroweak interactions are taken into account, the situation might change, as its structure might be related with the particle spectrum. Experiments can nowadays test independently charged and neutral weak interactions, giving precious information or constraints on the physics beyond the Standard Model.

Recently, the existence of neutrino oscillation between the different families has been established experimentally and theoretical speculations suggest different form of lepton universality violation [14][15].

The Standard Model for electroweak interactions is based on the SU(2) $\otimes$ U(1) gauge theory, with gauge bosons W_i^μ $(i = 1, 2, 3)$ and B_μ and coupling constant g and $g^{'}$ coupling constant respectively for SU(2) and for U(1). The left-handed fermionic fields $\psi_i = \binom{\nu_i}{l_i^-}$ and $\binom{u_i}{d_i^{'}}$ of the i^{th} family transform as a SU(2) doublet, while the right-handed fields are SU(2) singlets. $d_i^{'}$ is defined as:
$d_i^{'} \equiv \sum_k V_{ik} d_k$, where V is the Cabibbo-Kobayashi-Maskawa mixing matrix.

Focusing the interest on the part of the Lagrangian describing the charged current of weak interactions of leptonic fields we obtain, after spontaneous symmetry breaking[1]:

$$-\frac{g}{2\sqrt{2}}[W_\mu^- \bar{l}\gamma^\mu(1-\gamma^5)\nu_l + W_\mu^+ \overline{\nu_l}\gamma^\mu(1-\gamma^5)l \qquad l = e, \mu, \tau$$

where g is the coupling constant for charged weak interactions. In its original form, Standard Model assumes $g = g_e = g_\mu = g_\tau$.

Many theoretical models and scenario foresee the possibility or even call for lepton asymmetry at tree or 1 loop level.

For instance, in Minimal Supersimmetric extensions of the Standard Model, the Yukawa coupling of the Higgs doublet with leptons, being proportional to lepton masses, explicitly violates universality [22]. Observable effects would be the different mass values for leptons and different coupling of Higgs scalar and Goldstone bosons to leptons.

[1]No extension of the Standard Model including neutrino masses has been included in the present Lagrangian formulation. In fact it is still not yet known whatever if neutrinos are Majorana or Dirac particles; hence the Standard Model extension is still not unique.

Recently, leptonic asymmetry has been included in theoretical scenarios accommodating NuTeV measurement of the effective neutrino-quark interaction coupling parameter g_L^2 with Standard Model prediction [14].

For example, in the framework of Seesaw model for neutrino masses and mixing, a breaking of the lepton universality at the level of $\Delta\frac{g_\mu}{g_e} \simeq 0.1\%$ would explain the actual 3σ discrepancy between NuTeV result and Standard Model prediction [16] .

2.3 V - A coupling

A priori, the interaction amplitude of 4 fermions under the hypothesis of locality, lepton number conservation and of a derivative-free Langrangian can contain up to 12 independent complex coupling constants [13] :

$$M = \frac{4G}{\sqrt{2}} \sum_{\gamma=S,V,T}^{\lambda,\mu=R,L} g^\gamma_{\lambda\mu} [\overline{q}_\lambda \Gamma_\gamma q^{'}][\overline{\nu_l} \Gamma^\gamma l_\mu] \tag{2.1}$$

The V - A structure of the weak interaction has been introduced for the first time by Feynman and Gell-Mann [17] to explain the Parity violation observed in nuclear β decay [19] .
In the present formalism, this vertex structure is interpreted as the coupling of the left-handed component of fermions with the charged bosons $W^\pm$, meaning that the number of coupling constants is drastically reduced to 1: $g^V_{LL} = 1$ and all other $g^\gamma_{\lambda\mu} = 0$.

For instance, the most natural and simple extension of the electroweak interaction is the $SU(2)_R \otimes SU(2)_L \otimes U(1)$, where parity symmetry is restored at some high energy scale. In this model the two SU(2) groups bosons W_R and W_L mix to generate W_1, the observed mediator of weak interactions, and W_2, a boson of higher mass.
Another simple extension is the contribution of the charged Higgs bosons which will contribute to the weak scalar currents proportional to g^S_{RR} and g^S_{LL}.

2.4 Experimental tests

The measurement at CERN in 1958 [18] of

$$R_\pi \;=\; \frac{\pi^+ \to e^+\nu(\gamma)}{\pi^+ \to \mu^+\nu(\gamma)} \tag{2.2}$$

represented a striking verification of the V-A structure and μ-e universality.
A conceptually identical test can come from the measurement of the ratio:

$$R_K \;=\; \frac{K^\pm \to e^\pm\nu(\gamma)}{K^\pm \to \mu^\pm\nu(\gamma)} \tag{2.3}$$

of the branching ratios of K_{e2} and $K_{\mu 2}$. The prediction depends only on kinematic factors and rather directly on the coupling of the leptons to the W boson (see Fig. 2.1).

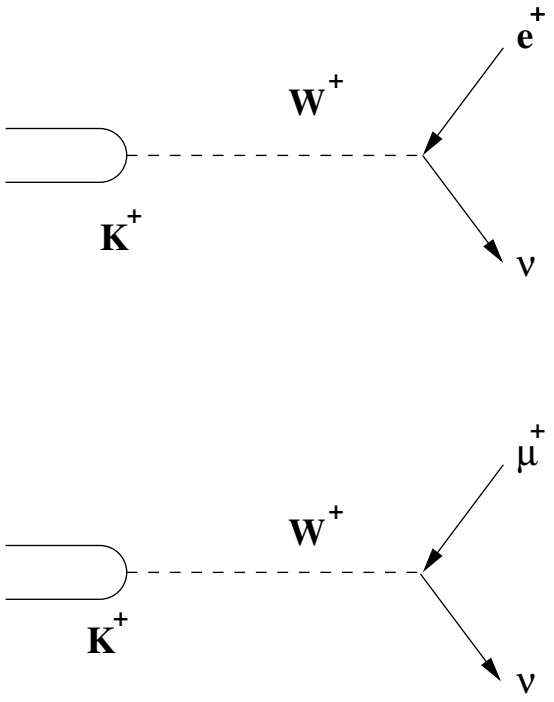

Figure 2.1: *Feynman diagrams of the K_{e2} and $K_{\mu 2}$ decays at tree level.*

An interesting feature of this measurement is that it is sensible only to the longitudinal component ($J_z = 0$) of the W exchange and thus it is complementary to other measurements, like the pure leptonic decay modes of the τ or the

leptonic decays of a real W, that receive contributions also from the transverse component of the charged current (see Fig. 2.2).

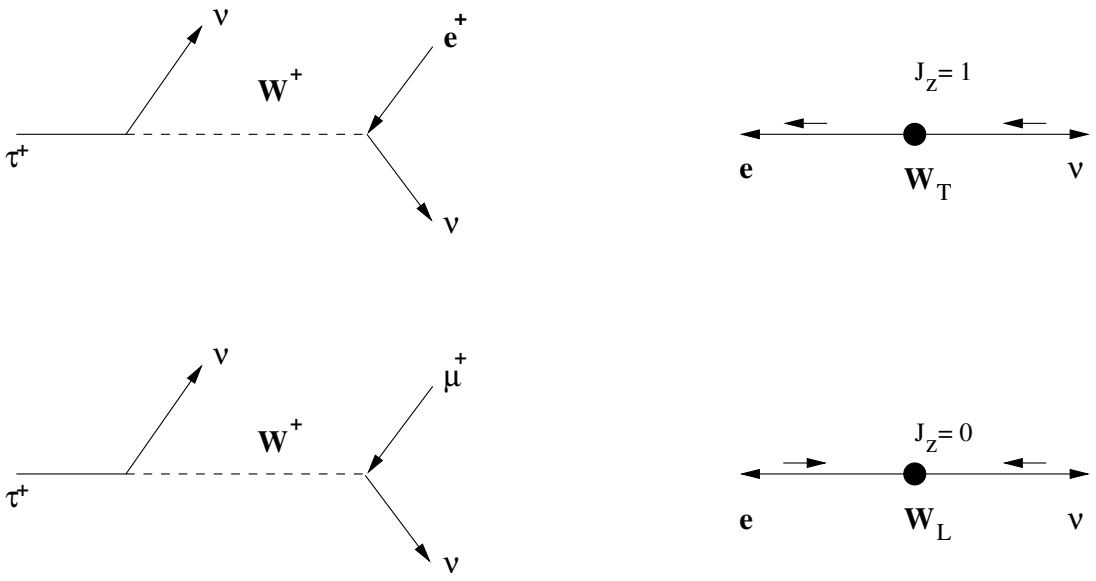

Figure 2.2: *Feynman diagrams of longitudinal and transverse components of virtual and real W decays.*

Theory predicts $R_K = \frac{\Gamma(K_{e2})}{\Gamma(K_{\mu 2})}$ with the convention of including all possible photon emissions contribution, but photon direct emission, that depends on Kaon structure.
The Standard Model prediction is:

$$R_K = R_{TreeLevel} \times (1 + \delta R_K) = (\frac{m_K^2 - m_e^2}{m_K^2 - m_\mu^2})^2 \frac{m_e^2}{m_\mu^2} \times (1 + \delta R_K) = \\ = 2.57 \times (1 + \delta R_K) \times 10^{-5}, \quad (2.4)$$

where δR_K, close to 0, is the radiative correction factor, that can be precisely calculated once the condition of the experimental measurement are properly specified.

PDG average [20] is based on the results from three experiments [25] [26] [27], all performed during the '70s, which carried out the measurement of the K_{e2} Branching Ratio and have tested the validity of the theoretical prediction of the ratio R. The published results, well compatibles with the Standard Model

predictions, are:

$R_K = \Gamma(e^+\nu(\gamma))/\Gamma(\mu^+\nu(\gamma))$		
Publication	Events	Value of R_K (in units of 10^{-5})
Clark et al. (1972)[25]	112	2.45 ± 0.42
Heard et al. (1975)[26]	534	2.37 ± 0.17
Heintze et al. (1976)[27]	404	2.51 ± 0.15
PDG Average		2.45 ± 0.11

As can be seen from the Table above, the K_{e2} Branching Ratio is presently known only at the level of 5%, where the precision of the measurement is dominated by the statistical error.
In the months before the beginning of the data collection, the NA48/2 collaboration had investigated the possibility of an improvement of the accuracy of this measurement, given the large statistics of charged Kaon decays that it was expecting to collect and realized that the experiment could have easily collected a statistics much higher than the combined one of the previous experiments.
Moreover, the past measurements had been carried out only with positive Kaons, while in NA48/2 experiment positive and negative Kaons are simultaneously present in the beam, allowing concurrent K^+_{e2} and K^-_{e2} Branching Ratio measurements.

Chapter 3

Experimental Set-up and Apparatus

The NA48/2 apparatus and beam line are an upgraded and modified versions of the previous NA48 experiments.
The experiment is installed in the ECN3 hall in the North Area of the SPS site at CERN.
The improved set-up includes a new beam line, two new detectors, an extended decay region, the full instrumentation of all planes of the third drift chamber (DCH3), the remapping of the drift chamber electronics in order to be left-right symmetric and the improvement of the level 2 charged trigger system (MBX). The two new detectors are KABES, a TPC detector used to measure momentum and position of the incoming charged Kaons (see section 3.2.1) and the Beam position monitor, a 2×64 pixel scintillator detector employed to monitor on line with high resolution the position of the beam (see section 3.3.8).

3.1 Simultaneous K^+/K^- beams

The beam line, shown in Fig. 3.1, represents the most innovative element of the experimental setup.

The primary protons, produced by the SPS accelerator, have a nominal momentum of 400 GeV/c, the machine has a period of 16.8 s and a flat top of 4.8 s. The beam line has been designed to deliver simultaneous positive and negative beams of 60 GeV/c of average momentum. The target, where the charged par-

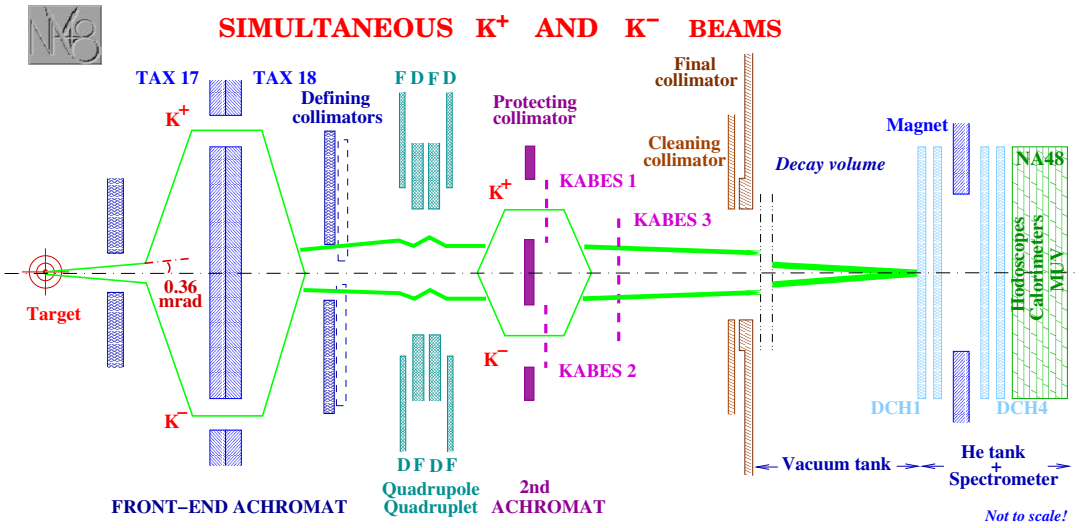

Figure 3.1: *Vertical view of the NA48/2 simultaneous K^+/K^- beams. The positive and negative beams are split and selected in momentum at the first achromat, then they pass into a defining collimator and are focused by magnetic quadrupoles. KABES is located downstream the focusing quadrupoles in the middle (for station 1 and 2) and 8 m after the second achromat. The positive and negative particles follow overlapping trajectories in the fiducial decay region.*

ticles are produced, is installed in the T10 target station. The target is a beryllium rod of 2 mm diameter and 400 mm length, corresponding to one interaction length for protons. The angle of the impinging protons is zero degrees relatively to the experiment beam line, while the acceptance angle is of ± 0.36 $mrad$ in both planes, defined by a collimator placed at 24 m from the target. The 400 GeV/c proton beam intensity is $7 \cdot 10^{11}$ ppp.

Upstream the defining collimator, neutral particles are dumped and the momentum of the charged ones is selected by an 'achromat' system, constituted by 4 dipole magnets with zero net deflection. The collimators in the middle of the achromat, where the beam is split, select for both signs a momentum band centered around 60 GeV/c and has an r.m.s. of $\pm 3.8\%$.

Instead of a parallel charged beam, as proposed at the beginning [28], the NA48/2 collaboration concluded that for the experiment purpose would be preferable a beam 'focused' in such a way to have a spot size at the spectrometer position of only $\sim$ 5 mm (r.m.s.) as shown in Fig. 3.2. In this way any transverse structure of the beam (the beam spot of the parallel beam had a r.m.s of $\sim$ 2 cm) has been minimized. The beam focusing has been realized with a system of four

quadrupoles of alternate polarity that gives to the beam an angle of convergence of $\sim$ 0.04 *mrad*. The beams are steered in such a way to coincide to better then 2 mm at the end of the decay region as can be seen in Fig. 3.20.

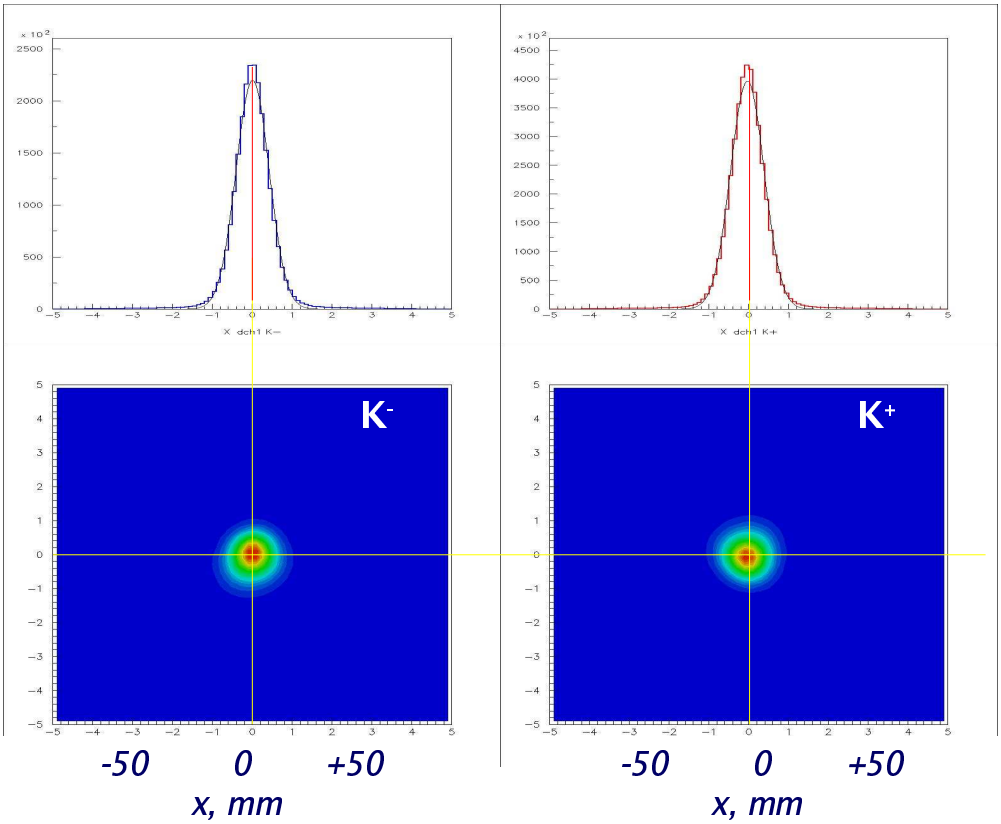

Figure 3.2: *Beam spot at the spectrometer position for K^+ and K^- particles.*

Both cleaning and final collimator are placed roughly 100 m after the target position. The fluxes at the final collimator are shown in Table 3.1.

The particles cited as 'Other' in the list are mainly muons in the halo of the beam not swept away by the muon sweeper, installed upstream of the final

Particle fluxes		
Particle	Particles per pulse in units of 10^6	
	+	-
K	2.2	1.3
π	23	17
p	6.1	0.6
e	6.0	6.0
Other	~ 1	~ 1
Total	38	26

Table 3.1: *Fluxes of positive and negative particles at the beginning of the decay region.*

collimator. The flux of muons at the detector position coming from π and K decays in the 114 m of the decay region is $\sim 2.5 \cdot 10^5$ ppp/m^2.

3.2 Detectors

3.2.1 KABES - Beam momentum Measurement

KABES (KAon BEam Spectrometer) is a TPC detector using MICROMEGAS [29] with an amplification gap of 50 μm (see Fig. 3.3).
The necessity for a detector of this sort in the NA48/2 experiment arises mainly for resolution enhancement in rare decays studies, where it is crucial to have the best possible separation of the signal from the background. This detector also allows to measure A_g (defined in Section 2.1) using samples of events where only two of the three pions are detected.
The KABES detector is made of three double stations, each of them recording the passage time of the particle and its vertical and horizontal coordinates. Two stations are placed in the center of the second achromat, where positive and negative beams are displaced vertically and nearly parallel. The third station is located downstream the achromat, where the positive and negative beams are again collinear. The momentum of the beam particles is measured by the difference of the vertical coordinate measured in station 1 or 2 and in station 3.

The gas mixture employed is $Ne(79\%) + C_2H_6(11\%) + CF_4(10\%)$, similar to

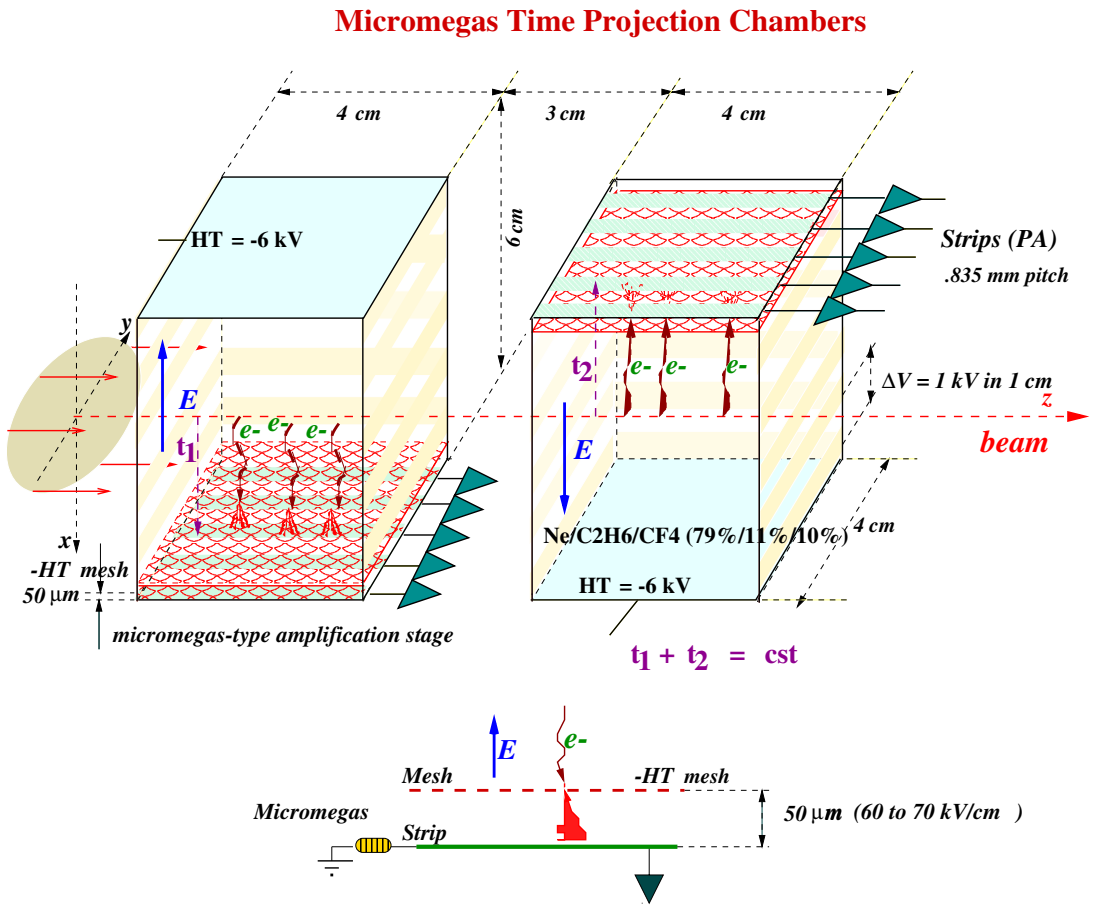

Figure 3.3: *Principle of NA48/2 MICROMEGAS Time Projection Chamber functioning.*

the one used by COMPASS micromegas detector. The peak hit rate of the strips located in the center of the beam spot at KABES station 3 is $\sim$ 2 MHz.
The read-out electronics employs the HPTDC (High Performance TDC) chip, developed at CERN [30]. The system is designed in VME standard and it is able to stand a rate per single strip of 8 Mhits/s and a total rate of 40 Mhits/s. The control of the system is done remotely using a normal desktop PC equipped with an optical S-link interface and an S-link to PCI card converter.

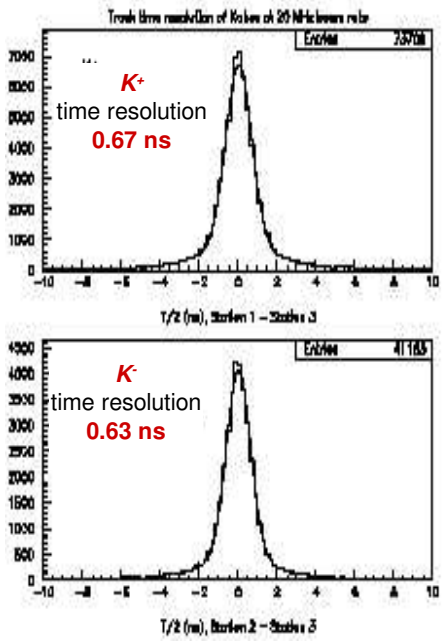

Figure 3.4: *Kabes time resolution*

The performances of the KABES system at nominal proton intensity of $7{\cdot}10^{11}$ ppp[1] are:

Measure	Resolution (r.m.s.)
Horizontal position	100 μm
Vertical position	130 μm
Time	$\sim$ 0.65 ns

The momentum resolution of the KABES system has been evaluated studying the $K^{\pm} \to \pi^{\pm}\pi^{+}\pi^{-}$ decays. The measured K momentum has been compared to the sum of the 3 pion momenta measured by the spectrometer. The convolution of the two resolutions has been found to be 1.1 % (see Fig. 3.5).

3.3 Decay region

The NA48/2 decay region, schematically reproduced in Fig. 3.6, is contained in a cylindrical tank (called *blue tube*) of diameter 1.9 m, increasing to 2.4 m in its

[1]As seen in Table 3.1, this corresponds to a rate of 7.9 Mhit/s

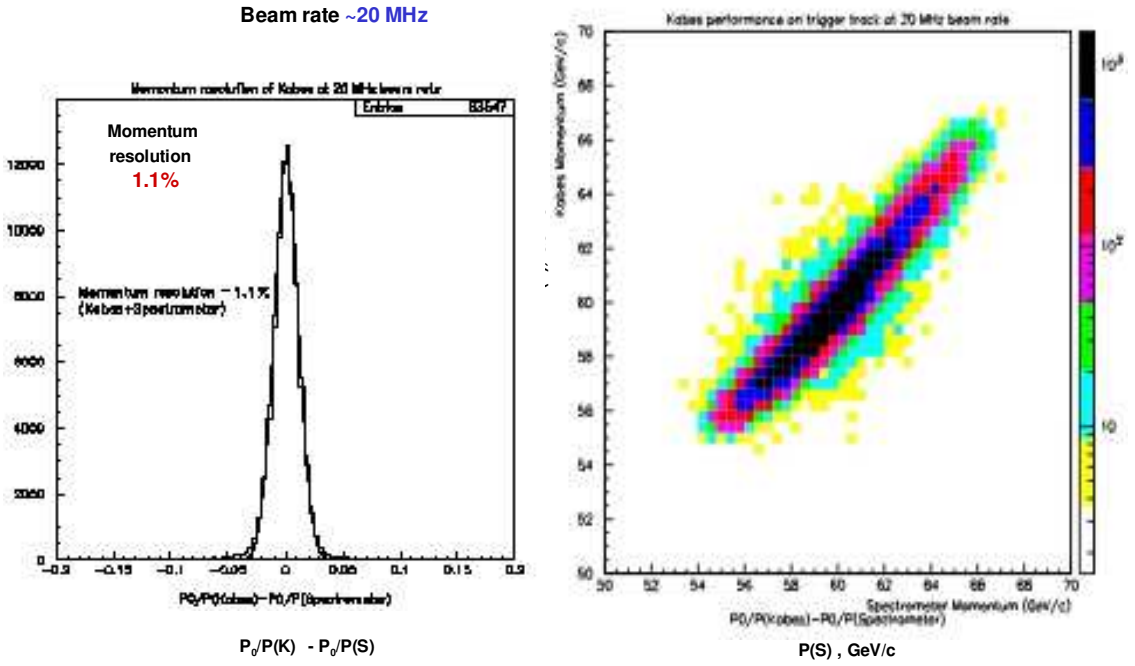

Figure 3.5: *[Kabes - Spectrometer] momentum resolution and Kabes versus spectrometer momenta. The r.m.s. quoted in the first plot is the convolution of the two resolutions (Kabes+Spectrometer).*

last 48 m. Its total length is 111 m and it is evacuated to a pressure $< \ 10^{-4}$ mbar, avoiding that the products of Kaon decays interact with matter before having reached the detectors.

The downstream end of the decay region is closed by a thin Kevlar window, separating the vacuum from the volume of the magnetic spectrometer, filled in

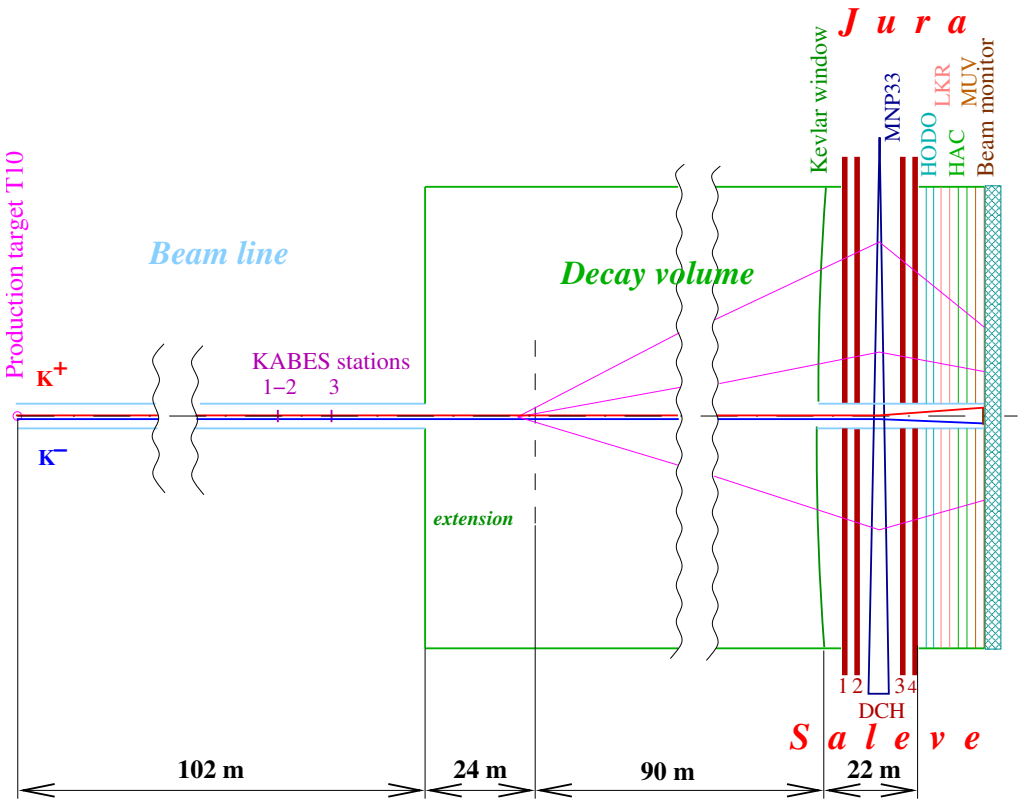

Figure 3.6: *Schematic view of the NA48/2 decay volume with the 24 m extension in evidence.*

with Helium at atmospheric pressure. The window has a convex hemispherical shape of 1.3 m of curvature. The thickness of the window is of 0.9 mm, corresponding to $3 \cdot 10^{-3}$ radiation lengths. Downstream the Kevlar window the beam continues in vacuum contained in a carbon fiber beam pipe of 152 mm diameter and 1.2 mm thick.

A small residual magnetic field, mostly due to Earth field, is present in this region. During 2003 winter it has been carefully measured and mapped in order to allow its effect correction in the analysis of the 3π A_g measurement and to include its map in the experiment Monte Carlo simulations. In Fig. 3.7 the values of the residual magnetic field x and y component are reported.

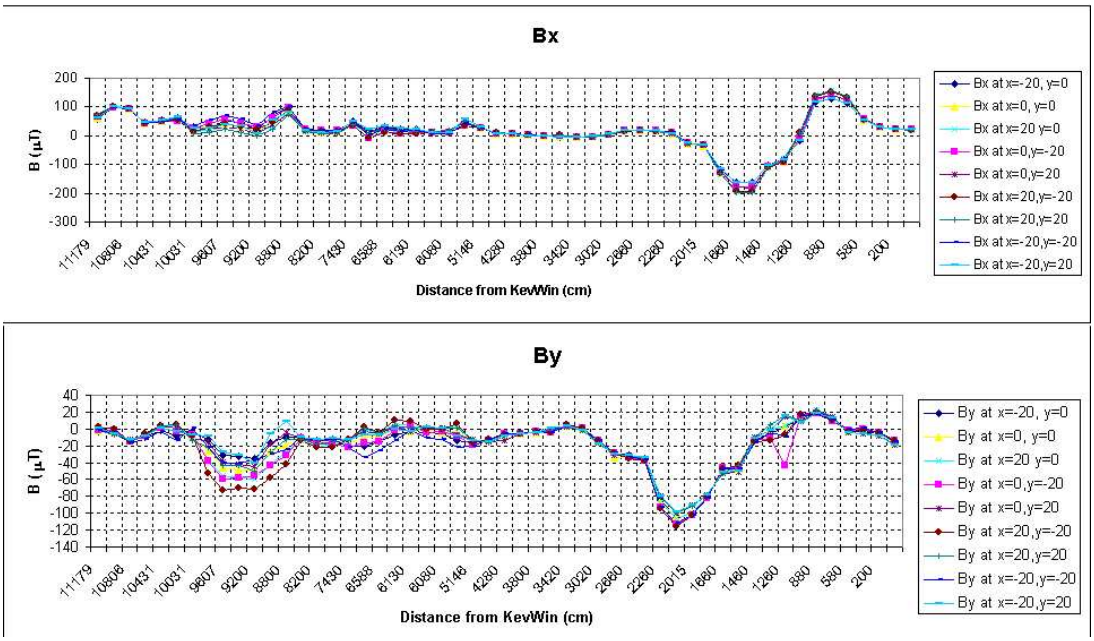

Figure 3.7: *Residual Magnetic Field x and y component. The different colors correspond to different x and y value at which the measurement has been effectuated.*

3.3.1 AKL anti-counters

The AKL anti-counter system consists of 7 rings (pockets) of iron and scintillators placed between the final collimator and the electromagnetic calorimeter. Each pocket is composed of two layers of scintillator, preceded by a steel plate 3.5 *cm* thick acting as photon converter. Each layer is composed of 12 plastic scintillators 10 *mm* thick for pockets 1 to 4 and of 8 scintillators for layers 5 to 7. In total, 144 counters are present. The placement of the pockets was designed to veto most of the photons and charged particles outside the acceptance of the $K_L \to 3\pi^0$ decays during $\epsilon^{'}/\epsilon$ data taking (see Fig. 3.8).

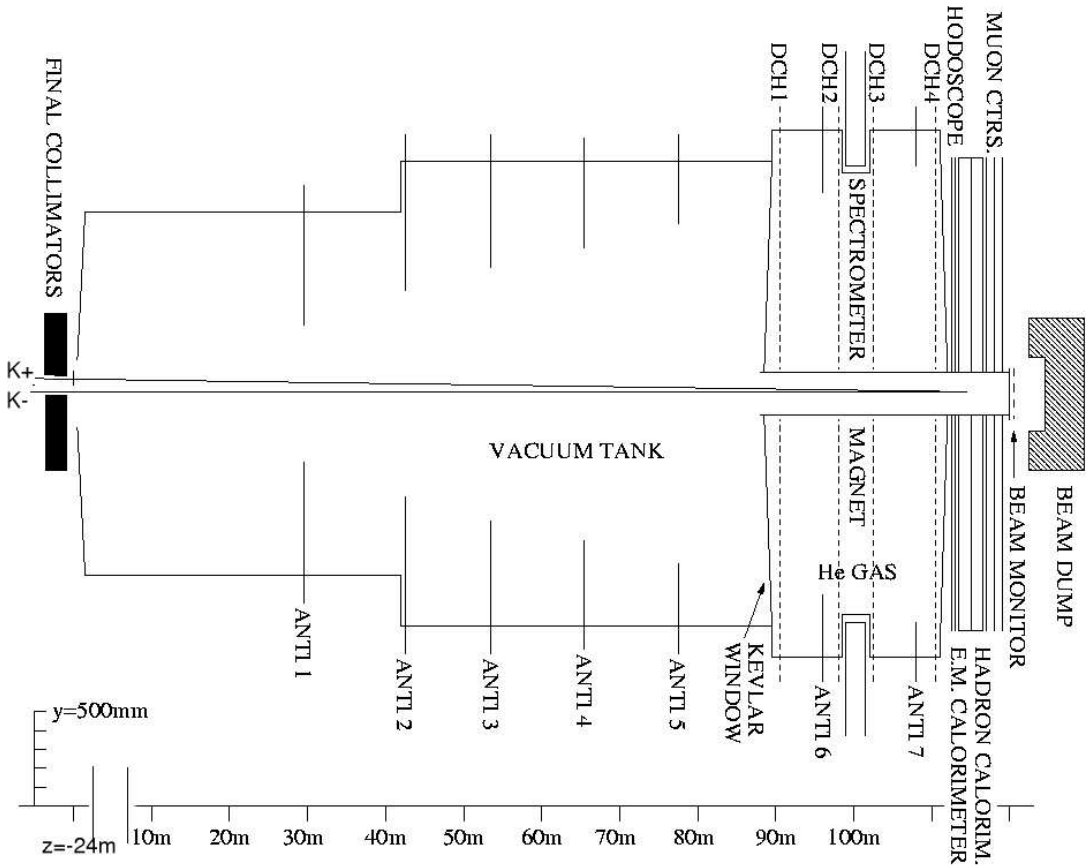

Figure 3.8: *Decay region and AKL rings (pockets) position. The location of AKL pockets had been chosen in order to veto completely the region outside the central detector geometrical acceptance for decay originating from the middle of the former K_S decay region during ϵ'/ϵ data taking.*

Central Detectors

The placement of the elements of the NA48 central detectors is shown in Fig. 3.9. The Kevlar window separates the evacuated decay region from the region filled with Helium at atmospheric pressure (Helium Tank), where the wire chambers and the magnet are placed. The Helium Tank is at atmospheric pressure, because the drift chambers composing the magnetic spectrometer are not able to stand a large pressure gradient. The choice of He as filling gas has been done in order to minimize the multiple scattering and the probability of beam particle interaction with the medium[2].

3.3.2 Magnetic Spectrometer

Four high resolution drift chambers (DCH) equip the magnetic spectrometer. A dipole magnet (Fig. 3.10) of p_T kick equal to $\sim$ 120 MeV/c is placed in the middle of the spectrometer, between DCH2 and DCH3.
In order to reduce systematic effects linked to apparatus acceptances and efficiencies, the magnetic field has been inverted in polarity every 24 hours during 2003 data taking and every $30 \cdot 10^6$ collected triggers ($\sim$ 3 hours) during 2004 data taking. The value of the magnetic field intensity and its correct inversion is monitored by Hall probes placed inside the Helium Tank.

The drift chambers have an octagonal shape, the length from side to side is 121 cm. The chambers are composed of 4 views, along the orthogonal directions $x,\ y$ and along the directions $u,\ v$ rotated of $\pm 45^o$ with respect to the x axis in order to remove possible ambiguities in track reconstruction (see Fig. 3.11). Each view is equipped by 2 planes shifted by half the sense wire pitch, in such a way to remove the left right ambiguity and therefore increasing the resolution of the reconstructed space points. Each plane contains 256 wires each. The maximum drift distance is 5 mm (corresponding to a drift time of 100 ns). The chambers are filled in with a mixture of $Argon$ (50%) + $Ethane$ (50%).

The resolution on the spatial position of the space points is $\lesssim$ 100 μm. The fast rise time of the pulses and the response of the time-to-digital converter are such to allow a time resolution of 0.7 ns.
The momentum resolution, for tracks reconstructed with magnet p_T kick of

[2]The radiation length of the Helium at n.p.t. is $L_0 = 5.3$ km.

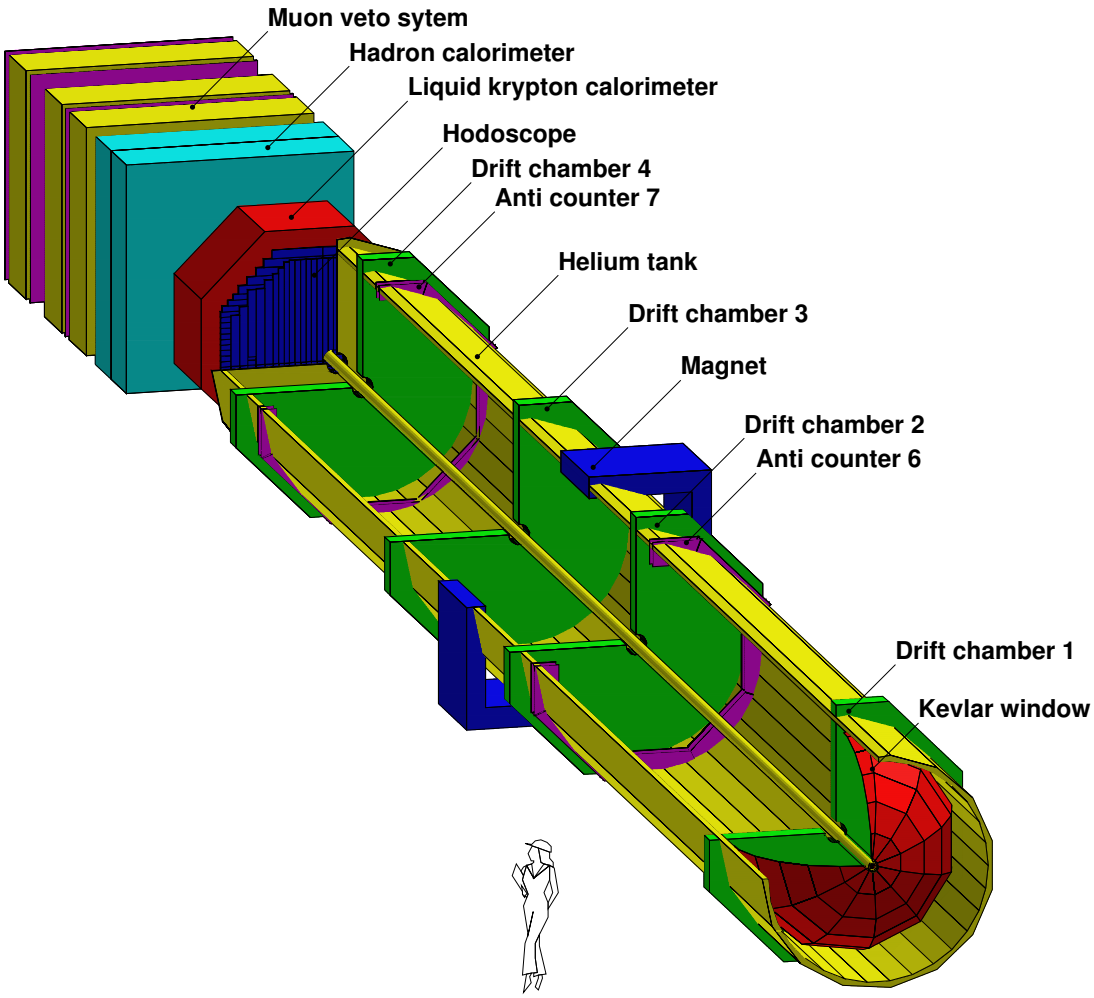

Figure 3.9: *NA48 detectors. Charged particle momentum measurement is performed by the magnetic spectrometer, time measurement by charged hodoscope and muon ID by muon veto. Photons are detected by the Liquid Krypton calorimeter and the embedded Neutral Hodoscope.*

120 MeV/c, is estimated to be:

$$\frac{\sigma(P)}{P} = 1.0\% \oplus 0.044 \cdot P(GeV)\% \tag{3.1}$$

The first term is related to the multiple scattering, while the second one is due to the accuracy on the space point measurement. The resolution of the $K^{\pm}$ mass obtained from the $K^{\pm} \to \pi^{\pm}\pi^{+}\pi^{-}$ decay reconstruction is 1.7 MeV/c^2 (see Fig. 3.12).

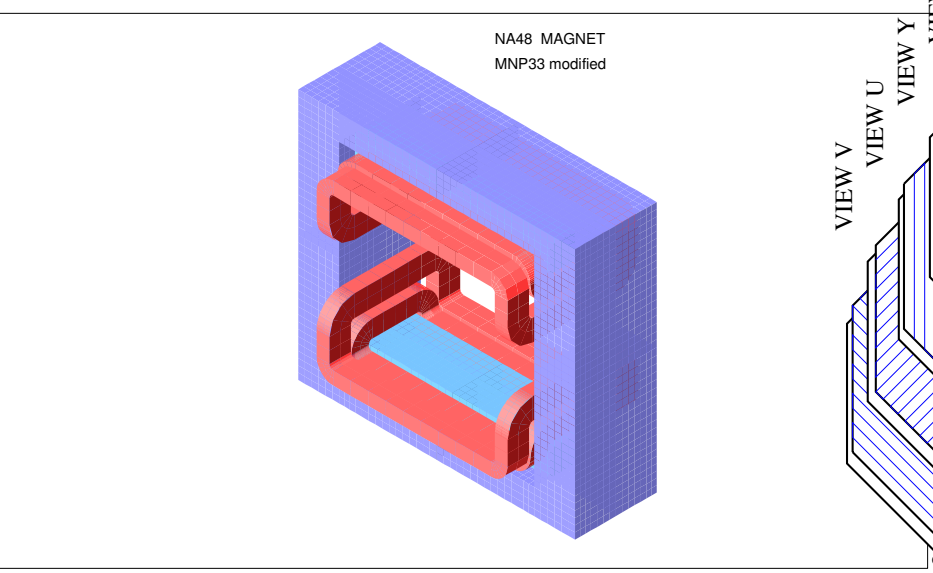

Figure 3.10: *Dipole magnet of the NA48 experiment.*

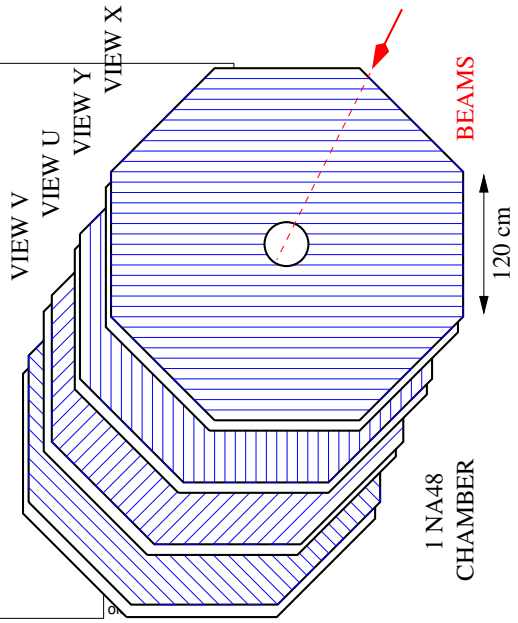

Figure 3.11: *Orientation of the drift chamber views.*

3.3.3 Charged Hodoscope

The charged hodoscope provides a fast trigger for charged events and it is used as reference time detector both in the online and offline reconstructions. It is placed downstream the 'Helium tank', in front of the LKr calorimeter.

The hodoscope, as shown in Fig. 3.13, is composed of two planes, one horizontal plane and one vertical plane. Each one of them is composed of 64 plastic scintillators and is divided in 4 quadrants of 16 counters. Each counter is 2 cm thick, corresponding to 0.05 L_0; the length vary in the range 60 cm to 121 cm and the width in the range 6.5 cm to 9.9 cm. The distance between the two planes (75 cm) and the distance of the second plane with respect to the calorimeter (80 cm) has been chosen in order to reduce the effect of any possible back splash from the calorimeter front end.

The combination of the signals from the 4×4 quadrants of the two planes gives raise to different trigger logics. A single track event will generate a $Q1$ trigger signal if a quadrant for each view of the hodoscope is activated by the passage of a particle and only if the two quadrant are geometrically compatibles.

The Hodoscope single event time resolution is $\sim$ 150 ps.

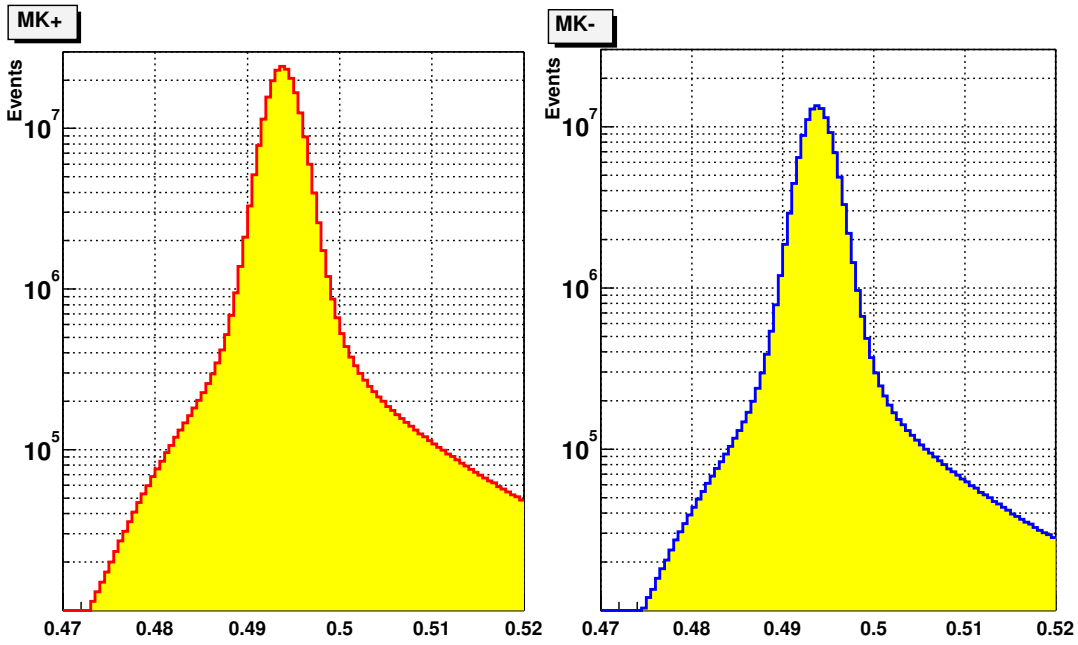

Figure 3.12: *K^+ and K^- masses reconstructed from $K^\pm \to \pi^\pm\pi^+\pi^-$ decay.*

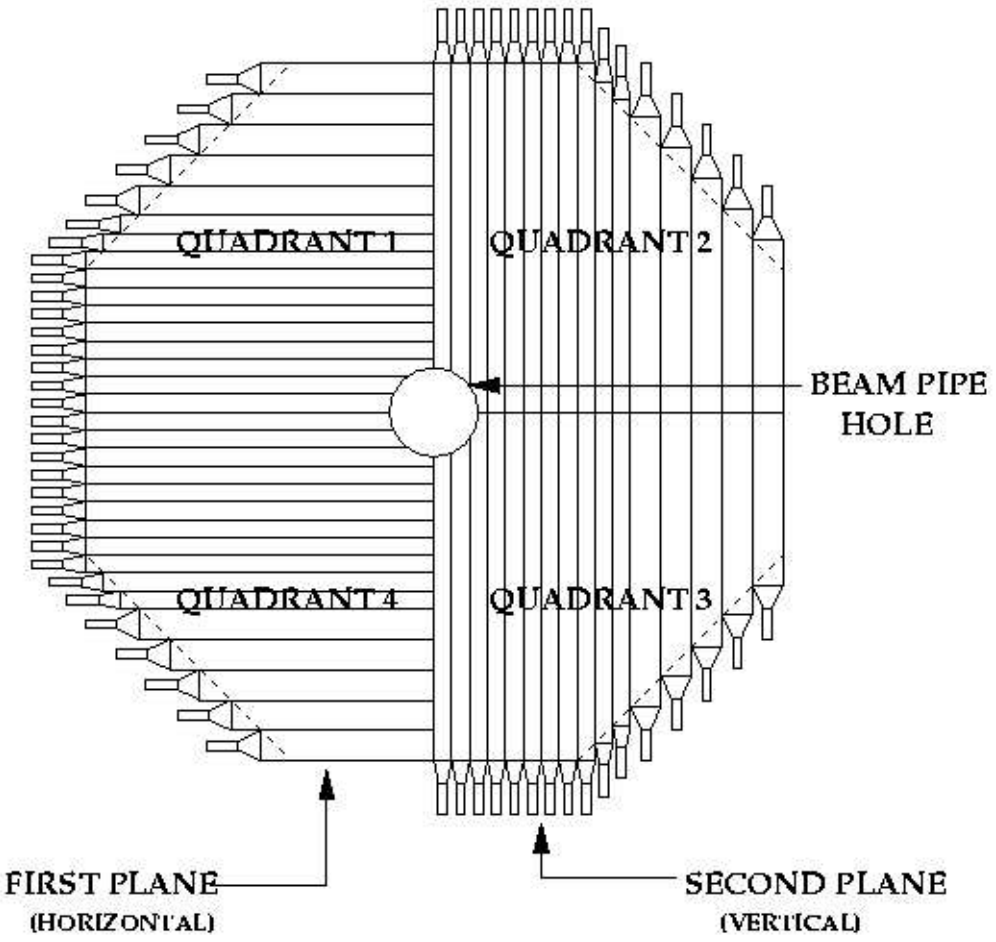

Figure 3.13: *Hodoscope layout.*

3.3.4 The LKr electromagnetic calorimeter

The NA48/2 electromagnetic calorimeter is a quasi homogeneous liquid Krypton ionization chamber. The choice of employing a liquefied noble gas is due to the linearity response in energy of the detector, to the absence of aging problems and to the relative short radiation length which allows a compact design without the need of heavy passive parts, typical of sampling calorimeters. Working at cryogenic temperature greatly increases the stability of the detector response and accuracy of its calibration.

Calorimeter Description

The shape of the calorimeter is approximately octagonal (see Fig. 3.14) and its total volume is of 9 m^3. The active part of the calorimeter is 127 cm long corresponding to 27 radiation length (X_0)[3]. It is divided into 13248 cells by Cu-Be-Co ribbons of dimensions: $40\mu m \times 18\ mm \times 127cm$ (see Fig. 3.15). The dimension of each cell is 2 $cm \times$ 2 cm. The cells increase in transverse dimensions as a function of the distance from the front of the calorimeter up to a maximum of 1.1% at its back. They define a projective geometry of the calorimeter pointing at about 90 m in front of it, inside the decay region. This particular geometry has been realized in order to achieve the best possible accuracy in the measurement of the angle between the flight path of photons and the beam direction.
In order to ensure a good uniformity of the response over the whole front surface of the calorimeter, the distance between electrodes must be known with high accuracy. For this reason the electrode ribbons are passed through spacer plates that fix their transverse position at 5 longitudinal positions in addition to the front and back planes. The tension of the ribbon is $\sim 2\ N$. The passage through the spacing plates, gives to the electrodes a peculiar 'zig-zag' shape that minimizes inefficient ionization of the showers developing along the anode.
In the middle of the cells (cathodes) is placed a collecting anode to which is applied a voltage of 3 kV. Only the initial part of the current induced by the electromagnetic shower is read-out by the electronic chain in order to improve the time resolution.

[3] A shower of 50 GeV energy deposits 95% of its energy in 24 radiation lengths.

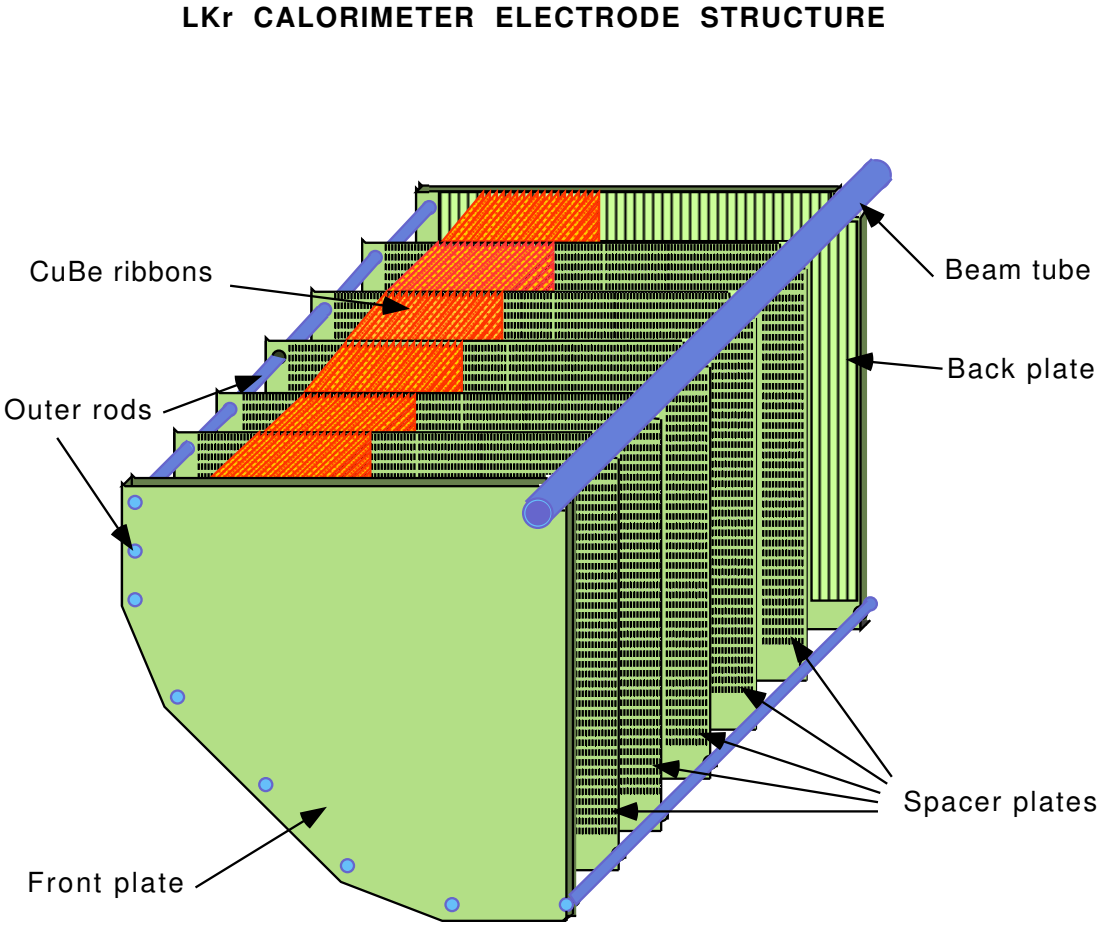

Figure 3.14: *Layout of Calorimeter longitudinal structure.*

Cryogenics

The boiling temperature of the Kr at normal pressure is 119.8 K, while the variation of drift speed of the electron is of $-0.87\%/\mathrm{K}$. Therefore the calorimeter has been enclosed in a cryostat, composed by an outer aluminium vessel and a vacuum insulated inner stainless steel container, which keeps stable the temperature of the LKr calorimeter at 121 K to within ± 0.1 K.

Calorimeter Read-out

The calorimeter read-out has no dead time. Asynchronous digital sampling of the output signals is done every 25 *ns* by a 10 bit FADC with automatic gain

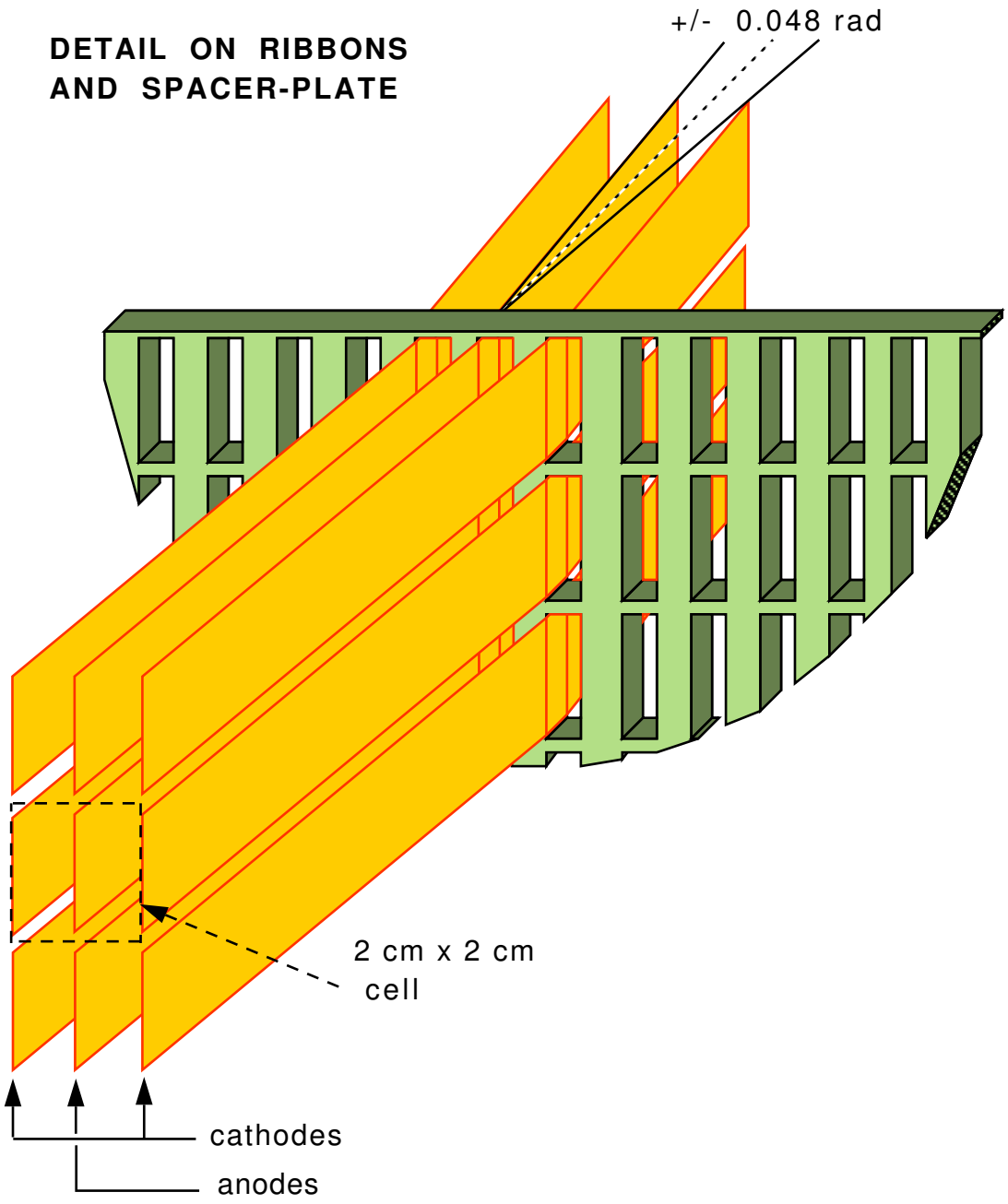

Figure 3.15: *Calorimeter ribbon and spacing plate detail. The cells of the LKr calorimeter are defined by the distance of the cathodes ribbons and the width of the ribbons.*

switching. Two more bits are used to record the gain of the amplifier, increasing the dynamic range of the system. The digitalized signals are stored in a 3.2 μs

deep pipeline memory for each cell and are sent to a dedicated processor, called Data Concentrator that operates a 'zero-suppression' on the cell signals below a certain threshold and apply a cluster finder algorithm to the cells above threshold. In this way it is possible to reduce to ~ 100 the number of cells read for each electromagnetic shower.

Dead Cells

A small fraction of the 13248 cells of the LKr calorimeter, known as *dead cells*, has electronic faults preventing their correct calibration and utilization. Their number is in the order of 60 (see Fig. 3.16) and the most common problems are faulty preamplifiers, no calibration, bad pedestal and/or a very unstable response to calibration pulses.

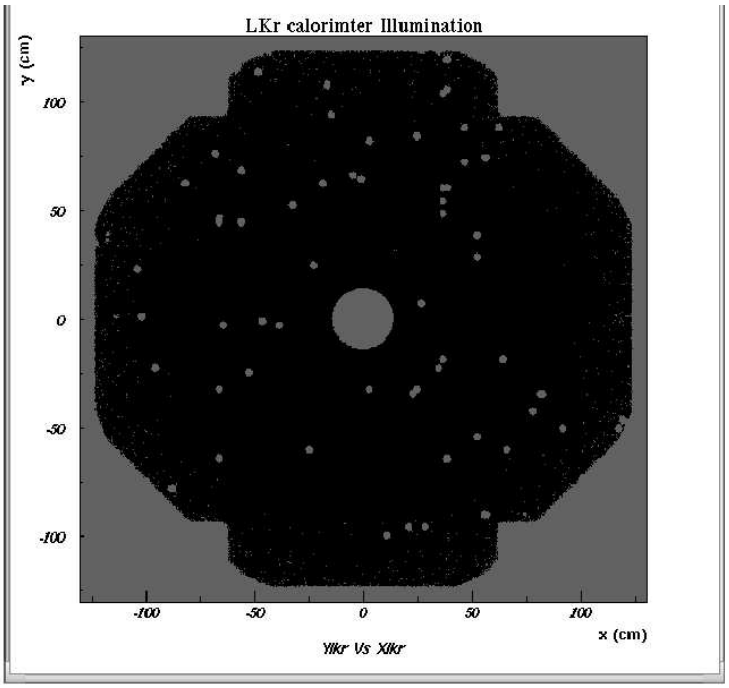

Figure 3.16: *Calorimeter illumination by* $K^{\pm} \rightarrow \pi^{\pm}\pi^0\pi^0$ *events The low intensity spots identify the location of the dead cells, while the outer shape of the calorimeter is given by the fiducial cut on the distance from the borders of the calorimeter.*

Calorimeter Performances

The imperfection of the linearity response of the calorimeter and the cells inter calibration have been measured by comparing the electron energy from $K_L \to \pi^{\pm} e^{\mp} \nu_e$ ($K_L e3$) decay as measured by the calorimeter with the momentum measured by the spectrometer. In Fig. 3.17 the average electron E/p in the range 5 GeV - 100 GeV is plotted.

The resolution in energy has been calibrated and checked with $K_L e3$ events (see Fig. 3.18) and with special η runs, where η particles decaying in $\gamma\gamma$ and $\pi^0\pi^0\pi^0$ are produced by hadronic interaction in two polythene targets placed for this purpose at known positions and employing a special charged hadron beam. In 1997 the energy resolution of the calorimeter was also tested with an electron beam of 0.1% momentum bite at adjustable values of the average momentum. The results are reported in the Table below:

Energy (GeV)	$\sigma(E)/E$ (%)
15	1.29
25	0.93
50	0.67
100	0.57

The energy resolution of the calorimeter can be parametrized as:

$$\frac{\sigma_E}{E} = \frac{0.09}{E_{(GeV)}} \oplus \frac{0.032}{\sqrt{E_{(GeV)}}} \oplus 0.0042 \tag{3.2}$$

where the first contribution is mainly due to electronic noise and Kr radioactivity, the second is the typical poissonian term coming from the stochastic fluctuations and the last one comes from the non perfect inter-calibration of the cells.

Space resolution of the showers has been measured comparing the extrapolated track of electrons from a special calibration run with the reconstructed center of energy deposition, yielding the following result:

$$\sigma_{x,y} = (\frac{4.2}{\sqrt{E(GeV)}} \oplus 0.6)\ mm \tag{3.3}$$

Summarizing, the performances of the LKr calorimeter are such that the impact point of a photon of 20 GeV is known with a precision of 1 mm and its energy is measured with the precision of $\lesssim 1\%$, while the average time resolution

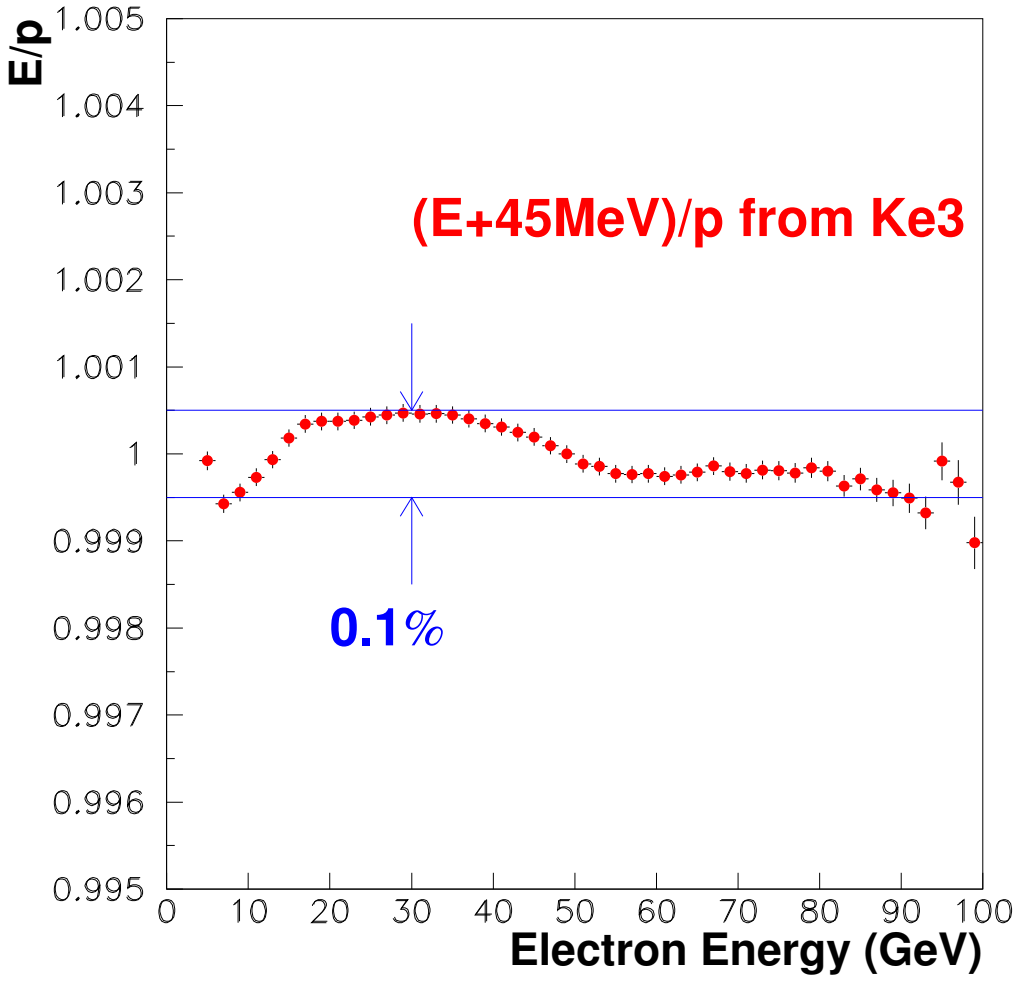

Figure 3.17: *Calorimeter non linearity as a function of the energy. The small 45 MeV compensation takes into account the average loss of energy due to the passage of the particles in the passive matter in front of the active part of the Krypton calorimeter.*

for a single electromagnetic cluster is in the order of 500 *ps*.

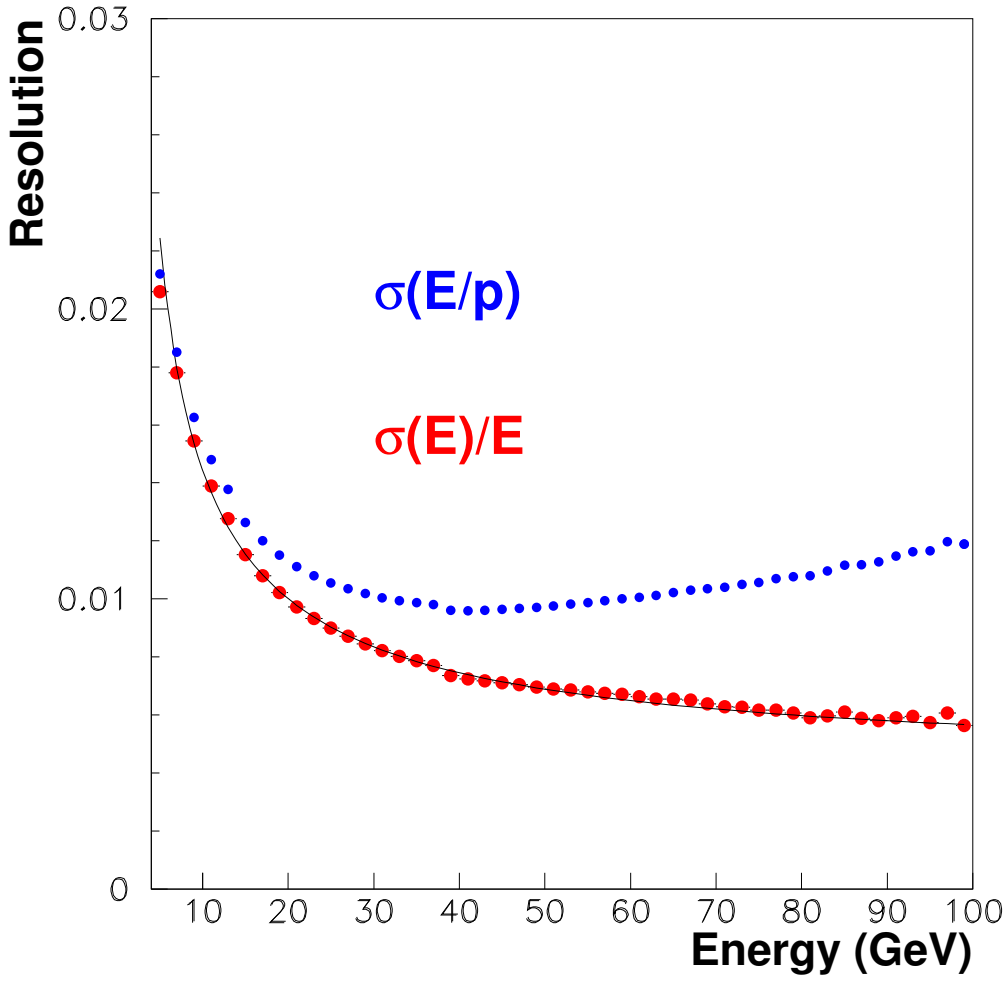

Figure 3.18: *Calorimeter energy resolution as a function of the energy for* $K_L e3$ *electrons .*

3.3.5 The Neutral Hodoscope

The neutral hodoscope is made of 256 bundles of scintillating fibers immersed inside the LKr volume at the depth of 9.5 X_0, where the shower of photons of 25 GeV reaches its maximum development. The signal is read by 32 photo-multipliers. The hodoscope is divided in 4 quadrants (8 read-out channel each) and it is used as an independent time signal source and as a trigger of minimum bias (called T0N), especially useful to measure the efficiency of primary trigger

systems. The typical time resolution is better than 250 ps for showers of energy greater than 15 GeV.

3.3.6 The Hadronic Calorimeter

NA48 employs a conventional iron-scintillator sampling calorimeter (see Fig. 3.19) to measure hadron energies. It is placed downstream the LKr calorimeter and it is composed of a front module and a back module. Each of them is composed of 24 iron planes alternated to an equal number of scintillator planes. The active area of the calorimeter is $2.7 \times 2.7\ m^2$. Each iron plane is 2.5 cm thick, for a total of 1.2 m (~ 7 hadronic interaction length). Its energy resolution for hadronic particles is:

$$\frac{\sigma(E)}{E} = \frac{65\%}{\sqrt{E_{(GeV)}}}$$

3.3.7 The Muon Veto

The NA48 muon veto was used during ϵ'/ϵ data taking to veto $K_L\mu 3$ decay. It is composed of three planes of scintillators, each one covering a surface of $2.7 \times 2.7\ m^2$. The first two planes are composed of 11 plates of plastic scintillators 1 cm thick, while the last one is composed of 6 plates 6 mm thick. In the first and third planes the scintillators are placed horizontally while in the second one they are vertical. Each plate of scintillator is connected to two photomultipliers placed at its extremities. In front of each scintillator plane there is an iron wall 80 cm thick (corresponding to $\sim$ 5 interaction length).
The time resolution of the Muon veto is $\sim$ 700 ps.

3.3.8 The Beam position Monitor

Beam stability is an important issue in the NA48/2 experiment. The beam position monitor has been designed and built in order to satisfy the need of a fast feedback of the beam steering and of an on-line check of the two beams position and geometry.
The monitor is composed of two 8×8 matrices of plastic scintillator blocks. Each pixel is 6 mm $\times$ 6 mm in transverse dimension and 9 mm thick. The two matrices are kept at a relative distance of $\sim$ 100 mm, which is the typical separation of the two charged beam at the end of the beam line. They can be

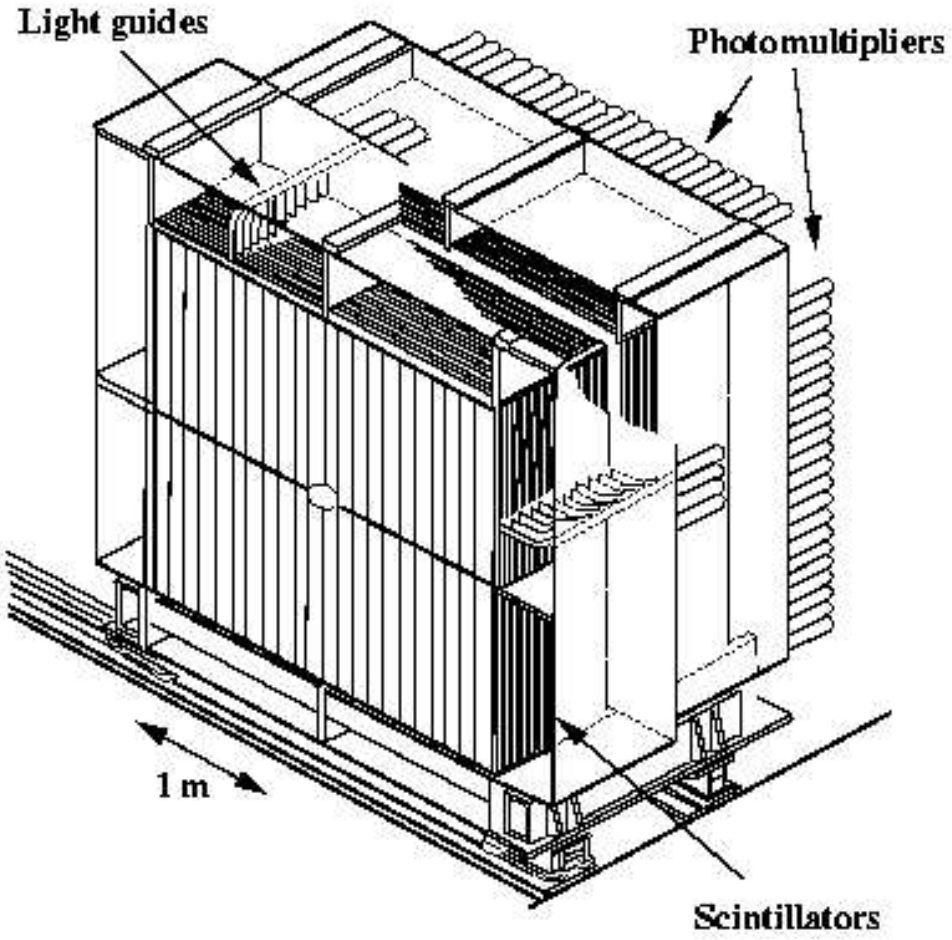

Figure 3.19: *Hadronic calorimeter layout.*

moved remotely in the horizontal direction (independently) and in the vertical direction (by common displacements).
The scintillator pixels are separated by aluminum foils in oder to keep the optical cross talk as low as possible. The light from the scintillators is collected by two 8×8 multi-anode PMTs. The supply voltage in 2003 was set at 650 V, corresponding to a gain of $\sim 1.5 \cdot 10^5$. The gain of each pixel is not uniform and one 8×8 filter mask has been applied on the scintillators in order to compensate the gain variation.
The residual non-uniformity is at the level of 10%.

The beam monitor read-out is composed of amplifiers. Discriminator circuits are housed on 8 daughter cards and one mother board displaced by 70 *cm* from the two matrices in order to avoid radiation damage[4].
The detector is able to measure displacement of the center of gravity of the beam at the level of 0.1 *mm*.
The detector proved successful in detecting the beam displacement within the burst. This displacement is due to the movement of the primary proton beam impinging on the T10 target.

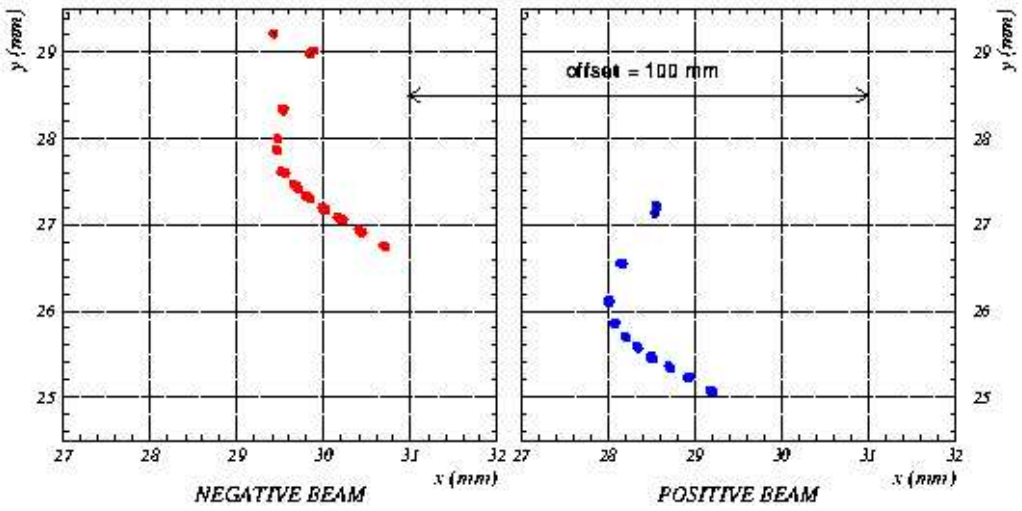

Figure 3.20: *Center of gravity for positive and negative beam within the burst. They show a common anti-clockwise displacement due to the movement of the primary proton beam of the SPS. The relative displacement of positive and negative beams in y direction is of 2 mm.*

3.4 Trigger System

NA48/2 trigger is a multilevel system, designed to have in principle no dead time and to be able to cope with rates of particles in the detectors at the level of one

[4]In the original design the PMT output was read directly from the back of the photomultipliers, but the beam radiation damaged the integrated chips of the daughter boards.

MHz.

The full acquisition system is pipelined, synchronized by a 40 MHz clock. Every 25 ns the detectors write their output to a circular memory 204.8μs deep.

The system, schematically represented in Fig. 3.21, is divided in two parts:

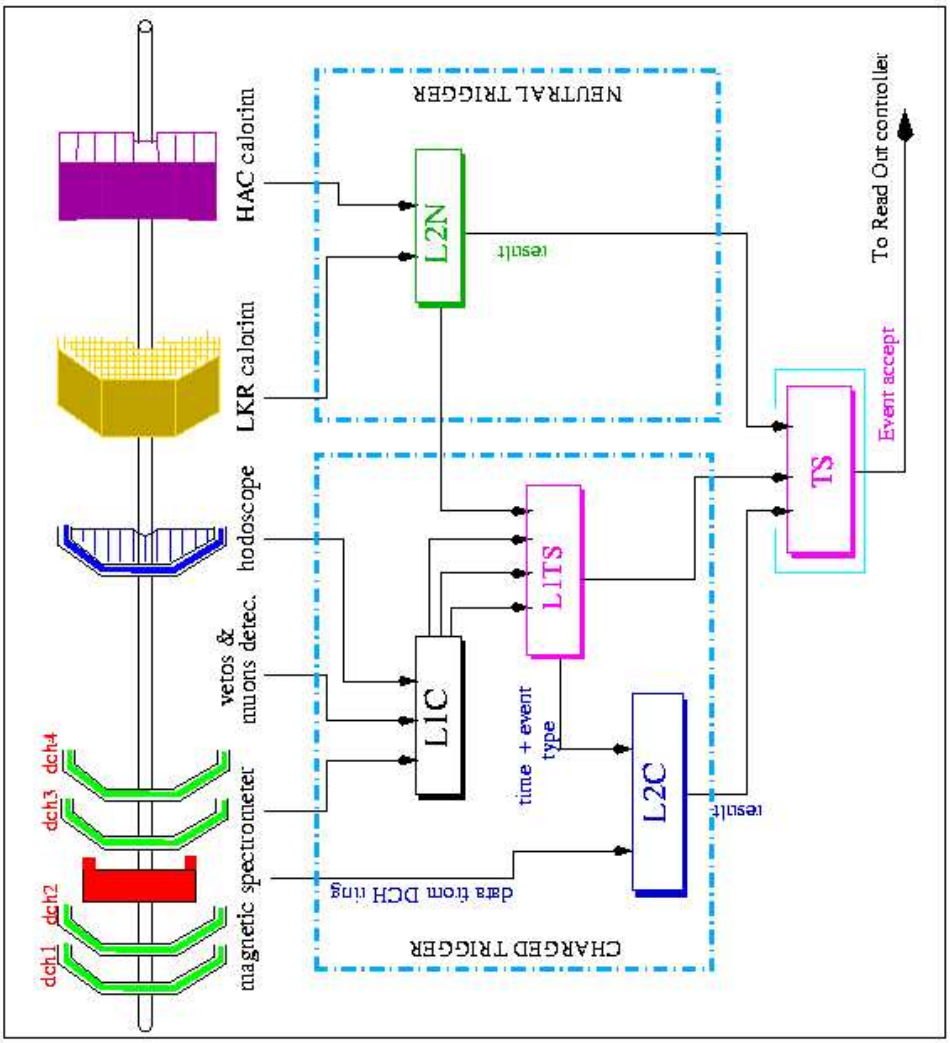

Figure 3.21: *Scheme of the Trigger System. It is formed by two independent trigger subsystems, Charged and Neutral Trigger. They send their results to a third subsystem, called Trigger Supervisor, that collects and correlates the information and takes the final decision on event recording.*

Charged and Neutral Trigger. The last one was particularly relevant when NA48

experiment was running with neutral beams, while NA48/2 used it for $K^{\pm} \rightarrow \pi^{\pm}\pi^0\pi^0$ collection and for minimum bias triggers. It exists a third subsystem, called Trigger Supervisor, that collects the information from the two subsystems and takes the final decision on recording or not the event.

3.4.1 Charged Trigger

The Charged Trigger is segmented in two levels in order to reduce the rate of events from the $2 \cdot 10^6$/burst registered by the detectors to the $\sim 5 \cdot 10^4$ written to disk per burst. Each level of the trigger system has a reduction factor from input to output of the order of 10.

L1C

The goal of the first level of the Charged Trigger (L1C) is to reduce the input rate to the second trigger level below 150 kHz. It is a fast hardware system collecting the information from the drift chambers, charged hodoscope and AKL detectors. These signals are sent to the L1 Trigger Supervisor (L1TS) subsystem that combines them with the energy information from the calorimeters. Here some loose selection based on the topology and energy of the events are made. Before that the event is sent in input to the second level of the charged trigger system, a time alignment of the signals from the detectors is performed, a 30 bit time-stamp is attached to the event, and a 3 bit code (strobe) identifying the topology of the event is produced.
In the table below are reported the typical rates at the Level 1 trigger stage for the most significative signals assuming a proton intensity on target of $6 \cdot 10^{11}$ ppp :

L2C

The second level of trigger for charged particles, called Massbox (MBX) is a software trigger processor farm. It asynchronously handles events on the base of the 3 bit identification code and produces an answer within 100 μs. The MBX effects a fast on line reconstruction of the events employing the data sent from the drift chambers. Its capability of performing rather complicated algorithms (like vertex reconstruction and invariant mass calculation) is a key element of

Trigger	Rate
Q1	$1.8 \cdot 10^6$
Q2	$2.9 \cdot 10^5$
Q2*!AKL	$2.5 \cdot 10^5$
T0N	$7.0 \cdot 10^4$
E(LKr)> 10 GeV	$2.4 \cdot 10^5$
1μ	$1.6 \cdot 10^6$

Table 3.2: *Q1 signal requires at least 1 time coincidence between a signal from a vertical scintillator and a signal from a horizontal scintillator in the same hodoscope quadrant (see Section 3.3.3); Q2 signal requires 2 or more time coincidences between pairs of signals coming from corresponding elements of a* 4×4 *subdivision of each hodoscope quadrant;* $!AKL$ *signal vetoes on a time coincidence between the two layers of at least one AKL pocket,* 1μ *signal requires at least 1 signal coming from the* μ*-veto scintillators.*

the NA48/2 trigger chain.
The upgrade to charged beams operated in 2003, required an improvement of the calculation power of the MBX, in order to be able to stand a higher rate of charged events. A processor upgrade of the system increased the upper limit of input events from 120 kHz to 170 kHz.

Space Points Reconstruction

Starting from drift chambers data, MBX reconstructs the impact points for drift chamber 1, 2 and 4. The algorithm receives in input from each chamber the list of coordinates X[1,..n_x], Y[1,..n_y], U[1,..n_u] and V[1,..n_v] and gives as output a list of space points P[1,..,n_p] carrying abscissa and ordinate information of the space points. In order to reconstruct a space point, at least 3 of the 4 coordinates must be consistent. A space point is reconstructed if one of the following condition is satisfied within a tolerance of 1.5 mm:

$$\begin{aligned} u &= \frac{x+y}{2} \\ v &= \frac{y-x}{2} \\ y &= \frac{u+v}{2} \end{aligned}$$

Vertex Reconstruction

Once the list of space points of chamber 1 and 2 is defined, all combinations are

checked to form tracks. A space point can belong to one track only. All combination of space points yielding a track coming from downstream the chamber 1 are discarded.
A vertex is successfully reconstructed if the closest distance of approach of two tracks[5] is below 5 cm .

3.4.2 Neutral Trigger

NA48/2 employs also a Level 2 neutral trigger. It is a self triggering full pipelined trigger with no dead time. It is employed primarily to monitor $K^{\pm} \to \pi^{\pm}\pi^0\pi^0$ MBX trigger, but it also provides calorimeter signals to the L1TS. It is synchronized with the 40 MHz clock of the experiment and it operates in the following order:

- The analogical signal of the calorimeter cells are grouped in 2x8 super cells.
- The signal is digitalized by a 10 bit 40 MHz FADC, filtered to remove noise below threshold and summed in 64 horizontal and 64 vertical projections.
- The Peak Sum System (PSS) applies a peak finder algorithm to detect the peaks of energy deposition in the vertical and horizontal projections and calculates the energy moments:

$$m_n^x = \sum_{0<i\leqslant N_{cells}} x_i^n E_i \quad m_n^y = \sum_i y_i^n E_i \quad 0 \leqslant n \leqslant 2$$

- In the Look-Up Tables these informations are merged, and then sent to the Trigger Supervisor.

3.4.3 Trigger Supervisor

The MBX and Neutral Trigger results are sent to the L2 Trigger Supervisor which correlates the information coming from different trigger sources and takes

[5]In order to speed up vertex reconstruction algorithm, the closest distance of approach is (well) approximated with the minimum distance between the track's intersection with a plane orthogonal to the z axis having z coordinate inside the fiducial region.

the final decision on the selection of the event. It also provides a final trigger word and time-stamp and sends to the Read Out Controllers the command to record the event information before the end of the $\sim$ 200 μs data persistence time.

3.4.4 Data acquisition

The NA48/2 data acquisition system (also called PC farm) is composed of 11 sub-detector PCs, 8 event builders and a control PC. All PCs are equipped with Linux operating system and they are connected to a fast switch operating at 200 Mbit/s (see Fig. 3.22).

The use of commercial hardware reduces the cost of design, purchase and

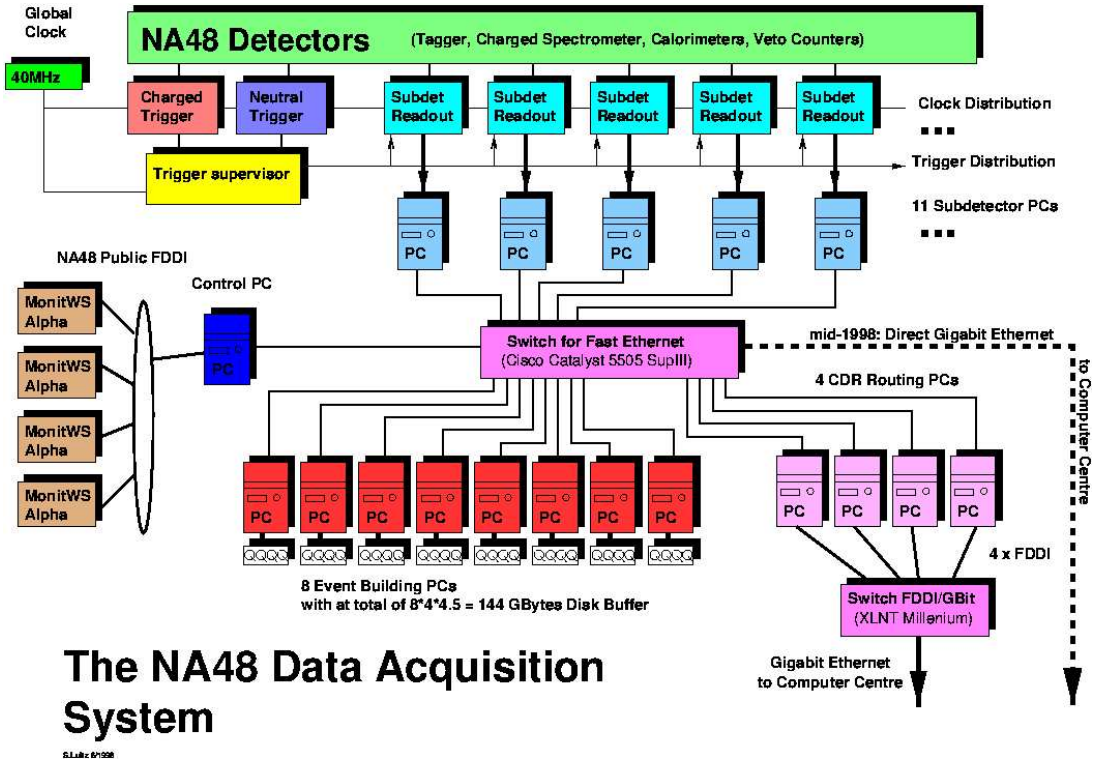

Figure 3.22: *Layout of the NA48/2 Data Acquisition System.*

maintenance, improves the reliability and upgrade possibility of the system.
The 11 sub-detector PCs store the data sent by the sub-detectors during the SPS burst. Then they are assembled and partitioned in 8 blocks and sent to

the event builder PCs in such a way that all data of any single event are in the same block and go to the same event builder PC. The event builders arrange the data in complete events and then they are sent to disk servers of the CERN computing center via a Giga-switch connection, where they are processed. In case of mismatching of event number from the sub detectors, the whole data sample of the burst is discarded.

3.5 Data processing and format

The raw-data coming from the PC farm are stored on 10 disk servers of 1TB average capacity installed at the IT division of CERN. At full efficiency, $\sim 3\ TB$ of data are transferred from the experimental area every day.
A daemon software checks that all the 8 parts forming the burst data (burstlets) have been transferred before dispatching the burst data to be processed. A process running on a CERN public PC connects to this daemon and submits jobs to the CERN batch system (lxbatch) for the final stage of the data taking.
The collected raw-data are analyzed by a software (*L3*) working on the computer batch system of CERN, filtering data and creating 5 different output streams. L3 software ran in flagging mode in 2003 and 2004, meaning that all the $\sim$ 50K raw events were written to tape. Two different types of file go to tape: Compact and Raw files. Raw files contain unreconstructed sub-detector information. Compact files, produced by L3, contain reconstructed information and physical variables. The typical time between the transfer of data from the experimental site and the end of its processing is of 30 minutes, allowing its use already during data taking to check the quality of the data collected (see Fig. 3.23) and to have a fast feedback in response to changes in trigger selection and experimental conditions.

The overall efficiency of the offline processing is slightly greater then 99%.
The typical size of one burst raw-data is $\sim$ 500 MB, while a typical Compact file size is $\sim$ 120 MB; the statistics of 2003 and 2004 data taking are reported in the table below:

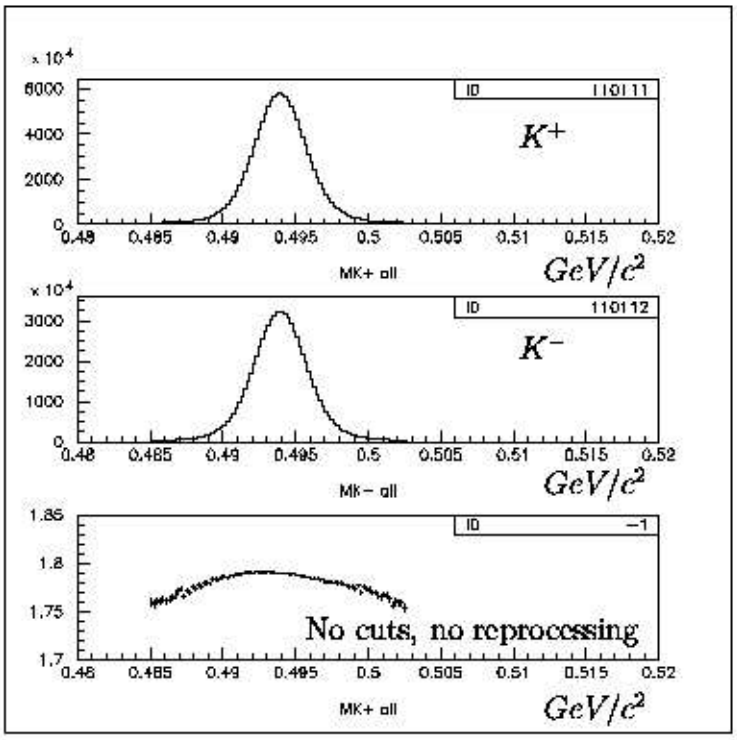

Figure 3.23: *K^+ and K^- masses and their ratio as reconstructed from the Compact Monitor, soon after their collection.*

Central Data Recording Statistics		
	2003	2004
Total number of triggers	$7 \cdot 10^9$	$11 \cdot 10^9$
Number of Bursts	$2.2 \cdot 10^5$	$3 \cdot 10^5$
Raw Data Total Size	80 TB	120 TB
Compact Data Total Size	20 TB	25 TB
Calibration Data Total Size	3.5 TB	4 TB

3.6 2003 Data Taking

The NA48/2 data collection in 2003 lasted 80 days. It started on June the 12th and ended on September the 8th. In addition to that, a week of proton time at nominal condition was available in May and has been employed for the final

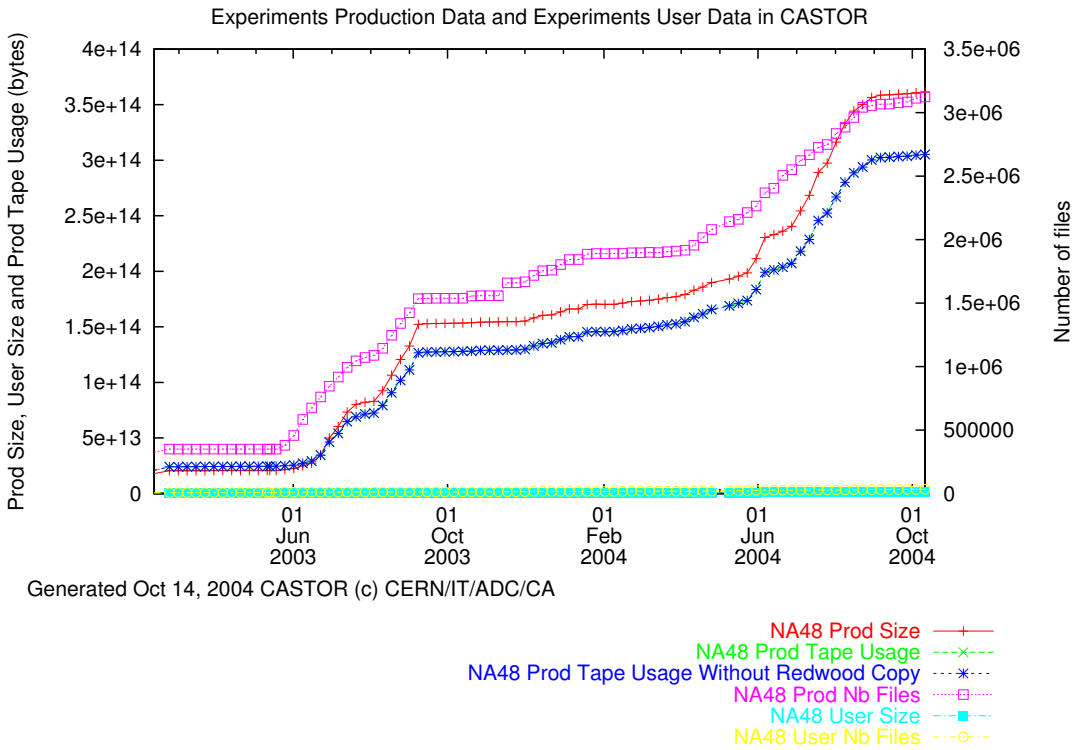

Figure 3.24: *Statistics of data stored in tapes by NA48/2 in 2003 and 2004.*

set-up of the beam line, detector and trigger condition tuning. Another week of highly bunched protons (25 *ns* r.f. structure) was of little use to the NA48/2 set-up and has been devoted mainly to calibration and special η runs.
During the first 10 days of data taking, beam line, trigger condition and detectors performances were studied and tuned.
In order to minimize systematic effects of left-right apparatus asymmetry on the A_g measurement, the spectrometer magnetic field has been cycled and inverted every day. Also the beam line magnets (achromats) were inverted on weekly basis during the SPS machine development stops. Frequency and timing were chosen to minimize losses of data taking, since the procedure is rather long and requires a subsequent steering of the beams. A complete set of data including samples for both beam line and spectrometer magnet orientation is called *super-sample* and it was usually accumulated over a period of two weeks.
Many efforts have been devoted to the alignment and tuning of the drift chambers. Five special runs were taken in order to adjust the spectrometer geometry relative to the beam line geometry. In three of these runs, muons with demag-

netized spectrometer were collected in order to investigate drift chamber relative alignment. In the two other runs, the charged beams have been deflected by ± 20 *cm* outside the beam pipe along the x, y, u and v directions (defined as in Fig. 3.11).
The efficiency of the data taking has been about 50% only, mainly due to problems not under the control of the collaboration, since more than 30 days couldn't have been used due to absence of beam, power cuts, lack of cooling and vacuum leak problems in the beam transportation system.

3.7 2004 Data Taking

The 2004 data collection of NA48/2 started in May 15th and finished in August 18th. The data taking was divided in two periods by a week of highly bunched protons (25ns r.f. structure) started on June 6th. During the second period the readout of the experiment was modified to discard calorimeter data for a part of the the $K^{\pm} \to \pi^{\pm}\pi^{+}\pi^{-}$ event in order to increase the band-with available for other decays and increase the trigger collection rate of 20%, up to 60 thousands triggers per burst.
In 2003 the alignment of the spectrometer drift chambers showed a slow drift: for that reason in 2004 muon runs were taken regularly twice a month and chamber alignment was found to be stable within 20 μm.
In the Table below are shown the number of *super-sample* collected in 2003 and 2004 data taking:

Data Taking Period	Number of super-sample
12/6 - 5/8 2003	no stable
6/8 - 8/9 2003	3
15/5 - 11/8 2004	5

The last week of data taking has been devoted to special runs and to one test run for a future $K^{\pm} \to \pi^{\pm}\nu\overline{\nu}$. In particular it has been collected a 56 hours long run dedicated to the study of leptonic and semileptonic decays. After 25 hours of data taking, the polarity of the spectrometer magnet has been inverted in order to collect data with both orientation of spectrometer magnetic field. The peculiarity of this special run was the trigger configuration (see Chapter

10). During the normal data taking the potentially useful triggers for K_{e2} and $K_{\mu 2}$ collection are strongly downscaled, while, during the special run, the trigger bandwidth was completely saturated by K_{e2} and $K_{\mu 2}$ triggers.

Chapter 4

Methodology of the analysis

This chapter outlines the strategy of the analysis to select the events of interest, the tools which will be employed and the backgrounds that will be studied; these topics will be analyzed throughly in the next chapters.
The goal of the analysis is the measurement of the ratio of the K_{e2} over the $K_{\mu 2}$ decay rate. The measurement of the ratio allows to neglect important uncertainties, like the ones connected with the knowledge of the Kaon flux; some trigger and detector efficiency and some acceptance correction can be factorized out as well. A standalone measurement of the K_{e2} and $K_{\mu 2}$ decay fraction would be much less precise in the NA48/2 experimental set-up, because it would require the knowledge of many factors, like absolute detector efficiency and absolute Kaon flux, that depends on the instantaneous rate of impinging protons and therefore it is known with poor accuracy.
The flux of K_{e2} candidates collected during data taking can be written as:

$$\begin{aligned} \Phi(K_{e2}\ candidates) \ = \\ = \Phi(Kaons) \times P_{dec} \times B.R.(K_{e2}) \times \epsilon_{Trig}^{K_{e2}} \times D^{K_{e2}} \times A_{cuts}^{K_{e2}} + \\ + \Phi(K_{e2}\ background) \end{aligned} \tag{4.1}$$

where:
$\Phi(Kaons)$ is the Charged Kaon flux.
P_{dec} is the probability of a Kaon decay in the decay region.
ϵ_{Trig} is the Trigger efficiency.
$D^{K_{e2}}$ is the downscaling factor of K_{e2} trigger selection.
$A_{cuts}^{K_{e2}}$ is the acceptance of K_{e2} events, including the geometrical acceptance and selection cuts acceptance.

$\Phi(K_{e2}\ background)$ is the flux of background events passing the selection cuts.

Analogously, the number of $K_{\mu 2}$ candidates can be written as:

$$\begin{aligned} \Phi(K_{\mu 2}\ candidates) \ = \\ = \Phi(Kaons) \times P_{dec} \times B.R.(K_{\mu 2}) \times \epsilon_{Trig}^{K_{\mu 2}} \times D^{K_{\mu 2}} \times A_{cuts}^{K_{\mu 2}} + \\ + \Phi(K_{\mu 2}\ background) \end{aligned} \tag{4.2}$$

from the ratio of equation 4.1 and 4.2 it is possible to write:

$$\begin{aligned} R_K \ = \ \frac{BR(K^{\pm} \to e^{\pm}\nu(\gamma))}{BR(K^{\pm} \to \mu^{\pm}\nu(\gamma))} \ = \\ \frac{\Phi(K_{e2}(\gamma)\ candidates) - \Phi(K_{e2}(\gamma)\ background)}{\Phi(K_{\mu 2}(\gamma)\ candidates) - \Phi(K_{\mu 2}(\gamma)\ background)} \cdot \frac{\epsilon_{Trig}^{K_{\mu 2}} \times D^{K_{\mu 2}} \times A_{cuts}^{K_{\mu 2}(\gamma)}}{\epsilon_{Trig}^{K_{e2}} \times D^{K_{e2}} \times A_{cuts}^{K_{e2}(\gamma)}} \end{aligned} \tag{4.3}$$

The measurement of the Ratio of the two rates is independent of the Kaon flux and the probability of a Kaon decay in the fiducial region, that depends on the Kaon lifetime and momentum. Moreover the topological similarity between $K_{\mu 2}$ decay and K_{e2} decay allows also to factorize out of the ratio a part of the trigger and detection efficiencies.

4.1 Reprocessing and Data Reduction

The data analysis procedure of NA48/2 starts with the reprocessing of the collected data. A few months after the end of the data taking, the raw-data are reanalyzed in order to provide a good and unbiased sample of COMPACT data. This procedure is employed in NA48 collaboration after the first processing of data. It allows to include the last detector's calibrations, the improvements of the event reconstruction routines, the definition of time correlation among the detectors and the application of software corrections to detectors relative position (in particular drift chambers).
The typical effective speed of the reprocessing procedure is of $\sim 6\ TB$ per day, limited mostly by the staging of raw-data files from tape to disk. Thus the timescale for data reprocessing is of the order of a few weeks.
Starting from the reprocessed COMPACT files, three samples of more compressed data are produced. This data format is called Super-Compact and it is

6 times more dense then COMPACT. This reduction of data volume is achieved by using a *gzip* compression of the files and discarding a part of COMPACT variables that is not relevant for the analysis. The size reduction operated at the Super-Compact level makes possible to handle the whole statistics collected in one year in a reasonable time scale. Only one of the three Super-Compact stream comprises all the collected events; a second sample is produced by applying a filter, selecting only events of interest for the 3 charged pions asymmetry measurement, while the third sample is the output of the *one track filter*, conceived for rare decays and 1 charged pion asymmetry measurement.

The starting point for K_{e2} and $K_{\mu 2}$ analysis is the complete set of Super-Compact events. A private filter routine is passed over the Super-Compact files and it creates a smaller sample of events of interest, whose data volume is of the order of a few GB. Finally an analysis routine reads the K_{e2} and $K_{\mu 2}$ data sample to produce Column Wise Ntuple containing all the relevant variables and informations for the final analysis. The summary of the data reduction process is plotted in Fig. 4.1 .

4.2 Monte Carlo

Monte Carlo simulations are a common tool in high energy physics research.
The goal of an experiment is to correctly interpret the measurements of the apparatus in order to understand the physics laws that underlies the observed phenomenon. As the detector response to physical phenomenons can be very complicated, in most of the cases it cannot be described analytically. Therefore simulation tools are employed in experimental particle physics to reproduced particle decays according to a known theoretical law and simulating the detector response on the basis of the known laws of particle interaction with matter. The aim is to reproduce as precisely as possible the observed measurements, in order to calculate analysis selection acceptances, systematic effects of the detectors and background contamination on the measurement of interest.
NA48 collaboration developed many different simulation programs during these years. Two different Monte Carlo employed in the analysis, that will be presented in Section 6, are:

- the official NA48/2 simulation software, called *CMC*, and based on GEANT

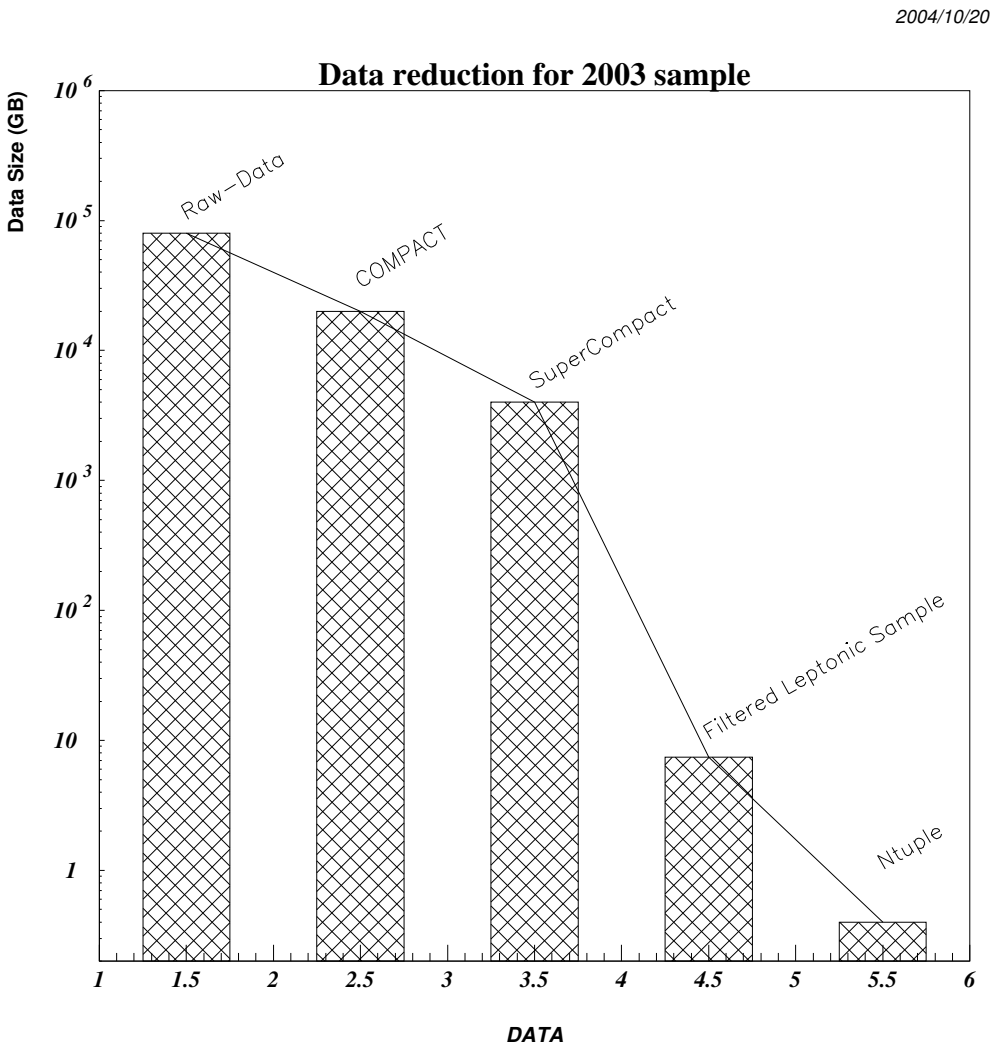

Figure 4.1: *Data reduction of 2003 sample. Up to the Super-Compact level, no selection is applied to the data sample. The filter routine applied on Super Compact is a loose selection, avoiding to regenerate a new filtered sample every time the selection is changed.*

library.

- *Flyo*, a very fast simulation tool developed by some members of Pisa group.

These two Monte Carlos have been employed in the study of geometrical and cut acceptances of signal events, in the study of background decay for both K_{e2} and

$K_{\mu 2}$ and in the study of some systematic effects of detector inefficiencies.

4.3 Background

The measurement of the ratio of K_{e2} over $K_{\mu 2}$ decay rate is complicated by the presence of background which could seriously limit the systematic accuracy achievable.
The study of the cuts in order to reject as much background events as possible, without decreasing significantly the signal statistics is one of the point of the analysis which should be addressed carefully.
Being the K_{e2} Branching Ratio of the order of 10^{-5}, a particular care has been devoted to the study of background sources and its rejection. The major sources of physical background can originate from the occasional misidentification of Kaon or π decays and their study is presented in Chapter 8 .
In the case of the $K_{\mu 2}$ channel, due to its much larger Branching Ratio, the physical sources of background are not as relevant as in the case of the K_{e2} . However, the goal of this analysis is to achieve a measurement of R_K, the ratio between K_{e2} and $K_{\mu 2}$ branching ratios, much better than the present 5% accuracy and this implies that all possible sources of background should be taken into account, studied and eventually subtracted from the $K_{\mu 2}$ signal, if their contamination is of the same order or greater than a few per mille.

The most relevant sources of physical background for K_{e2} and $K_{\mu 2}$ decays are listed in the Table below:

K_{e2} **Background source**	Decay Mode	Branching Ratio
Kaon decays	$K^{\pm} \to \pi^0 e^{\pm} \nu$	4.9%
	$K^{\pm} \to \mu^{\pm} \nu$	63.4%
	$K^{\pm} \to \pi^{\pm} \pi^0$	21.1%
	$K^{\pm} \to \pi^{\pm} \pi^0_D$	B.R. 0.049%
Pion decays[a]	$\pi^{\pm} \to e^{\pm} \nu$	B.R. $1.23 \cdot 10^{-4}$
$K_{\mu 2}$ **Background source**	Decay Mode	Branching Ratio
Kaon decays	$K^{\pm} \to \pi^0 \mu^{\pm} \nu$	3.2%
	$K^{\pm} \to \pi^{\pm} \pi^0$	21.1%
	$K^{\pm} \to \pi^0 e^{\pm} \nu$	4.9%

[a]Note that, at the beginning of the fiducial region, the flux of Pions in NA48/2 beam is 11 times the Kaon flux.

Chapter 5

Reconstruction and Preselection of K_{e2} and $K_{\mu 2}$ events

5.1 Event Reconstruction

The second step of the analysis is the event reconstruction. For each detector a reconstruction program has been developed that elaborates the raw information from the read-out into physical quantities (particle momentum, deposed energy, interaction position, etc.).

5.1.1 Track reconstruction

The track reconstruction of the spectrometer determines the number of charged particle crossing the detector, their direction, momentum and crossing time.
The logic of the track reconstruction is slightly different from the one used by the MBX on-line reconstruction procedure. Since the CPU time is not a strict limitation for off-line reconstruction, the used algorithm allows the inclusion of more hit wires in the space point reconstruction and it is more efficient than the level 2 trigger.
The reconstruction algorithm is composed of two parts. In the first stage, the information on the drift times are not used in order to reduce the combinatory of the space point finding procedure: tracks are reconstructed only employing the hit wire positions. First, space points on chamber 1 and 2 are connected to form mini-tracks, then a complete track is formed if the the vertical (y) projection[1]

[1]The matching is done on the vertical direction because the magnet deflection is negligible in this view.

of the mini-track extrapolation to chamber 4 is close to a space point to better then 4 cm.
A relevant detail of the reconstruction algorithm is that only mini-tracks which intercept an ideal cylinder of 10 cm of diameter along the decay region are reconstructed, as in Fig. 5.1.

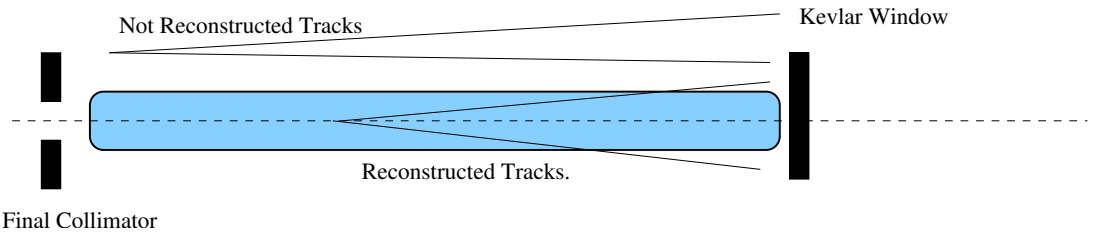

Figure 5.1: *Example of a track satisfying and of a track not satisfying the condition necessary to be considered for reconstruction.*

In the second stage of the reconstruction, the drift time measurements are employed to improve the space resolution of the impact points. A quality variable is associated to each track (χ^2), taking into account the hit position on each view and tracks with high χ^2 are rejected. The charge and the momentum of the track is then calculated, employing an accurate map of the magnet magnetic field.

5.1.2 LKr Calorimeter shower reconstruction

The shower reconstruction of the LKr calorimeter determines the energy deposition, the crossing time, the position and the shower transverse size of crossing particles.
The starting point of the reconstruction is the energy deposition in the calorimeter cells. Each cell with an energy deposition greater than 0.1 GeV is considered as a candidate (*seed*) for the center of development of an electromagnetic shower. A *cluster* is reconstructed if the energy deposition of the seed cell is greater then that of the eight surrounding cells and if it satisfies the following condition defined by the average deposition of the surrounding cells $< E >$:

$$E_{seed} > 0.18\ GeV + 1.8 \cdot < E > (GeV)$$

The second stage of the reconstruction performs a loop over the clusters, including in each cluster the 121 cells in a 22 $cm \times 22$ cm squared box centered on the

seed position. If a cell belongs to more then a cluster, then its energy content is shared among the clusters according to their profile distribution[2]. At this point the energy of the cluster is corrected for energy loss due to proximity to the hole of the beam pipe and calorimeter borders, *dead cells* (as seen Section 3.3.4) and then another correction is applied for the energy scale of the calorimeter.
The cluster position is calculated as the barycenter of the energy deposition in a 3×3 cell box around the seed position, while cluster development size is calculated independently in both x and y directions as the r.m.s. of the energy distribution in a 5×5 cell box around the seed position. Finally, the cluster time is defined as the average of the event time recorded by the cells in the the 5×5 cell box around the seed cell.

5.2 $K_{\mu 2}$ and K_{e2} Event Preselection for R_K analysis

The main principle of the event selection for the measurement of R_K ratio is to symmetrize as much as possible the K_{e2} and $K_{\mu 2}$ selections. This principle follows the logic of exploiting the cancellation effects which appear in Eq. 4.3 in order to achieve a smaller sensitivity of R_K measurement to detector efficiency and selection acceptance cuts.
The choice of detectors employed and the selection cuts applied reflect this principle. For example, the use of the AKL detector information to veto events with extra photons in time with the track is useful for background rejection in K_{e2} selection (especially from $K^{\pm} \to \pi^0 e^{\pm} \nu$) and it has been employed also in $K_{\mu 2}$ selection in order to be less sensitive to AKL detector inefficiency and calibration, although if it is of little help in $K_{\mu 2}$ background rejection, given the much smaller relative branching ratio of $K^{\pm} \to \pi^0 \mu^{\pm} \nu$ relative to $K_{\mu 2}$.
The detector used in the analysis are:

[2]The shower profile is estimated using GEANT simulation library.

Detector	K_{e2} Analysis	$K_{\mu 2}$ Analysis
Spectrometer	yes	yes
KABES	no	no
AKL	yes	yes
LKr Calorimeter	yes	yes
μ-veto	no	no

The K_{e2} event selection is complicated by the small Branching Ratio value of the decay. The achievement of a clear separation of the K_{e2} signal from the background has been one of the major priority of the selection and it required a detailed study of detector performances.

5.2.1 KABES Performances

KABES detector has been conceived to improve background rejection for rare decays and possibly to increase the statistics of events for the 3π asymmetry measurement (A_g), by accepting events with only two detected pions. Its employment in the R_K measurement has been carefully checked. KABES reconstruction of the initial Kaon momentum and flight direction can be employed to refine missing mass calculation and improve background rejection:

$$MM^2_{KBS}(l) \equiv S = (P_K^{KBS} - P_l)^2 \qquad l = e, \mu$$

where P_l and P_K^{KBS} are the 4-vector momenta of the lepton and Kaon employed in place of the $\overrightarrow{P}_K = (0, 0, 60\ GeV/c)$ hypothesis used by the on-line reconstruction for the Kaon momentum.

The Kaon track association for K_{e2} and $K_{\mu 2}$ events is made by choosing the KABES track with lowest time difference relative to the spectrometer track. The matching is accepted only if KABES reconstructed track has the same charge of spectrometer track. A sample of $K^{\pm} \to \pi^{\pm}\pi^{+}\pi^{-}$ has been used to check the reconstruction of Kaon tracks performed by KABES. The distribution for the difference between the Kaon momentum measured by KABES and the sum of the π momenta measured by the spectrometer is plotted In Fig. 5.2. The difference between the momentum measured by KABES and by the spectrometer is plotted as a function of the time for positive and negative Kaons in Fig. 5.3 and the comparison of difference distribution between negative and positive Kaons is plotted in Fig. 5.4. It is possible to conclude that:

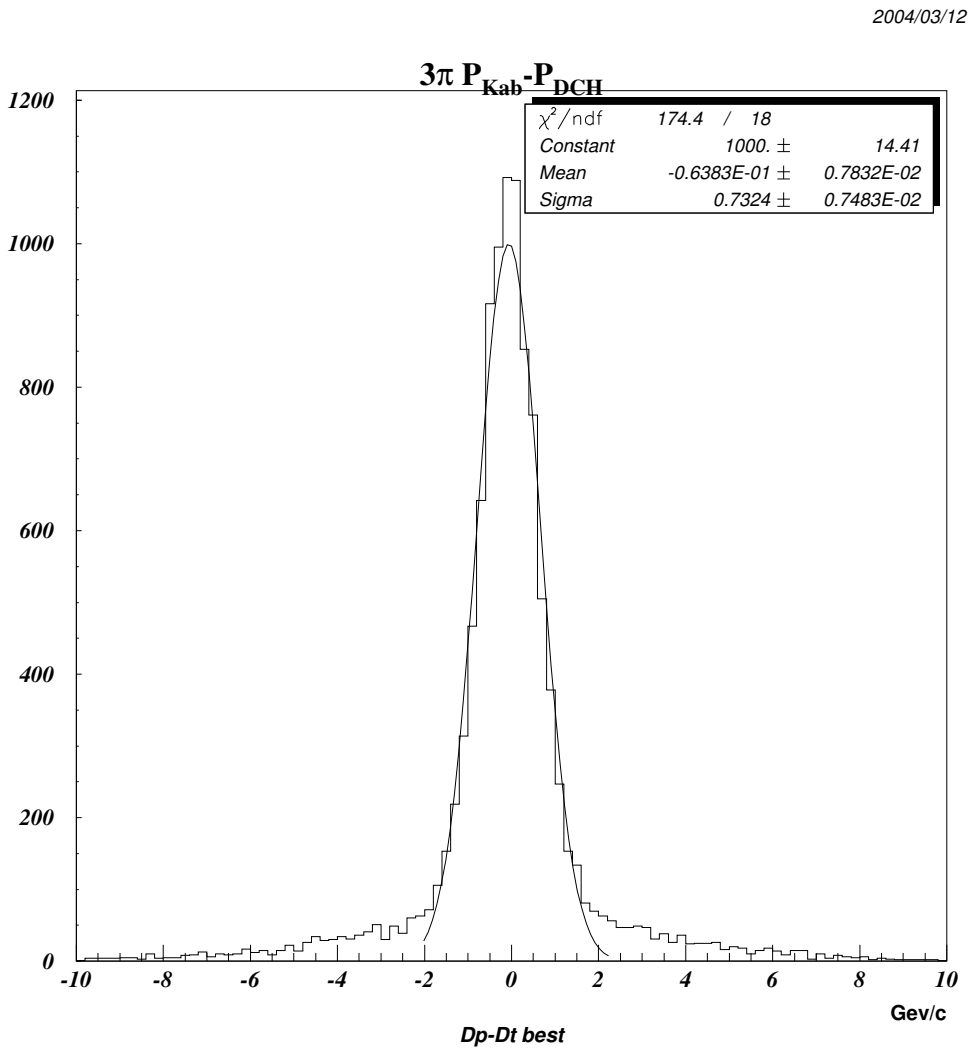

Figure 5.2: *Difference between Kaon momentum measured by KABES and the sum of the 3 π momenta measured by the spectrometer for $K^{\pm} \to \pi^{\pm}\pi^{+}\pi^{-}$ events. The convolution of the two resolution is $\sim 0.7\ GeV/c$. The tails of the distribution are due to mistagging of the incident Kaon with another particle close in time and of same charge.*

- On average, the convolution of KABES and spectrometer resolutions is around 1% (0.7 GeV/c).

- The average residual miscalibration between KABES and spectrometer mo-

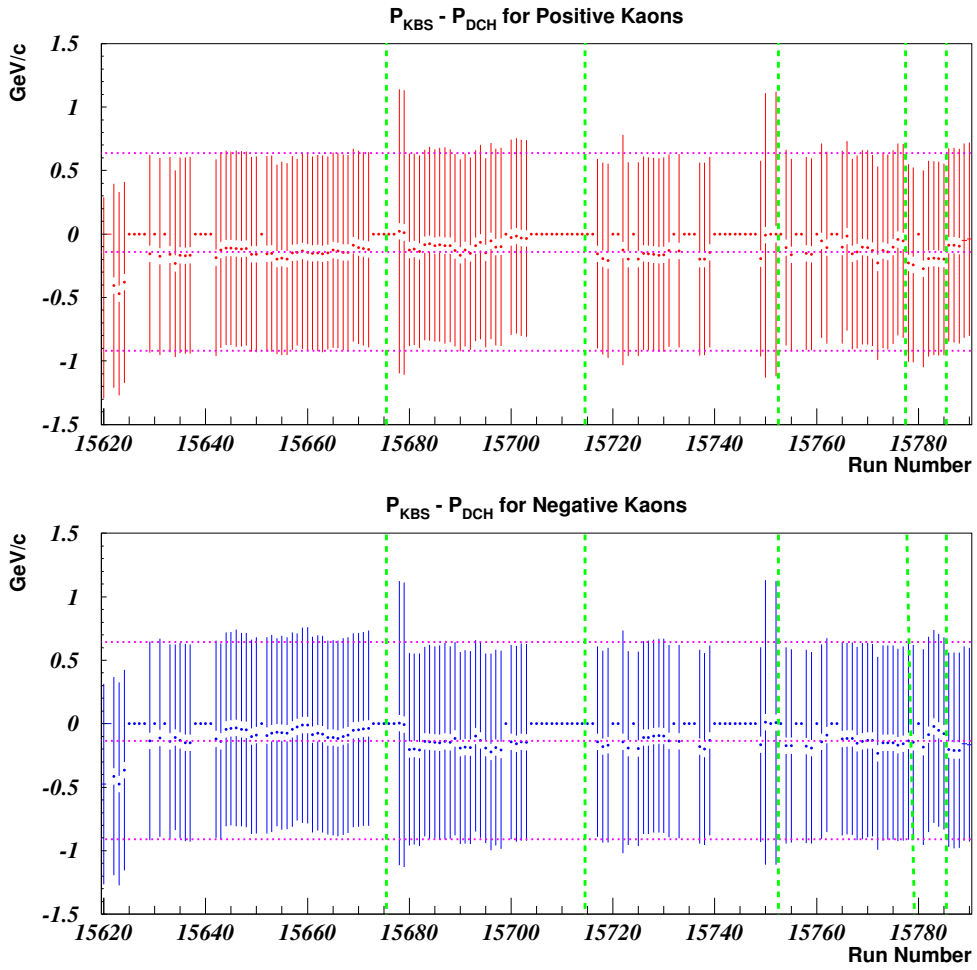

Figure 5.3: *Distribution of mean difference between the momentum measured by Kabes and by the spectrometer as a function of the time for positive and negative Kaons. The error bar represents the r.m.s. of the distribution. Hatched lines represent the inversion of polarity of the achromat magnets.*

mentum is of the order of 0.2% (0.14 GeV/c).

- From Fig. 5.4, it can be seen that the difference of $P_{KAB} - P_{DCH}$ between positive and negative kaons changes systematically of sign at every achromat magnetic field inversion. Knowing the polarity of the achromat field,

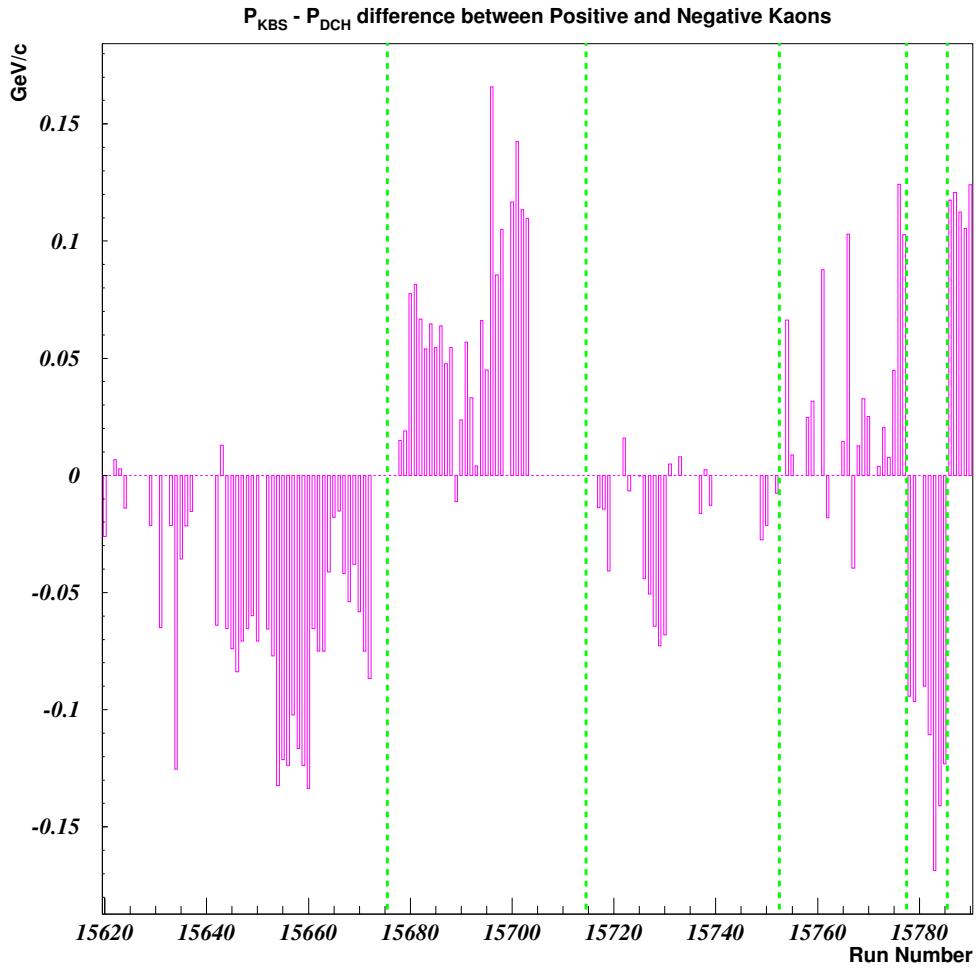

Figure 5.4: *Difference between positive and negative kaons of the distribution of mean difference between the momentum measured by Kabes and by the spectrometer as a function of the time. The hatched lines represent the inversion of polarity of the achromat magnets.*

it can be inferred that the momentum of Kaons passing through station UP of KABES is systematically higher then Kaons passing through station DOWN by 0.15%. This difference can be explained by an error on the intercalibration of the y coordinate of the hit position of $\sim 50\ \mu m$ between

station UP and station DOWN[3].

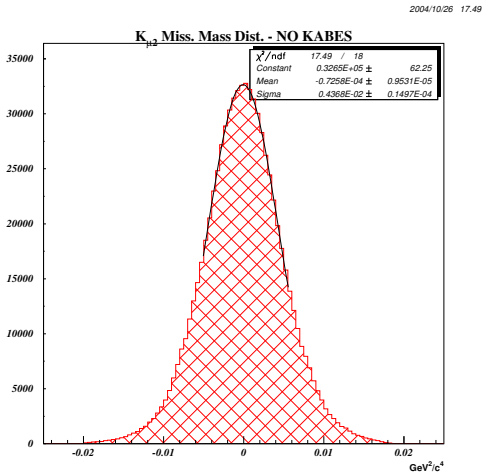

Figure 5.5: *Missing Mass squared distribution for $K_{\mu 2}$ events, under the assumption of 60 GeV/c Kaon momentum.*

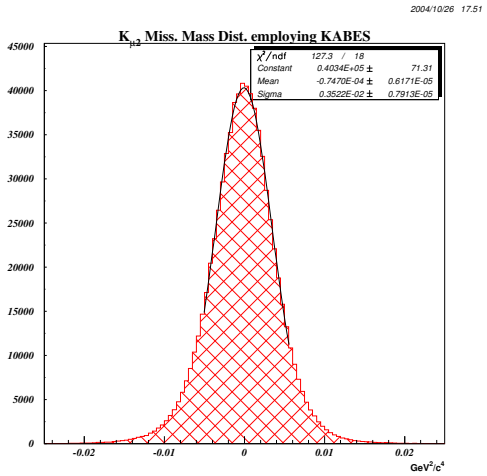

Figure 5.6: *Missing Mass squared distribution for $K_{\mu 2}$ events employing KABES Kaon momentum reconstruction.*

The improvement of the resolution that can be achieved by the employment of KABES Kaon momentum reconstruction is shown in Fig. 5.5 and 5.6 for $K_{\mu 2}$ events and in Fig. 5.7 and 5.8 for K_{e2} . The improvement on the missing mass squared resolution is of $\sim 20\%$.

The employment of KABES reconstruction allows a sensible improvement of the missing mass squared distributions, but it involves also some drawback:

- KABES detector behavior has been flagged as bad in a non negligible part of data taking. Its employment will reduce the statistics of R_K analysis by 8%.

[3]As seen in Section 3.2.1 the resolution on y measurement is of $\sim 100\ \mu m$.

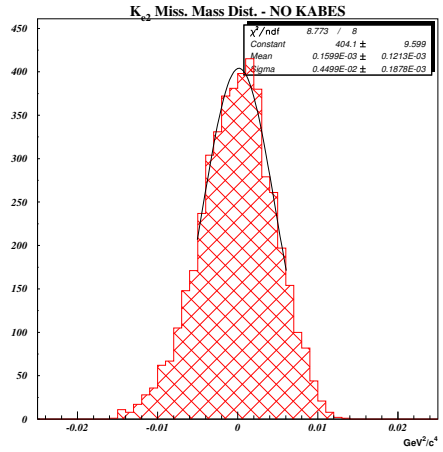

Figure 5.7: *Missing Mass squared distribution for K_{e2} events, under the assumption of 60 GeV Kaon momentum.*

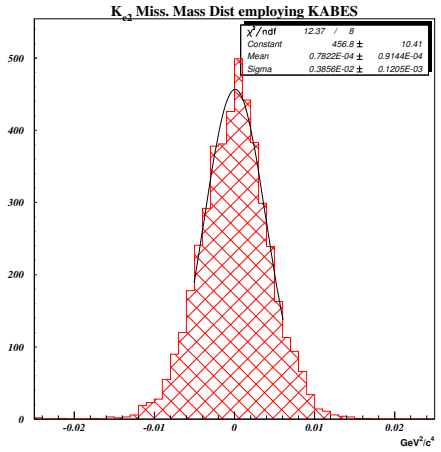

Figure 5.8: *Missing Mass squared distribution for K_{e2} events employing KABES Kaon momentum reconstruction.*

- Another 3% of statistics loss would be due to the failure of the KABES reconstruction routine to find a Kaon candidate with the same charge of the spectrometer track and close to it in time.

- The KABES detector implementation in the official NA48/2 Monte Carlo is still preliminary and, at the moment, it cannot reproduces some important systematic effects, like the mistagging of the Kaon track due to the high rate of particles in the beam.

For these reasons, the gain on missing mass resolution has been judged not enough significant to justify the employment of KABES in the present analysis[4].

5.2.2 K_{e2} and $K_{\mu 2}$ Preselection

A loose preselection of K_{e2} and $K_{\mu 2}$ events is performed on the basis of the topology of the event and detectors geometry. It is intended to reduce the data

[4]As it will be shown in Section 8 the background correction to R_K measurement can be kept well under control without the employment of KABES reconstruvtion.

volume, avoiding any possible bias on the final selection. In particular it has been avoided the inclusion of cuts on track and cluster time at this level of the selection. The list of the preselection cuts is presented in the table below:

Preselection Cuts		
Type of cut	K_{e2} preselection	$K_{\mu 2}$ preselection
Topology Cuts	$N_{tracks} \geq 1$	
	$N_{LKrcluster} \geq 1$ Track - cluster association	
Geometric Cuts	120 cm $> r_{DCH1} >$ 12 cm 120 cm $> r_{DCH4} >$ 13 cm LKr Geometric shape cut	
Loose Cuts	Extra cluster Energy $<$ 1.5 GeV 500 cm $<$ z decay vertex $<$ 10000 cm cda $<$ 10 cm 12 GeV/c $<$ p_{track} $<$ 60 GeV/c	
	E/pc > 0.85 $MM^2(e) < 0.1$ GeV^2/c^4	$MM^2(\mu) < 0.1$ GeV^2/c^4

Most of the cuts are in common between K_{e2} and $K_{\mu 2}$ preselection. The preselections start from the requirement of at least one reconstructed track. The K_{e2} preselection requires on top of that at least one LKr reconstructed cluster associated with the track[5].

The geometrical cuts are in common between K_{e2} and $K_{\mu 2}$ preselection. It is required that reconstructed track impact points at chamber 1 and 4 are more then 12 cm away from the center of the beam pipe (the physical inner radius of the drift chambers is ~ 10 cm); the fiducial cut on the LKr geometrical shape is performed both in K_{e2} and $K_{\mu 2}$ preselection[6].

A cut on the extra activity of the LKr calorimeter is made: the reconstructed energy of all clusters non associated to the event track must be less than 1.5 GeV. The vertex decay position is reconstructed by minimizing the distance between

[5]a track-cluster association is fulfilled if the extrapolated track position at the face of LKr calorimeter is less then 5 cm away from the center of a reconstructed cluster.

[6]The LKr acceptance cut is applied also to the $K_{\mu 2}$ selection to symmetrize K_{e2} and $K_{\mu 2}$ acceptances. As the majority of the $K_{\mu 2}$ events ($\sim$ 60%) doesn't have an associated cluster, a cut on the extrapolated track position at LKr face is made.

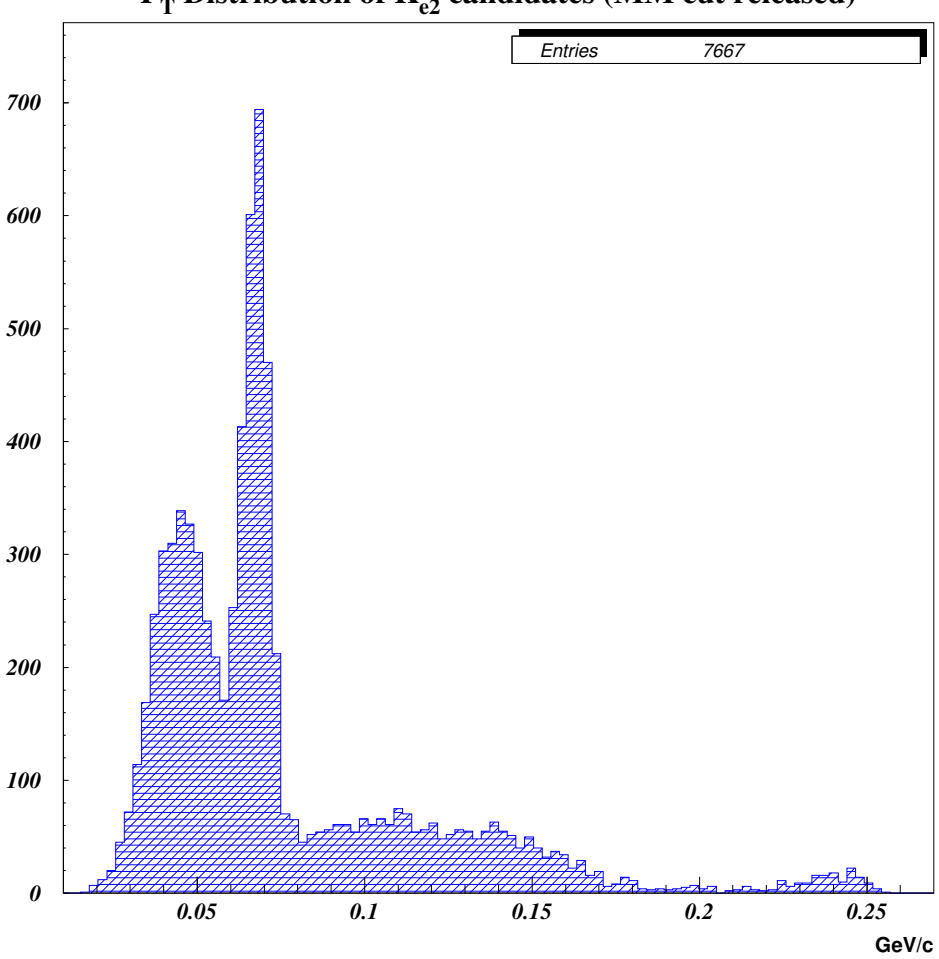

Figure 5.9: *Transverse momentum distribution of K_{e2} candidates passing preselection cuts. The clear peak visible around $\frac{1}{2}$ of the π mass is due to the pion component of the beam undergoing the decay $\pi \rightarrow l\nu_l$. The K_{e2} candidates are concentrated around the small peak on the right side (at $\sim \frac{1}{2}$ the Kaon mass), while the broad shoulder in between is mostly due to K_{e3} and $K^{\pm} \rightarrow \pi^{\pm}\pi^0$ events.*

the spectrometer track and the Kaon track[7]. Common cuts on the longitudinal

[7]As KABES detector reconstruction is not used, the Kaon direction of flight is supposed to be the beam-line axis.

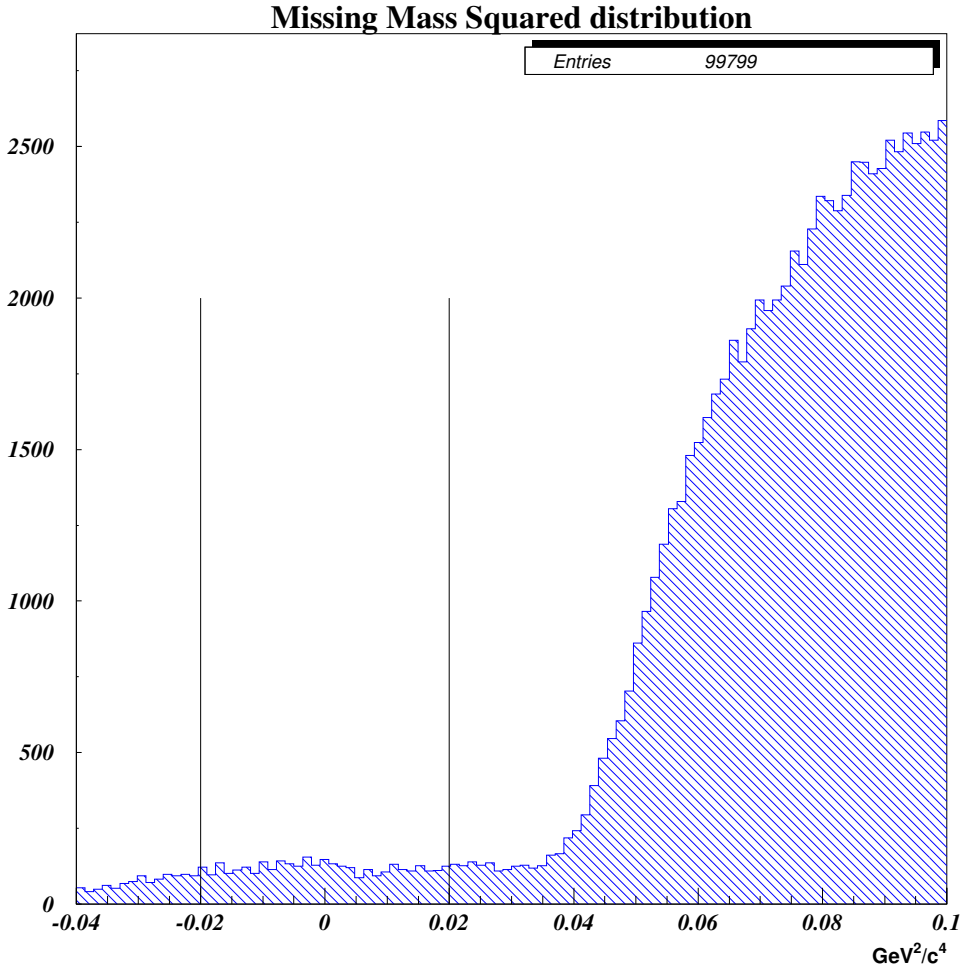

Figure 5.10: *Missing Mass squared distribution of K_{e2} events selected by the set of preselection cuts. The lines on the plot correspond to the borders of K_{e2} signal region.*

coordinate of the vertex[8], on the minimum distance of approach (cda) and on the spectrometer track momentum are performed. Similar selection cuts are required on the missing mass value for K_{e2} and $K_{\mu 2}$ candidates. A loose electron

[8]The $z = 0$ coordinate position corresponds to the former K_S target, dismantled in NA48/2 set-up. It is just for mere convention that the collaboration continues to use its position as coordinate reference.

identification is performed cutting on the ratio E/p between the energy of the LKr cluster and the momentum of the associated track.
As the goal of the preselection is just to reduce the size of the data sample, it is not very effective in signal background separation, in fact the K_{e2} candidates selected by preselection cuts are mostly background events, as it can be seen in Fig. 5.9 and Fig. 5.10. The final event selection will be presented in Chapter 7.

Chapter 6

Monte Carlo simulations

Monte Carlo simulations have been used in the R_K analysis to calculate K_{e2} and $K_{\mu 2}$ events acceptance (Chapter 7), for background rejection study (Chapter 8) and to calculate radiative corrections to K_{e2} and $K_{\mu 2}$ events acceptance (Chapter 11).
Monte Carlo samples have been employed also in the study of the optimization of the kinematics and geometrical selection cuts. For this reason other decays besides K_{e2} and $K_{\mu 2}$ have been simulated allowing to understand the composition of the physical background and cuts rejection power.

K_{e2} and $K_{\mu 2}$ decays are topologically similar: they are both one track decays with similar illumination at DCH1 and have similar acceptance as a function of decay vertex position (differences are at most of the order of 5% as shown in Fig. 6.1). The overall difference between the absolute geometrical acceptances is less then 10%. Apart kinematics, another difference between the two decays is the probability of bremstrahlung interaction in the Kevlar window and Spectrometer: negligible for muons, but not for electrons.
All relevant elements of difference between K_{e2} and $K_{\mu 2}$ decays are simulated by the Monte Carlo programs. Kinematic and topological similarities between the two decays help to limit the sensitivity of R_K measurement to imperfections in Monte Carlo acceptance evaluation.
Two Monte Carlo simulations have been used in the R_K analysis. The official NA48/2 Monte Carlo (CMC) and a fast NA48/2 Monte Carlo developed by the Pisa group of the collaboration (*Flyo*) and in particular by Prof. G. Pierazzini. The first one incorporates a detailed simulation of all the detectors crossed by particles, a complete simulation of the detectors reconstruction and an accurate

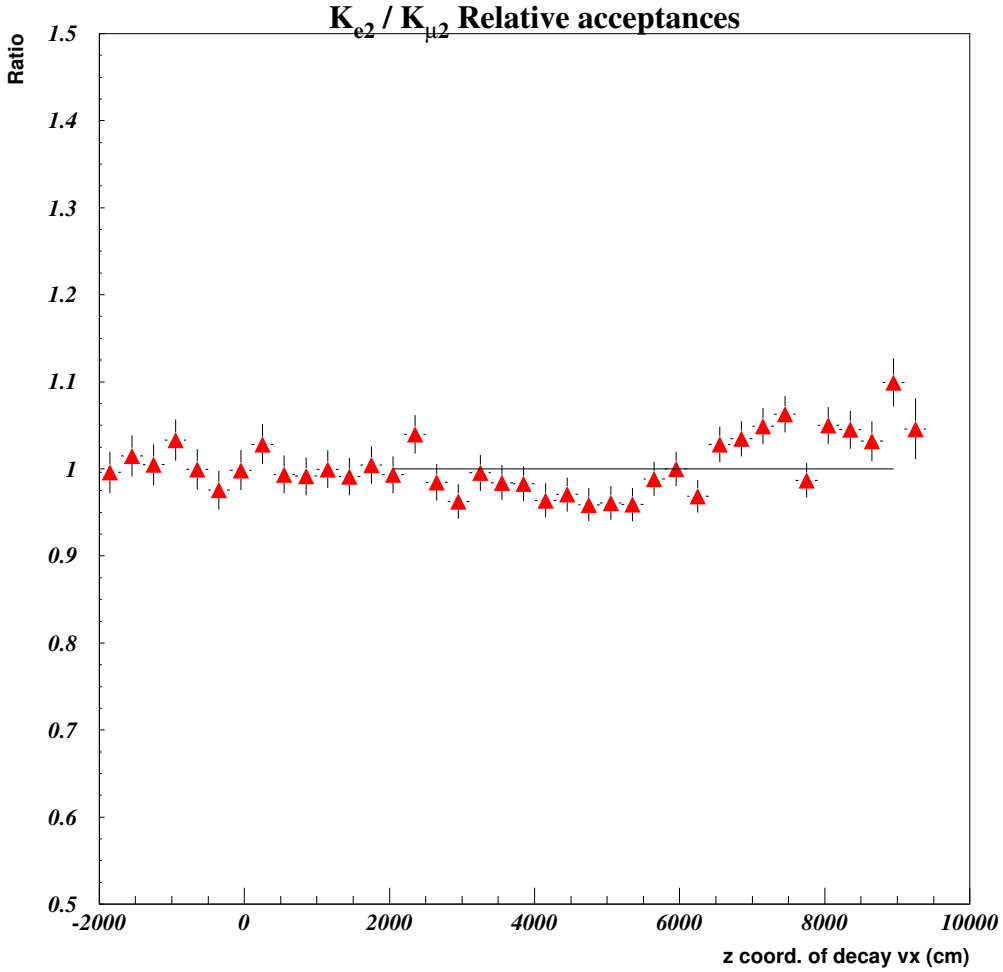

Figure 6.1: *K_{e2} over $K_{\mu 2}$ relative acceptance as a function of the decay vertex position.*

description of the showers developed in the calorimeter. It is based on GEANT package of the CERNLIB libraries. Its detailed simulation is very expensive in terms of CPU time consumption.
Flyo answers to the necessity of a fast simulation for the generation of a large statistics at the prize of a deterioration of accuracy[1]. Its geometric description of detectors is simplified, shower development and interaction with matter are

[1] *Flyo* is roughly 200 times faster than CMC.

parametrized.

6.1 CMC Monte Carlo

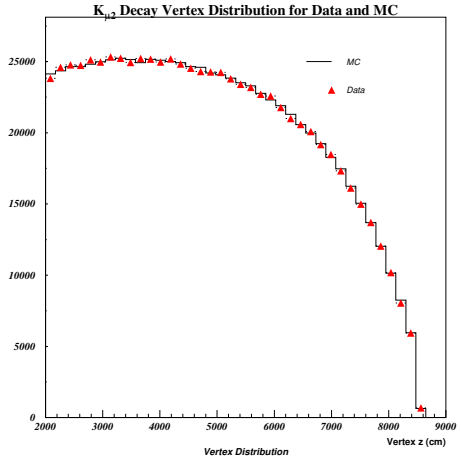

Figure 6.2: *$K_{\mu 2}$ decay vertex distribution for Data and Monte Carlo.*

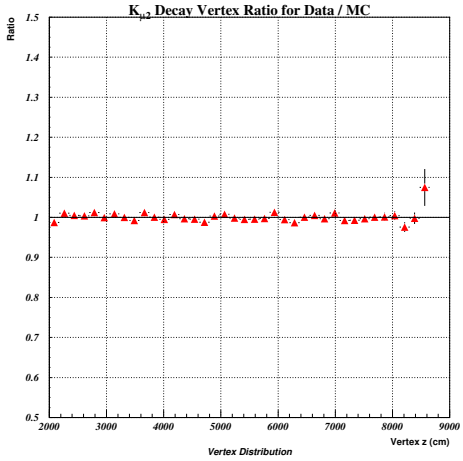

Figure 6.3: *Data over Monte Carlo Ratio as a function of the $K_{\mu 2}$ decay vertex position.*

CMC simulation has been used for the acceptance calculation of K_{e2} and $K_{\mu 2}$ events and for the rejection factor calculation of some physical sources. It is based on the GEANT package and it includes:

- Detailed simulation of the beam optics and geometry, including the small magnetic field in the decay region upstream of the spectrometer.

- Simulation of the movement of the beam during the burst and burst by burst tuning of the beam using data as input.

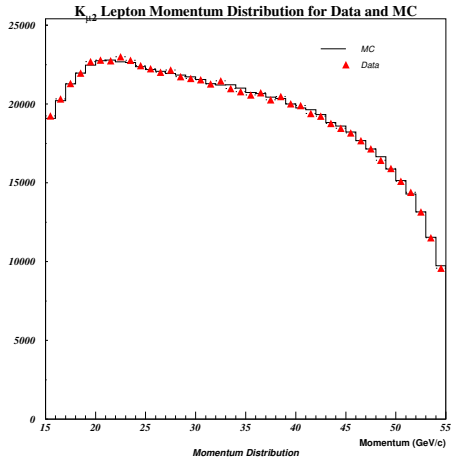

Figure 6.4: *$K_{\mu 2}$ lepton momentum distribution for Data and Monte Carlo.*

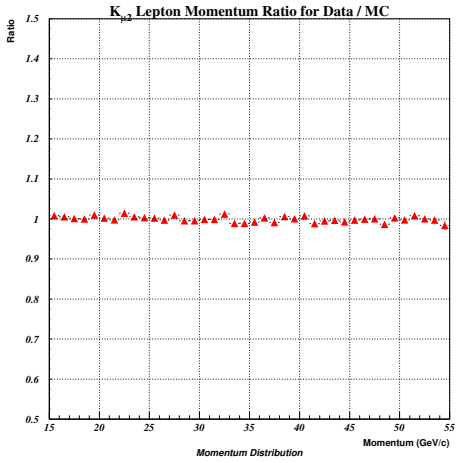

Figure 6.5: *Data over Monte Carlo Ratio as a function of $K_{\mu 2}$ muon momentum.*

- Secondary particle production, like $\mu^{\pm} \rightarrow e^{\pm}\overline{\nu}\nu$ decay.

- GEANT based simulation of the electromagnetic shower development inside the LKr Calorimeter.

- Detailed detector geometry and reconstruction, including single wire efficiency, dead cells position, electron drift time in drift chambers and time collection of light in scintillators.

- Simulation of the interaction of particles with matter, effect like multiple scattering, bremsstrahlung and pair production are reproduced.

- Simulation data are recorded in the same format of the experimental data, allowing the use of the same analysis tools.

The Monte Carlo doesn't simulate the tails of the E/p distribution. These tails are mostly due to the underestimation of LKr cluster energy following an

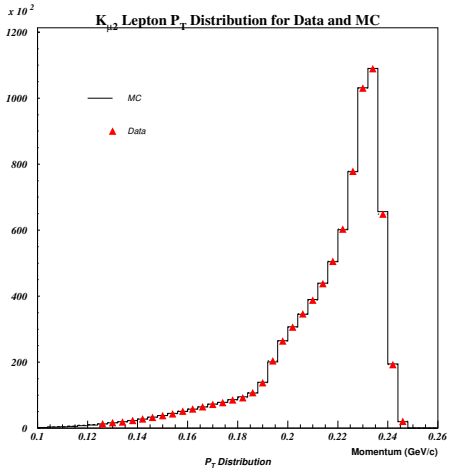

Figure 6.6: *$K_{\mu 2}$ lepton transverse momentum distribution for Data and Monte Carlo.*

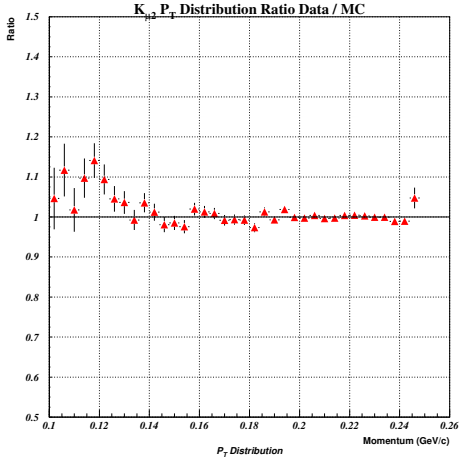

Figure 6.7: *Data over Monte Carlo Ratio as a function of the $K_{\mu 2}$ muon transverse momentum.*

hadronic interaction of particles produced in the shower development with the nucleons of the Krypton. For this reason, to calculate K_{e2} events acceptance as a function of E/p selection a technique based on experimental data has been used. Comparison between Data and Monte Carlo simulation are illustrated in Fig. 6.3, Fig. 6.5, Fig. 6.7 and Fig. 6.9.
From Fig 6.9, it appears that the tails of Monte Carlo distribution of $MM^2(\mu)$ is significantly different from Data distribution. The possible systematic effect induced on Acceptance measurement is discussed in Chapter 9.

6.2 *Flyo* Monte Carlo

Flyo simulation has been used to improve the K_{e2} and $K_{\mu 2}$ selection and to calculate the acceptance correction to R_K due to radiative decays $K^{\pm} \to e^{\pm}\nu\gamma$ and $K^{\pm} \to \mu^{\pm}\nu\gamma$. It includes:

- Detailed simulation of the beam optics and geometry, including the residual magnetic field in the decay region.

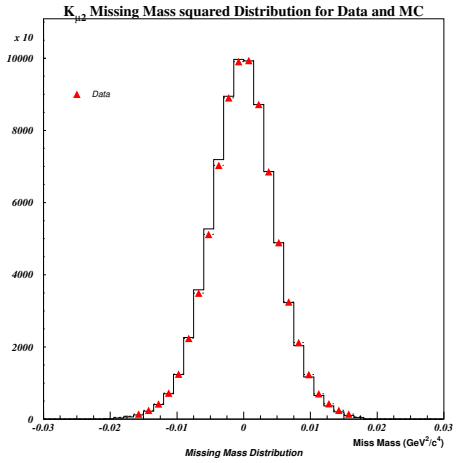

Figure 6.8: $K_{\mu 2}$ $MM^2(\mu)$ *distribution for Data and Monte Carlo.*

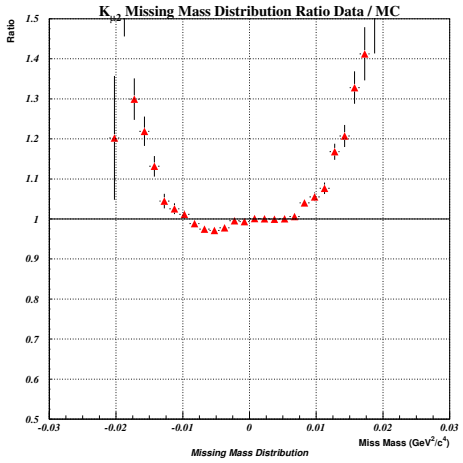

Figure 6.9: *Data over Monte Carlo Ratio as a function of the* $K_{\mu 2}$ $MM^2(\mu)$.

- Secondary particle production, like $\mu^{\pm} \rightarrow e^{\pm}\overline{\nu}\nu$ decay.
- Simplified detector geometry and reconstruction.
- Parametrized reproduction of particle interactions with matter, like multiple scattering, bremsstrahlung, pair production.
- Parametrized simulation of the hadronic loss of visible energy in LKr.
- Optional event correlation in random number sequence generation.

Chapter 7

Analysis Selection and Acceptance for K_{e2} and $K_{\mu 2}$ events

In this Chapter the analysis selection of K_{e2} and $K_{\mu 2}$ events is presented. Kinematical acceptances of the selection cuts are calculated.
The choice of the analysis cuts is based on Monte Carlo simulation of signal and background channels and on the analysis of a small fraction (of the order of 5% of the total) of the data.
Acceptance for every single cut will be presented in two forms. In the first form, acceptance depend only on the specific cut studied. The number of events surviving the single cut (N_{Single}) is divided by the total number of preselected events N_{Total}:

$$A_S = \frac{N^{MC}_{Single}}{N^{MC}_{Total}}$$

The second form depends on the ordering of the cuts: the number of events surviving that specific cut and all the previous ones is divided by the total number of preselected events N_{Total}:

$$A_C = \frac{N^{MC}_{Cumulative}}{N^{MC}_{Total}}$$

7.1 Monte Carlo Production

The Monte Carlo productions used to calculate K_{e2} and $K_{\mu 2}$ acceptance corrections exploit the capability of CMC simulation to follow the time evolution of

the beam geometry and detectors efficiency. Monte Carlo productions for each run are proportional to the collected data. In this way, all the characteristics of the data sample, like the ratio between positive charge and negative charge triggers and the ratio between samples of both signs of achromat and spectrometer field, are respected in the Monte Carlo. The correct fraction of triggers for each particular beam geometry and detector efficiency map are also preserved. The Data over Monte Carlo ratio of triggers collected for each run is plotted in Fig. 7.1, while in Fig. 7.2 the Data over Monte Carlo ratio of positive over negative triggers is plotted.

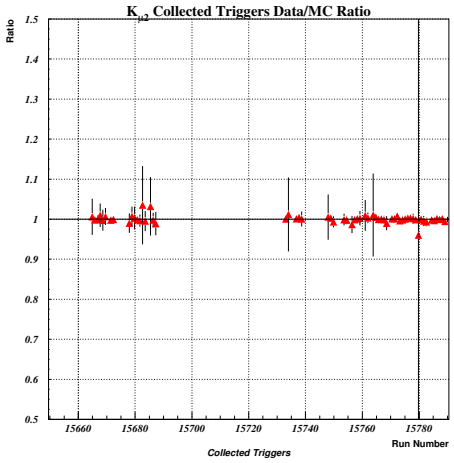

Figure 7.1: *Data over Monte Carlo ratio of the $K_{\mu 2}$ collected triggers as a function of time.*

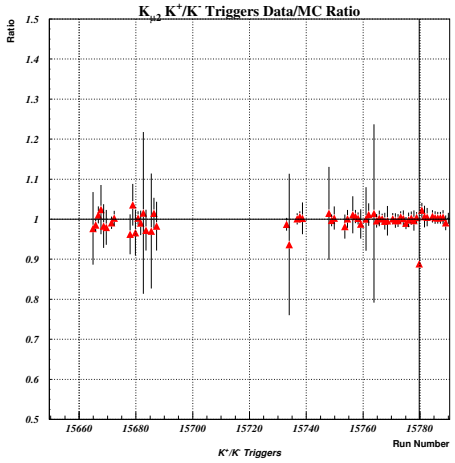

Figure 7.2: *Data over Monte Carlo ratio of the collected positive over negative $K_{\mu 2}$ triggers as a function of time.*

7.2 K_{e2} Selection

In table 7.1 are stated the K_{e2} selection cuts and acceptance; explanation of the cuts and their effects follow in the text.

K_{e2} **Selection Cuts**			
	Cut	$A_S(\%)$	$A_C(\%)$
	Preselection		
	n. track > 0 and n. clus. > 0	100	65.1
	General Selection		
1	Bad Bursts	99.97	65.1
	Track Selection		
2	Track Quality > 0.7	99.99	65.0
3	Ghost tracks	99.93	64.9
4	$15\ GeV/c\ <\ P\ <\ 55\ GeV/c$	84.0	54.7
5	$\lvert t^{Track} - t_i^{Track}\rvert\ >\ 5\ ns$	-	-
6	$\lvert t^{Track} - t^{AKL}\rvert\ >\ 10\ ns$	-	-
7	$P_T VsP$	86.7	50.9
8	$cda\ <\ 4\ cm$	99.2	50.9
9	$2000\ cm\ <\ z_{vrtx}\ < 8500\ cm$	62.0	31.6
	Cluster Selection		
10	$d_{dcell}\ >\ 2\ cm$	98.4	31.1
11	$E_{extraclusters}\ <\ 1.5\ GeV$	95.3	31.0
12	$0.514\ GeV/c^2\ <\ M_{Fake}(\pi)\ <\ 0.55\ GeV/c^2$	69.1	24.3
13	Geometry Cut	90.7	23.0
14	L1 $\times$ L2 Trigger	-	-
	Final	-	23.0

Table 7.1: *K_{e2} event selection and acceptance for each single cut (A_S) and cumulative acceptance including the previous cuts (A_C). A line (-) means that the acceptance factors are not applicable for that particular cut. A_S acceptance is normalized to the number of events with at least one reconstructed track and one reconstructed calorimeter cluster associated to the track. A_C acceptance is normalized to the number of generated K_{e2} decays in signal region.*

The selection of K_{e2} events starts from the events with al least 1 track and 1 track associated LKr cluster. In first place, all the events collected when the functioning of one of the detectors involved in the analysis was not excellent[1] are discarded (cut 1 in Table 7.1. A selection on the trigger word of the event, asking for the correct L1 and L2 trigger signals, is performed (see Chapter 10 for explanation of K_{e2} trigger logic).

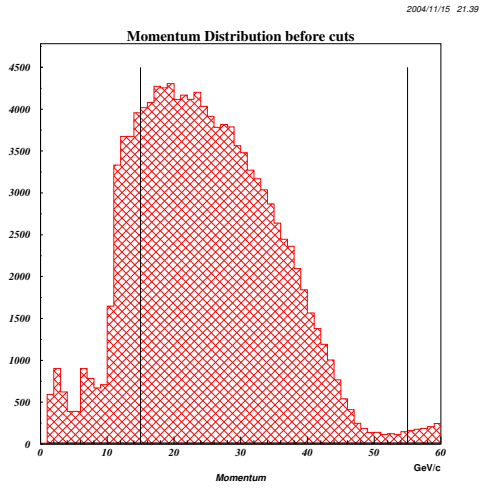

Figure 7.3: *Lepton momentum distribution for K_{e2} candidates with only preselection cuts.*

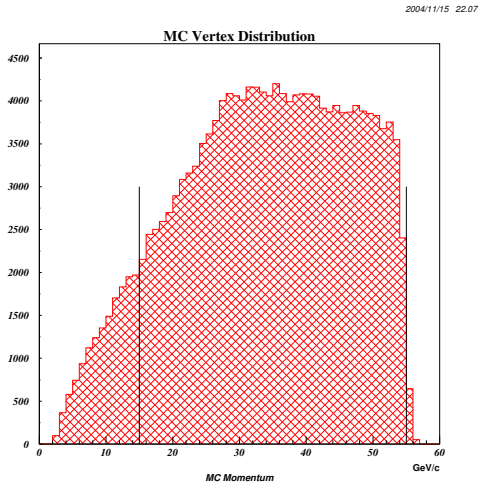

Figure 7.4: *Monte Carlo reconstructed K_{e2} momentum distribution.*

At this point, a selection routine is applied to every remaining track of each event. For every track, a check on the quality of its reconstruction is performed, rejecting tracks of poor quality (cut 2). The so called *ghost tracks* are also rejected. Ghost tracks are artifacts of the track reconstruction; the track reconstruction routine efficiency is improved by allowing reconstructed tracks to have common space points, but it might happen that non physical tracks are reconstructed in the proximity of the physical one. These tracks are close to the physical one (less than 1 *cm*) and have worse track quality than the physical one

[1] A few weeks after the end of the data taking, experts of each detector provide a list of bursts during which a detector shows a malfunctioning. Most common malfunctionings are hardware faults of an electronic card, of a Read-out card or of a Memory board.

(cut 3).

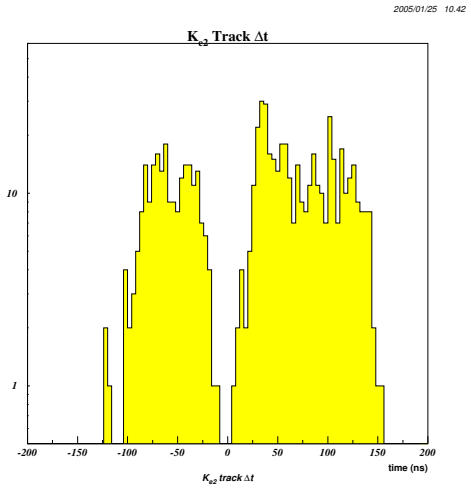

Figure 7.5: *Distribution of the time difference between the candidate K_{e2} track and the nearest in time track. The lines represent the limits of the time cut.*

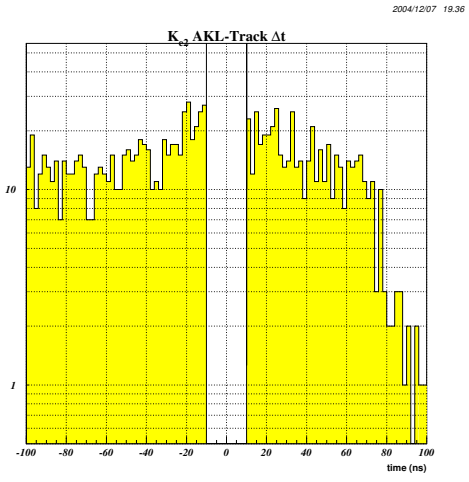

Figure 7.6: *Distribution of the time difference between the candidate K_{e2} track and the nearest in time hit in a AKL pocket.*

Cut 4 rejects low momentum tracks and it requires that track momentum is a few GeV/c lower than the nominal Kaon momentum. The lower bound has been chosen to reject 3 body decays background, while preserving most of the signal. An upper bound (below 60 GeV/c) is necessary to avoid unphysical value of reconstructed variables (like the missing mass) under the hypothesis of 60 GeV/c Kaon beam. The actual value has been chosen to cut away a region of low signal acceptance, mostly populated by misreconstructed tracks (see Fig. 7.3 and 7.4). A cut on the distance of track impact point from the center of the beam pipe at chamber 1 and 4 (12 $cm < r_{DCH1} < 120$ cm, 13 $cm < r_{DCH4} < 120$ cm) has been already done in the preselection and it is not refined.
Cut 5 rejects tracks too close in time to other tracks to remove background from decay with more than 1 track (see Fig. 7.5). Cut 6 rejects tracks too close in time with a signal in pocket 2, 3, 4 or 5 of the AKL detector to remove background from $\pi^{\pm}\pi^0$ and K_{e3} decays having one of the particles produced in the decay outside the central detectors acceptance (see Fig. 7.6). The study of systematic

effects of these cuts on the acceptance are studied on Section 9.2.
A bidimensional cut on the transverse momentum versus the total track momentum is performed (cut 7). The two quantities are strictly linked by a elliptic relation correlated with the missing mass value:

$$MM^2(e) \simeq \frac{m_K^2}{p_K}(p_K - p_{el}) - p_K\frac{p_T^2}{p_{el}} \tag{7.1}$$

In Fig. 7.7 the Monte Carlo distributions of K_{e2} , K_{e3} and $\pi^{\pm}\pi^0$ events are plotted. The fiducial region cut has been placed at 3 σ from the mean value.
The decay vertex reconstruction is performed minimizing the distance of approach of the track with respect to the beam line. As KABES detector informations are not used in the reconstruction, the beam line direction is assumed as flight direction for K particles. Cut 8 on the distance of approach of the track from the Kaon flight direction removes background of events with secondary decay in flight and removes poorly reconstructed tracks (see Fig. 7.11). Cut 9 on the longitudinal coordinate of the decay vertex (see Fig. 7.8 and Fig. 7.9) is a duplication of a cut of the $K_{\mu 2}$ analysis. Explanations of this cut will be given in $K_{\mu 2}$ selection Section. The upper bound removes background events originating from photon conversions at the Kevlar window and events whose acceptance is strongly dependent on the beam transverse distribution.

A cut on the electromagnetic cluster distance from the border and edges of the LKr calorimeter has been already done in the preselection. Cut 10 requires that the center of the electromagnetic cluster is more than 2 *cm* away from any *dead cell* in order to avoid any systematic bias on the E/p value of the track. The LKr geometrical acceptance is plotted in Fig. 7.10.
Cut 11 requires that all LKr clusters, except the one associated with the track, have an energy lower than 1.5 GeV. This cut remove most of the background events with photons from a π^0 decay, like K_{e3} and $\pi^{\pm}\pi^0$.

Cut 12 is related with the trigger signal of Level 2 used for K_{e2} events, called M_{Fake}:

$$M^2_{Fake}(\pi) = M_K^2 - M_\pi^2 - S \tag{7.2}$$

$$where:$$

$$S \equiv (P_K - P_u)^2 \qquad \vec{P_k} = (0,0,60)\ GeV/c \qquad u = e, \pi$$

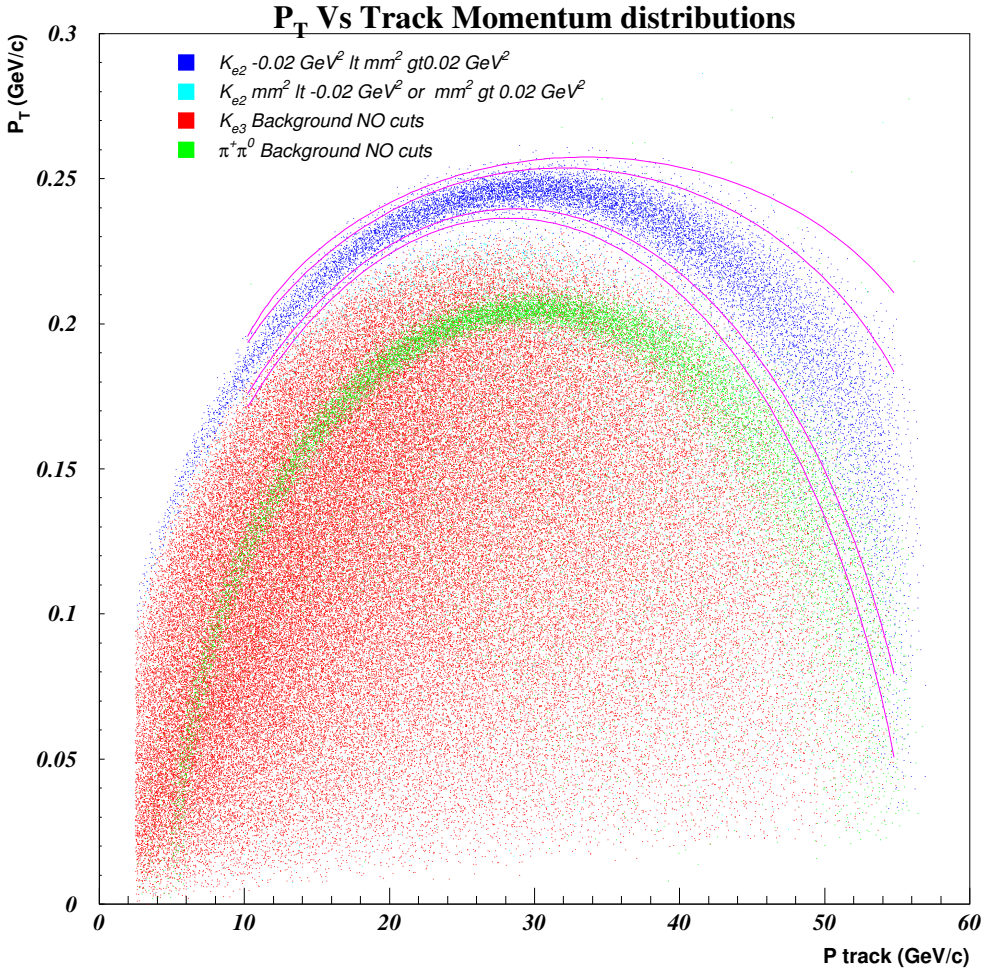

Figure 7.7: *Monte Carlo P_T versus total momentum distribution for K_{e2} , K_{e3} and $\pi^{\pm}\pi^0$ events.*

Details and efficiency of this trigger variable are presented in Chapter 10. The only relevant consideration at the moment is that the boundary limits have been chosen to include a region of flat trigger efficiency (see Fig. 10.5).

A final cut, not presented here, is done to identify the K_{e2} signal involving the E/p value of the track and its missing mass. This cut is directly linked to the background rejection and its study will be presented in details in Chapter 8.

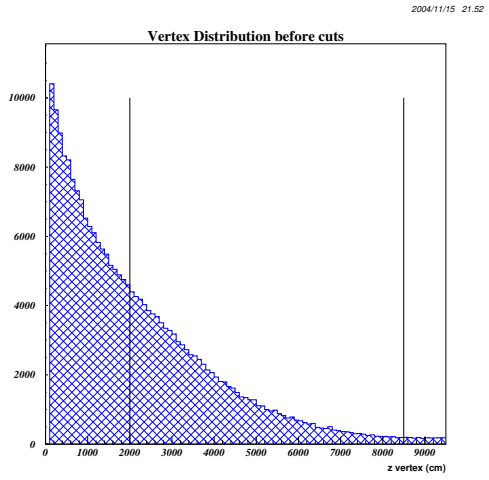

Figure 7.8: *z coordinate of the decay vertex distribution for K_{e2} candidates with only preselection cuts.*

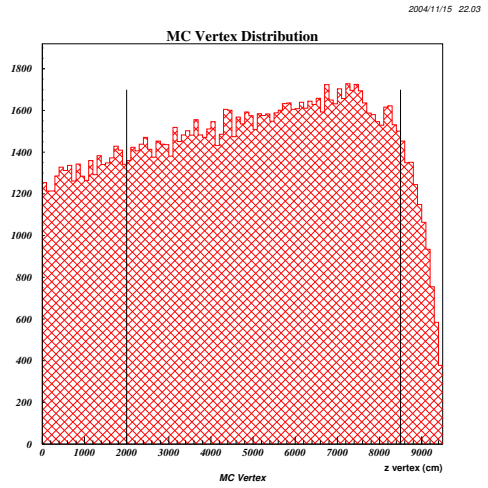

Figure 7.9: *Monte Carlo reconstructed K_{e2} z coordinate of the decay vertex distribution.*

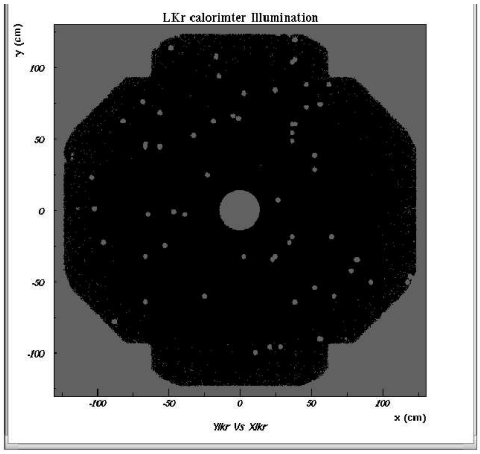

Figure 7.10: *Calorimeter illumination by $K^{\pm} \to \pi^{\pm}\pi^0\pi^0$ events The low intensity spots identify the location of the dead cells, while the outer shape of the calorimeter is given by the fiducial cut on the distance from the borders of the calorimeter.*

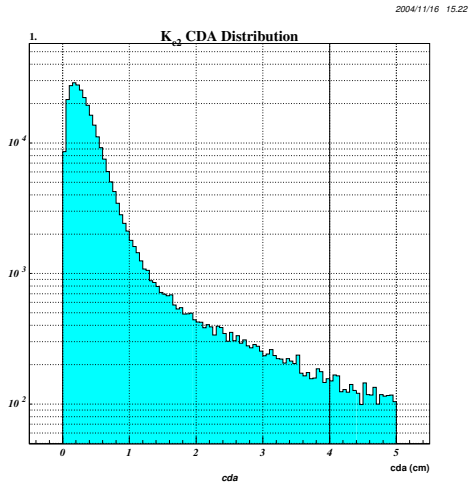

Figure 7.11: *K_{e2} candidates distribution of the closest distance of approach (cda) between lepton track and beam line.*

7.3 $K_{\mu 2}$ Selection

In table 7.2 are shown the $K_{\mu 2}$ selection cuts and acceptance; as for K_{e2} , explanation of the cuts follows in the text.

$K_{\mu 2}$ **Selection Cuts**			
	Cut	$A_S(\%)$	$A_C(\%)$
	Preselection		
	n. track > 0	100	71.8
	General Selection		
1	Bad Bursts	99.97	71.7
	Track Selection		
2	Track Quality > 0.7	99.99	71.7
3	Ghost tracks	99.93	71.7
4	$15\ GeV/c\ <\ P\ <\ 55\ GeV/c$	82.2	58.9
5	$\lvert t^{Track} - t_i^{Track}\rvert\ >\ 5\ ns$	-	-
6	$\lvert t^{Track} - t^{AKL}\rvert\ >\ 10\ ns$	-	-
7	$P_T VsP$	92.1	57.9
8	$cda\ <\ 4\ cm$	99.8	57.9
9	$2000\ cm\ <\ z_{vrtx}\ < 8500\ cm$	62.5	35.2
	Cluster Selection		
10	$d_{dcell}\ >\ 2\ cm$	98.5	34.7
11	$E_{extraclusters}\ <\ 1.5\ GeV$	99.99	34.7
12	$-0.02\ GeV^2/c^4\ <\ MM^2(\mu)\ <\ 0.02\ GeV^2/c^4$	99.3	34.7
13	Geometry Cut	91.4	32.4
14	$0.512\ GeV/c^2\ <\ M_{Fake}(\pi)\ <\ 0.531\ GeV/c^2$	69.4	25.7
15	L1 $\times$ L2 Trigger	-	-
	Final	-	25.7

Table 7.2: *$K_{\mu 2}$ event selection and acceptance for each single cut (A_S) and cumulative acceptance including the previous cuts (A_C). A line (-) means that the acceptance factors are not applicable for that particular cut. A_S acceptance is normalized to the number of events with at least one reconstructed track by the spectrometer. A_C acceptance is normalized to the number of generated $K_{\mu 2}$ decays in signal region.*

The selection of $K_{\mu 2}$ events is very similar to K_{e2} selection: as already mentioned, many cuts are present in both selection to exploit the cancellation of systematic effects in the acceptance ratio. The selection starts from the events with al least 1 track and with the appropriate $K_{\mu 2}$ trigger word. Again, all the events collected in a burst with the malfunctioning of one of the detectors involved in the analysis are discarded (cut 1 in Table 7.2). A cut is performed on the trigger signals, asking that the L1 trigger signal used for $K_{\mu 2}$ is present (see Chapter 10 for explanation of $K_{\mu 2}$ trigger logic).

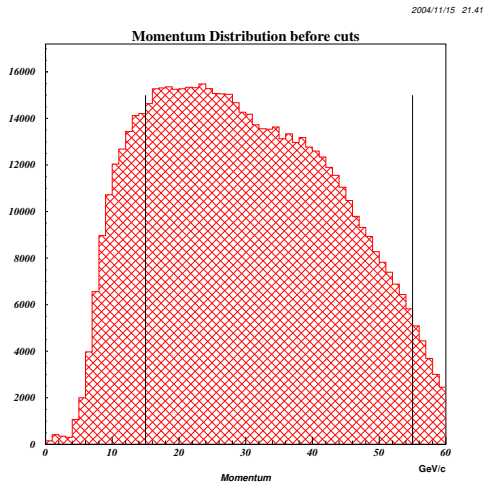

Figure 7.12: *Lepton momentum distribution for $K_{\mu 2}$ candidates with only preselection cuts.*

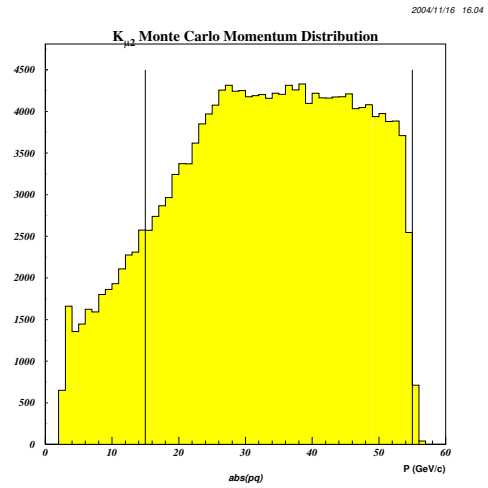

Figure 7.13: *Monte Carlo reconstructed $K_{\mu 2}$ momentum distribution.*

At this point, a selection routine is applied to every remaining track of each event. The selection routine is applied to an event, even if that event has been already flagged as a K_{e2} candidate, to avoid any bias on the ratio. In fact K_{e2} and $K_{\mu 2}$ selections are not exclusives and, in principle, an event might be flagged as both K_{e2} and $K_{\mu 2}$ candidate. A posteriori, it is possible to conclude that no event has passed both analysis selections. The strong downscaling of the trigger signal, compared to the available statistics, makes very unlikely for an event to pass both selections having at the same time a positive response from both triggers.

As for K_{e2} selection, a check on the quality of reconstruction of every track is

performed and *ghost tracks* are rejected (cuts 2 and 3).
Cut 4 rejects tracks of low and very high momentum (see Fig. 7.12 and 7.13). The bounds have been chosen to be the same of K_{e2} selection.
The next two cuts are examples of selections present in K_{e2} selection duplicated in $K_{\mu 2}$ selection to minimize systematic effects of the acceptance correction to the R_K ratio. Cut 5 rejects tracks too close in time to other tracks to remove background from decay with more than 1 track (see Fig. 7.14). Cut 6 rejects tracks too close in time with a signal in pocket 2, 3, 4 or 5 of the AKL detector to remove background from $\pi^{\pm}\pi^0$ and $K_{\mu 3}$ decays having one of the particles produced in the decay outside the central detectors acceptance (see Fig. 7.15). The study of systematic effects of these cuts on the acceptance is reported in Section 9.2.

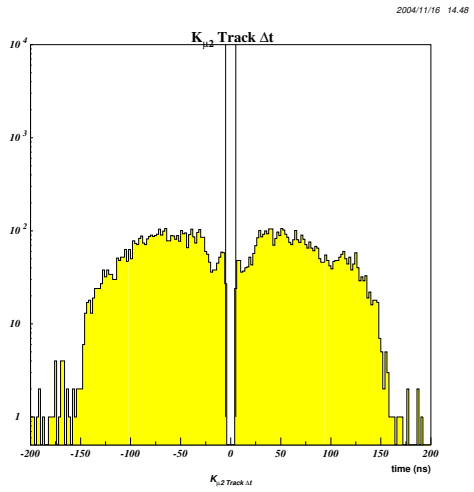

Figure 7.14: *Distribution of the time difference between the candidate $K_{\mu 2}$ track and the nearest in time track. The lines represent the limits of the time cut.*

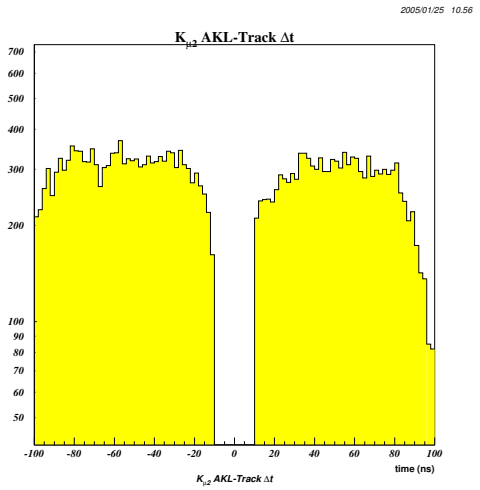

Figure 7.15: *Distribution of the time difference between the candidate $K_{\mu 2}$ track and the nearest in-time hit in a AKL pocket.*

A bidimensional cut on the transverse momentum versus the total track momentum is performed (cut 7). It is similar to K_{e2} cut, but its mean value is displaced due to the difference in mass between electron and muon. In fact

$K_{\mu 2}$ elliptic relation between momentum and its transverse component is:

$$MM^2(\mu) \simeq (\frac{m_K^2}{p_K} - \frac{m_\mu^2}{p_\mu})(p_K - p_\mu) - p_K \frac{p_T^2}{p_\mu} \tag{7.3}$$

In Fig. 7.16 the Monte Carlo distributions of $K_{\mu 2}$, $K_{\mu 3}$ and $\pi^\pm\pi^0$ events are plotted. The fiducial region cut has been placed at 3 σ from the mean value, as for the K_{e2} cut.

Cut 8 on the distance of approach (see Fig. 7.20) is a duplication of the analog K_{e2} cut. The lower bound of cut 9 (see Fig. 7.17 and Fig. 7.18) on the decay vertex position has been placed to reject muons produced upstream the decay region. As shown in Fig. 7.19, a muon can cross the iron flanges of the final collimator and its reconstructed vertex position can be inside the decay region. The upper bound removes background events originating from conversions of photons passing through the Kevlar window.

In K_{e2} selection a cut on the electromagnetic cluster distance from the border and edges of the LKr calorimeter is performed along with a cut on the cluster distance from *dead cells*. Following the principle of symmetrization of the acceptance cuts between $K_{\mu 2}$ and K_{e2} , an equivalent cut should be done for $K_{\mu 2}$ events. Often the muon energy deposition in the calorimeter is too low to allow the reconstruction of a cluster ($\sim$ 61 % of the times). For this kind of events, the cut is done on the extrapolated position of the track at the face of the LKr calorimeter. The systematic effect of this cut on $K_{\mu 2}$ acceptance have been calculated on section 9.3.

Cut 12 is a copy of the K_{e2} selection cut requiring that all LKr clusters, but the one associated with the track, have an energy lower than 1.5 GeV. This cut remove most of the background events with photons from a π^0 decay, like $K_{\mu 3}$ and $\pi^\pm\pi^0$.

Cut 13, not present in K_{e2} analysis, is done on the track reconstructed missing mass (see Fig. 7.21). The cut is very broad (4.5 σ from the peak).

Cut 14 is similar to Cut 12 of K_{e2} selection, The range is displaced due to the difference in mass between electron and muon.

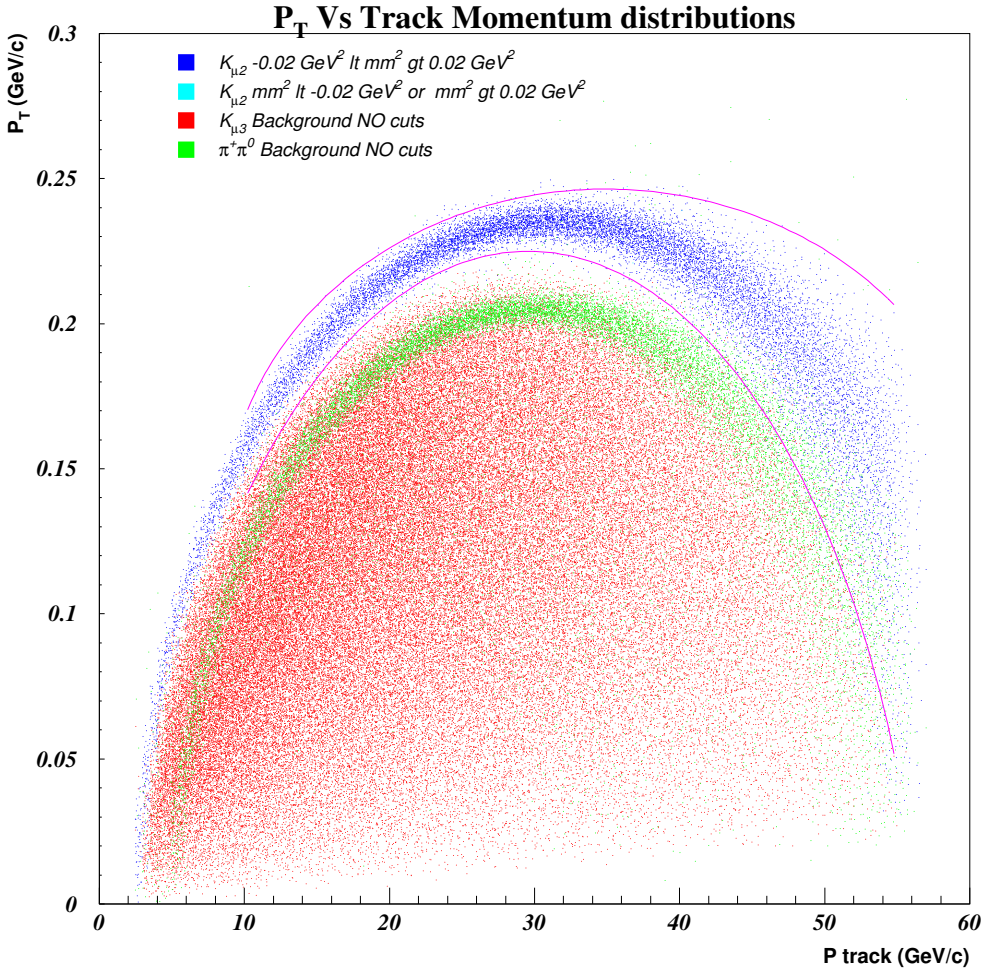

Figure 7.16: *Monte Carlo P_T versus total momentum distribution for $K_{\mu 2}$, $K_{\mu 3}$ and $\pi^{\pm}\pi^0$ events.*

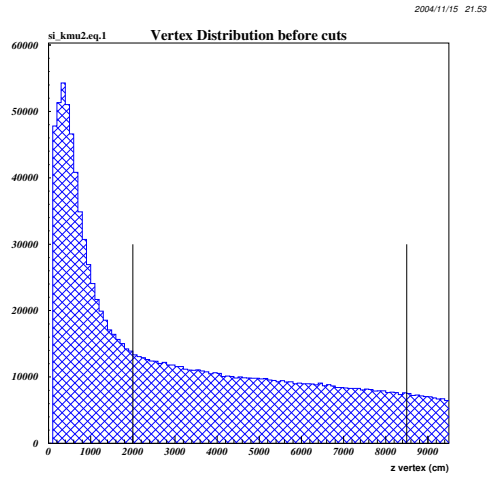

Figure 7.17: *z coordinate of the decay vertex distribution for $K_{\mu 2}$ candidates with only preselection cuts.*

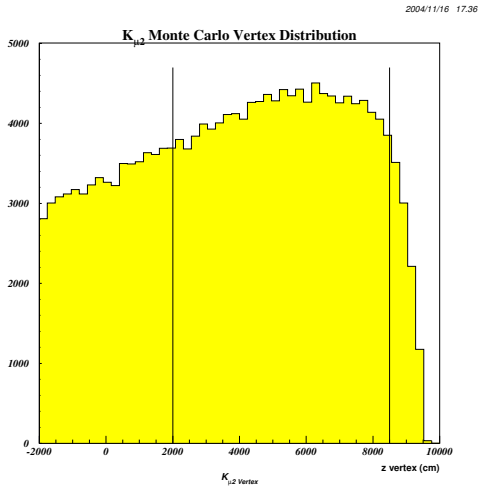

Figure 7.18: *Monte Carlo reconstructed $K_{\mu 2}$ z coordinate of the decay vertex distribution.*

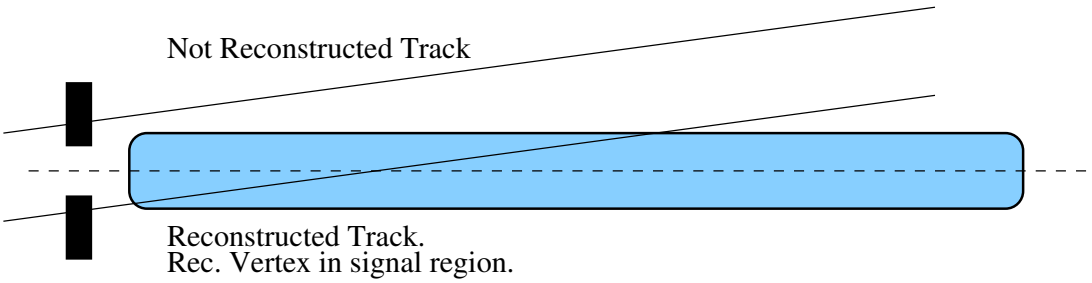

Figure 7.19: *Two muon tracks traversing the flanges of the final collimator. One is not reconstructed, because it doesn't satisfy the condition required for reconstruction (see Section 5.1.1). The second track satisfy such condition and the event vertex is reconstructed inside the decay region.*

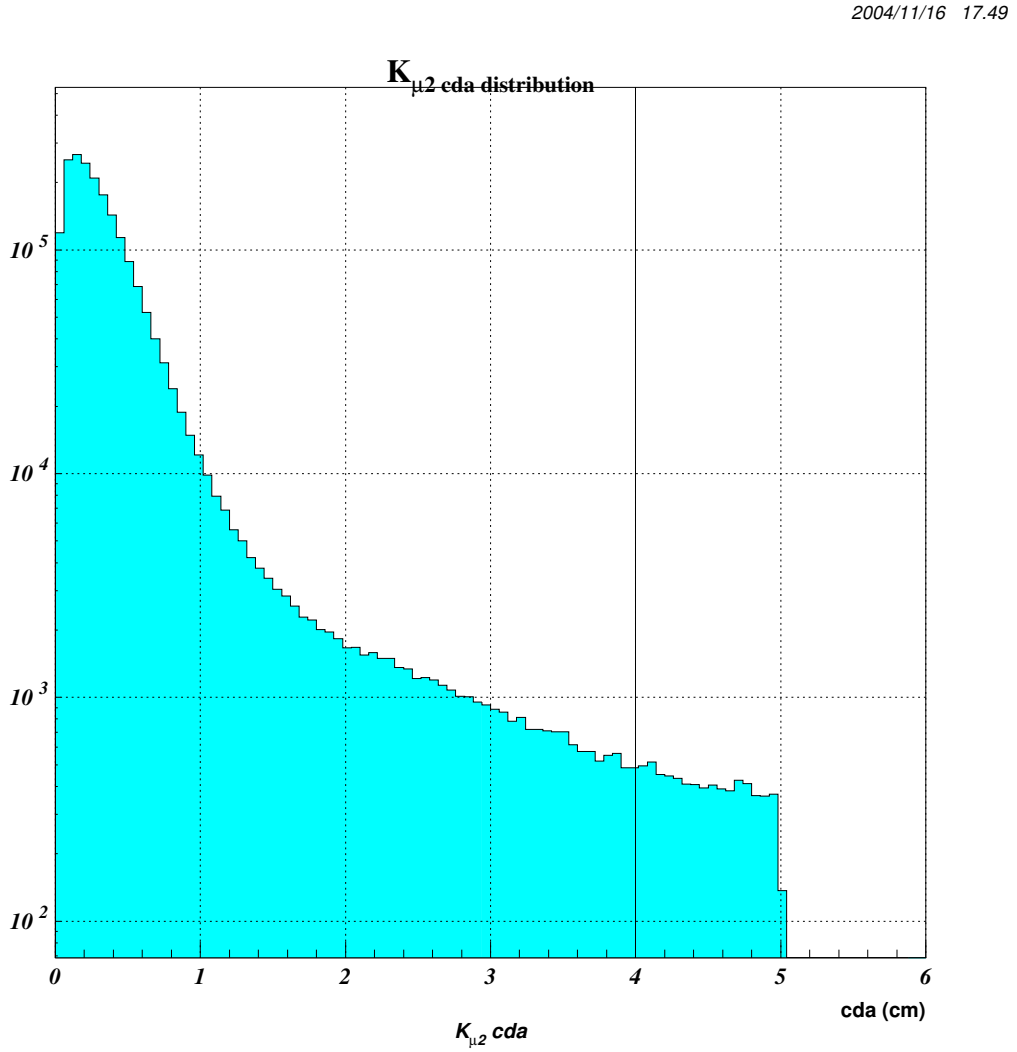

Figure 7.20: *$K_{\mu 2}$ candidates distribution of the closest distance of approach (cda) between lepton track and beam line direction.*

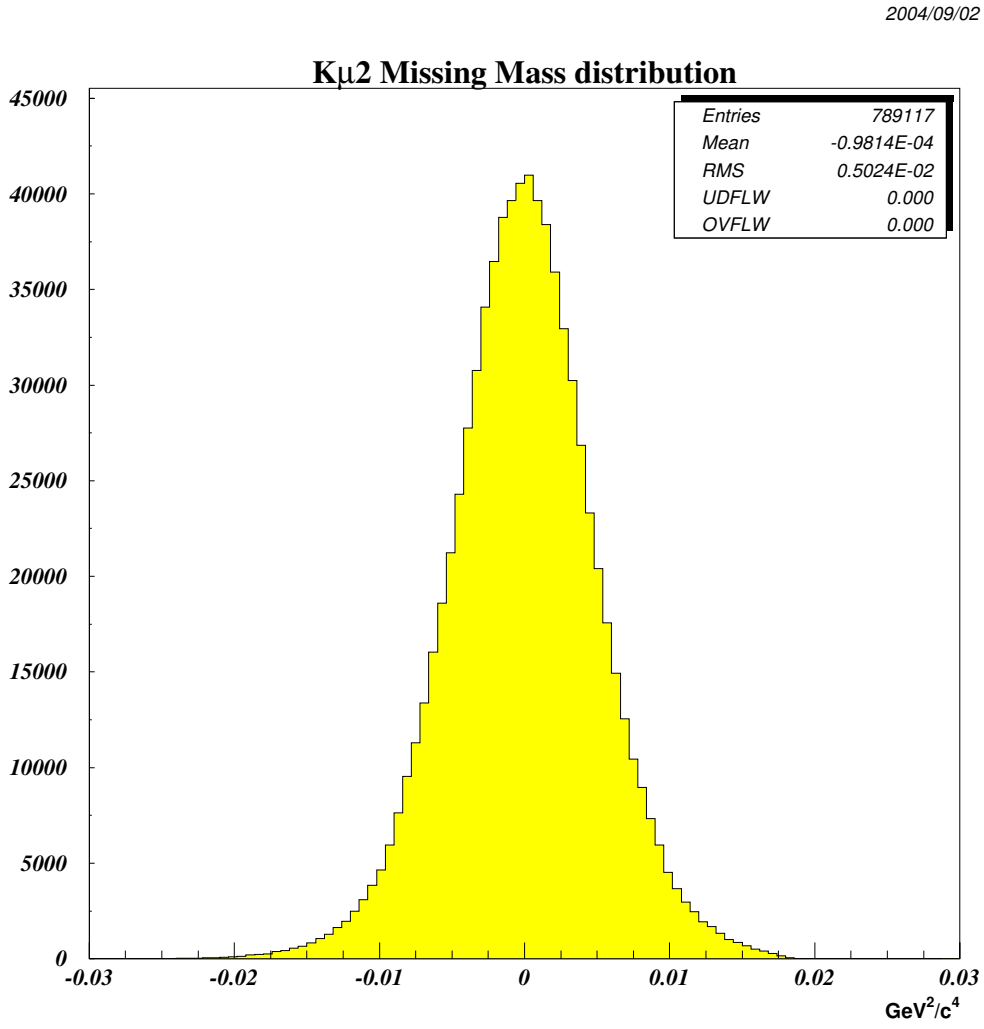

Figure 7.21: *Distribution of the missing mass for $K_{\mu 2}$ reconstructed events. The signal is almost completely contained in the signal region* $-0.02\ GeV^2/c^4 < MM^2(\mu) < 0.02\ GeV^2/c^4$

7.4 Acceptance Results

The two selections were intended to be as similar as possible to exploit the topological similarity of K_{e2} and $K_{\mu 2}$ decays and therefore lowering the effect of any eventual disagreement between Data and Monte Carlo in R_K ratio. It can be interesting to remark that the $K_{\mu 2}$ and K_{e2} acceptances differ for $\sim 10\%$. This difference depends almost entirely on the different geomtrical acceptance of the two decays and on the different bremsstrahlung probability for muons and electrons, while the chosen selection cuts are very similar.
The correction to R_K ratio due to the different K_{e2} and $K_{\mu 2}$ acceptance factors can be extracted from the final numbers in Table 7.1 and Table 7.2. The results obtained are shown in Table 7.3.

R_K **Acceptance correction**	
K_{e2} Acceptance	$0.2305 \pm 0.0004_{(stat)}$
$K_{\mu 2}$ Acceptance	$0.2573 \pm 0.00015_{(stat)}$
$\frac{\Delta R_K}{R_K}$ **correction**	$+0.1162 \pm 0.0018_{(stat)}$

Table 7.3: *Summary of the Acceptance Correction to R_K. Only statistical errors are taken into account. Chapter 9 is devoted to the study of systematics uncertainties linked to the acceptance correction.*

The error on the result quoted here takes into consideration the statistical uncertainty only. Chapter 9 is devoted to the study of systematics uncertainties linked to the acceptance correction.

Chapter 8

Background Study

Background rejection is probably the most important issue of the R_K ratio measurement. The smallness of the K_{e2} Branching Ratio requires a high rejection of all the possible sources of background. Among the corrections to R_K ratio, background correction is potentially asymmetric between K_{e2} and $K_{\mu 2}$. In fact the incidence of background on $K_{\mu 2}$ channel is very different from the incidence of background on K_{e2} channel, given the large difference of branching ratios. A significative reference in the study of the background is the product of the signal branching ratio times acceptance: $B.R.(Signal) \times A(Signal)$. The contamination of the background relative to the signal will be expressed using that value as normalization as shown in the following equations (B.R.(K_{e2}) and B.R.($K_{\mu 2}$) from PDG):

$$\frac{B.R.(Bkg) \times A_{MC}(Bkg)}{B.R.(K_{e2}) \times A_{MC}(K_{e2})} = \frac{B.R.(Bkg) \times A_{MC}(Bkg)}{3.9 \cdot 10^{-6}} \tag{8.1}$$

$$\frac{B.R.(Bkg) \times A_{MC}(Bkg)}{B.R.(K_{\mu 2}) \times A_{MC}(K_{\mu 2})} = \frac{B.R.(Bkg) \times A_{MC}(Bkg)}{0.20} \tag{8.2}$$

The background has been studied both in MC simulations and real data. Many possible decays have been taken in consideration and many studies have been carried out in order to have a good background rejection without an excessive loss in signal acceptance. Background channels simulation has been produced proportionally to the number of signal triggers in each run in order to exploit the CMC capability to follow the detector efficiency and beam geometry behaviors in time.

8.1 K_{e2} Backgrounds

The capability to successfully reject background contaminations to K_{e2} signal is crucial for the R_K ratio measurement. An important remark to be done is that no direct electron identification has been performed in K_{e2} selection presented in Chapter 7. To distinguish decays with an electron in the final state from decays with pions or muons, the ratio E/p between the cluster energy measured by the calorimeter detector and the associated track momentum measured by the spectrometer can be used.
Fixing a conservative lower bound ($E/pc > 0.85$), it is possible to reject the majority of events having a pion or a muon in the final state. The E/p distribution for electrons collected in 2002 from $K_L \to \pi^{\pm} e^{\mp} \nu$ decays is shown in Fig. 8.1. The E/p distribution of charged pions collected from $K^{\pm} \to \pi^{\pm}\pi^0\pi^0$ decays is shown in Fig. 8.2, while the E/p of muons from $K_{\mu 2}$ decay is shown in Fig. 8.3.

In the following, a panoramic based on Monte Carlo simulations of the physical sources of K_{e2} background will be shown, then the background subtraction technique used in the analysis will be presented. This technique is based on data distributions and uses Monte Carlo simulation only for guidance and checks on the kind of background sources.

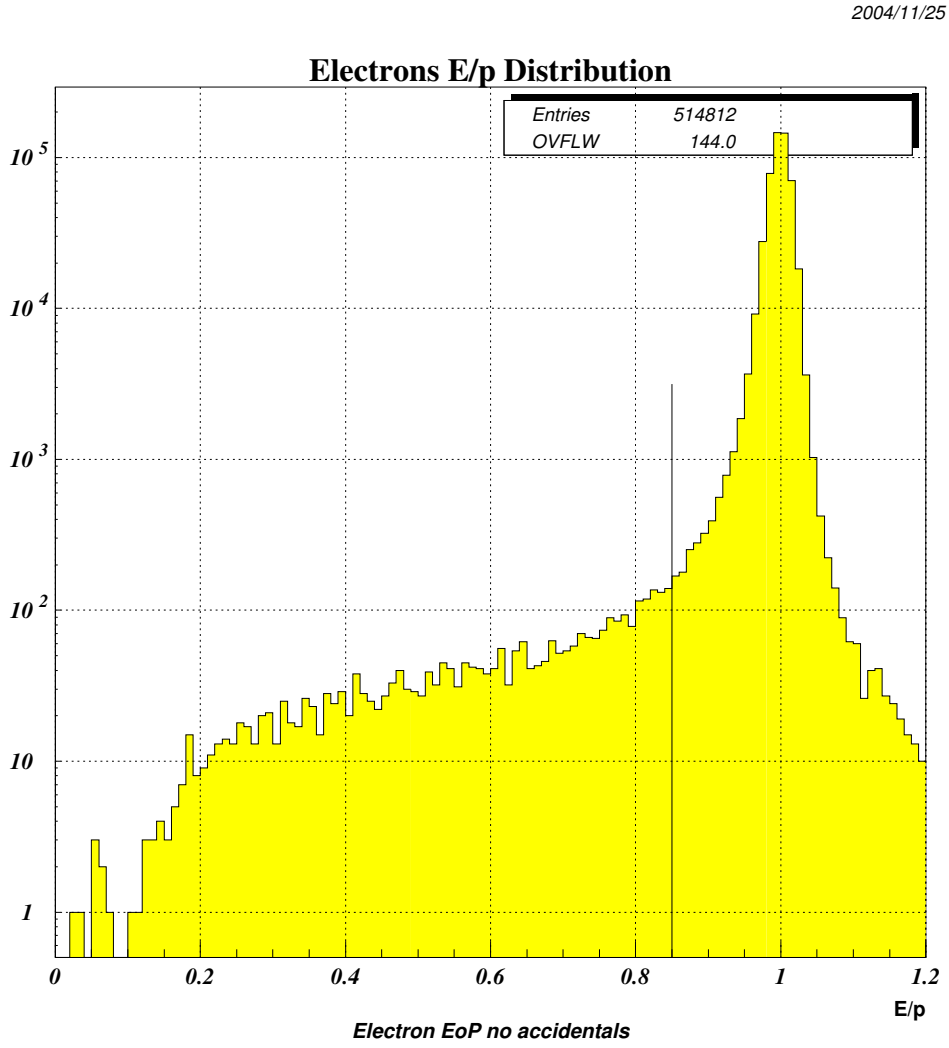

Figure 8.1: *E/p distribution for electrons candidates. The electrons have been selected from $K_L \to \pi^{\pm} e^{\mp} \nu$ decays collected during 2002 data taking. The tail at low E/p is attributed to electroproduction of hadrons at an early stage of the showering process within the LKr calorimeter.*

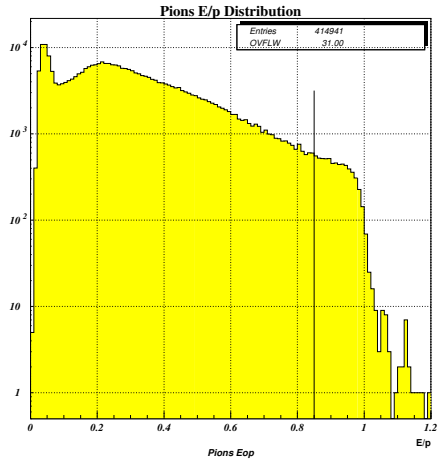

Figure 8.2: *E/p distribution for pions candidates. The pions have been selected from $K^{\pm} \to \pi^{\pm}\pi^0\pi^0$ decays. The peak at low values of E/p is due to muons from the in flight decay $\pi^{\pm} \to \mu^{\pm}\nu$ and to pions which do not interact hadronically in LKr calorimeter.*

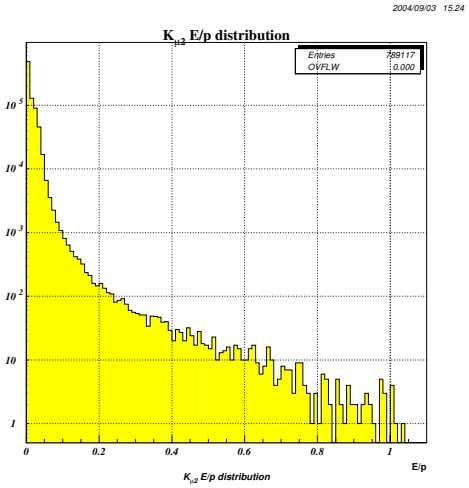

Figure 8.3: *E/p distribution for muons candidates. The muons have been selected from $K_{\mu 2}$ decays. No time coincidence with a signal from the muon veto detector has been required.*

8.1.1 K_{e3} Contamination

The 3 body decay $K^{\pm} \to e^{\pm}\pi^0\nu$ is topologically very different from K_{e2} decay signature. The distribution of the transverse momentum versus total momentum distribution for K_{e3} events doesn't significantly overlap K_{e2} signal region, as shown in Fig. 8.4. In Fig 8.5, the $MM^2(e)$ versus E/p distribution is presented.

The rejection of K_{e3} is improved by the detection of the photon produced by

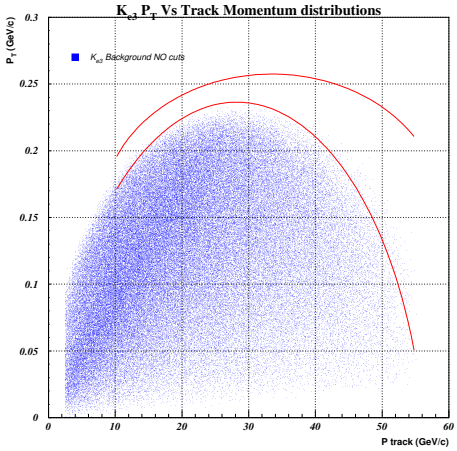

Figure 8.4: *Transverse momentum versus total momentum distribution for electron in K_{e3} events. The curves limit the K_{e2} signal region. No cuts have been applied.*

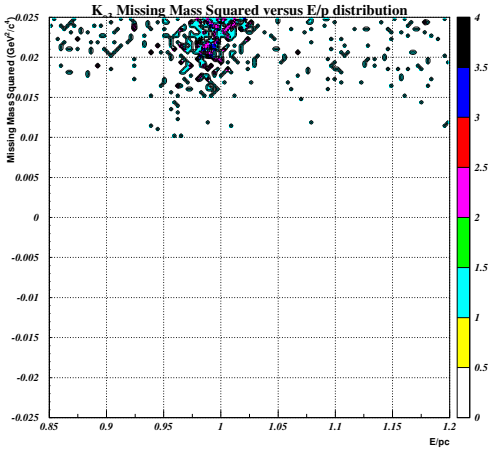

Figure 8.5: *Missing mass squared versus E/p distribution for K_{e3} events. The histogram is centered on the K_{e2} signal region.*

π^0 decay, made possible by the cut on the extra activity of the LKr calorimeter and on the time coincidence with an hit in one of the AKL pockets.

8.1.2 $K_{\mu 2}$ Contamination

The $K_{\mu 2}$ decay can constitute background to the K_{e2} signal in two different ways. In one case, the muon of the $K_{\mu 2}$ can decay in $e\nu\overline{\nu}$ final state and the event might be reconstructed as a K_{e2} event; in a second case, the $K_{\mu 2}$ can pass the selection cuts of the K_{e2} events, by having an $E/pc > 0.85$ Both cases are very unlikely, nevertheless the $K_{\mu 2}$ background is one of the most tricky sources of background, given the kinematical similarity of the two decays and the 4 order of magnitude between $K_{\mu 2}$ and K_{e2} Branching Ratios. In Fig. 8.7, it can

be observed how close are the missing mass squared distributions for these two decays. The transverse momentum versus total momentum distributions of the two decays overlap extensively as shown in Fig. 8.6.

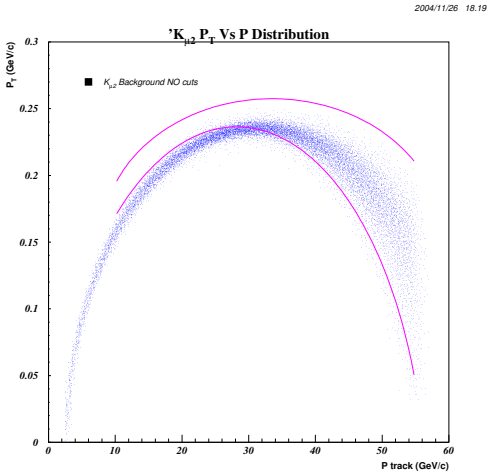

Figure 8.6: *Transverse momentum versus total momentum distribution for $K_{\mu 2}$ events. The curves limit the K_{e2} signal region. No cuts have been applied.*

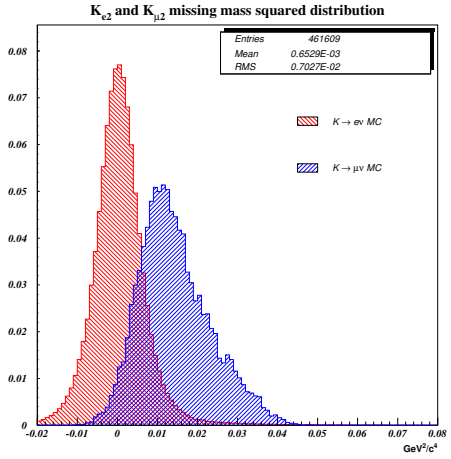

Figure 8.7: *MC Missing Mass squared comparison between $K_{\mu 2}$ events and K_{e2} events.*

8.1.3 $K^{\pm} \to \pi^{\pm}\pi^0$ Contamination

To reconstruct a $K^{\pm} \to \pi^{\pm}\pi^0$ decay as a K_{e2} events, it is necessary that the pion deposit more than 85% of its energy in the LKr calorimter and that none of the particles produced by the subsiquent π^0 decay are detected by the LKr calorimeter or by the AKL detector. The missing mass squared distribution of $K^{\pm} \to \pi^{\pm}\pi^0$ events is shown in Fig. 8.8. In Fig. 8.9 it can be seen that at high momentum values $K^{\pm} \to \pi^{\pm}\pi^0$ can populate K_{e2} signal region.

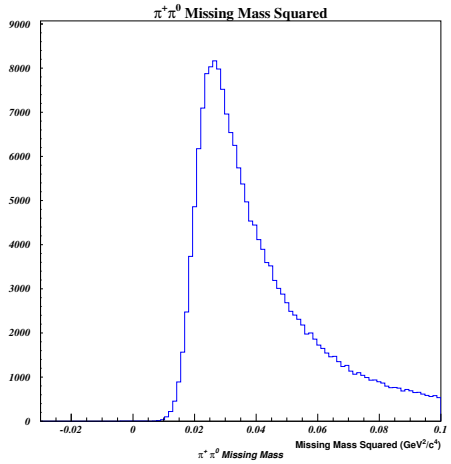

Figure 8.8: *Missing Mass squared distribution for* $K^{\pm} \to \pi^{\pm}\pi^{0}$ *events, under the assumption of* 60 *GeV/c Kaon momentum. No cut has been applied.*

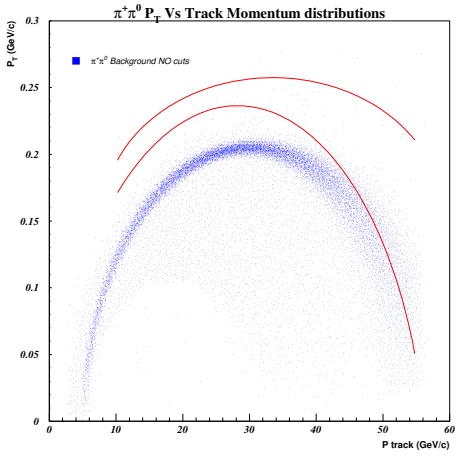

Figure 8.9: *Transverse momentum versus total momentum distribution for* $K^{\pm} \to \pi^{\pm}\pi^{0}$ *events. The lines limit the* K_{e2} *selection cut region. No cut has been applied.*

8.1.4 $\pi^{\pm}$ Decays Contamination

Pions are the most abundant particles in the NA48/2 beam. Pion decays can pass the K_{e2} selection in two different ways: $\pi^{\pm} \to \mu^{\pm}\nu$ decay in the case of subsequent muon decay in $e\nu\overline{\nu}$ final state or direct $\pi^{\pm} \to e^{\pm}\nu$ decay.
The first source of background is not very relevant, since it is smaller than the analogue $K_{\mu 2}$ background, in consideration of the longer pion life-time and smaller kinematic acceptance.
The second source of background has been studied by MC simulation. The acceptance of $\pi^{\pm} \to e^{\pm}\nu$ events in the K_{e2} signal region is suppressed by kinematic considerations, as the transverse momentum of the electron from this decay is relatively small (see Fig. 8.11) and because the event missing mass squared in the hypothesis of a K_{e2} decay is shifted towards high values, as shown in Fig. 8.10.

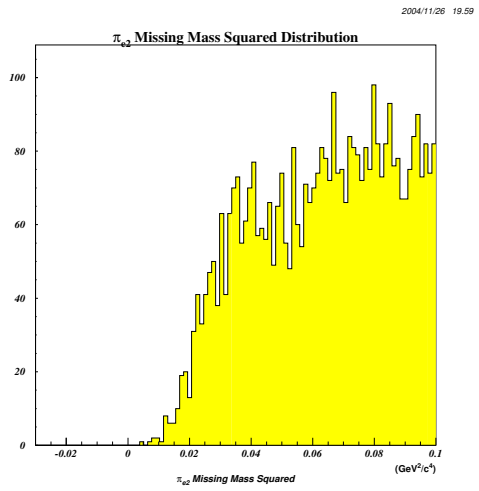

Figure 8.10: *Missing Mass squared distribution for $\pi^{\pm} \to e^{\pm}\nu$ events, under the assumption of 60 GeV/c Pion momentum. No cut has been applied.*

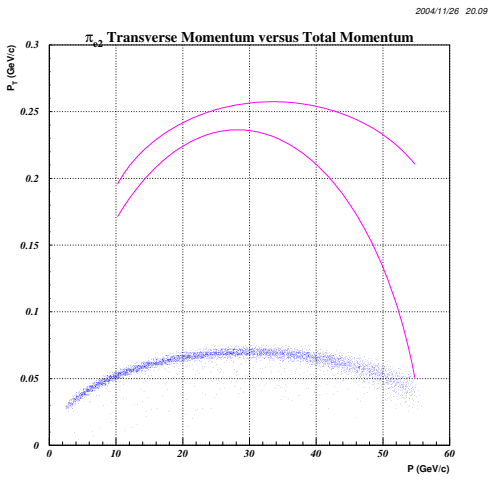

Figure 8.11: *Transverse momentum versus total momentum distribution for $\pi^{\pm} \to e^{\pm}\nu$ events. The lines limit the K_{e2} selection cut region. No cut has been applied.*

8.1.5 K_{e2} Background Subtraction

Before describing the technique employed to subtract the background, the distribution of missing mass squared and E/p of data events collected in 2003 by the K_{e2} selection will be presented. The scatter plot of the missing mass squared versus the E/p of K_{e2} candidates is represented in Fig. 8.12.

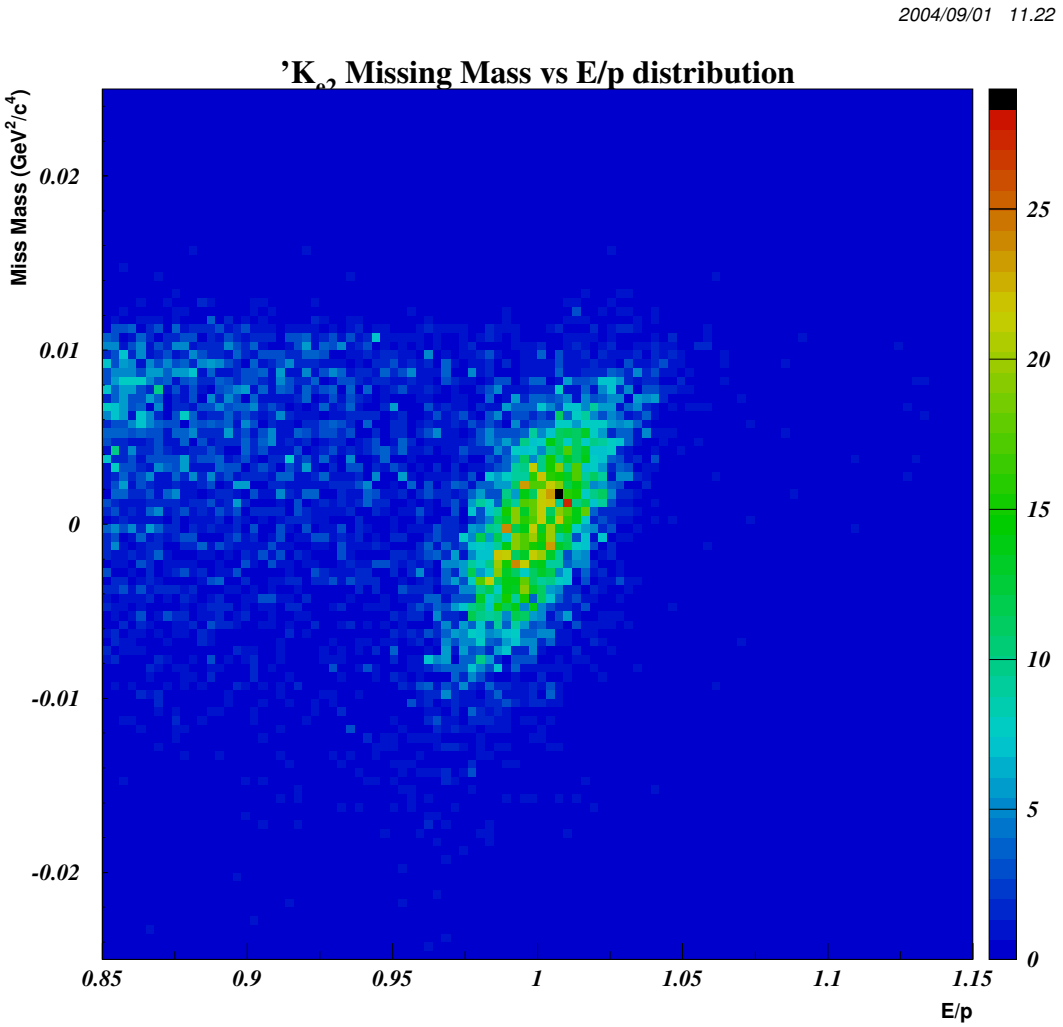

Figure 8.12: *$MM^2(e)$ versus E/p distribution for K_{e2} candidates. The signal events accumulates under the gaussian peak centered at $\mu = (E/pc = 1, MM^2(e) = 0)$. There is an accumulation of events a low values of E/p.*

In the bidimensional plot 8.12 a gaussian peak is visible in the density of events at $E/pc \simeq 1$ and $MM^2(e) \simeq 0$. The events show an expected correlation between their E/p and $MM^2(e)$ values, due to the spectrometer resolution. In fact, if, for instance, a mismeasurement of the track momentum due to resolution effects lowers the reconstructed momentum value, it will induce an increase in both E/p and $MM^2(e)$ in a correlated way. The correlation relation between E/p and $MM^2(e)$, shown in Fig. 8.13, is almost straight in the K_{e2} signal region. It can be seen that the major axis of the elliptical contour of the region under the gaussian peak follow rather well the correlation function.

On the left side of Fig. 8.12, at low values of E/p and high values of $MM^2(e)$, events outside the gaussian distribution are clearly visible. These events have been interpreted as a signature of background contamination. In fact, in Fig. 8.14 the Monte Carlo distribution of K_{e2} events reproduces correctly the gaussian distribution and correlation of data under the gaussian, but doesn't show the accumulation of events at low values of E/p.

The E/p projection of Fig. 8.12 shows a rapidly decreasing component in the distribution at low values of E/p (see Fig. 8.16) that doesn't have correspondence in the electron E/p distribution shown in Fig. 8.1. The $MM^2(e)$ distribution of these events differs from the K_{e2} Monte Carlo distribution shape, as shown in Fig. 8.15.

8.1.6 Background Identification

It is evident that the investigation of background physical origin contributes to understand the relevant effects in the determination of R_K ratio measurement.
Considering only the events far from the gaussian peak, selected as in Fig. 8.17, it can be observed that they are not uniformly distributed inside the K_{e2} signal region (see Fig. 8.18). In particular the background enters the K_{e2} signal region from the low p_T side and it accumulates in a region of momentum between 30 and 45 GeV/c at transverse momentum around 0.22 GeV/c.

It can be excluded that background derives from K_{e3} decays, as K_{e3} events would have a E/p distribution similar to K_{e2} events and higher $MM^2(e)$ values as seen in Fig. 8.5. Looking at Fig. 8.9, it can be seen that the maximum transverse momentum reachable by pions produced in $\pi^{\pm}\pi^0$ decays is well below

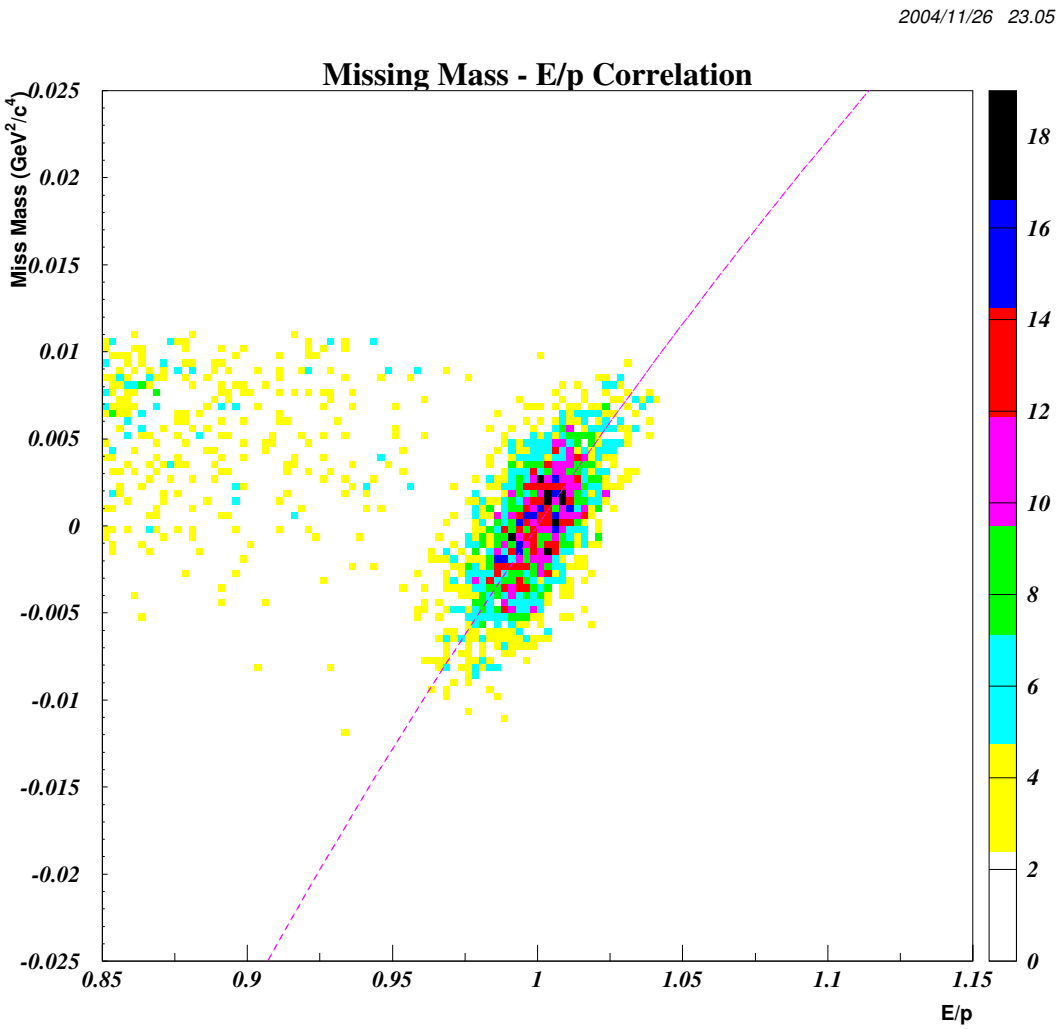

Figure 8.13: *The hatched line show the correlation function between E/p and $MM^2(e)$ passing by the point (E/pc=1 , $MM^2(e)$=0). The correlation is due to the dependence of both quantities on the track momentum.*

the p_T value of background events observed in Fig. 8.18. Muons originating from $K_{\mu 2}$ decays, instead, have a transverse momentum versus total momentum distribution compatible with the background events (see Fig. 8.6). Moreover, the $K_{\mu 2}$ $MM^2(e)$ distribution, seen in Fig. 8.7, is compatible with the missing mass squared of the background events. In Fig. 8.19, it has been plotted the transverse momentum of the background events. Their distribution has been superimposed

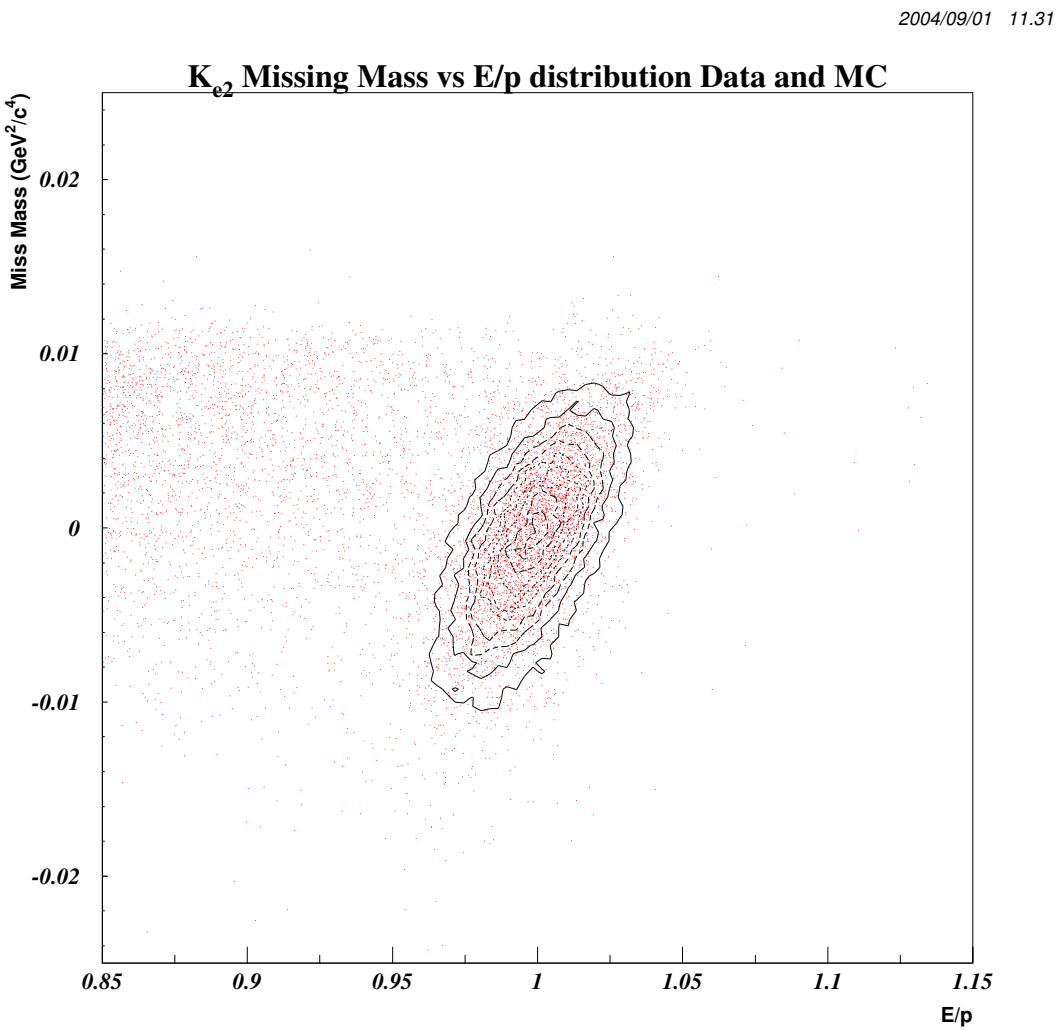

Figure 8.14: *$MM^2(e)$ versus E/p distribution for Data and Monte Carlo events. The contour lines represent the Monte Carlo distribution. Monte Carlo simulation reproduces the gaussian distribution of K_{e2} candidate events and the E/p versus $MM^2(e)$ correlation.*

to the p_T distribution of K_{e2} candidates under the gaussian peak (red histogram) and with the p_T distribution of $K_{\mu 2}$ candidates selected by $K_{\mu 2}$ selection. (yellow histogram). It can be seen that the background transverse momentum distribution is not compatible with the K_{e2} candidates distribution, but is agrees with the $K_{\mu 2}$ p_T distribution.

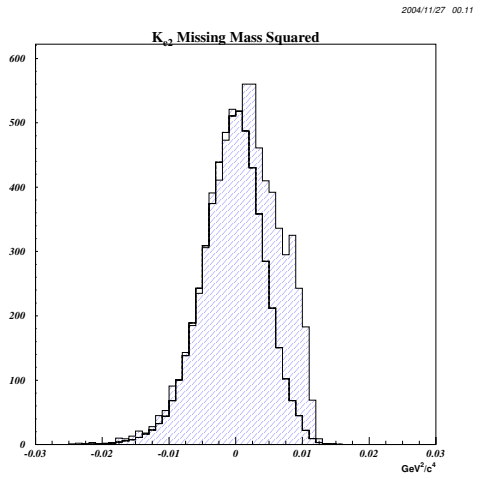

Figure 8.15: *Missing Mass squared distribution for K_{e2} events, under the assumption of 60 GeV/c Kaon momentum. Monte Carlo distribution (black line) has been superimposed. The presence of background events deformates the gaussian distribution for value of $MM^2(e)$ greater than zero.*

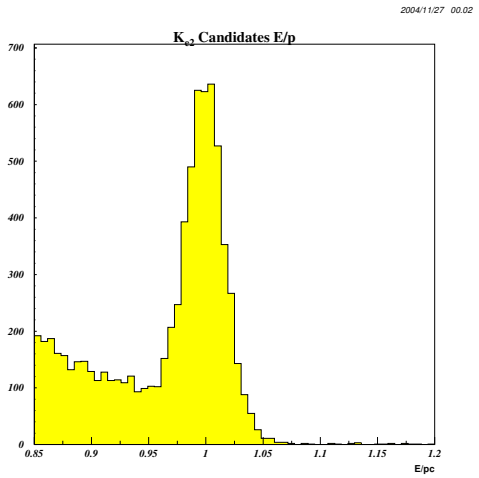

Figure 8.16: *E/p distribution for K_{e2} events. The presence of background events deformates the distribution seen on Fig. 8.1 at low values of E/p.*

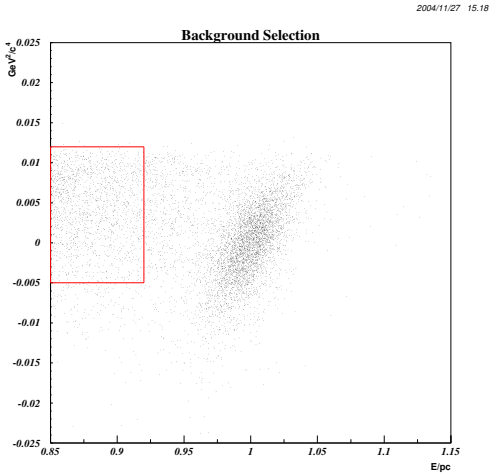

Figure 8.17: *Red box limiting the region taken into consideration for the K_{e2} background study. The events inside the box have been considered as a significative sample of K_{e2} background.*

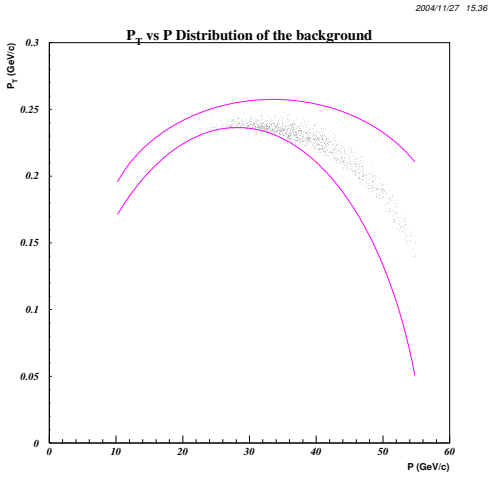

Figure 8.18: *Transverse momentum versus Total Momentum distribution of background sample events. The lines limit the K_{e2} signal region.*

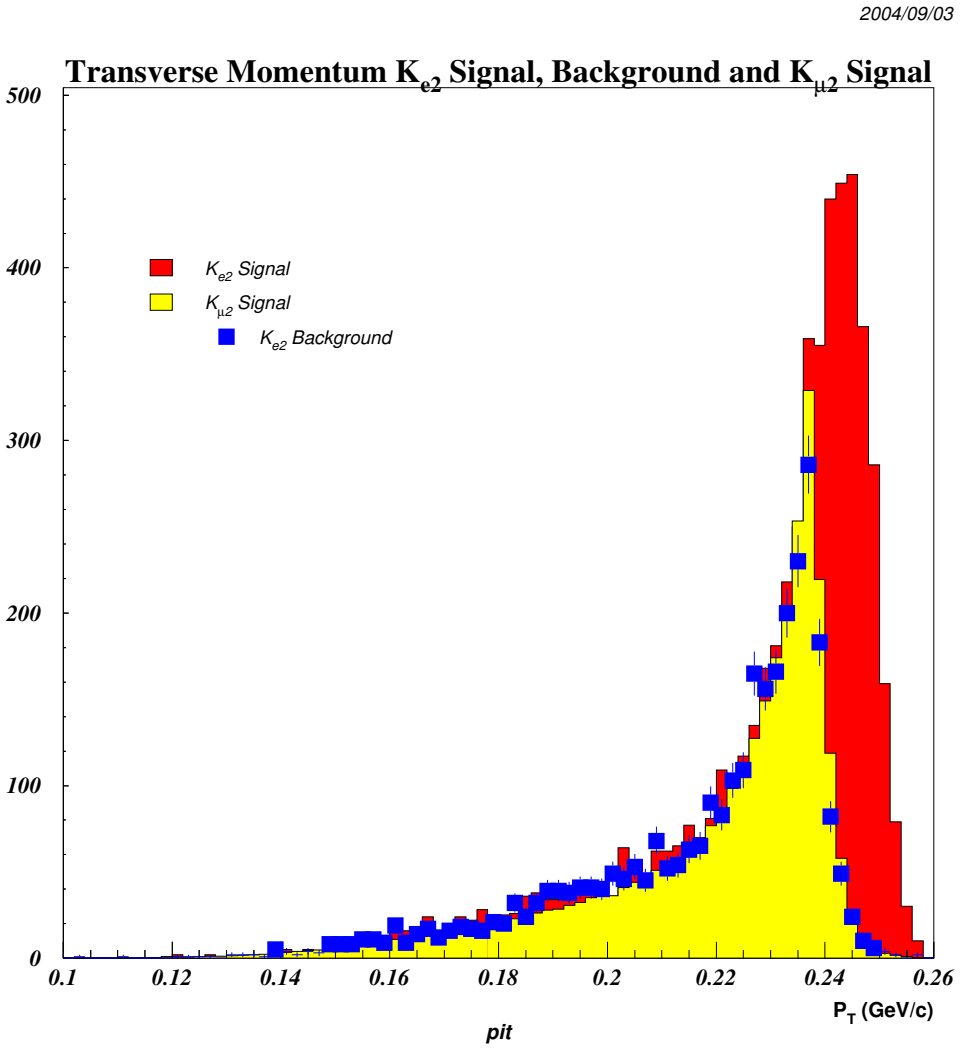

Figure 8.19: *Transverse Momentum distribution for background sample events, for K_{e2} candidates events under the gaussian peak and for $K_{\mu 2}$ candidate events. The background sample is represented with blue squares, K_{e2} candidates by the red histogram and $K_{\mu 2}$ events by the yellow histogram.*

8.1.7 Background Subtraction Technique

In this section the background subtraction technique will be presented. It has been shown that K_{e2} signal distribution in E/p versus $MM^2(e)$ scatter plot is a guassian (see Fig. 8.20). It has been shown also that the background decreases rapidly as a function of E/p (as seen in Fig. 8.16) and that it is almost completely contained in the region $MM^2(e) > 0\ GeV^2/c^4$ (as shown in Fig. 8.12). In particular, the contour levels of the K_{e2} signal distribution have the typical elliptical shape of the bidimensional gaussian distributions (as seen in Fig. 8.20).

Removing the lower bound of the selection cut on lepton p_T versus p, events with high values of missing mass squared can be studied. The event distribution in $MM^2(e)$ versus E/p plane, now expanded in $MM^2(e)$ axis, is plotted in Fig. 8.21. Signal and Background populations are shown in Fig. 8.22.

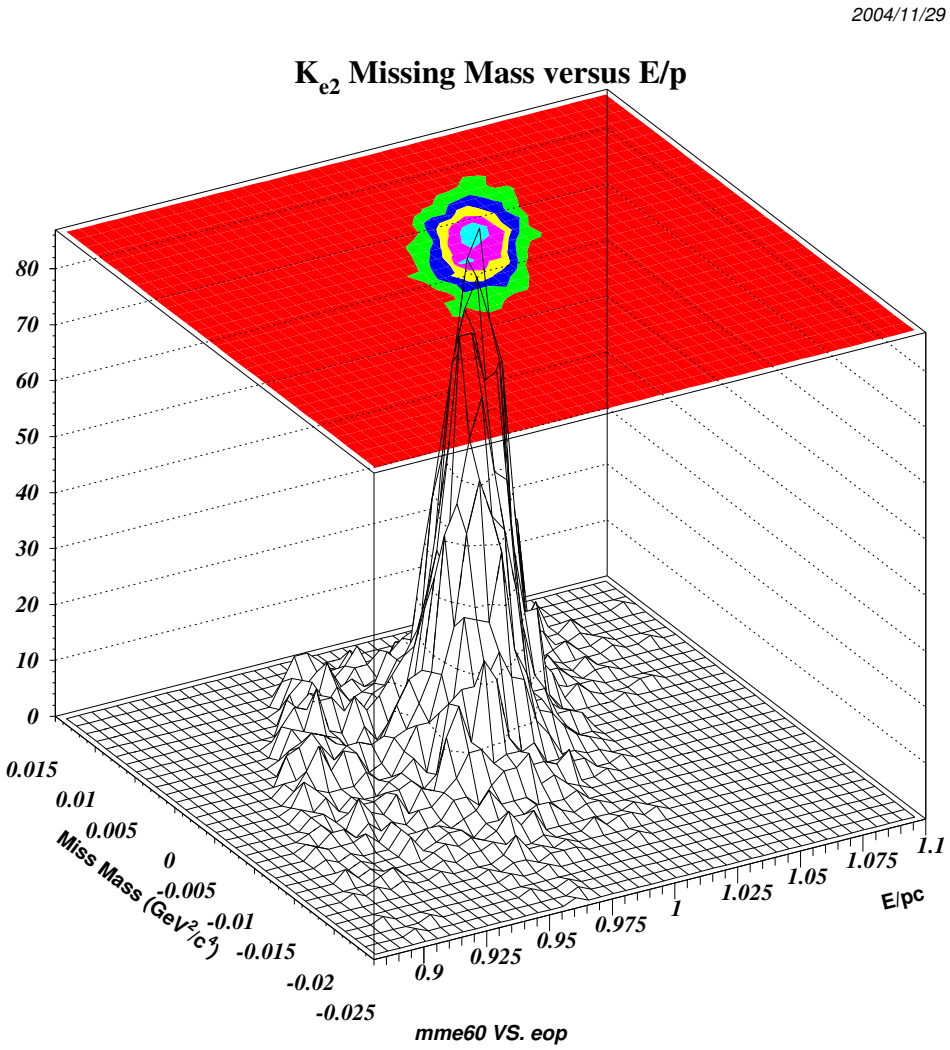

Figure 8.20: *$MM^2(e)$ versus E/p distribution for K_{e2} event candidates close to the gaussian peak. the contour levels of K_{e2} distribution are compatible with concentric ellipses.*

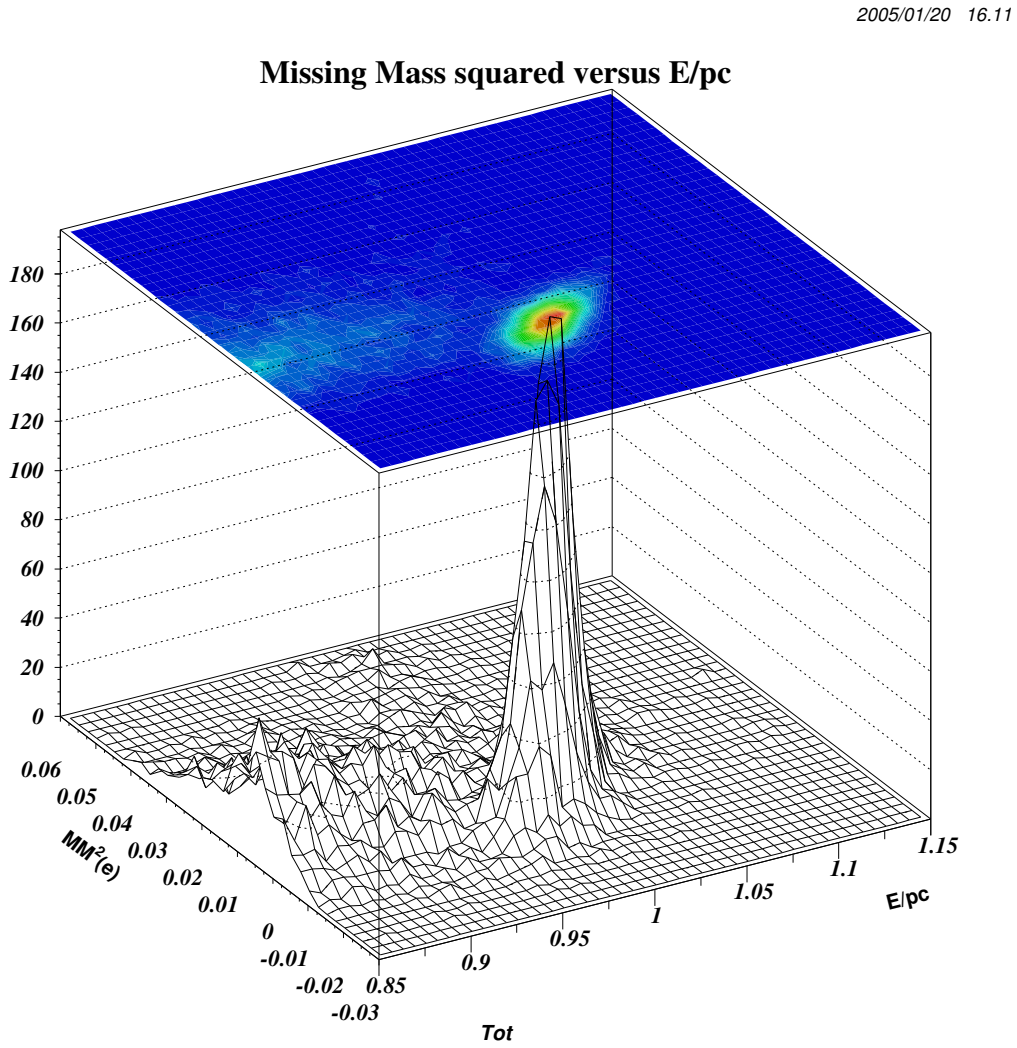

Figure 8.21: *$MM^2(e)$ versus E/p distribution for K_{e2} event candidates. The lower bound on lepton p_T versus p has been removed, allowing to explore background events at high values of missing mas squared.*

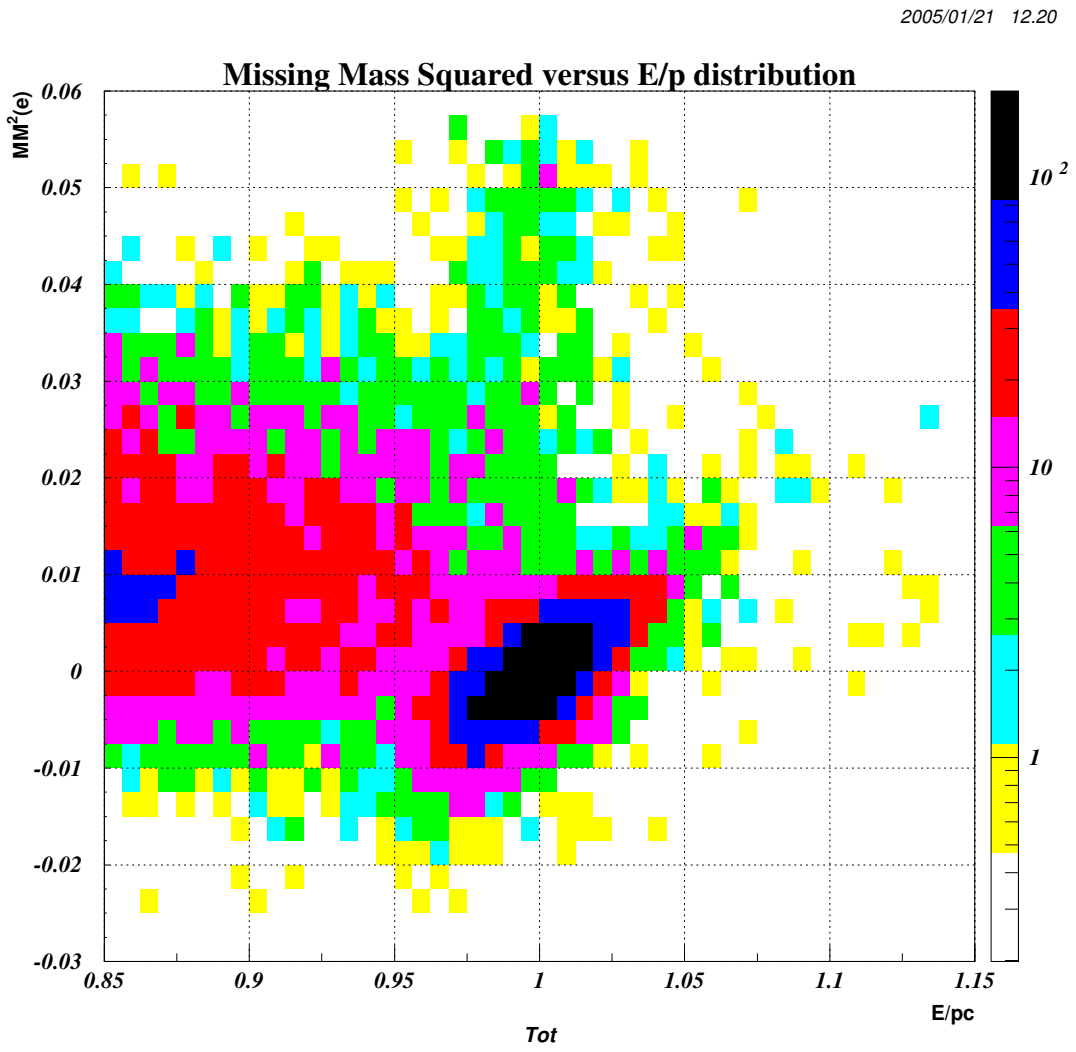

Figure 8.22: *$MM^2(e)$ versus E/p distribution for K_{e2} event candidates. The lower bound on lepton p_T versus p has been removed, allowing to explore background events at high values of missing mas squared. $K_{\mu 2}$ and K_{e3} background are visible in the plot. Logarithmic scale has been used to highlight background.*

The explanation of the presence of events at low E/p values in terms of $K_{\mu 2}$ background, already proved in Fig. 8.19, finds a new argument comparing Data events in $0.85 < E/pc < 0.9$ with Monte Carlo distribution as shown in Fig. 8.23. The explanation of the presence of events at high missing mass and $E/pc \simeq 1$ in terms of K_{e3} can be proved comparing Data with Monte Carlo distribution as shown in Fig. 8.24.

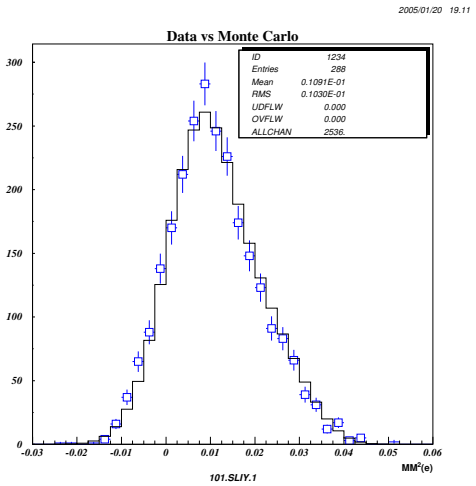

Figure 8.23: *Comparison of $MM^2(e)$ distribution of Data events in $0.85 < E/pc < 0.9$ region with $K_{\mu 2}$ Monte Carlo distribution.*

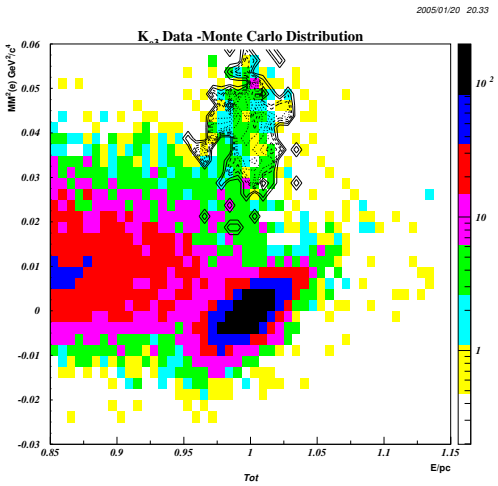

Figure 8.24: *Comparison of K_{e3} Monte Carlo with Data distribution in $MM^2(e)$ versus E/p plane.*

As shown by Monte Carlo simulation, the contribution of K_{e3} background is negligible under K_{e2} signal region, thus the background contamination under K_{e2} peak derives only from $K_{\mu 2}$ background events.
The $K_{\mu 2}$ population density in each bin of $MM^2(e)$ versus E/p distribution can be extracted by its $MM^2(e)$ and E/p profile distributions. This procedure is rigorous if $K_{\mu 2}$ $MM^2(e)$ and E/p variables are uncorrelated. In Section 8.1.5 it has been shown that there is a correlation between $MM^2(e)$ and E/p distributions for K_{e2} events, because they both depends on momentum resolution. For $K_{\mu 2}$ events, however, the E/p dependence on p resolution is completely negligible compared to the spread on energy deposition of muons in the LKr calorimeter. For this reason, $K_{\mu 2}$ $MM^2(e)$ and E/p distributions are uncorrelated to a very good approximation.

$K_{\mu 2}$ $MM^2(e)$ distribution has been derived by Data $MM^2(e)$ distribution in the $0.85 < E/pc < 0.9$ region, subtracting the small contribution of K_{e2} and K_{e3} events in that region (see Fig. 8.25).
$K_{\mu 2}$ E/p distribution has been derived by a fit of Data E/p distribution in $-0.02\ GeV^2/c^4 < MM^2(e) < 0.02\ GeV^2/c^4$ region. K_{e2} distribution is well known in this region (see Fig 8.27), while $K_{\mu 2}$ contribution has been parametrized with a broken line distribution. The choice of such distribution is due to the fact that if for $E/pc < 1$ two effects contribute to E/p distribution (the muon's energy release in LKr calorimeter and resolution effects), for $E/pc > 1$ muon's energy release in LKr contribution vanishes, causing a change in muon E/p distribution slope. The fit result is presented in Fig. 8.26. It has been checked that the E/p distribution doesn't change significantly as a function of $MM^2(e)$, comparing the $K_{\mu 2}$ parametrized distribution with the Data in $0.015\ GeV^2/c^4 < MM^2(e) < 0.06\ GeV^2/c^4$ range (see Fig. 8.28).

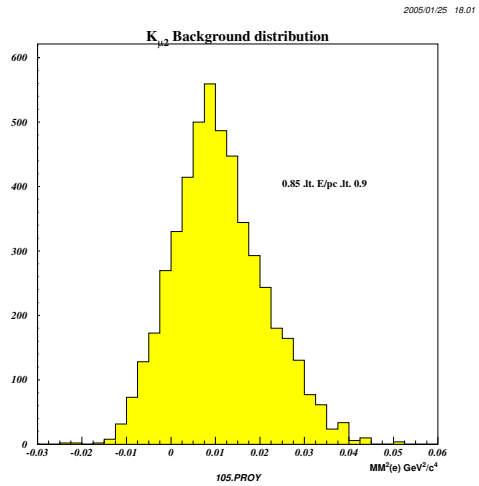

Figure 8.25: *$MM^2(e)$ distribution of events in $0.85 < E/pc < 0.9$ region, where $K_{\mu 2}$ background is the most relevant component.*

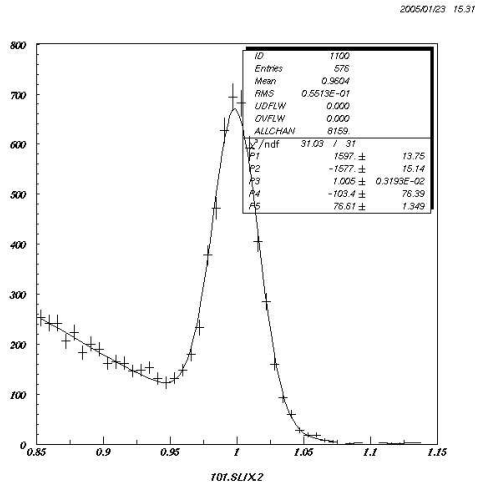

Figure 8.26: *Fit of the E/p distribution for events in $-0.02\ GeV^2/c^4 < MM^2(e) < 0.02\ GeV^2/c^4$ region. The variable $P(3)$ indicates the point where the $K_{\mu 2}$ distribution change of slope. It is close to 1, as expected. $P(2)$ and $P(4)$ are the slopes of $K_{\mu 2}$ events distribution.*

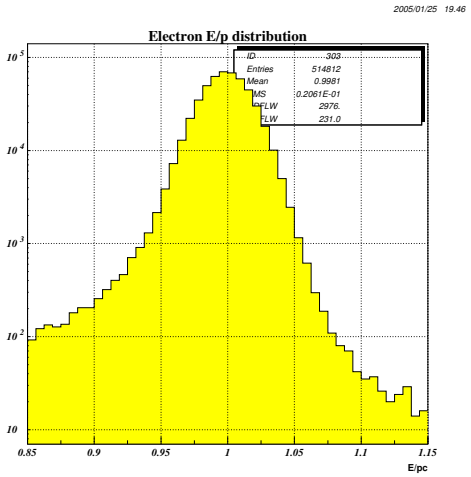

Figure 8.27: *2003 Electron E/p distribution.*

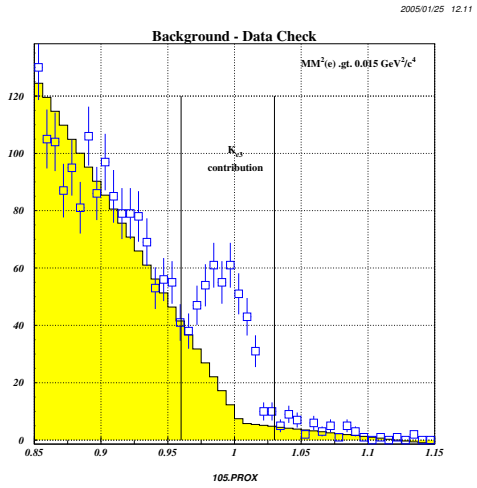

Figure 8.28: *Comparison of $K_{\mu 2}$ parametrized E/p distribution with Data in* $0.015\ GeV^2/c^4 < MM^2(e) < 0.06\ GeV^2/c^4$ *range. The bump at* $E/p \simeq 1$ *is due to* K_{e3} *contribution.*

From the profile distribution in E/p and $MM^2(e)$, the bidimensional distribution of $K_{\mu 2}$ background has been reconstructed (see Fig.8.29) and subtracted to the Data distribution. The event distribution without $K_{\mu 2}$ background component is presented in Fig. 8.30. The E/p distribution of K_{e2} candidates minus $K_{\mu 2}$ background in the region $-0.02\ GeV^2/c^4 < MM^2(e) < 0.02\ GeV^2/c^4$ is presented in Fig. 8.31 The total number of K_{e2} signal events in the region

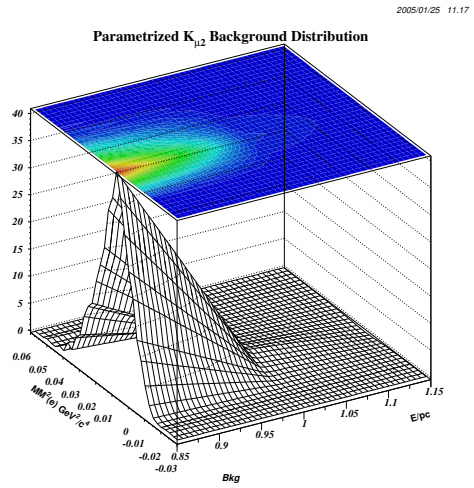

Figure 8.29: *$K_{\mu 2}$ parametrized background distribution.*

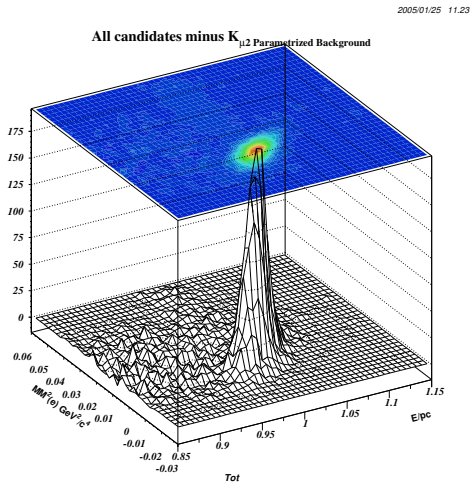

Figure 8.30: *K_{e2} candidates distribution minus $K_{\mu 2}$ parametrized background.*

$1.05 > E/pc > 0.95$ and $-0.02\ GeV^2/c^4 < MM^2(e) < 0.02\ GeV^2/c^4$ is:

$$N(total) = 5329 \pm 73_{(stat)}$$
$$N(Background) = 659 \pm 26_{(stat)}$$
$$N(K_{e2}) = 4670 \pm 77_{(stat)}$$

The quoted error includes only the statistical error. The systematic stability of the result will be checked in the following Section (Section 8.1.8).

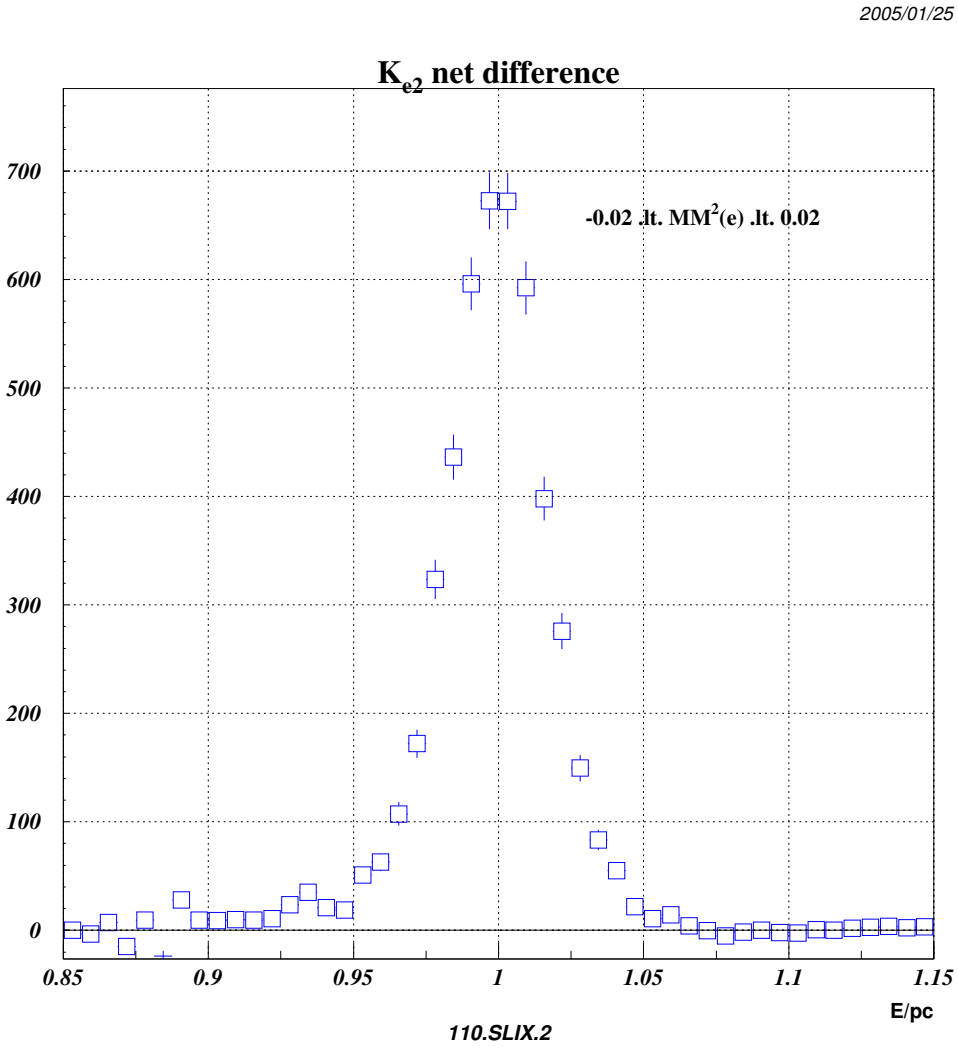

Figure 8.31: *E/p distribution of K_{e2} candidates events minus $K_{\mu 2}$ background in the region $-0.02\ GeV^2/c^4\ < MM^2(e) <\ 0.02\ GeV^2/c^4$.*

E/p and $MM^2(e)$ corrections

The E/p distribution of electron and positron is not gaussian far from the peak, as it has been shown in Fig. 8.27. The change in acceptance due to the non guassian tails of the E/p distribution must be taken into account. The correction can be derived directly from the electron E/p distribution presented in Fig. 8.27. The resulting correction to R_K ratio is:

$$\frac{\Delta R_K}{R_K} = (+2.77 \pm 0.41_{(syst)}) \cdot 10^{-2}$$

The systematic error has been obtained by varying the Drift Chamber resolution shown in Eq. 3.1 by 20%.
Analogously the change in acceptance due to the cut on $-0.02\ GeV^2/c^4 < MM^2(e) < 0.02\ GeV^2/c^4$ implies a correction to R_K ratio of:

$$\frac{\Delta R_K}{R_K} = (+1.9 \pm 0.02) \cdot 10^{-3}$$

8.1.8 Background Subtraction Stability

The K_{e2} background subtraction technique, presented in the previous section, successfully described the background under the K_{e2} signal and provided a corrected value of the number of K_{e2} candidates in the signal region.
The study of the background subtraction technique, to be complete, requires a check of the stability of the result under the change of the used background distribution. The background subtraction results should not be sensitive on the actual shape of $K_{\mu 2}$ E/p and $MM^2(e)$ distributions, if they are varied reasonably.
A first check of the stability of the background subtraction has been done changing of the region used to extract $K_{\mu 2}$ $MM^2(e)$ profile distribution. It has been changed from $0.85 < E/pc < 0.90$ to $0.875 < E/pc < 0.925$. The result is reported in Table 8.1

Background Stability against $MM^2(e)$	
E/p cut	$\frac{\Delta N}{N} \cdot 10^3$
$0.85 < E/pc < 0.90$	0
$0.8625 < E/pc < 0.9125$	$+1.8 \pm 0.9$
$0.875 < E/pc < 0.925$	$+3.8 \pm 0.9$

Table 8.1: *Background subtraction stability check under the change of the region used to extract $K_{\mu 2}$ $MM^2(e)$ profile distribution. $\frac{\Delta N}{N}$ is the relative variation of $K_{\mu 2}$ signal events.*

Another check of the stability of the background subtraction has been performed changing the slope of $K_{\mu 2}$ E/p profile distribution as shown in Fig. 8.32. All other parameters have been changed according to their covariance, as obtained from the fit in Fig. 8.26. The result has been reported in Table 8.32

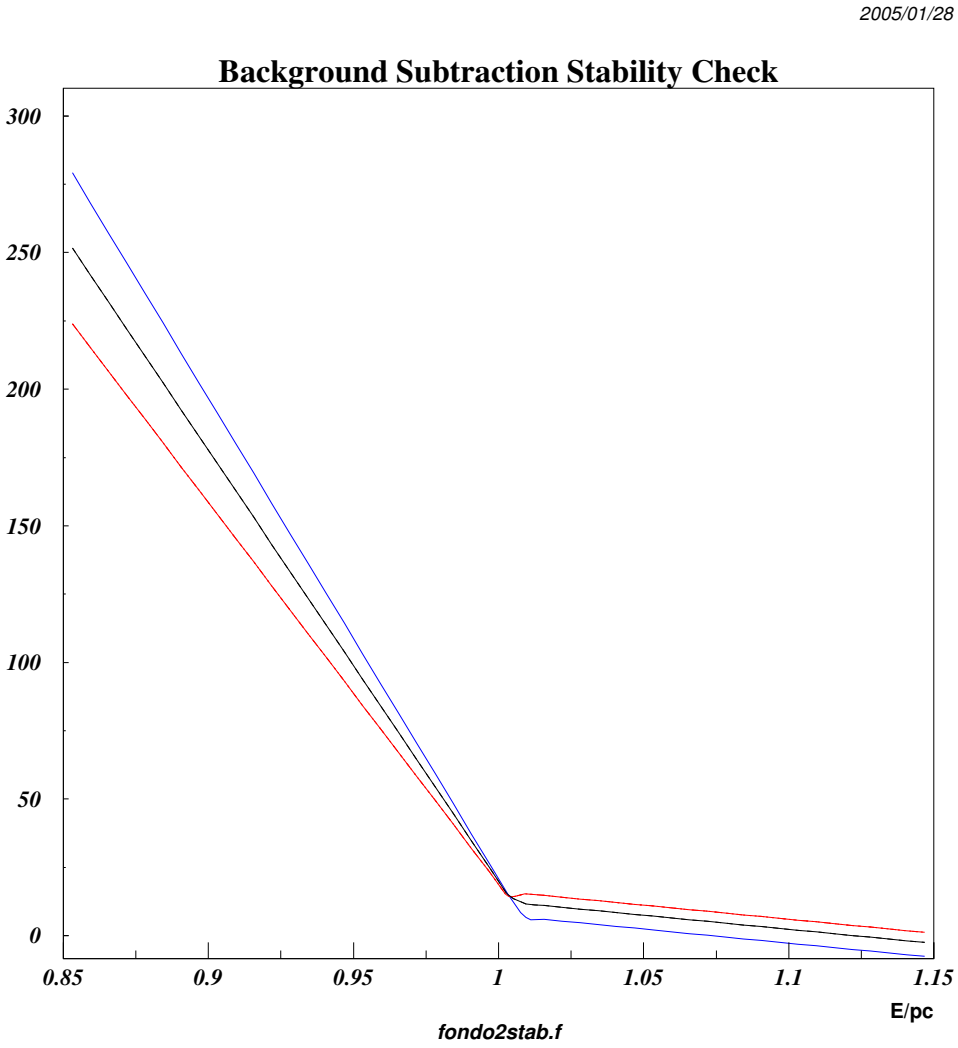

Figure 8.32: *Variation of the E/p distribution slope. The black line represents the nominal value. Blue line corresponds to a change of +10% of the slope and red line to a change of -10%. Note the correlation of the parameter variation.*

Background Stability against E/p	
Slope change	$\frac{\Delta N}{N} \cdot 10^3$
-10%	-1.6 ± 2.1
0%	0
+10%	$+6.2 \pm 2.0$

Table 8.2: *Background subtraction stability check under the change of the region used to extract* $K_{\mu 2}$ E/p *profile distribution.* $\frac{\Delta N}{N}$ *is the relative variation of* K_{e2} *signal events.*

Systematic Error of the Background Correction ($\frac{\Delta N}{N}$)		
	Relative Negative deviation (10^{-3})	Relative Positive deviation (10^{-3})
$MM^2(e)$	0.	+3.8
E/p slope	-1.6	+6.2
Total	**-1.6**	**+7.2**

Table 8.3: *Summary of systematic uncertainties on the Background Correction.*

The maximum excursion of $\frac{\Delta N}{N}$ can be taken as relative systematic error of the Background correction procedure on the number of K_{e2} signal events. The obtained result is presented in Table 8.3.

8.2 $K_{\mu 2}$ Backgrounds

$K_{\mu 2}$ decay is not very sensitive to background contamination given its high acceptance and Branching Ratio. The signal region for the $K_{\mu 2}$ decay is defined by the cut in Missing Mass:

$$-0.02\ GeV^2/c^4\ < MM^2(\mu)\ <\ 0.02\ GeV^2/c^4$$

A few background sources enters the $K_{\mu 2}$ signal region and their contamination to the $K_{\mu 2}$ signal has been studied with CMC Monte Carlo, exactly the same simulation used for the study of $K_{\mu 2}$ acceptance. The samples have been generated in the same decay region.

8.2.1 $K_{\mu 3}$ Contamination

$K_{\mu 3}$ is a 3 body decay. Its transverse momentum versus total momentum distribution is very different from $K_{\mu 2}$ event distribution, as shown in Fig. 7.16 and they overlap only for high values of the track momentum. The rejection of $K_{\mu 3}$ is improved by the detection of photons produced by π^0 decay, made possible by the selection on the extra activity of the LKr calorimeter and on the time coincidence with an hit in one of the AKL pockets.
The distributions in Fig. 8.33 and in Fig. 8.34 are made before any cut is applied.

$K_{\mu 3}$ **Background**	
Branching Ratio	$(3.27 \pm 0.06)\%$
Acceptance	$(4 \pm 2) \cdot 10^{-6}$

$$\frac{B.R.(K_{\mu 3}) \times A(K_{\mu 3})}{B.R.(K_{\mu 2}) \times A(K_{\mu 2})} = (6.5 \pm 3.3) \cdot 10^{-7}$$

8.2.2 $K^{\pm} \to \pi^{\pm}\pi^0$ Contamination

The charged Kaon decay into two pion has a Branching Ratio of $\sim 21\%$. Its $MM^2(\mu)$ distribution is shifted to higher value of missing mass in comparison with $K_{\mu 2}$ event distribution (as shown in Fig. 8.35). As for $K_{\mu 3}$ background, $K^{\pm} \to \pi^{\pm}\pi^0$ events overlap $K_{\mu 2}$ signal region expecially at high momentum values of the charged track (see Fig. 8.36). The direct detection of at least one of the photons emitted by the π^0 decay is performed by the means of the selection

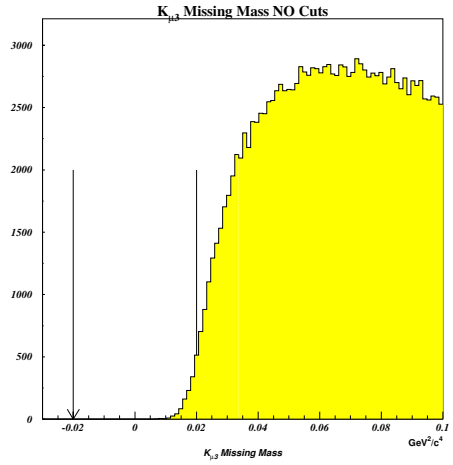

Figure 8.33: *Missing Mass squared distribution for $K_{\mu 3}$ events, under the assumption of 60 GeV/c Kaon momentum. The arrows limit the signal region of $K_{\mu 2}$ selection. No cut has been applied.*

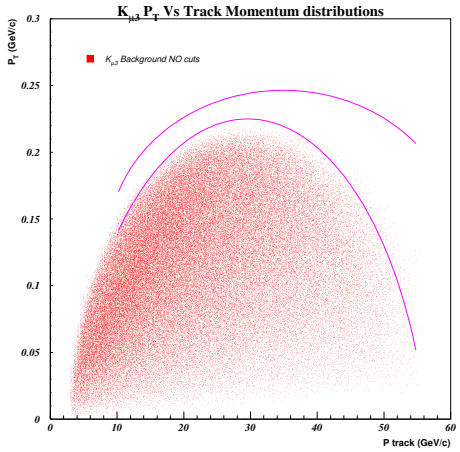

Figure 8.34: *Transverse momentum versus total momentum distribution. The lines limit the $K_{\mu 2}$ selection cut region. No cut has been applied.*

on the extra activity of the LKr calorimter and on the time coincidence with an hit in one of the AKL pockets.

The missing mass distribution of $K^{\pm} \to \pi^{\pm}\pi^0$ events passing the $K_{\mu 2}$ selection cuts are plotted in Fig. 8.37, while in Fig. 8.38 the distribution of track reconstructed transverse momentum versus the track total momentum is plotted.

$K^{\pm} \to \pi^{\pm}\pi^0$ **Background**	
Branching Ratio	$(21.13 \pm 0.13)\%$
Acceptance	$(1.2 \pm 0.1) \cdot 10^{-3}$

$$\frac{B.R.(K^{\pm} \to \pi^{\pm}\pi^0) \times A(K^{\pm} \to \pi^{\pm}\pi^0)}{B.R.(K_{\mu 2}) \times A(K_{\mu 2})} = (1.3 \pm 0.1) \cdot 10^{-3}$$

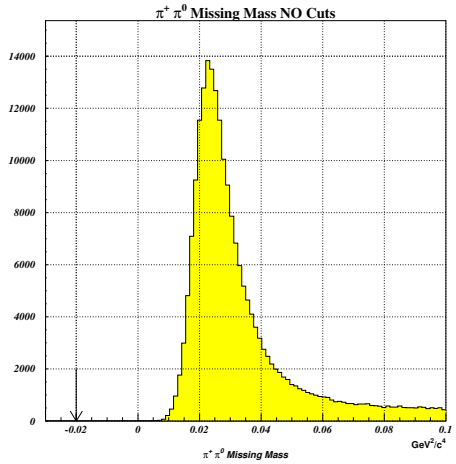

Figure 8.35: *Missing Mass squared distribution for $K^{\pm} \to \pi^{\pm}\pi^0$ events, under the assumption of 60 GeV/c Kaon momentum. The arrows limit the signal region of $K_{\mu 2}$ selection. No cut has been applied.*

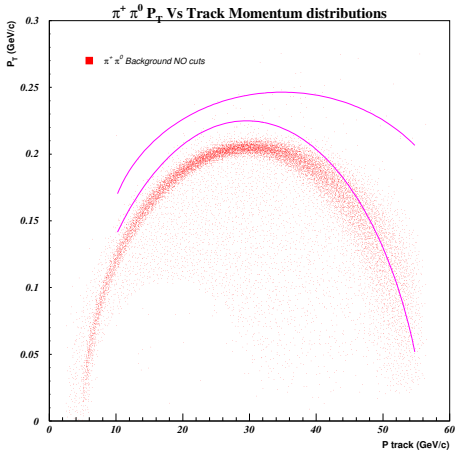

Figure 8.36: *Transverse momentum versus total momentum distribution for $K^{\pm} \to \pi^{\pm}\pi^0$ events. The lines limit the $K_{\mu 2}$ selection cut region. No cut has been applied.*

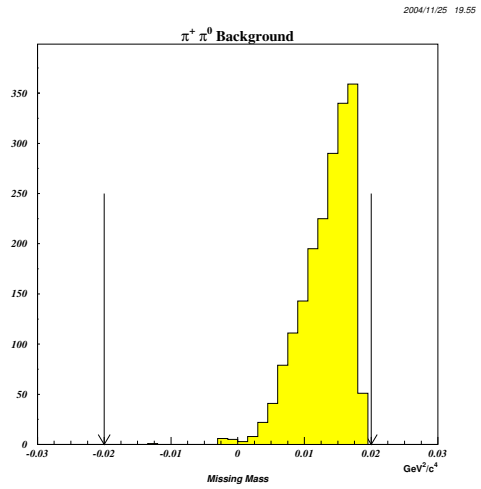

Figure 8.37: *Missing Mass squared distribution for* $K^{\pm} \rightarrow \pi^{\pm}\pi^0$ *events passing the* $K_{\mu 2}$ *selection, under the assumption of* 60 *GeV/c Kaon momentum. The arrows limit the signal region of* $K_{\mu 2}$ *selection.*

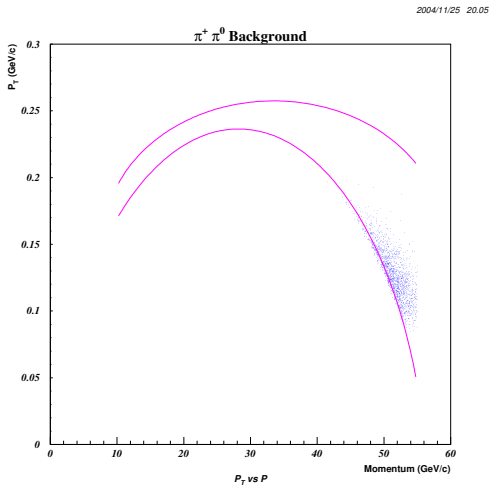

Figure 8.38: *Transverse momentum versus total momentum distribution for* $K^{\pm} \rightarrow \pi^{\pm}\pi^0$ *events passing the* $K_{\mu 2}$ *selection. The lines limit the* $K_{\mu 2}$ *selection cut region. The lines limit the signal region of* $K_{\mu 2}$ *selection.*

8.2.3 K_{e3} Contamination

K_{e3} decay can be a possible background also for $K_{\mu 2}$ channel. In fact, no direct muon identification is used in the selection, nor cuts on the track E/p to reject electrons. Its transverse momentum versus total momentum distribution overlaps the $K_{\mu 2}$ signal region only at low values of the track momentum, as shown in Fig. 8.39. The rejection of K_{e3} events is improved by the detection of the photon emitted in the subsequent π^0 decay, analogously at the $K_{\mu 3}$ background rejection.

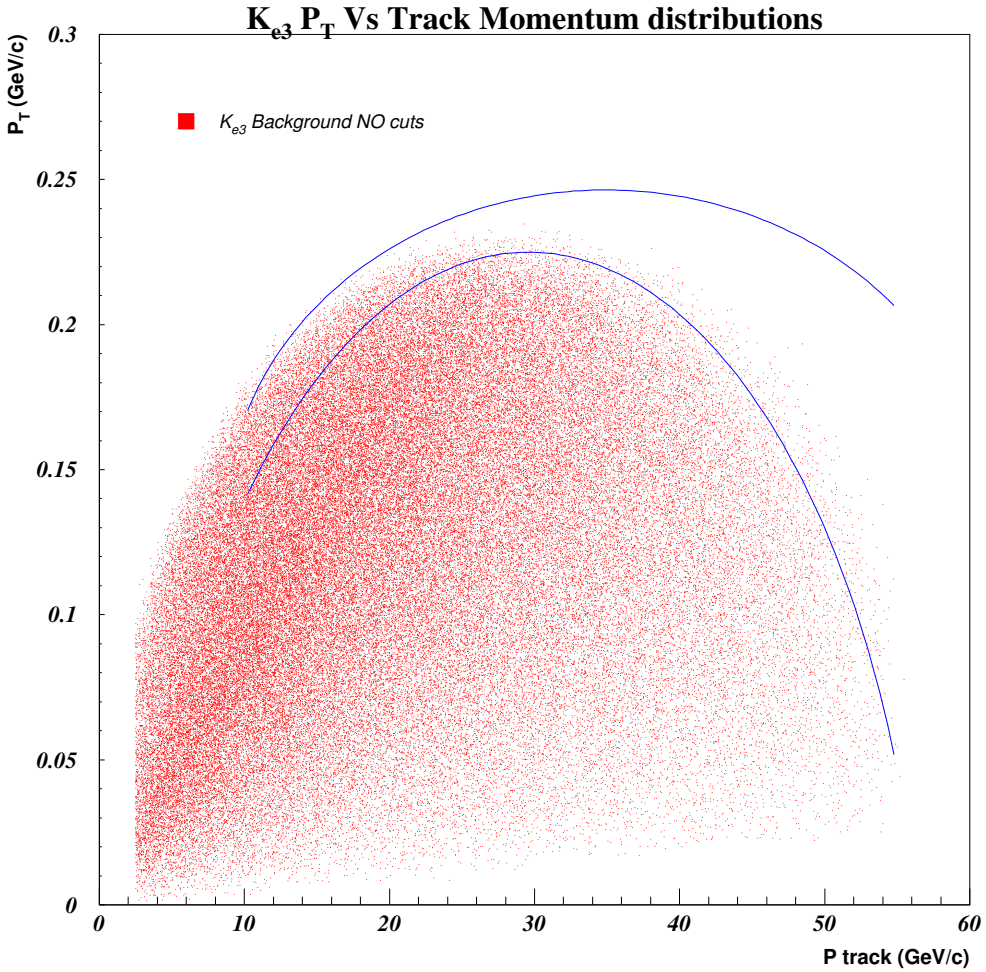

Figure 8.39: *Transverse momentum versus total momentum distribution for K_{e3} events. The lines limit the $K_{\mu 2}$ signal region. No cuts have been applied.*

K_{e3} Background	
Branching Ratio	$(4.87 \pm 0.06)\%$
Acceptance	$(1.1 \pm 0.1) \cdot 10^{-5}$

$$\frac{B.R.(K_{e3}) \times A(K_{e3})}{B.R.(K_{\mu 2}) \times A(K_{\mu 2})} = (2.6 \pm 0.2) \cdot 10^{-6}$$

8.2.4 $K_{\mu 2}$ Background Conclusion

The $K_{\mu 2}$ channel proved to be almost free of physical background. The acceptance of the most relevant Kaon decays has been measured with CMC Monte Carlo simulation and the relative contamination to the signal sample calculated. The background contamination due to $K_{\mu 3}$ and K_{e3} is completely negligible for the purpose of R_K ratio measurement, while there is a small contamination of $K^{\pm} \to \pi^{\pm}\pi^0$ inside the signal region.
The correction to R_K due to background contamination to the $K_{\mu 2}$ channel is:

$$\frac{\Delta R_K}{R_K} = +(1.3 \pm 0.1) \cdot 10^{-3}$$

Chapter 9

Study of the systematic effects of the Acceptance correction on R_K

The similarity of the K_{e2} and $K_{\mu 2}$ decays and the suitable choice of selection cuts, allow to keep small and understandable (by mean of Monte Carlo simulation) the effects on the ratio due to the acceptance correction.
The estimation of the systematic corrections and their uncertainties is presented in this Chapter. In particular the study of the cut stability against *reasonable* changes of the selection cuts is reported in detail.
Under the assumption of a good understanding of the background and provided that the Monte Carlo simulation is reliable, the K_{e2} and $K_{\mu 2}$ acceptance corrections (and in particular their ratio) shouldn't depend critically on the actual value of the cuts. This is shown to be the case.
A few selection cuts, namely the cuts on track and AKL hit time, cannot be treated in this way and are studied apart in the following sections.

9.1 Cut Stability

A check of the behavior of the acceptance correction has been performed by varying one at the time the most relevant acceptance cuts in both Monte Carlo simulation and Data Collection. The cuts have been changed, whenever possible, up to 10% in both directions of tighting and loosening the selection, or, otherwise, only in one of the two directions. The effect of these changes on K_{e2} acceptance, $K_{\mu 2}$ acceptance and on their ratio are shown in the following tables and plots.

Stability Result			
Cut	K_{e2} $\Delta\alpha \times 10^3$	$K_{\mu 2}$ $\Delta\alpha \times 10^3$	$\frac{\Delta R_K}{R_K} \times 10^3$
$p_l > 15$ GeV/c	0	0	0
$p_l > 16.5$ GeV/c	0.00 ± 0.05	-0.25 ± 0.07	0.25 ± 0.09
$p_l > 18$ GeV/c	0.05 ± 0.17	-0.39 ± 0.11	0.44 ± 0.20
$p_l > 19.5$ GeV/c	-0.37 ± 0.4	-0.54 ± 0.14	0.17 ± 0.44
$p_l > 21$ GeV/c	0.79 ± 0.74	-0.87 ± 0.18	1.67 ± 0.76

Table 9.1: *Summary of result stability for K_{e2} , $K_{\mu 2}$ and R_K against the change of the cut on the momentum. For K_{e2} and $K_{\mu 2}$ the quantity $\Delta\alpha$ has been quoted, while for R_K the quantity $\frac{\Delta R_K}{R_K}$ has been reported. The quoted errors are uncorrelated errors. Note the 10^3 scale factor.*

For each cut variation, the relative acceptance variation is evaluated:

$$\Delta\alpha \;=\; \frac{\frac{N'}{A'} - \frac{N^0}{A^0}}{\frac{N^0}{A^0}} \tag{9.1}$$

where A^0 is the acceptance for the nominal cuts and N^0 is the number of events collected with nominal cuts corrected for the background

$$N^0 \;=\; N_S \;=\; N_T - N_B \tag{9.2}$$

while the primed quantities represent the acceptance and the collected events varying the cut. $\Delta\alpha$ quantity has been chosen, because, in the limit of independent cuts, it is a good estimator of the relative correction to the R_K ratio:

$$\frac{\Delta R_K}{R_K} \;=\; \frac{R'_K - R^0_K}{R^0_K}$$

9.1.1 Momentum Selection

The cut on the lepton momentum has been moved in such a way to change the range of the selection by $\sim$ 10%. The lower bound has been moved from 15 GeV/c up to 21 GeV/c. The stability results obtained are reported in Table 9.1. They include stability results for K_{e2} and $K_{\mu 2}$ selections and for R_K ratio. The trend of result dependency on the cut has been plotted in Fig. 9.1, and in Fig. 9.2.

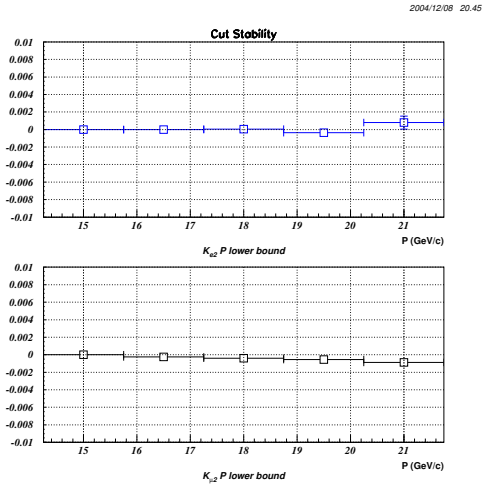

Figure 9.1: *Result stability for K_{e2} and $K_{\mu 2}$ events against the change of momentum lower limit. The quantity $\Delta\alpha$ is plotted as a function of the lower bound on momentum.*

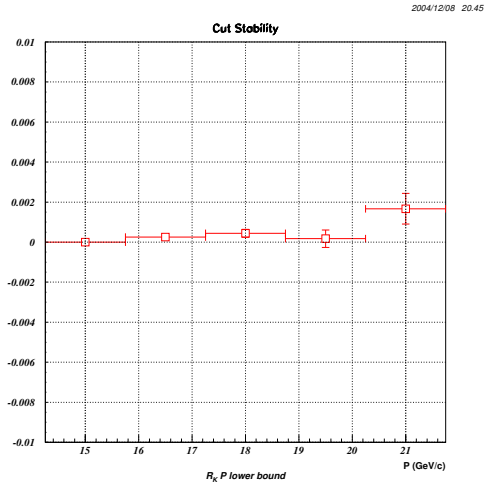

Figure 9.2: *Result stability of R_K ratio. The quantity $\frac{\Delta R_K}{R_K}$ is plotted as a function of the lower bound on momentum.*

The upper bound of the lepton momentum selection has been moved independently from the lower bound. The cut has been varied from 50.5 GeV/c up to 56.5 GeV/c. The stability results obtained are reported in Table 9.2. The trend of result dependency on the cut have been plotted in Fig. 9.3 and in Fig. 9.4.

Stability Result			
Cut	K_{e2} $\Delta\alpha \times 10^3$	$K_{\mu 2}$ $\Delta\alpha \times 10^3$	$\frac{\Delta R_K}{R_K} \times 10^3$
$p_l < 50.5\ GeV/c$	2.27 ± 0.80	-0.05 ± 0.25	2.31 ± 0.84
$p_l < 52\ GeV/c$	0.89 ± 0.60	0.25 ± 0.08	0.64 ± 0.60
$p_l < 53.5\ GeV/c$	0.65 ± 0.41	0.21 ± 0.05	0.44 ± 0.41
$p_l < 55\ GeV/c$	0	0	0
$p_l < 56.5\ GeV/c$	-0.96 ± 0.37	-0.16 ± 0.04	-0.80 ± 0.37

Table 9.2: *Summary of result stability for K_{e2} , $K_{\mu 2}$ and R_K against the change of the cut on the momentum. For K_{e2} and $K_{\mu 2}$ the quantity $\Delta\alpha$ has been quoted, while for R_K the quantity $\frac{\Delta R_K}{R_K}$ has been reported. The quoted errors are uncorrelated errors. Note the 10^3 scale factor.*

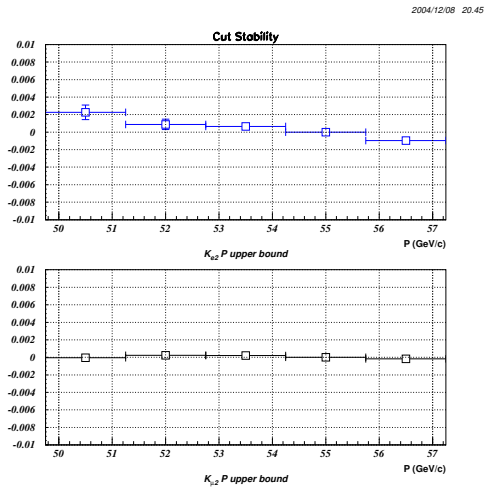

Figure 9.3: *Result stability for K_{e2} and $K_{\mu 2}$ events against the change of momentum upper limit. The quantity $\Delta\alpha$ is plotted as a function of the upper bound on momentum.*

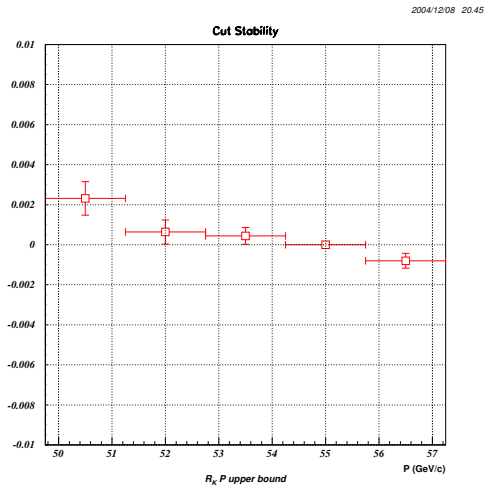

Figure 9.4: *Result stability of R_K ratio. The quantity $\frac{\Delta R_K}{R_K}$ is plotted as a function of the upper bound on momentum.*

Stability Result			
Cut	K_{e2} $\Delta\alpha \times 10^3$	$K_{\mu 2}$ $\Delta\alpha \times 10^3$	$\frac{\Delta R_K}{R_K} \times 10^3$
$z > 1850\ cm$	1.33 ± 0.52	0.37 ± 0.06	0.97 ± 0.53
$z > 2000\ cm$	0	0	0
$z > 2150\ cm$	-0.51 ± 0.58	0.53 ± 0.06	-1.04 ± 0.59
$z > 2300\ cm$	-1.59 ± 0.85	0.20 ± 0.09	-1.79 ± 0.86
$z > 2450\ cm$	-2.09 ± 0.11	0.10 ± 0.11	-2.19 ± 1.08

Table 9.3: *Summary of result stability for K_{e2} , $K_{\mu 2}$ and R_K against the change of the cut on the decay vertex position. For K_{e2} and $K_{\mu 2}$ the quantity $\Delta\alpha$ has been quoted, while for R_K the quantity $\frac{\Delta R_K}{R_K}$ has been reported. The quoted errors are uncorrelated errors. Note the 10^3 scale factor.*

Stability Result			
Cut	K_{e2} $\Delta\alpha \times 10^3$	$K_{\mu 2}$ $\Delta\alpha \times 10^3$	$\frac{\Delta R_K}{R_K} \times 10^3$
$z < 8200\ cm$	1.39 ± 0.35	0.24 ± 0.04	1.16 ± 0.35
$z < 8350\ cm$	1.13 ± 0.20	-0.07 ± 0.03	1.21 ± 0.20
$z < 8500\ cm$	0	0	0
$z < 8650\ cm$	-0.93 ± 0.12	-0.04 ± 0.02	-0.89 ± 0.12
$z < 8800\ cm$	-0.67 ± 0.14	0.05 ± 0.03	-0.73 ± 0.14

Table 9.4: *Summary of result stability for K_{e2} , $K_{\mu 2}$ and R_K against the change of the cut on the decay vertex position. For K_{e2} and $K_{\mu 2}$ the quantity $\Delta\alpha$ has been quoted, while for R_K the quantity $\frac{\Delta R_K}{R_K}$ has been reported. The quoted errors are uncorrelated errors. Note the 10^3 scale factor.*

9.1.2 Decay vertex position Selection

The cut on the reconstructed decay vertex position has been moved in such a way to change the range of the selection by $\sim$ 10%. The lower bound has been moved from 1850 *cm* to 2450 *cm*. The stability results obtained are reported in Table 9.3 and in Fig. 9.5 and in Fig. 9.6.

The upper bound of the reconstructed vertex position has been moved independently from the lower bound. The cut has been changed from 8200 *cm* to 8800 *cm*. The stability results obtained are reported in Table 9.4 and plotted in Fig. 9.7 and in Fig. 9.8.

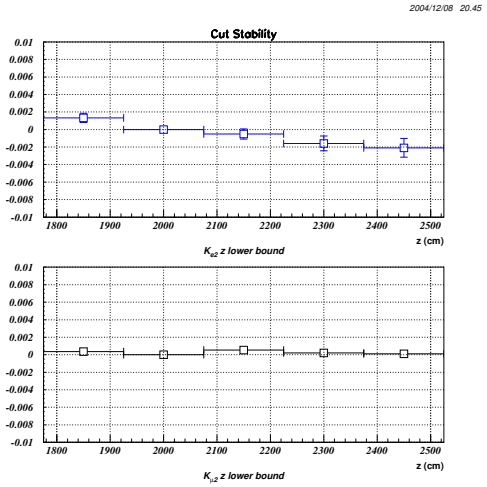

Figure 9.5: *Result stability for K_{e2} and $K_{\mu 2}$ events. The quantity $\Delta\alpha$ is plotted as a function of the lower bound on the decay vertex position.*

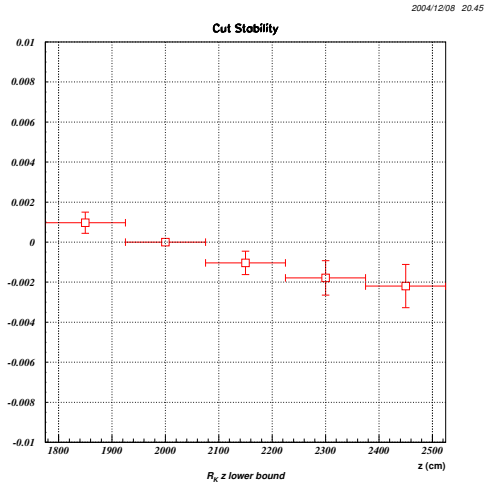

Figure 9.6: *Result stability of R_K ratio. The quantity $\frac{\Delta R_K}{R_K}$ is plotted as a function of the lower bound on the decay vertex position.*

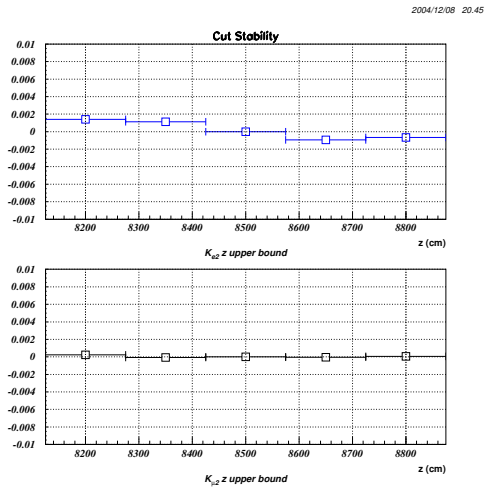

Figure 9.7: *Result stability for K_{e2} and $K_{\mu 2}$ events. The quantity $\Delta\alpha$ is plotted as a function of the upper bound on the decay vertex position.*

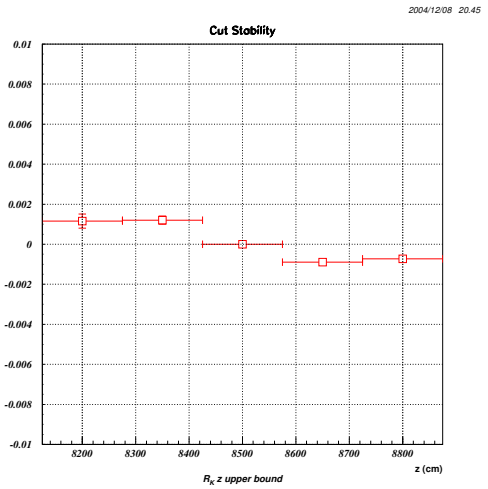

Figure 9.8: *Result stability of R_K ratio. The quantity $\frac{\Delta R_K}{R_K}$ is plotted as a function of the upper bound on the decay vertex position.*

Stability Result			
Cut	K_{e2} $\Delta\alpha \times 10^3$	$K_{\mu 2}$ $\Delta\alpha \times 10^3$	$\frac{\Delta R_K}{R_K} \times 10^3$
2 σ	-7.88 ± 0.39	-3.35 ± 0.57	-4.53 ± 3.96
2.5 σ	-2.12 ± 2.04	-1.97 ± 0.57	-0.15 ± 2.05
3 σ	0	0	0
3.5 σ	0.87 ± 0.14	2.51 ± 0.11	-1.64 ± 1.37

Table 9.5: *Summary of result stability for K_{e2} , $K_{\mu 2}$ and R_K against the change of the cut on p_T vs P. For K_{e2} and $K_{\mu 2}$ the quantity $\Delta\alpha$ has been quoted, while for R_K the quantity $\frac{\Delta R_K}{R_K}$ has been reported. The quoted errors are uncorrelated errors. Note the 10^3 scale factor for $\Delta\alpha$.*

9.1.3 P_T versus P Selection

The limits of the signal region defined by the elliptic relation between P_T and P have been moved up to 1 σ. The lower and upper bounds have been moved coherently from 2 σ to 3.5 σ. The stability results obtained are reported in Table 9.5. They include stability results for K_{e2} and $K_{\mu 2}$ selections and for R_K ratio. The trend of result dependency on the cut have been plotted in Fig. 9.9 and in Fig. 9.10.

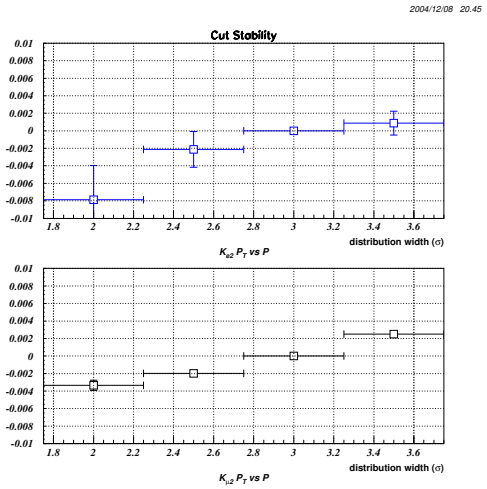

Figure 9.9: *Result stability for K_{e2} and $K_{\mu 2}$ events. The quantity $\Delta\alpha$ is plotted as a function of the width of the signal region.*

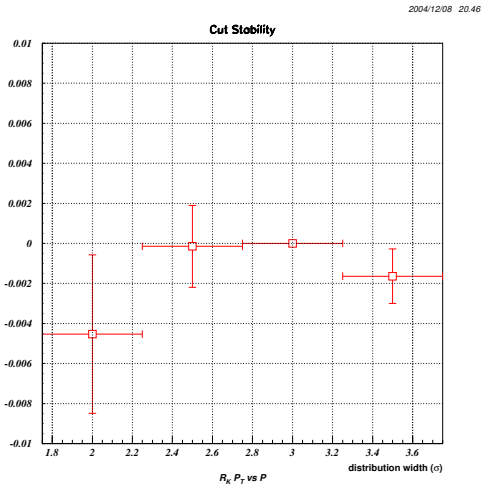

Figure 9.10: *Result stability of R_K ratio. The quantity $\frac{\Delta R_K}{R_K}$ is plotted as a function of the width of the signal region.*

9.1.4 M_{Fake} Selection cut

The limits of the signal region defined by the cut on the trigger variable M_{Fake} defined in Eq. 7.2 have been moved similarly for K_{e2} and $K_{\mu 2}$. The signal regions have been chosen in such a way to have roughly the same acceptance for K_{e2} and $K_{\mu 2}$. The lower and upper bounds are different due to the difference in mass of electrons and muons. The stability results obtained are reported in Table 9.6, 9.7 and 9.8. They include stability results for K_{e2} and $K_{\mu 2}$ selections and for R_K ratio. The trend of result dependency on the cut have been plotted in Fig. 9.11 and in Fig. 9.12.

Stability Result	
Cut (GeV/c^2)	K_{e2} $\Delta\alpha \times 10^3$
$0.514 < M_{Fake}(\pi) < 0.550$	0
$0.516 < M_{Fake}(\pi) < 0.548$	$+2.9 \pm 0.9$
$0.518 < M_{Fake}(\pi) < 0.546$	$+4.8 \pm 1.5$
$0.520 < M_{Fake}(\pi) < 0.544$	$+6.0 \pm 2.3$

Table 9.6: *Summary of result stability for K_{e2} against the change of the cut on $M_{Fake}(\pi)$. The quantity $\Delta\alpha$ has been quoted. The quoted errors are uncorrelated errors. Note the 10^3 scale factor.*

Stability Result	
Cut (GeV/c^2)	$K_{\mu 2}$ $\Delta\alpha \times 10^3$
$0.512 < M_{Fake}(\pi) < 0.531$	0
$0.513 < M_{Fake}(\pi) < 0.530$	$+0.9 \pm 0.3$
$0.514 < M_{Fake}(\pi) < 0.529$	$+1.4 \pm 0.4$
$0.515 < M_{Fake}(\pi) < 0.528$	$+1.6 \pm 0.4$

Table 9.7: *Summary of result stability for $K_{\mu 2}$ against the change of the cut on $M_{Fake}(\pi)$. The quantity $\Delta\alpha$ has been quoted. The quoted errors are uncorrelated errors. Note the 10^3 scale factor.*

Stability Result	
Cut (GeV/c^2)	$\frac{\Delta R_K}{R_K} \times 10^3$
K_{e2} : $0.514 < M_{Fake} < 0.550$ $K_{\mu 2}$: $0.512 < M_{Fake} < 0.531$	0
K_{e2} : $0.516 < M_{Fake} < 0.548$ $K_{\mu 2}$: $0.513 < M_{Fake} < 0.530$	2.0 ± 0.4
K_{e2} : $0.518 < M_{Fake} < 0.546$ $K_{\mu 2}$: $0.514 < M_{Fake} < 0.529$	3.5 ± 1.0
K_{e2} : $0.520 < M_{Fake} < 0.544$ $K_{\mu 2}$: $0.515 < M_{Fake} < 0.528$	4.4 ± 2.1

Table 9.8: *Summary of result stability for R_K against the change of the cut on M_{Fake}. The quantity $\frac{\Delta R_K}{R_K}$ has been reported and the quoted errors are uncorrelated errors. Note the 10^3 scale factor for $\Delta\alpha$.*

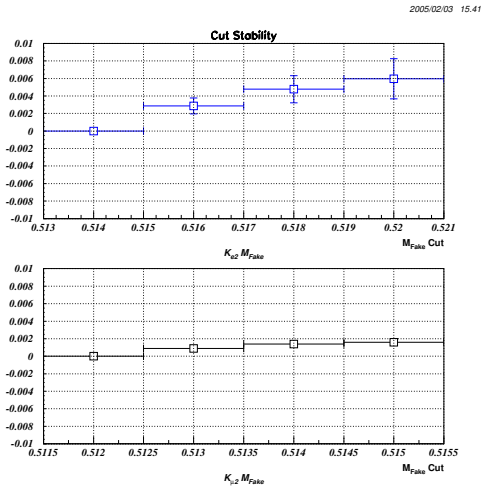

Figure 9.11: *Result stability for K_{e2} and $K_{\mu 2}$ events. The quantity $\Delta\alpha$ is plotted as a function of the width of the M_{Fake} signal region.*

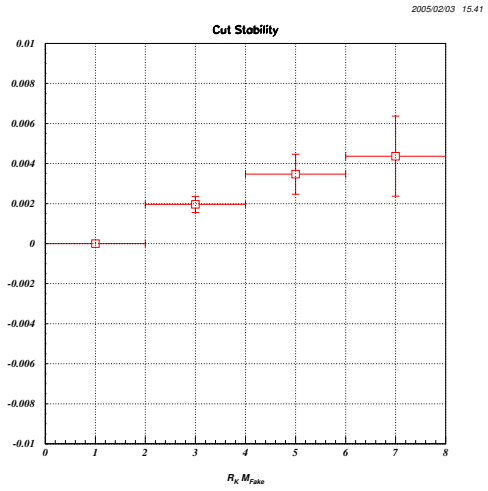

Figure 9.12: *Result stability of R_K ratio. The quantity $\frac{\Delta R_K}{R_K}$ is plotted as a function of the variation of the M_{Fake} signal region.*

9.1.5 Missing Mass Squared

The stability of the results has been checked against the change of the cut on $MM^2(\mu)$ in $K_{\mu 2}$ selection. As seen in Fig. 6.9, the Monte Carlo didn't reproduce properly the tails of $MM^2(\mu)$ distribution. For this reason, the cut on $MM^2(\mu)$ has been moved in such a way to change the range of the selection by $\sim$ 20%. The lower and upper bounds have been moved simmetrically from ± 0.016 GeV^2/c^4 (3.5 σ from the peak) to ± 0.024 GeV^2/c^4 (5.3σ from the peak), letting the selection region centered at 0. The stability results obtained are reported in Table 9.10. Only the stability result for $K_{\mu 2}$ selection is presented, because in this case $\frac{\Delta R_K}{R_K}$ coincides with $\Delta\alpha$. The trend of result dependency on the cut have been plotted in Fig. 9.5.

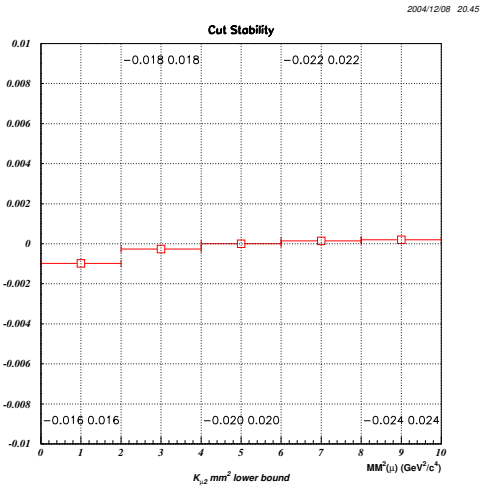

Table 9.9: *Result stability for $K_{\mu 2}$ events. The quantity $\Delta\alpha$ is plotted as a function of the $MM^2(\mu)$ cut range.*

Stability Result	
Cut (GeV^2/c^4)	$K_{\mu 2}$ $\Delta\alpha \times 10^3$
$-0.016 < MM^2(\mu) < 0.016$	-0.98 ± 0.02
$-0.018 < MM^2(\mu) < 0.018$	-0.26 ± 0.01
$-0.020 < MM^2(\mu) < 0.020$	0
$-0.022 < MM^2(\mu) < 0.022$	0.14 ± 0.07
$-0.024 < MM^2(\mu) < 0.024$	0.19 ± 0.01

Table 9.10: *Summary of result stability for $K_{\mu 2}$ against the change of the cut on $MM^2(\mu)$. The quantity $\Delta\alpha$ has been quoted. The quoted errors are uncorrelated errors. Note the 10^3 scale factor.*

Systematic Error of the Acceptance Correction		
	Rel. Negative deviation $\times 10^3$	Rel. Positive deviation $\times 10^3$
Momentum cut (lower bound)	0	+1.7
Momentum cut (upper bound)	-0.8	+2.3
Vertex cut (lower bound)	-2.2	+1.0
Vertex cut (upper bound)	-0.9	+1.2
p_T vs P	-4.5	0
M_{Fake}	0	+4.4
$MM^2(\mu)$	-1.0	+0.2
Total	**-5.3**	**+5.5**

Table 9.11: *Individual contributions to the systematic error of the Acceptance Correction in the measurement of R_K ratio. The quoted relative deviations are the maximum excursions of $\frac{\Delta R_K}{R_K}$ for each variation.*

9.1.6 Results

The stability of R_K ratio has been checked against the variation of the most relevant cuts. Variation of K_{e2} and $K_{\mu 2}$ event number have been checked also independently. In particular, $K_{\mu 2}$ sample appears to be less sensitive to cut variations than K_{e2} sample. This is mostly due to the uncertainty in the background subtraction procedure. As shown in Table 8.3, the uncertainty on the K_{e2} signal is of the order of a few per mill. The smallest changes as a function of the cut variations for K_{e2} occur in the cases expected to be less affected by background, like the lower cut on momentum and the upper cut on the vertex position[1]. The $K_{\mu 2}$ sample, being essentially free of background contaminations, is practically not affected by the uncertainty on background estimation.
Since the maximum excursions of $\frac{\Delta R_K}{R_K}$ have been taken as relative systematic errors of the acceptance correction for K_{e2} and $K_{\mu 2}$, the found result is an overestimation of the acceptance systematic error. The obtained results are presented in Table 9.11.

[1]It has been shown in Section 8.1.6 that background events are mostly concentrated at high values of the lepton momentum.

9.2 Systematic effect of the Accidental Rate

The pile-up of extra particles in time with a good event can cause a loss of statistics, depending on the crossing time and hit position of the accidental particles. The method employed to study the effect of the overlap of an accidental with a good event avoids the use of Monte Carlo simulation. For every collected event, the detector contents in several timeslices adjacent to the one at which the event occurred are also dumped[2]. This feature of the data acquisition allow the possibility to study the distribution of out of time events in large sidebands outside the signal region and to extrapolate the rate of accidental events inside the signal region.

A K_{e2} selection cut is performed on time coincidence within 10 ns between the track and a hit in the pockets 2, 3, 4 and 5 of the AKL detector. This cut allows to reject in particular background events like K_{e3} and $\pi^{\pm}\pi^0$ having a photon of the π^0 decay emitted at large angles. The same cut is applied in the $K_{\mu 2}$ selection, having the effect of rejecting $K_{\mu 3}$ and $\pi^{\pm}\pi^0$ background and minimizing the systematic correction of the cut to R_K ratio. The rate of accidental time coincidences under $t_{track} = t_{AKL}$ peak is extracted by a fit of the sidebands with a constant function for K_{e2} and $K_{\mu 2}$ as shown in Fig. 9.13 and Fig 9.14.

It is expected that the extrapolated accidental rate doesn't change extrapolating from the right sideband or from the left sideband to the signal region, the difference of the two is accounted as a systematic error and the weighted average is taken as correction value. Analogously, no physical reasons can explain a different accidental activity for K_{e2} and $K_{\mu 2}$ events, thus the difference between the K_{e2} and $K_{\mu 2}$ corrections ratio is added to the systematic error of R_K. The summary of the AKL accidental rate correction to R_K for K_{e2} and $K_{\mu 2}$ is reported in Table 9.12.

Another cut sensible to the accidental rate is the cut performed on the time coincidence within 5 ns of the candidate track and the closest track in time. The cut is made in both K_{e2} and $K_{\mu 2}$ selection to minimize the systematic correction of the cut to R_K ratio. The rate of accidental time coincidences under $\Delta t_{track} = 0$

[2]Each timeslice is equivalent to a 25 ns region. The number of timeslices dumped depends on the detector: 32 for drift chambers, 20 for AKL, 16 for LKr.

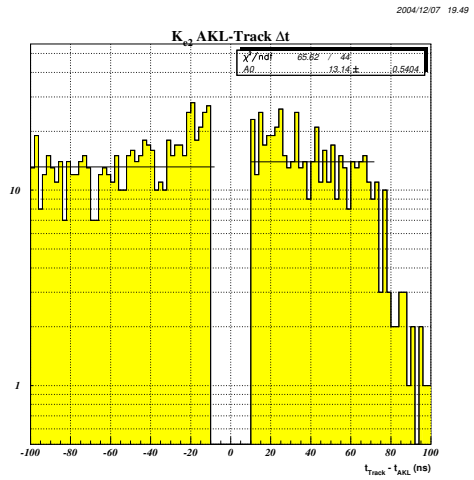

Figure 9.13: *K_{e2} fit of the time difference between track and AKL hit for one of the AKL pocket. The vertical lines limit the peak region inside the cut.*

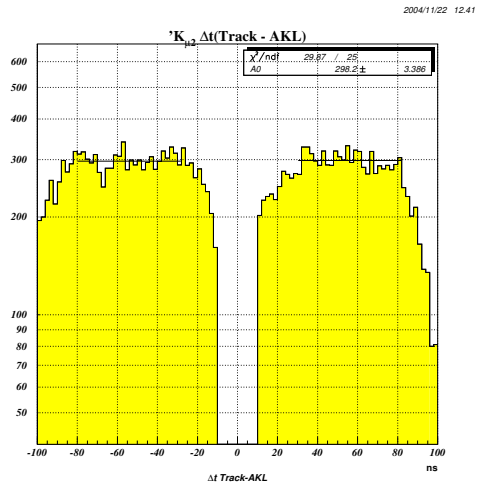

Figure 9.14: *$K_{\mu 2}$ fit of the time difference between track and AKL hit for one of the AKL pocket.*

peak is extracted with the same technique used for the AKL accidental rate. The difference between the two is that in this fit the sidebands cannot exceed 1 timeslice (25 ns) on each side of the peak. This constraint comes from the particular definition of the K_{e2} trigger, that has a lower efficiency in case of more tracks in the same timeslice (see Section 10.1). Therefore, to avoid double counting of the trigger inefficiency, only events in 1 timeslice from the peak are employed in the fit. Trigger logic and efficiency are presented in Chapter 10. The fits are shown in Fig. 9.15 and Fig. 9.16 .

The summary of the accidental rate correction to R_K for K_{e2} and $K_{\mu 2}$ for tracks occurring in the same time slice of an event is reported in Table 9.13.

AKL Accidental Rate correction (%)	
K_{e2} correction	$(0.93 \pm 0.09(stat))$ %
K_{e2} left-right sideband difference	$(0.05 \pm 0.09(stat))$ %
$K_{\mu 2}$ correction	$(1.17 \pm 0.01(stat) \pm 0.03(syst))$ %
$K_{\mu 2}$ left-right sideband difference	$(0.03 \pm 0.01(stat))$ %
K_{e2} - $K_{\mu 2}$ correction difference	$(0.25 \pm 0.09(stat) \pm 0.03(syst))$ %
R_K **correction**	$-(0.24 \pm 0.09(stat) \pm 0.22(syst))$ %

Table 9.12: *Summary of the AKL accidental time coincidence correction to R_K.*

Accidental in time track Rate correction (%)	
K_{e2} correction	$(0.28 \pm 0.09(stat) \pm 0.04(syst))$ %
K_{e2} left-right sideband difference	$(0.10 \pm 0.09(stat))$ %
$K_{\mu 2}$ correction	$(0.28 \pm 0.01(stat) \pm 0.03(syst))$ %
$K_{\mu 2}$ left-right sideband difference	$(0.03 \pm 0.01(stat))$ %
K_{e2} - $K_{\mu 2}$ correction difference	$(0.00 \pm 0.09(stat) \pm 0.05(syst))$ %
R_K **correction**	$(0.00 \pm 0.09(stat) \pm 0.05(syst))$ %

Table 9.13: *Summary of the accidental time coincidence track correction to R_K for tracks occurring in the same timeslice of an event.*

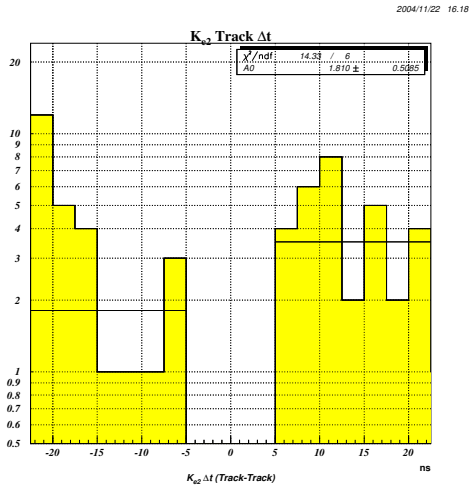

Figure 9.15: *K_{e2} fit of the time difference between event track and the closest in time track. The vertical lines limit the peak region inside the cut.*

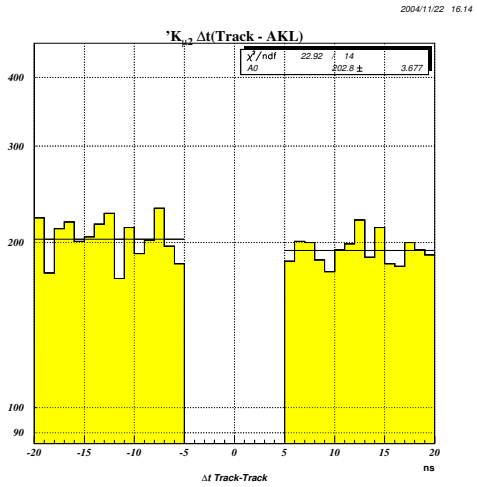

Figure 9.16: *$K_{\mu 2}$ fit of the time difference between event track and the closest in time track.*

9.3 Systematic effect of the LKr geometry cut on $K_{\mu 2}$ acceptance

As seen in Section 7.3, the geometrical acceptance cut at LKr calorimeter face is made differently for $K_{\mu 2}$ candidate events if there is a cluster associated to the track or if there is no track-cluster association. NA48/2 Monte Carlo doesn't simulate properly the interactions of muons inside the LKr calorimeter and, for this reason, the geometrical acceptance of Monte Carlo events is calculated always on the track extrapolated position at the LKr face, disregarding the possible presence of an associated cluster.
In this Section, it will be studied and quantified the possible bias induced by the different estimation of geometrical acceptance for Data and Monte Carlo.

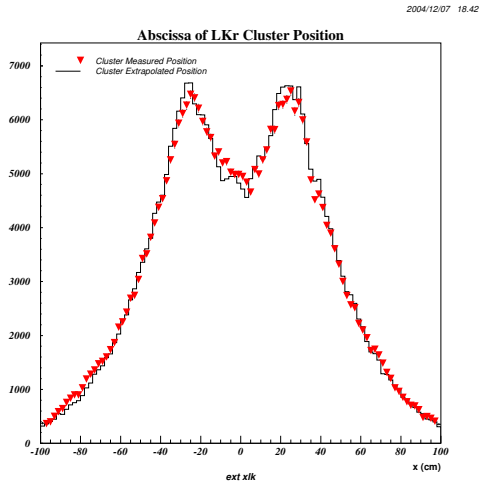

Figure 9.17: *Distribution of the lepton position abscissa at LKr calorimeter for $K_{\mu 2}$ events with an associated cluster and without a track associated-cluster (in this case the extrapolated position has been plotted).*

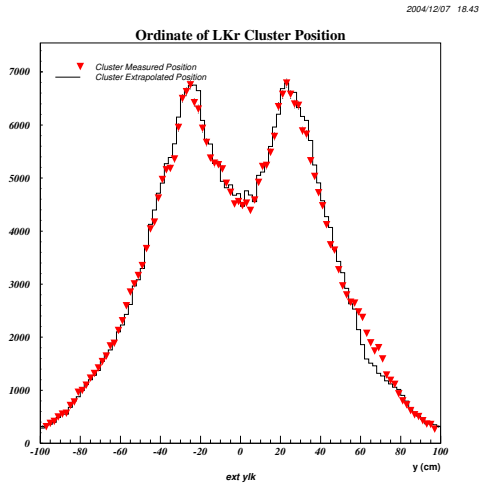

Figure 9.18: *Distribution of the lepton position ordinate at LKr calorimeter for $K_{\mu 2}$ events with an associated cluster and without a track associated-cluster (in this case the extrapolated position has been plotted) .*

The cluster and track extrapolated position at LKr calorimeter face for $K_{\mu 2}$ events are presented in Fig. 9.17 and in Fig. 9.18. To calculate the different geometrical acceptance using the track extrapolated position at LKr or the associated cluster position, a set of unbiased event with track-cluster association has been

considered. Their acceptance has been calculated in both ways, employing the associated LKr cluster position (A_{clu}) and the track extrapolated position at LKr (A_{ext}). A_{clu} and A_{ext} have been plotted in function of the cluster distance from the beam line (Fig. 9.19) and in function of time (Fig. 9.20).

The relative difference in acceptance is:

$$\frac{A_{ext} - A_{clu}}{A_{ext}} = (6.9 \pm 0.9) \cdot 10^{-4}$$

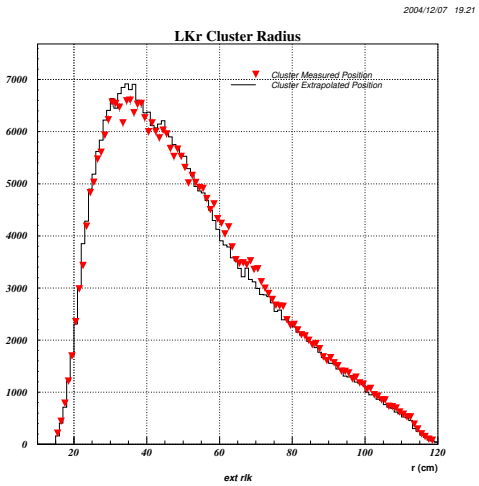

Figure 9.19: *Distribution of the lepton position distance from the beam line at LKr calorimeter face for $K_{\mu 2}$ events with an associated cluster and without a track associated-cluster (in this case the extrapolated position has been plotted).*

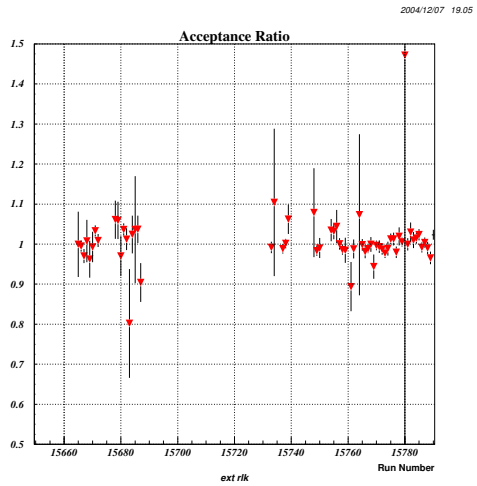

Figure 9.20: *Relative acceptance as a function of time for $K_{\mu 2}$ events with an associated cluster and without a track associated-cluster.*

The correction to R_K ratio is:

$$\frac{\Delta R_K}{R_K} = (-2.9 \pm 0.4) \cdot 10^{-4}$$

Chapter 10

Trigger

The study of a dedicated trigger for K_{e2} decay didn't start at the same time of the other principal channels for which tests were carried out already in 2001. K_{e2} trigger has been studied on the real data only from the beginning of the 2003 data taking. A certain number of changes and improvements have been applied to the trigger logic during the first 2 month of 2003 data taking, in order to have a trigger as much efficient as possible, without saturating the available data acquisition bandwidth.

10.1 K_{e2} and $K_{\mu 2}$ triggers

The triggers logic implemented for K_{e2} and $K_{\mu 2}$ events is divided in two parts: L1 trigger, where only some loose selections on the topology of the events is possible and L2 trigger, where the selection is based on quantities reconstructed on-line by the MBX dedicated processors.
L1 trigger logic for K_{e2} is presented in Table 10.1.

The $K_{\mu 2}$ L1 trigger logic is presented in Table 10.2.

With the following definitions:
$Q1$: It requires at least 1 time coincidence between a signal from a vertical scintillator and a signal from a horizontal scintillator in the same hodoscope quadrant (see Section 3.3.3).

K_{e2} L1 Trigger logic		
Date	Trigger logic	Downscaling
12/6 - 11/7 2003	$(Q1\cdot!Q2\cdot!AKL\cdot!1\mu) \times (E_{LKr} > 15 \cdot E_{HAC} < 10 \cdot M0T < 128)$	100
11/7 - 23/7 2003	$(Q1\cdot!Q2\cdot!AKL\cdot!1\mu) \times (E_{LKr} > 15 \cdot E_{HAC} < 10 \cdot M0T < 128)$	80
23/7 - 11/8 2003	$(Q1\cdot!AKL) \times (E_{LKr} > 15 \cdot E_{HAC} < 10 \cdot M0T < 2400)$	10
11/8 - 8/9 2003	$Q1 \times E_{LKr} > 10$	10
15/5 - 8/8 2004	$Q1 \times E_{LKr} > 10$	10
12/8 - 14/8 2004	$Q1 \times E_{LKr} > 10$	1

Table 10.1: *L1 Trigger logic for K_{e2} events.*

$K_{\mu 2}$ L1 Trigger logic		
Date	Trigger logic	Downscaling
12/6 - 23/7 2003	$(Q1\cdot!Q2\cdot!AKL \cdot 1\mu) \times (E_{LKr} < 10)$	100
23/7 - 11/8 2003	$(Q1\cdot!AKL) \times (E_{LKr} < 10)$	100
11/8 - 8/9 2003	$Q1$	100
15/5 - 8/8 2004	$Q1$	100
12/8 - 14/8 2004	$Q1$	10

Table 10.2: *L1 Trigger logic for $K_{\mu 2}$ events.*

$!Q2$: It vetoes on 2 or more time coincidences between pairs of signals coming from corresponding elements of a 4×4 subdivision of each hodoscope quadrant.
$!AKL$: It vetoes on a time coincidence between the two layers of at least one AKL pocket. Signals from pocket 1 and pocket 7 are not used in the trigger logic.
$!1\mu$: It vetoes on at least 1 signal coming from the μ-veto scintillators.
1μ : It requires at least 1 signal coming from the μ-veto scintillators.
$E_{LKr} > a\ (GeV)$: It requires a minimum energy a (in GeV) deposited in the electromagnetic calorimeter .
$E_{LKr} < a\ (GeV)$: It vetoes events on the basis of energy a (in GeV) deposition in the electromagnetic calorimeter .
$E_{HAC} < b\ (GeV)$: It vetoes an event if the energy deposition (in GeV) in the Hadronic calorimeter is greater than the threshold b
$M0T > c\ (cm^2)$: it is defined as:

$$M0T = \frac{M_2}{M_0} - (\frac{M_1}{M_0})^2$$

where

$$M_i = \sqrt{(\sum_{p=1,n} E_p x_p^i)^2 + (\sum_{p=1,n} E_p y_p^i)^2}$$

E_p is the energy of the $p-th$ hit cluster in the LKr calorimeter, x_p and y_p are the x and y transverse positions relative to the beam axis.

The M0T variable has been extensively used in the NA48 reconstruction procedure. This quantity, for a single e.m. shower in the calorimeter assumes a rather small value, related to the lateral development of the shower, while for a group of several showers originating from a single decay vertex it is proportional to the product of their invariant mass and the distance of the decay vertex from the LKr calorimeter. This condition has been preferred to the 1 *peak* condition[1].

The L2 trigger logic for K_{e2} events is based on the calculation of the missing mass in the hypothesis of a decay of a Kaon of 60 GeV flying along the beam axis:

[1] x and y projections of the calorimeter cell's are divided in slices. A peak is found if this relation on the energy contents of slice p is satisfied: $E_{p-2} < E_{p-1} < E_p$ and $E_{p+1} < E_p$, with E_p larger than an appropriate threshold value.

K_{e2} L2 Trigger logic		
Date	L2 Trigger logic	Downscaling
12/6 - 11/8 2003	$M_{Fake}(e) > 390 MeV/c^2$	20
11/8 - 20/8 2003	$(nsp = 1) \times 504\ MeV/c^2 < M_{Fake}(\pi) < 560\ MeV/c^2$	2
20/8 - 29/8 2003	$(nsp = 1) \times 504\ MeV/c^2 < M_{Fake}(\pi) < 560\ MeV/c^2$	4
29/8 - 8/9 2003	$(nsp = 1) \times 504\ MeV/c^2 < M_{Fake}(\pi) < 560\ MeV/c^2$	2
15/5 - 8/8 2004	$(nsp = 1) \times 504\ MeV/c^2 < M_{Fake}(\pi) < 560\ MeV/c^2$	2
12/8 - 14/8 2004	*Autopass*	1

The condition $(nsp = 1)$ means that the MBX algorithm of the space points reconstruction described in Section 3.4.1 has reconstructed one and only one space point in chamber 1, 2 and 4.
The reconstructed invariant mass M_{Fake} quantity is related to the missing mass and, for a particle of type u, is defined as:

$$M^2_{Fake}(u) \simeq M^2_K - M^2_u - S = P_K P_u \theta^2 + M^2_K \frac{P_K}{P_u} + M^2_u \frac{P_u}{P_K}$$

$$where:$$

$$S \equiv (P_K - P_u)^2 \qquad \vec{P_k} = (0, 0, 60)\ GeV/c \qquad u = e, \pi$$

$$\theta: \ Angle\ between\ beam\ and\ lepton$$

M_{Fake} is employed in place of the missing mass squared S to speed-up the on-line selection.

Data and Monte Carlo $M_{Fake}(\pi)$ variable distribution for $K_{\mu 2}$ events is plotted in Fig. 10.1. The ratio of Data and Monte Carlo distribution is plotted in Fig. 10.2

During the 2004 leptonic run (August 12th - August 14th) there was no L2 filtering on K_{e2} candidates. All the events satisfying the L1 condition ($Q1 * E_{LKr} > 10\ GeV$) were automatically stored by the trigger system (*Autopass*).

The L2 trigger logic implemented for $K_{\mu 2}$ decays is described in the Table below:

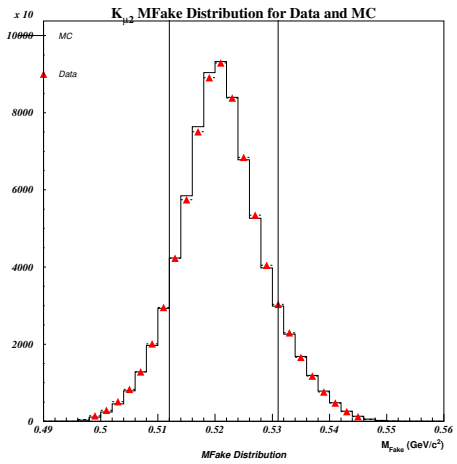

Figure 10.1: *Distributions of Data and Monte Carlo reconstructed $M_{Fake}(\pi)$ for $K_{\mu 2}$ events.*

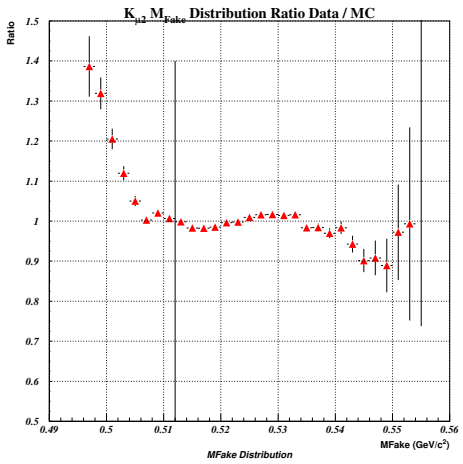

Figure 10.2: *Ratio of the distributions of reconstructed $M_{Fake}(\pi)$ for Data and Monte Carlo $K_{\mu 2}$ events.*

$K_{\mu 2}$ L2 Trigger logic		
Date	L2 Trigger logic	Downscaling
12/6 - 11/8 2003	$M_{Fake}(e) > 390 MeV/c^2$	20
11/8 - 8/9 2003	*Autopass*	100
15/5 - 8/8 2004	*Autopass*	100
12/8 - 14/8 2004	*Autopass*	5

Since August 11th 2003 the L2 trigger selection for $K_{\mu 2}$ candidates had been simply an *Autopass* of the L1 triggers downscaled by a factor 100. The downscaling was lowered to 5 for the 2004 leptonic run.

In the beginning of 2003 data taking the L1 and L2 trigger logic for K_{e2} and $K_{\mu 2}$ was as similar as possible in order to exploit the cancellation of the trigger efficiencies in the ratio seen in Eq. 4.3. In particular, L2 trigger selection was the same for K_{e2} and $K_{\mu 2}$. In principle, this logic was very attractive, because it would have allowed to avoid the calculation of trigger efficiency and to neglect the consequent incertitude on the measurement. Unfortunately, it proved unsatisfactory when the limits of the bandwidth at disposal for leptonic decays were taken into account. The concurrent necessities for the leptonic trigger to have a rate of $\sim$ 1500 collected events per burst and to be unbiased for both K_{e2} and

$K_{\mu 2}$ [2] forced to downscale the trigger of a 200 factor. In such a configuration the number of K_{e2} triggers collected per burst was judged insufficient for a proper R_K measurement (see Fig. 10.3).

Starting from August 11th, K_{e2} and $K_{\mu 2}$ trigger selection were split. $K_{\mu 2}$ events were collected by the already mentioned $Q1$ minimum bias trigger, while K_{e2} events were collected by a very selective L2 trigger ($(nsp = 1) \times 504\ MeV/c^2 < M_{Fake}(\pi) < 560\ MeV/c^2$) having as input a loose L1 selection ($Q1 \times E_{LKr} > 10\ GeV$). In Fig. 10.3 the rate of the leptonic triggers and their effective rate of good reconstructed K_{e2} and $K_{\mu 2}$ events have been plotted for the principal trigger logics.

In consideration o the frequent changes in trigger logic and of the low rate of K_{e2} and $K_{\mu 2}$ event collection in the first part of 2003 data taking, only the data collected as from August 11th 2003 has been used in the R_K analysis.

10.2 Trigger efficiency

The study of trigger efficiencies for $K_{\mu 2}$ and K_{e2} has been conducted separately for L1 and L2 trigger conditions. The procedure employed for the measurement of the trigger efficiencies has been to choose a trigger of minimum bias for the trigger of interest and then look at the Patter Unit contents of the events selected by the minimum bias trigger. Even if events passing through minimum bias trigger are collected independently of the responses of L2 and other L1 trigger, the complete set of trigger conditions is recorded in the above mentioned Pattern Unit.

10.2.1 L1 Trigger Efficiency

As already seen, the L1 trigger signal for K_{e2} is $Q1 \times E_{LKr} > 10\ GeV$, while the $K_{\mu 2}$ trigger is $Q1$.
The efficiency of the $Q1$ trigger condition, common both in the K_{e2} and $K_{\mu 2}$ triggers, is not relevant for the R_K ratio measurement. Its efficiency (ϵ_{Q1}) has been nev-

[2] $M_{Fake}(e) > 390 MeV/c^2$ cuts at $\sim 5\sigma$ from K_{e2} and $K_{\mu 2}$ mean value of the distribution.

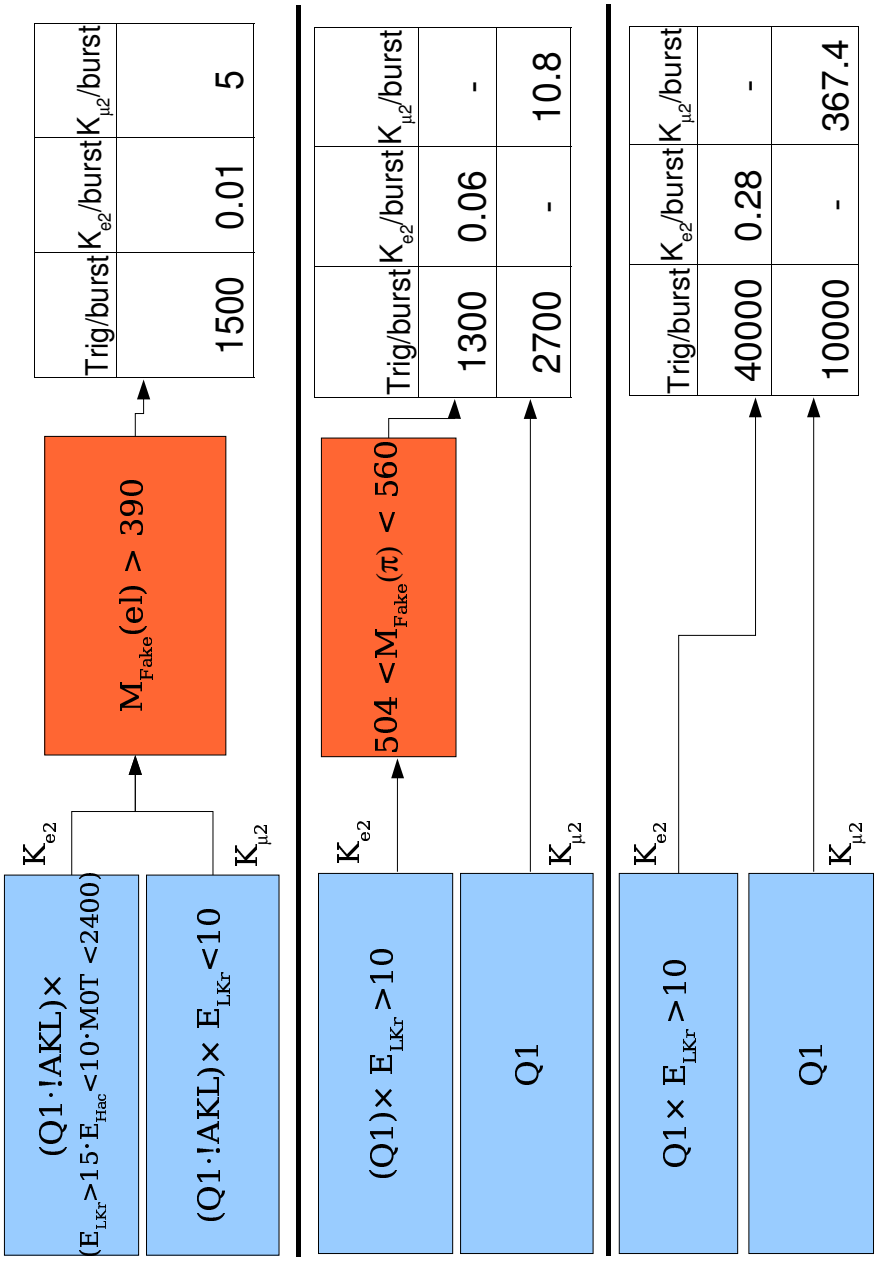

Figure 10.3: *Principal Trigger logics and rates for K_{e2} and $K_{\mu2}$. The first trigger selection employed a common L2 algorithm and common charged L1 signals for both selections. A significant increase of the collected signal events has been realized by splitting K_{e2} and $K_{\mu2}$ L2 logics. The last trigger configuration was employed during 2004 leptonic run, when no L2 selection was performed.*

ertheless measured selecting K_{e3} event passing $T0N$ and $NT-PEAK$ neutral triggers. The result is:

$$1-\epsilon_{Q1} \;=\; (2.3\pm 0.9)\cdot 10^{-3}$$

The efficiency of the $E_{LKr} > 10\ GeV$ condition has been measured using $Q1$ as minimum bias trigger and employing K_{e2} events and the topological similar K_{e3} events. The choice of the $Q1$ signal as minimum bias trigger had the advantage of being completely independent of calorimeter detector. Other possible minimum bias trigger, like $T0N$ logic, activated by a signal collected by the Neutral Hodoscope and $NT-PEAK$ logic, activated by a peak condition from the Neutral Trigger, would be partially biased for this measurement. On the other hand, $Q1$ control trigger has the disadvantage of being strongly downscaled, posing severe limits on the available statistics.
The results are presented in the table below:

L1 $E_{LKr} > 10GeV$ condition efficiency for K_{e2} events		
Event Sample employed	# Events collected by $Q1$	Efficient events
K_{e2} 2003	3	3
K_{e2} s. run 2003	10	10
K_{e3} 2003	22	22
K_{e2} s. run 2004	127	127
Average Efficiency		$> 99.0\%$ (90% C.L.)

10.2.2 L2 Trigger Efficiency

Only K_{e2} candidates pass through a L2 selection algorithm, while $K_{\mu 2}$ events are collected by the minimum bias $Q1$ signal. The L2 algorithm, described in Section 10.1 is: $504\ MeV/c^2 \;<\; M_{Fake}(\pi) <\; 560\ MeV/c^2 \times (nsp = 1)$ (from now on it will be called $1TRK-3$).
The efficiency of the $1TRK-3$ trigger has been evaluated with samples of K_{e2} , $K_{\mu 2}$ and K_{e3} events. The control trigger employed are: $Q1$ for K_{e2} sample and $K_{\mu 2}$ sample, $Q1$, $T0N$ and $NT-PEAK$ for K_{e3} sample. The results are presented in the table below:

K_{e3} sample contributes to large extent to the $1TRK-3$ trigger efficiency evaluation. The $1TRK-3$ efficiency for K_{e3} has been studied as a function of

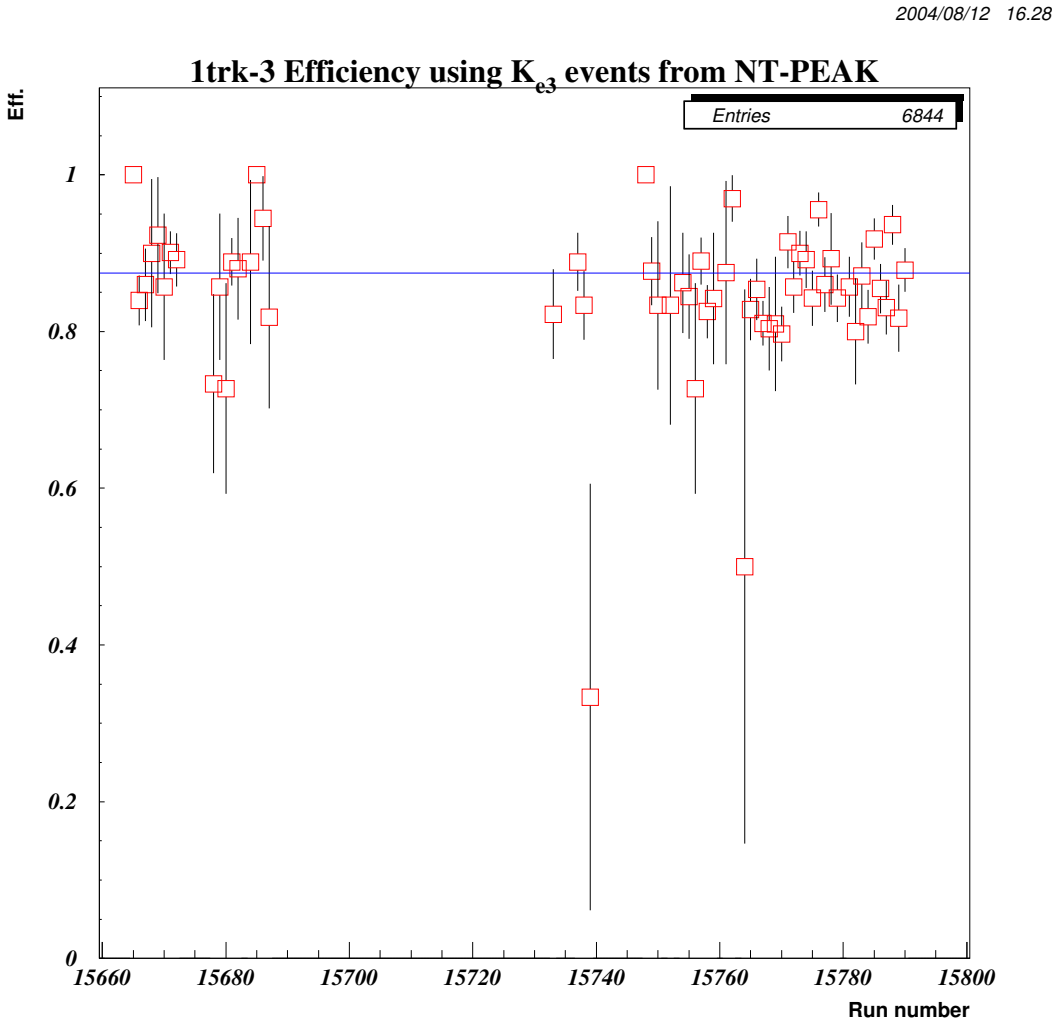

Figure 10.4: *Plot of* $1TRK-3$ *efficiency as a function of the run number for* K_{e3} *events in the period 11/8 - 8/9 2003.*

the time (Fig. 10.4), as a function of the $M_{Fake}(\pi)$ (Fig. 10.5), as a function of the reconstructed decay vertex position (Fig. 10.6) and as a function of the impact point at DCH1 (Fig. 10.7).
The systematic uncertainty on the efficiency measurement has been evaluated by changing the limits of K_{e2} M_{Fake} selection. The result is presented in Table 10.4 and plotted in Fig. 10.3.

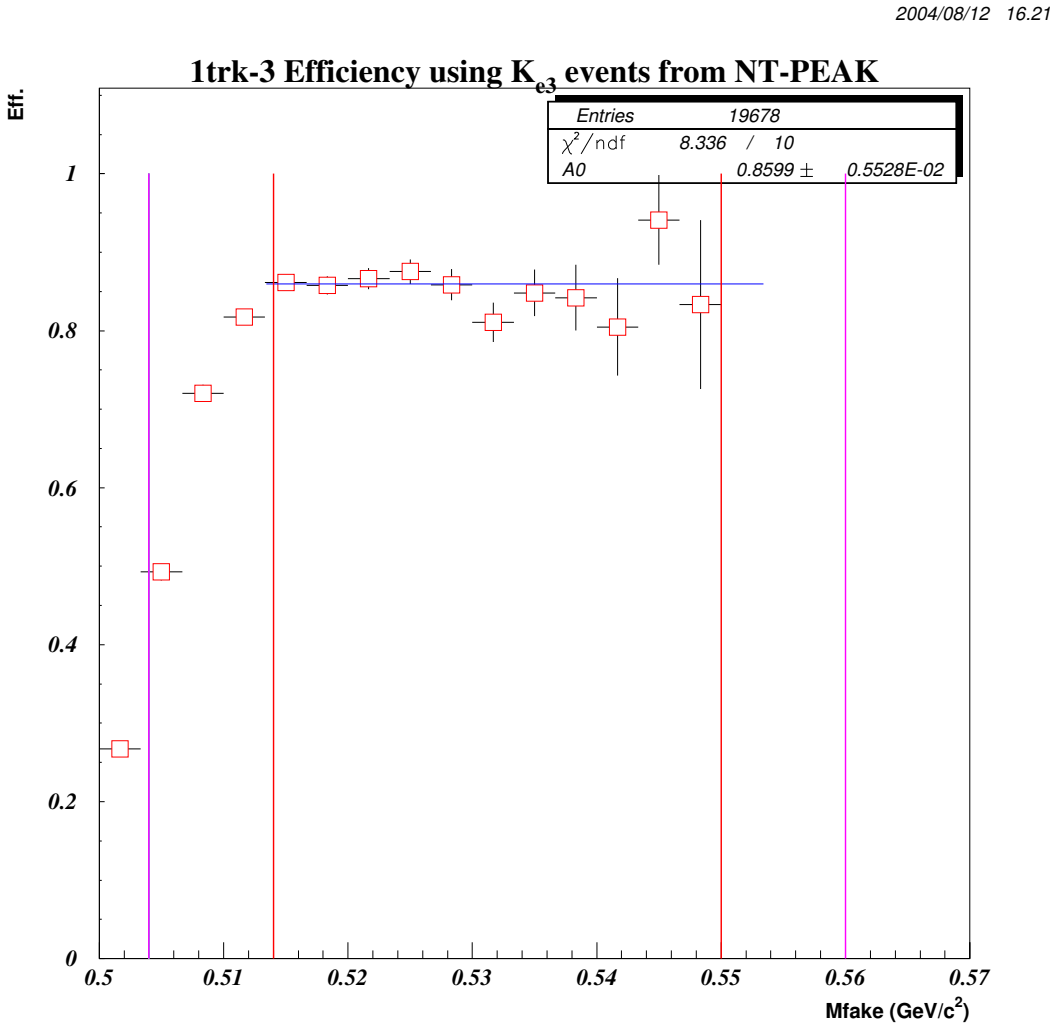

Figure 10.5: *Plot of* $1TRK-3$ *efficiency as a function of* $M_{Fake}(\pi)$ *for* K_{e3} *events. The outer region corresponds to the on-line selection region* $504\ MeV/c^2 < M_{Fake}(\pi) < 560\ MeV/c^2$*; the inner limits correspond to the analysis cut bounds* $514\ MeV/c^2 < M_{Fake}(\pi) < 550\ MeV/c^2$*.* $1TRK-3$ *efficiency is flat as a function of* $M_{Fake}(\pi)$ *inside the analysis region.*

L2 $1TRK-3$ **trigger efficiency for** K_{e2} **events**			
Event Sample employed	Control Trigger	Eff./Total Events	Efficiency
K_{e2}	$Q1$	20/24	$(83 \pm 8)\%$
$K_{\mu 2}$	$Q1$	56/62	$(90 \pm 4)\%$
K_{e3}	$Q1$	21/23	$(91 \pm 6)\%$
	$T0N$	1716/2045	$(85.2 \pm 0.8)\%$
	$NT-PEAK$	3162/3682	$(85.8 \pm 0.6)\%$
Average Efficiency			$(85.6 \pm 0.5_{(stat)})\%$

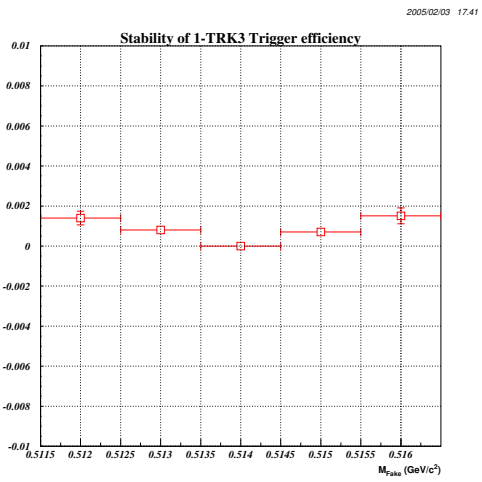

Table 10.3: *Stability result for K_{e2} events. The variation of efficiency of efficiency is plotted as a function of the $M_{Fake}(\pi)$ cut range.*

Stability Result	
Cut (GeV^2/c^4)	K_{e2} Efficiency Rel. var. $\times 10^3$
$0.512 < M_{Fake}(\pi) < 0.552$	$+1.4 \pm 0.3$
$0.513 < M_{Fake}(\pi) < 0.551$	$+0.8 \pm 0.1$
$0.514 < M_{Fake}(\pi) < 0.550$	0
$0.515 < M_{Fake}(\pi) < 0.549$	$+0.7 \pm 0.1$
$0.516 < M_{Fake}(\pi) < 0.548$	$+1.5 \pm 0.4$

Table 10.4: *Summary of result stability for K_{e2} against the change of the cut on $M_{Fake}(\pi)$. The efficiency relative variation has been quoted. The quoted errors are uncorrelated errors. Note the 10^3 scale factor.*

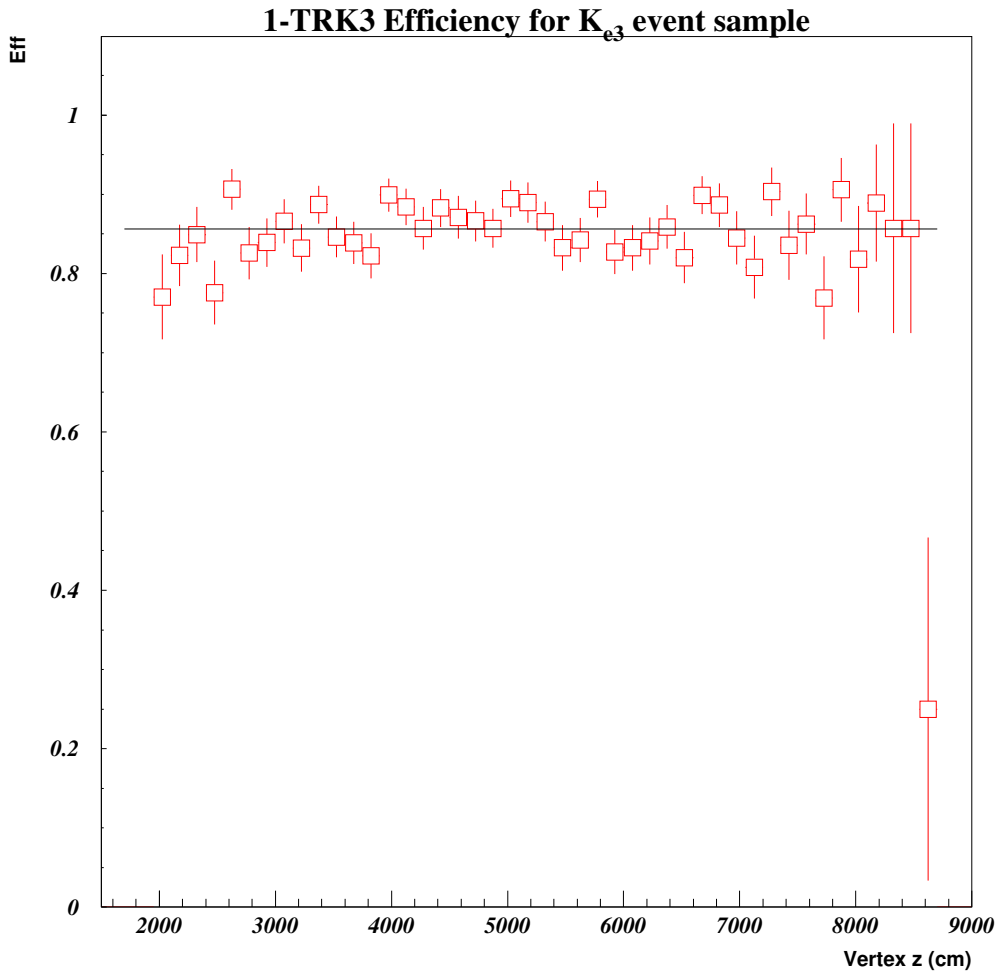

Figure 10.6: *Plot of* $1TRK-3$ *efficiency for* K_{e3} *events as a function of the reconstructed* z *coordinate of the vertex position.*

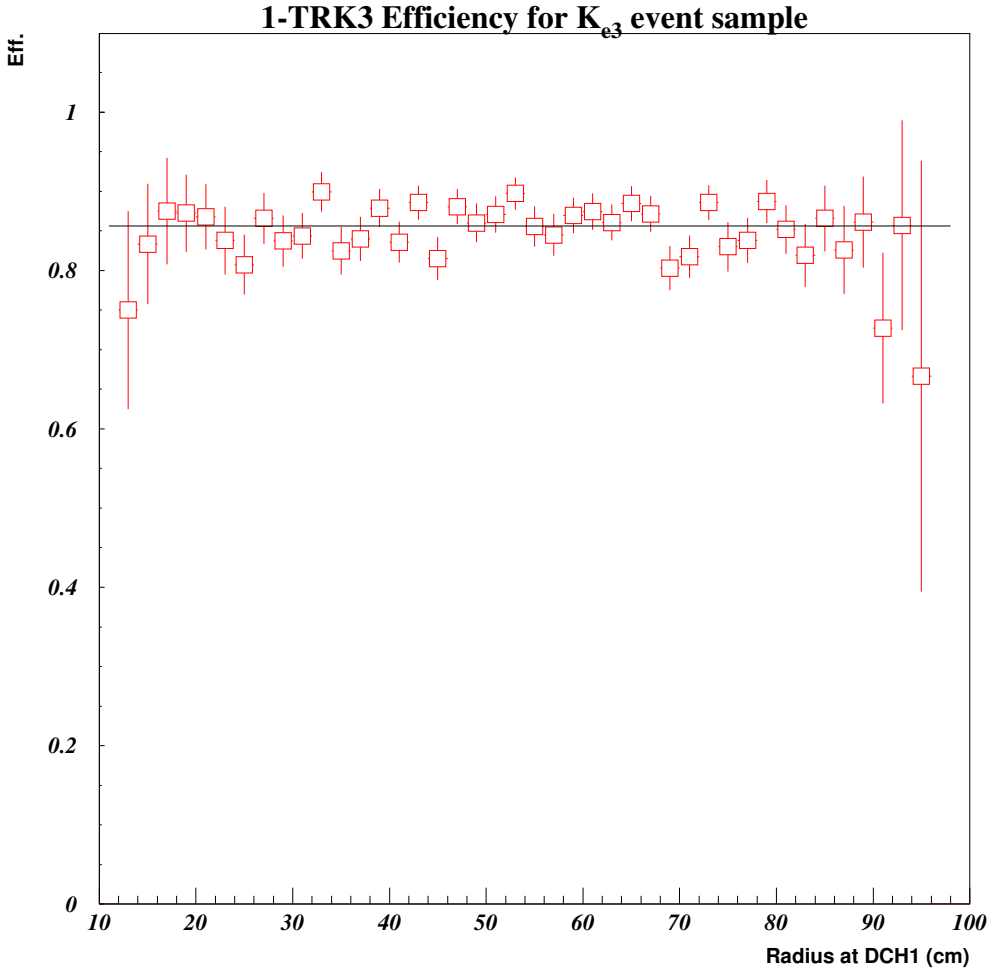

Figure 10.7: *Plot of* $1TRK-3$ *efficiency for* K_{e3} *events as a function of distance of the impact point at DCH1 from the center of the chamber.*

Chapter 11

Radiative Corrections to R_K measurement

As already discussed in Section 2.4, in order to test the lepton universality and V-A structure of the electroweak interactions, the ratio which has to be measured is R_K, the ratio of K_{e2} and $K_{\mu 2}$ Branching Ratio including the fraction of events with the emission of a real photon:

$$R_K = \frac{\Gamma(K^{\pm} \to e^{\pm}\nu(\gamma))}{\Gamma(K^{\pm} \to \mu^{\pm}\nu(\gamma))} \tag{11.1}$$

To compare the result obtained with the Standard Model prediction and the previous R_K measurements, it is thus necessary to take into account radiative corrections to the R_K measurement.

11.1 Theoretical Prediction

At the $O(\alpha)$ order, it is necessary to consider the sum of the decay rates into final states with and without an additional photon [31]:

$$\Gamma(K \to l\nu_l) + \Gamma(K \to l\nu_l\gamma)$$

because the infra-red divergences of both terms (in the virtual photonic correction for $K \to l\nu_l$ and in the soft photon corrections for $K \to l\nu_l\gamma$) cancel out only in the sum of the two processes.

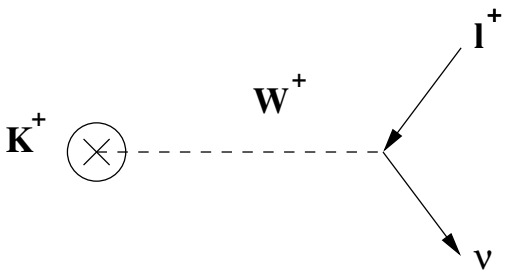

Figure 11.1: *Feynman diagram of the Born amplitude (M_0) of K_{l2} decay.*

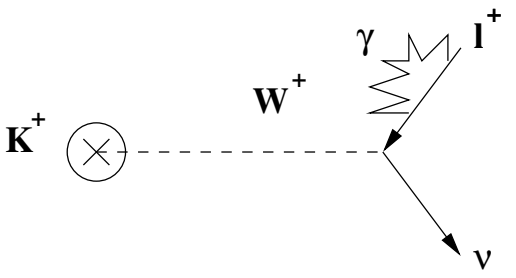

Figure 11.2: *Feynman diagram of one possible virtual 1-loop amplitude (M_v) of K_{l2} decay.*

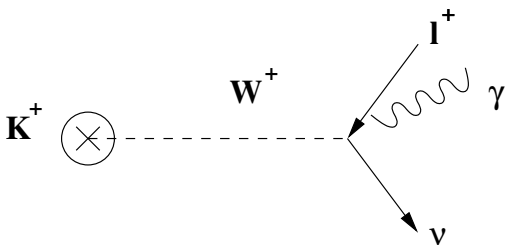

Figure 11.3: *Feynman diagram of the inner bremsstrahlung amplitude (M_{IB}) of $K_{l2\gamma}$ decay.*

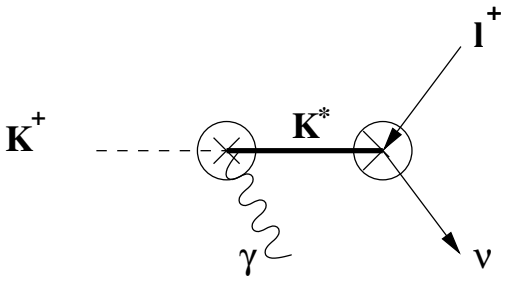

Figure 11.4: *Feynman diagram of the structure dominated amplitude (M_{SD}) of $K_{l2\gamma}$ decay. The amplitude with an intermediate K^* virtual resonance is dominating.*

In addition to the Born amplitude M_0 (see Fig. 11.1), the 1-loop virtual photon amplitude M_v (see Fig. 11.2) and the radiative decay amplitude M_r need to be taken into account. The latter is the sum of the inner bremsstrahlung M_{IB} amplitude (see Fig. 11.3) and structure dominated amplitude M_{SD} (see Fig. 11.4).

$$\begin{aligned} & M_0(K \to l\nu_l) \\ & M_v(K \to l\nu_l) \\ M_r(K \to l\nu_l\gamma) \;&=\; M_{IB} + M_{SD} \end{aligned} \tag{11.2}$$

Explanations of the calculations carried out for the proper inclusion of the K_{l2} radiative decay form factors are deferred to Appendix A.

In order to achieve an easier comparison of theoretical predictions with experimental results, the community adopted the following definition of $K \to l\nu_l(\gamma)$ decay width:

$$\Gamma(K \to l\nu_l(\gamma)) := \Gamma_0 + \delta\Gamma_v + \Gamma_{IB} \tag{11.3}$$

Therefore IB contribution, dominated by very soft photons is fully included, while SD contribution ($\Gamma_{SD} \propto |M_{SD}|^2$), dominated by hard photons, and the interference term of the two ($\Gamma_{INT} \propto 2Re(M_{IB}M_{SD}^2)$ are completely excluded. Using the above definition, the theoretical result obtained for R_K in [31], (same notation as in Section 2.4 for Eq. 2.4) is:

$$\begin{aligned} R_K &= (\frac{m_K^2 - m_e^2}{m_K^2 - m_\mu^2})^2 \frac{m_e^2}{m_\mu^2} \times (1 + \delta R_K) \\ \delta R_K &= -(3.729 \pm 0.023 \pm 0.025)\% + O(\alpha^2) \qquad (11.4) \\ R_K &= R_K^0(1 + \delta R_K) = (2.472 \pm 0.001) \cdot 10^{-5} \qquad (11.5) \end{aligned}$$

In Eq 11.4, the first error is systematic, while the second error comes from the uncertainty on the hadronic parameters.

11.2 K_{l2} Radiative Decays

As seen in the previous Section, the contributions of the different radiative decays are treated differently. While the Inner Bremsstrahlung contribution is included in the $K_{l2\gamma}$ decay amplitude, structure dominated and the interference term are excluded. This choice arises from the different phase space density of Inner Bremsstrahlung decays and structure dominated decays: while photons of Inner Bremsstrahlung decays are prevalently emitted al low energies, photons from structure dominated decays have prevalently a relevant fraction of the initial Kaon energy.

From an experimental point of view, a suitable set of cuts can roughly separate the two populations, but, of course, it is impossible to tell if a single $K_{l2\gamma}$ decay is a inner bremsstrahlung $K_{l2\gamma}$ decay or a structure dominated $K_{l2\gamma}$ decay. For this reason the $K_{l2\gamma}$(SD) and $K_{l2\gamma}$(INT) contamination to K_{e2} and $K_{\mu 2}$ signals will be studied and subtracted.

Analogously the acceptance of inner bremsstrahlung $K_{l2\gamma}$ decays will be studied and a correction applied to K_{l2} acceptances.

It has been necessary to include the theoretical form factors of the different $K_{l2\gamma}$

Branching Ratio of $K_{\mu 2}$ radiative decays	
Γ_0/Γ_{Total}	0.642
$\Gamma_{SD}/\Gamma_{Total}$	$1.1 \cdot 10^{-5}$
$\Gamma_{INT}/\Gamma_{Total}$	$2.4 \cdot 10^{-5}$

Table 11.1: *Theoretical Branching Ratio of $K_{\mu 2}$ radiative decays and $K_{\mu 2}$ tree level decay.*

decays in NA48 Monte Carlo. The calculation has been performed by Bijnens et. al. in [32], details can be found in Appendix A.

11.2.1 $K_{\mu 2}$ Radiative Decays

The Branching Ratio of $K_{\mu 2\gamma}$(SD) and $K_{\mu 2\gamma}$(INT) decays are shown in Table 11.1.
As seen in Table 11.1, the amplitude of the Structure Dominate and Interference radiative decays are completely negligible for the purpose of R_K measurement.

The signal loss of the inner bremsstrahlung decay, has been estimated applying a cut-off to the energy of the emitted photon. As the amplitude of the $K_{\mu 2\gamma}$(IB) decay diverges for photon of vanishing energy, a cut-off at 3 MeV on the center of mass energy of the emitted photon has been placed. Under that threshold, it has been assumed that the extra photon doesn't bias the event selection. In fact, the maximum possible energy deposition of a photon in the LKr calorimeter acceptance cannot exceed 0.7 GeV, much below the limit of 1.5 GeV fixed by $K_{\mu 2}$ selection and the shift induced on reconstructed variables, like missing mass and transverse momentum is much less than the reconstruction resolutions.

In Fig. 11.5 and in Fig. 11.6 the decay amplitude density of the $K_{\mu 2\gamma}$(IB) decay is plotted as a function of the energies of photon and muon in the center of mass. The matrix element divergence for $E_\gamma^{CM} \to 0$ is clearly visible.

The agreement between the theoretical $K_{\mu 2\gamma}$(IB) density of events calculated in [32] and the generated Monte Carlo event distribution can be seen in Fig. 11.7.

In Table 11.2, acceptance and Branching Ratio of $K_{\mu 2\gamma}$(IB) decays with $E_\gamma^* >$

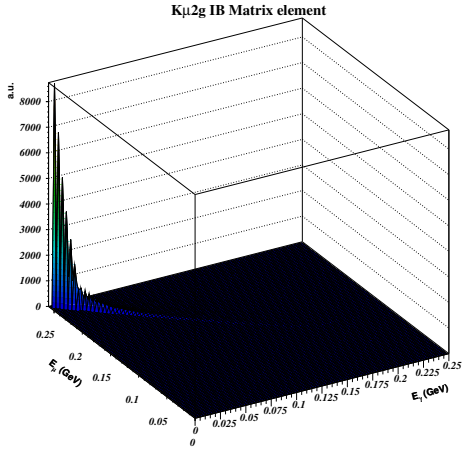

Figure 11.5: *$K_{\mu 2\gamma}$(IB)density of events as a function of the photon and muon energy. The space space diverges for $E_\gamma^{CM} \to 0$.*

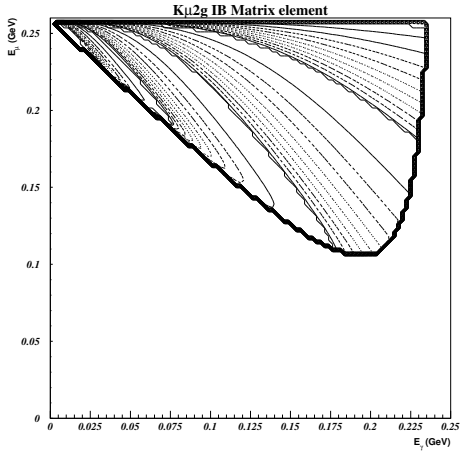

Figure 11.6: *Contour levels of the $K_{\mu 2\gamma}$(IB) density of events as a function of the photon and muon energy.*

3 MeV have been reported , while in Fig. 11.8 the $K_{\mu 2\gamma}$(IB) relative acceptance to $K_{\mu 2}$ has been plotted as a function of the center of mass photon energy.

$K_{\mu 2\gamma}$**(IB)** $E_\gamma^{CM} > 3MeV$
$\Gamma_{IB}(E_\gamma^{CM} > 3MeV)/\Gamma_0 \;=\; (1.01 \pm 0.01) \cdot 10^{-2}$
$\frac{A(K_{\mu 2}, E_\gamma^{CM} > 3MeV)}{A(K_{\mu 2})} \;=\; 0.37 \pm 0.002(stat) \pm 0.008(syst)$

Table 11.2: *Acceptance and Branching Ratio of $K_{\mu 2\gamma}$(IB) decays with $E_\gamma^{CM} >$ 3 MeV.*

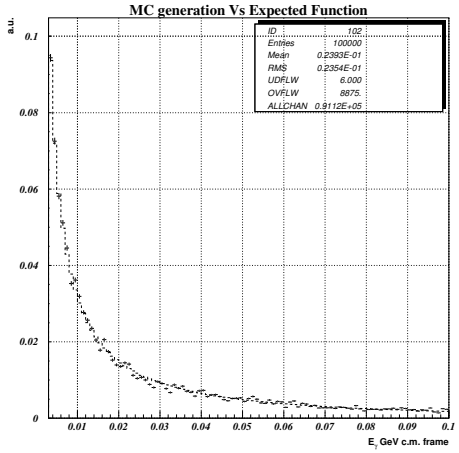

Figure 11.7: *$K_{\mu 2\gamma}$(IB) Monte Carlo events distribution as a function of the photon energy in the center of mass frame. The distribution is superimposed to the theoretical distribution density.*

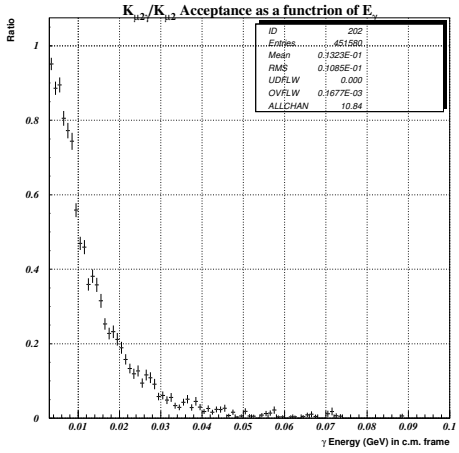

Figure 11.8: *$K_{\mu 2\gamma}$(IB) acceptance normalized to $K_{\mu 2}$ acceptance as a function of the center of mass photon energy.*

11.2.2 K_{e2} Radiative Decays

The Branching Ratio of $K_{e2\gamma}$(SD) and $K_{\mu 2\gamma}$(INT) decays are shown in Table 11.3.
Remarkably, the amplitude of the Structure Dominate term is of the same order of magnitude of the tree level, while Interference radiative decay contribution is negligible.

Branching Ratio of K_{e2} radiative decays	
Γ_0/Γ_{Total}	$1.61 \cdot 10^{-5}$
$\Gamma_{SD}/\Gamma_{Total}$	$1.50 \cdot 10^{-5}$
$\Gamma_{INT}/\Gamma_{Total}$	$1.1 \cdot 10^{-8}$

Table 11.3: *Theoretical Branching Ratio of K_{e2} radiative decays and K_{e2} tree level decay.*

The $K_{\mu 2\gamma}$(SD) form factor is plotted in Fig. 11.9 and in Fig. 11.10. In Fig. 11.11 and Fig. 11.12 it has been plotted the photon energy distribution for the two contributions (of positive and negative polarization) to the structure dominated amplitude.

The acceptance of the $K_{e2\gamma}$(SD) events is:

$$\frac{A(K_{e2\gamma}(SD))}{A(K_{e2})} \;=\; 0.0024 \pm 0.003(stat) \tag{11.6}$$

The correction to R_K ratio due $K_{e2\gamma}$(SD) events background is:

$K_{e2\gamma}$**(IB)** $E_\gamma^{CM} > 3MeV$
$\Gamma_{IB}(E_\gamma^{CM} > 3MeV)/\Gamma_0 \;=\; (9.69 \pm 0.01) \cdot 10^{-2}$
$\frac{A(K_{e2\gamma}, E_\gamma^{CM} > 3MeV)}{A(K_{e2})} \;=\; 0.33 \pm 0.002(stat) \pm 0.015(syst)$

Table 11.4: *Acceptance and Branching Ratio of $K_{\mu 2\gamma}$(IB) decays with $E_\gamma^* > 3\ MeV$.*

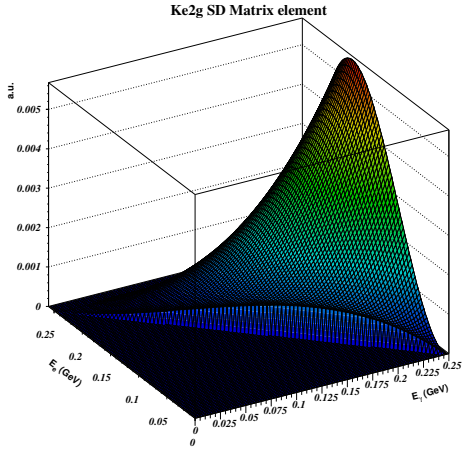

Figure 11.9: *$K_{e2\gamma}$(SD) density of events as a function of the photon and electron energy in the Center of Mass frame.*

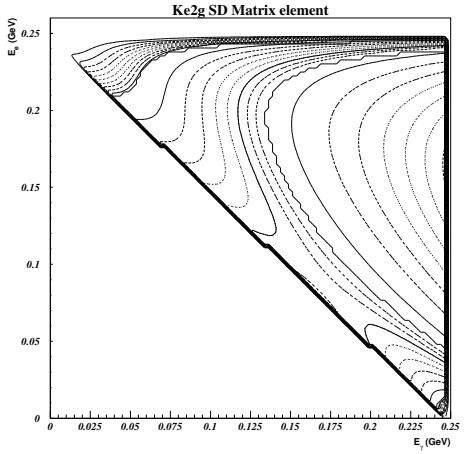

Figure 11.10: *Contour levels of the $K_{e2\gamma}$(SD) density of events as a function of the photon and electron energy in the Center of Mass frame.*

$$\frac{\Delta R_K}{R_K} = (-0.22 \pm 0.03)\%$$

The signal loss of the inner bremsstrahlung decay, has been estimated applying a cut-off to the energy of the emitted photon at 3 MeV, as for $K_{\mu 2\gamma}$(IB) decay.

In Table 11.4, it has been reported acceptance and Branching Ratio of $K_{e2\gamma}$(IB) decays with $E_\gamma^{CM} > 3\ MeV$, while in Fig. 11.13 and in Fig. 11.14 the $K_{e2\gamma}$(IB) relative acceptance to K_{e2} has been plotted as a function of the center of mass photon energy.

11.2.3 R_K Correction due to IB Radiative Decays

R_K, being the ratio of $\Gamma(K_{e2}(\gamma))/\Gamma(K_{\mu 2}(\gamma))$ includes the sum of both $\Gamma(K_{l2\gamma}(\text{IB}))$ and $\Gamma(K_{l2})$ contributions. The different acceptance of $K_{l2\gamma}$(IB) decay from the K_{l2} acceptance calculated in Chapter 7 has to be taken into account in the R_K measurement.

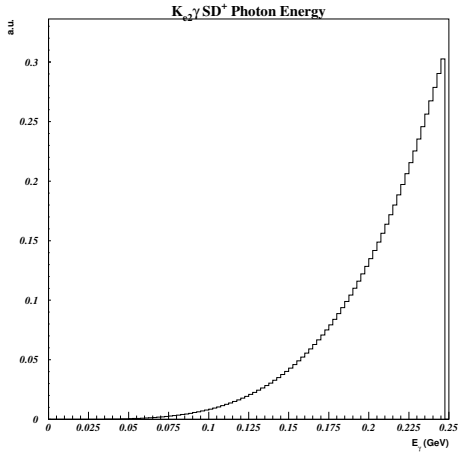

Figure 11.11: *Photon energy distribution for the positive helicity contribution to the $K_{e2\gamma}(SD)$ phase space.*

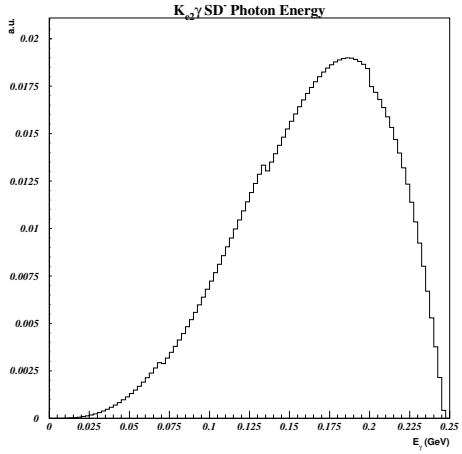

Figure 11.12: *Photon energy distribution for the negative helicity contribution to the $K_{e2\gamma}(SD)$ phase space.*

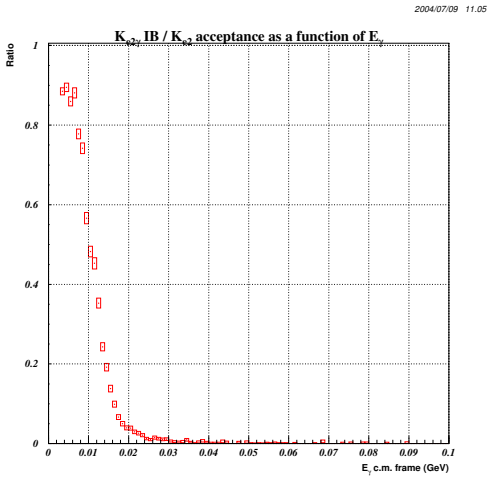

Figure 11.13: *$K_{e2\gamma}(IB)$ acceptance normalized to K_{e2} acceptance as a function of the center of mass photon energy.*

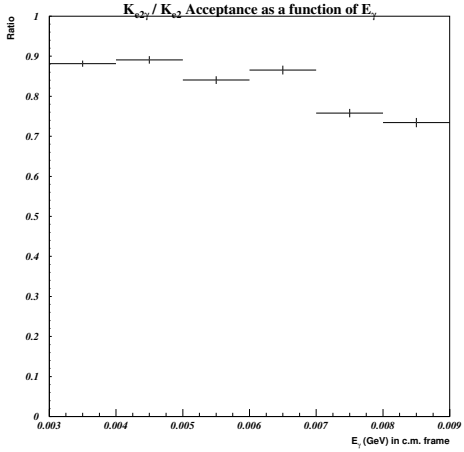

Figure 11.14: *$K_{e2\gamma}(IB)$ acceptance normalized to K_{e2} acceptance as a function of the center of mass photon energy in the $3\ MeV < E^*_\gamma < 9\ MeV$.*

As already mentioned, $\Gamma(K_{l2}(\gamma))$ is the inclusive width with or without a γ emission (SD and INT parts excluded).
Introducing the following definitions:

$$\begin{aligned} \Gamma(K^*_{l2}) &= \Gamma(K_{l2}) + BR(K_{l2}\gamma\ E_\gamma < E_{cut}) \\ \Gamma(K_{l2}\gamma \Uparrow) &= \Gamma(K_{l2}\gamma\ E_\gamma > E_{cut}) \end{aligned} \tag{11.7}$$

the final number of K_{e2} and $K_{\mu 2}$ candidates can be written as:

$$N_{Ke2} \propto Eff(Ke2) \cdot [BR(K^*_{e2})A(K_{e2}) + BR(K_{e2}\gamma \Uparrow)A(K_{e2}\gamma \Uparrow)]$$

In the same way for $K_{\mu 2}$:

$$N_{K\mu 2} \propto Eff(K\mu 2) \cdot [BR(K^*_{\mu 2})A(K^*_{\mu 2}) + BR(K_{\mu 2}\gamma \Uparrow)A(K_{\mu 2}\gamma \Uparrow)]$$

The part inside the squared brackets can be easily rewritten using the relation $BR(K_{l2}(\gamma)) = BR(K^*_{l2}) + BR(K_{l2}\gamma \Uparrow)$, derived directly from definitions.
The ratio of the two is then:

$$\frac{N_{Ke2}}{N_{K\mu 2}} = \frac{BR(K_{e2}(\gamma))A(K_{e2})Eff(K_{e2})[1 - \frac{BR(K_{e2}\gamma\Uparrow)}{BR(K_{e2}(\gamma))} + \frac{BR(K_{e2}\gamma\Uparrow)A(K_{e2}\gamma\Uparrow)}{BR(K_{e2}(\gamma))A(K_{e2})}]}{BR(K_{\mu 2}(\gamma))A(K_{\mu 2})Eff(K_{\mu 2})[1 - \frac{BR(K_{\mu 2}\gamma\Uparrow)}{BR(K_{\mu 2}(\gamma))} + \frac{BR(K_{\mu 2}\gamma\Uparrow)A(K_{\mu 2}\gamma\Uparrow)}{BR(K_{\mu 2}(\gamma))A(K_{\mu 2})}]}$$

therefore as $R_K := \frac{\Gamma(K_{e2}(\gamma))}{\Gamma(K_{\mu 2}(\gamma))}$:

$$R_K = \frac{BR(K_{e2}(\gamma))}{BR(K_{\mu 2}(\gamma))} = \frac{N_{Ke2}}{N_{K\mu 2}} \frac{A(K_{\mu 2})Eff(K_{\mu 2})}{A(K_{e2})Eff(K_{e2})} \frac{[1 - \frac{BR(K_{\mu 2}\gamma\Uparrow)}{BR(K_{\mu 2}(\gamma))} + \frac{BR(K_{\mu 2}\gamma\Uparrow)A(K_{\mu 2}\gamma\Uparrow)}{BR(K_{\mu 2}(\gamma))A(K_{\mu 2})}]}{[1 - \frac{BR(K_{e2}\gamma\Uparrow)}{BR(K_{e2}(\gamma))} + \frac{BR(K_{e2}\gamma\Uparrow)A(K_{e2}\gamma\Uparrow)}{BR(K_{e2}(\gamma))A(K_{e2})}]} \tag{11.8}$$

If the $A(K_{l2})$ acceptances shown in Table 7.3 of Chapter 7 are used for $K_{l2}(\gamma)$ decays, the correction to R_K ratio for the $A(K_{l2\gamma}(IB))$ acceptance can be calculated using the results presented in Table 11.1 and Table 11.3:

$$\begin{aligned} 1 + \frac{\Delta R_K}{R_K} &= \frac{[1 - \frac{BR(K_{\mu 2}\gamma\Uparrow)}{BR(K_{\mu 2}(\gamma))} + \frac{BR(K_{\mu 2}\gamma\Uparrow)A(K_{\mu 2}\gamma\Uparrow)}{BR(K_{\mu 2}(\gamma))A(K_{\mu 2})}]}{[1 - \frac{BR(K_{e2}\gamma\Uparrow)}{BR(K_{e2}(\gamma))} + \frac{BR(K_{e2}\gamma\Uparrow)A(K_{e2}\gamma\Uparrow)}{BR(K_{e2}(\gamma))A(K_{e2})}]} = \\ &= 1.063 \pm 0.0008(stat) \pm 0.005(syst) \end{aligned} \tag{11.9}$$

The correction calculated in Eq. 11.9 is necessary to take into account the different acceptance of $K_{l2\gamma}$ and K_{l2} events in the comparison of the experimental result with the theoretical prediction of R_K seen in Eq. 11.5.

Chapter 12

R_K measurement for positive and negative events

The past measurement of R_K ratio compared the decay fractions of $K^+ \to e^+\nu(\gamma)$ and $K^+ \to \mu^+\nu(\gamma)$ employing a beam of particles of positive charge exclusively. NA48/2 beamline is composed of two simultaneous and collinear beams of positive and negative particles, allowing a concurrent measurement of R_K ratio for events of both charge sign. Up to now, the corrections to R_K measurement have been studied summing up events of both charges; in this Chapter, the charge dependent differences in acceptance, trigger efficiency and in background subtraction will be studied.

12.1 Charge dependent effects

The main goal of NA48/2 experiment is the precise measurement of direct CP violation in $K^+ \to 3\pi$ and $K^- \to 3\pi$ decays. Many efforts have been devoted to render equal the acceptance of K^+ and K^- decays, as the frequent inversion of current polarity in the spectrometer magnet and the regular exchange of Kaon beam path are part of these efforts.

A few residual sources of asymmetry between acceptances of particles of different charge still persists: magnetic fields not under the experiment direct control or changes in acceptance and efficiency of detectors, that are both localized in space and time dependent, can bias the comparison of R_K measurement for positive (R_{K^+}) and negative particles (R_{K^-}).

The presence of a residual magnetic field of small magnitude in the decay region (see Section 3.3) is one example of possible bias for the comparison of R_{K^+} and R_{K^-}. The presence of the residual magnetic field inside the decay region can be spotted by the peculiar modulation of the $MM^2(\mu)$ distribution as a function of the azimuthal angle of the lepton track, as shown in Fig. 12.1.

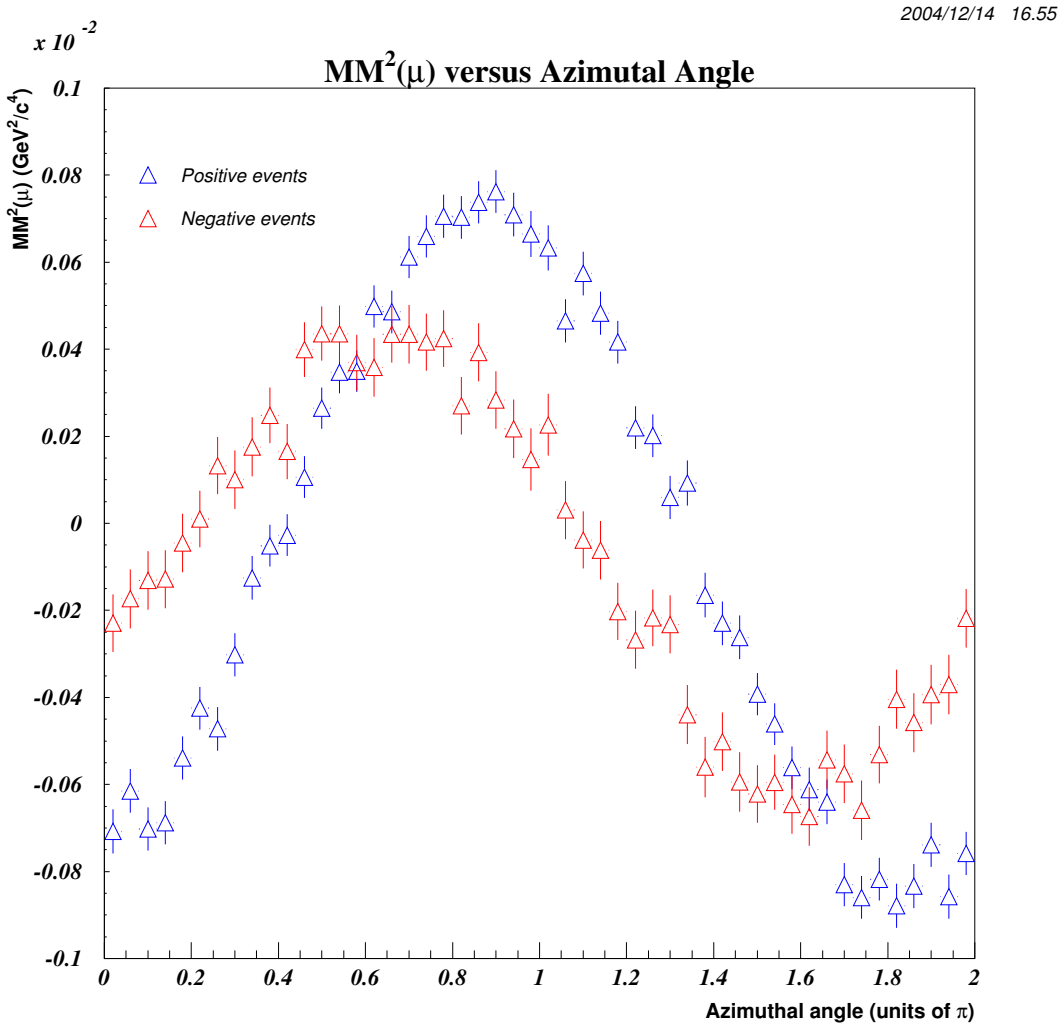

Figure 12.1: *Mean value of $MM^2(\mu)$ distribution as a function of the azimuthal angle of the lepton track before the spectrometer magnet. The abscissa is expressed in units of π radiants.*

Another possible source of bias is the time dependence of detectors acceptance

and efficiency. The ratio of collected $K^+_{\mu 2}$ and $K^-_{\mu 2}$ events as a function of time is presented in Fig. 12.2.

The trend of $MM^2(\mu)$ value with respect to time and spectrometer magnet field

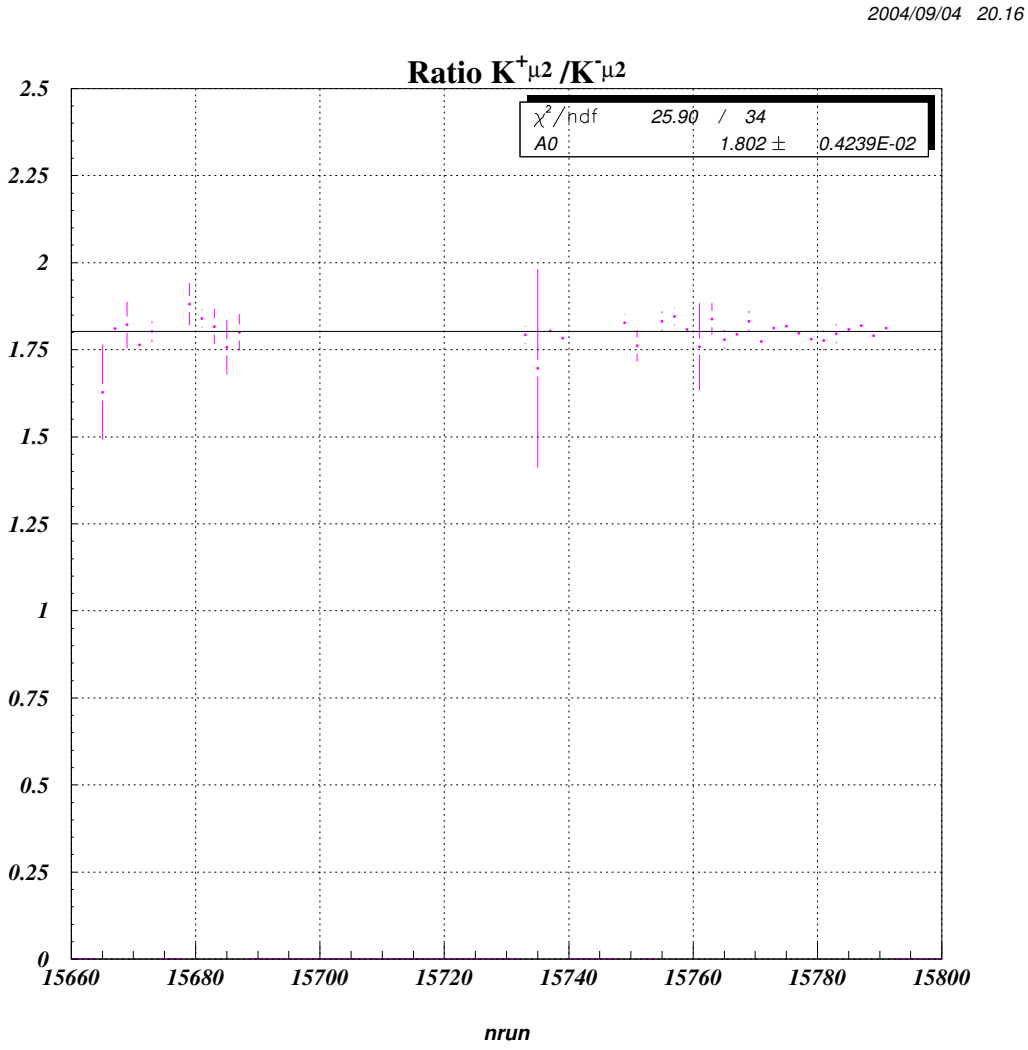

Figure 12.2: *Ratio of collected $K^+_{\mu 2}$ over $K^-_{\mu 2}$ events as a function of run number.*

orientation for $K^+_{\mu 2}$ and $K^-_{\mu 2}$ events is presented in Fig. 12.3 and in Fig. 12.4.

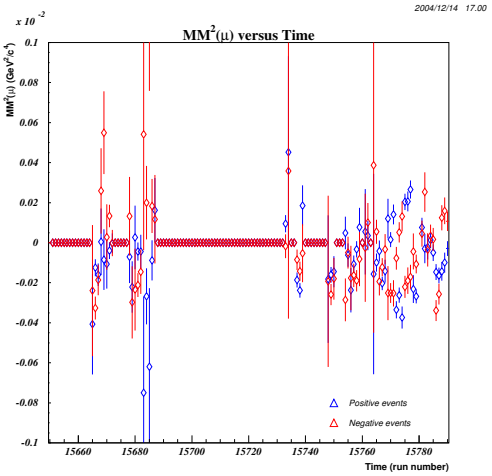

Figure 12.3: $MM^2(\mu)$ *value as a function of run number value for* $K^+_{\mu 2}$ *and* $K^-_{\mu 2}$ *events.*

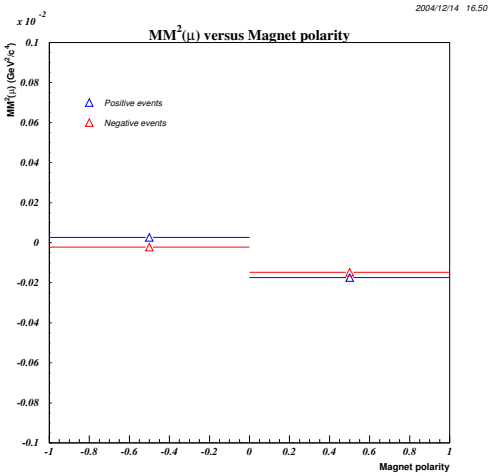

Figure 12.4: $MM^2(\mu)$ *value as a function of spectrometer magnetic field for* $K^+_{\mu 2}$ *and* $K^-_{\mu 2}$ *events.*

12.2 K^+_{l2} and K^-_{l2} acceptance

The differences in beamline optics, detector geometry and efficiency can affect differently the R_K measurement for events of positive and negative charge. The inversion of spectrometer magnet current (every 24 hours during 2003 data taking) and the exchange of Kaon beam path (every 7 days) average detector acceptance and illumination for particles of different charge. This procedure allows to compensate for detector left-right asymmetry and difference in achromat optics.
A comparison of distributions of the 2003 complete statistics for $K_{\mu 2}$ positive and negative events is presented: x and y illumination for $K^+_{\mu 2}$ and $K^-_{\mu 2}$ events at DCH1 are plotted in Fig. 12.5 and Fig. 12.7; x and y illumination at chamber 4 are plotted in Fig. 12.9 and Fig. 12.11.
For a fixed value of the spectrometer magnet polarity, the illumination at DCH4 is very different for μ^+ and μ^- originating from $K_{\mu 2}$ decays, because the magnet deflects positive and negative particles in opposite directions. However, as it can be seen from Fig 12.10, the illumination of positive and negative events is very similar, in both x and y, when averaged over the full data taking.
A few more comparison can be done on reconstructed variables. The vertex and momentum distributions are presented in Fig. 12.13 and in Fig. 12.15, while transverse momentum and missing mass squared distributions are plotted in Fig. 12.17 and in Fig. 12.19.

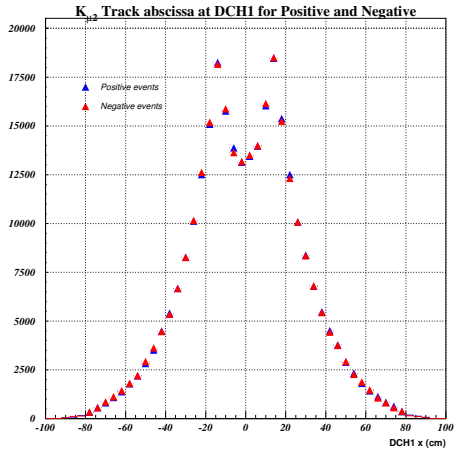

Figure 12.5: *Distribution of x coordinate of track impact point at DCH1 for positive and negative $K_{\mu 2}$ events.*

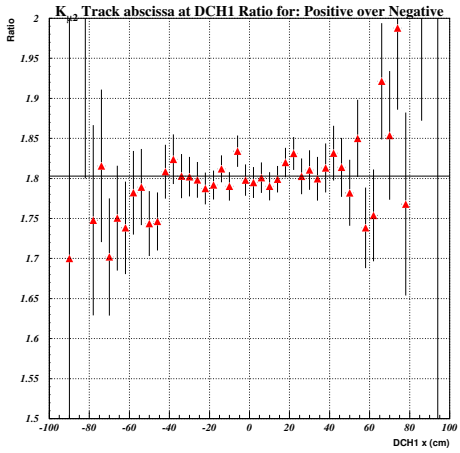

Figure 12.6: *Ratio of the distributions of x coordinate of track impact point at DCH1 for positive and negative $K_{\mu 2}$ events.*

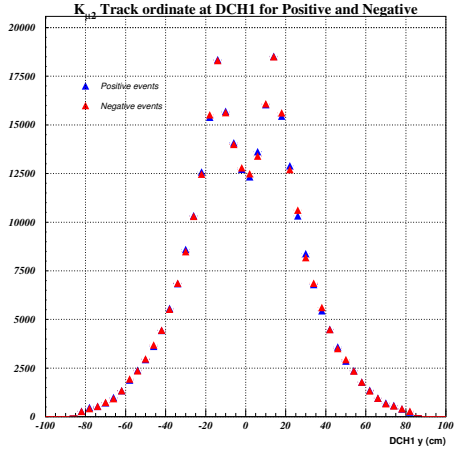

Figure 12.7: *Distribution of y coordinate of track impact point at DCH1 for positive and negative $K_{\mu 2}$ events.*

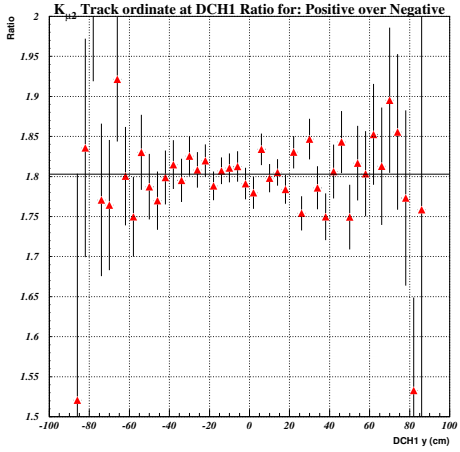

Figure 12.8: *Ratio of the distributions of y coordinate of track impact point at DCH1 for positive and negative $K_{\mu 2}$ events.*

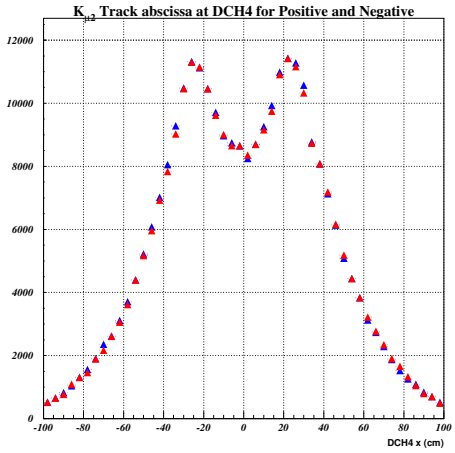

Figure 12.9: *Distribution of x coordinate of track impact point at DCH1 for positive and negative $K_{\mu 2}$ events.*

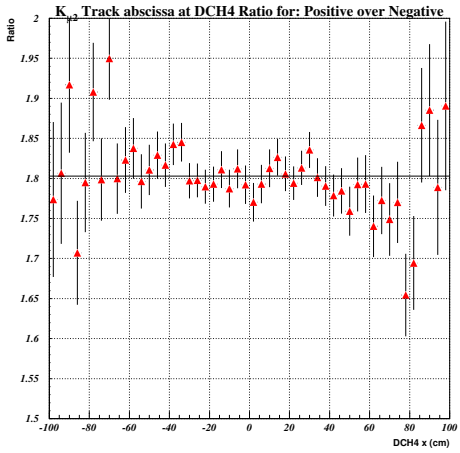

Figure 12.10: *Ratio of the distributions of x coordinate of track impact point at DCH1 for positive and negative $K_{\mu 2}$ events.*

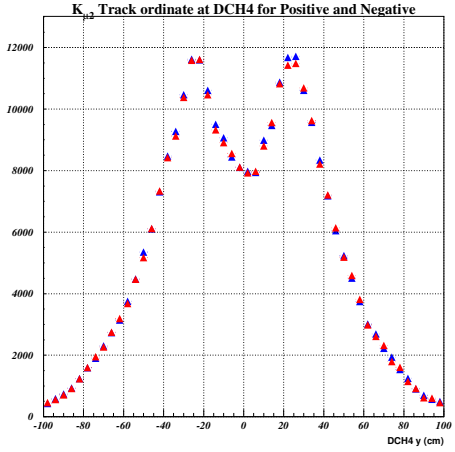

Figure 12.11: *Distribution of y coordinate of track impact point at DCH4 for positive and negative $K_{\mu 2}$ events.*

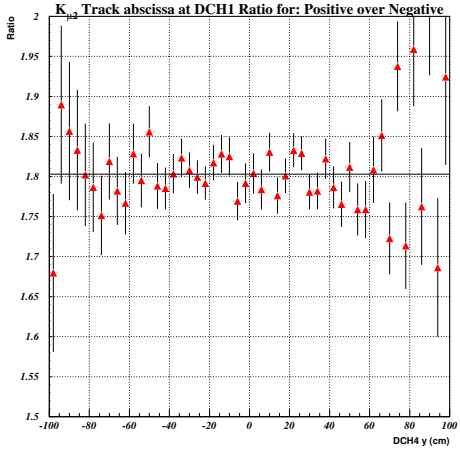

Figure 12.12: *Ratio of the distributions of y coordinate of track impact point at DCH4 for positive and negative $K_{\mu 2}$ events.*

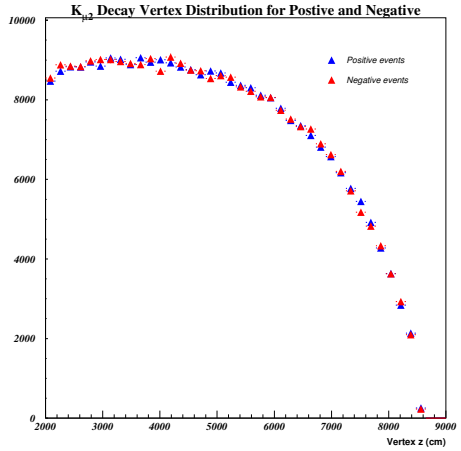

Figure 12.13: *Distribution of reconstructed vertex z coordinate for positive and negative $K_{\mu 2}$ events.*

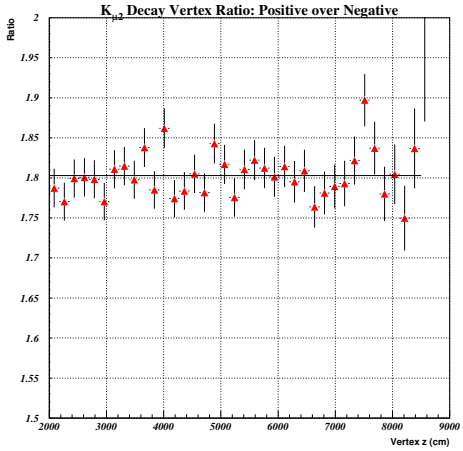

Figure 12.14: *Ratio of the distributions of reconstructed vertex z coordinate for positive and negative $K_{\mu 2}$ events.*

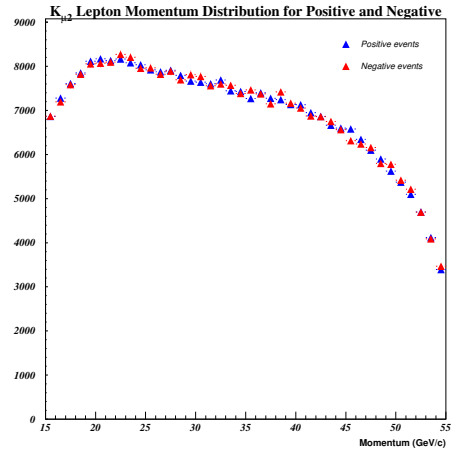

Figure 12.15: *Distribution of reconstructed lepton momentum for positive and negative $K_{\mu 2}$ events.*

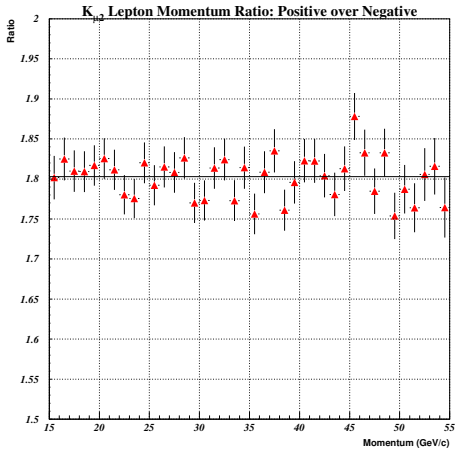

Figure 12.16: *Ratio of the distributions of reconstructed lepton momentum for positive and negative $K_{\mu 2}$ events.*

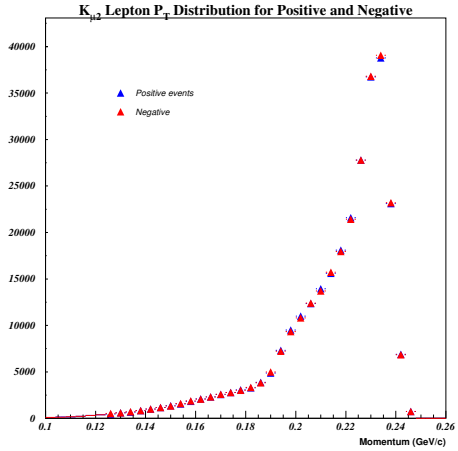

Figure 12.17: *Distribution of reconstructed lepton transverse momentum for positive and negative $K_{\mu 2}$ events.*

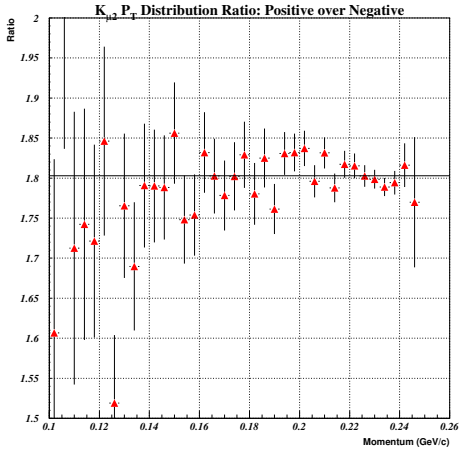

Figure 12.18: *Ratio of the distributions of reconstructed lepton transverse momentum for positive and negative $K_{\mu 2}$ events.*

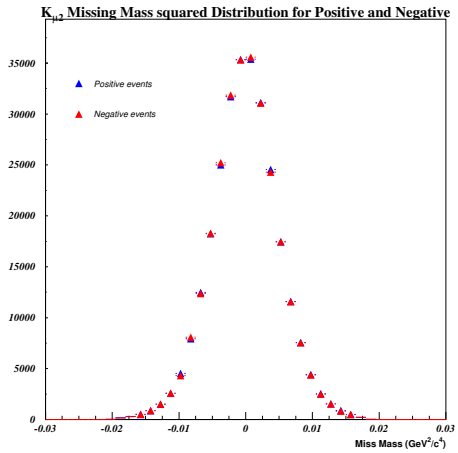

Figure 12.19: *Distribution of reconstructed $MM^2(\mu)$ for positive and negative $K_{\mu 2}$ events.*

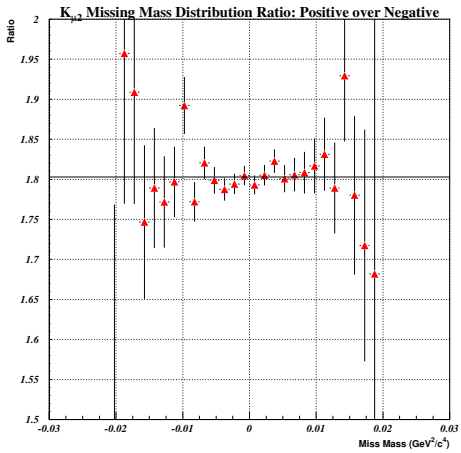

Figure 12.20: *Ratio of the distributions of reconstructed $MM^2(\mu)$ for positive and negative $K_{\mu 2}$ events.*

NA48/2 Monte Carlo (CMC) is able to simulate the most relevant differences of beamline and detector acceptance between particles of different charge as seen in Section 7.1. The production of Monte Carlo events proportionally to the number of data events collected for each run guarantees that Monte Carlo sample reflects data sample composition for each particular beam geometry and detector efficiency map (see Fig. 7.1 and Fig. 7.2 at page 71).
The acceptance of K_{e2} and $K_{\mu 2}$ decays has been calculated for positive and negative events, the obtained results are presented in Table 12.1.

R_K **Acceptance**		
	Positive charge	Negative charge
K_{e2} Acceptance	0.2307 ± 0.0004 $_{(stat)}$	0.2301 ± 0.0006 $_{(stat)}$
$K_{\mu 2}$ Acceptance	0.2575 ± 0.0002 $_{(stat)}$	0.2568 ± 0.0002 $_{(stat)}$

Table 12.1: *Summary of the Acceptance result for K_{e2} and $K_{\mu 2}$ events of both electric charge signs. Only statistical errors are taken into account.*

12.3 Trigger efficiency for K^+_{e2} and K^-_{e2} events

The efficiency of $1-TRK3$ trigger signal for K_{e2} events has been presented in Chapter 10.
Differences in trigger efficiency for positive and negative decays have been investigated. The trigger efficiency for positive and negative events as a function of M_{Fake} is presented in Fig. 12.21, while the efficiency as a function of the reconstructed decay vertex position is plotted in Fig. 12.22. No systematic dependence of the trigger efficiency has been found at the present level of statistical precision.
The $1-TRK3$ trigger efficiency for K^+_{e2} and K^-_{e2} events is reported in Table 12.2.

$1TRK-3$ **trigger efficiency for** K_{e2} **events**	
K^+_{e2}	0.855 ± 0.006
K^-_{e2}	0.856 ± 0.008

Table 12.2: *Summary of* $1TRK-3$ *trigger efficiency for* K^+_{e2} *and* K^-_{e2} *events.*

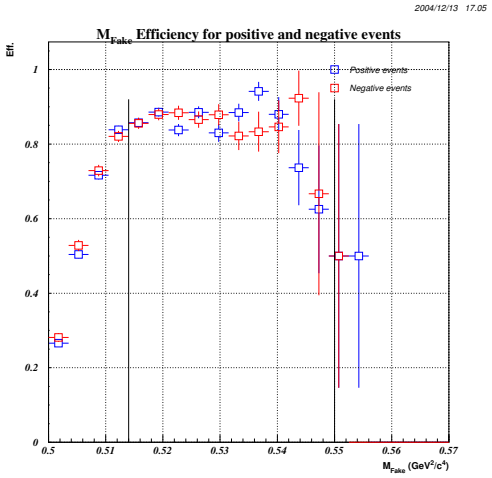

Figure 12.21: *Plot of* $1TRK-3$ *efficiency as a function of* $M_{Fake}(\pi)$ *for* K_{e3} *positive and negative events. The limits correspond to the analysis cut bounds* $514\ MeV/c^2 < M_{Fake}(\pi) < 550\ MeV/c^2$.

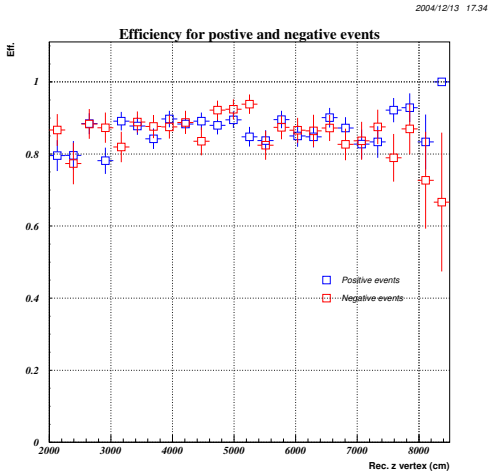

Figure 12.22: *Plot of* $1TRK-3$ *efficiency for* K_{e3} *events as a function of the reconstructed* z *coordinate of the vertex position.*

12.4 Background correction for K^+_{e2} and K^-_{e2} events

The background subtraction for K_{e2} events has been shown in Section 8.1.7. The same procedure has been used to estimate the number of K^+_{e2} and K^-_{e2} signal events. The fit of the background under the K_{e2} peak and of the number of signal events has been performed independently for K^+_{e2} and K^-_{e2} decays. The results are summarized in Table 12.3.

K_{e2} **Background correction**	
K^+_{e2} signal events	$3060 \pm 50_{(stat)}$
K^-_{e2} signal events	$1610 \pm 50_{(stat)}$

Table 12.3: *Summary of K_{e2} background correction for K^+_{e2} and K^-_{e2} decays. The quoted error is statistical only.*

Chapter 13

Results and Conclusions

This chapter collects the relevant results of the previous Chapters for the measurement of R_K ratio. A comparison of R_K measurement between positive and negative events is carried out.

13.1 Summary of corrections of R_K measurement

All the corrections and uncertainties on R_K ratio measurement are summarized in Table 13.1.

The most relevant correction is due to the acceptance of K_{e2} and $K_{\mu 2}$ events. Other large corrections are the trigger efficiency correction and the acceptance correction due to $K_{l2\gamma}$ decays. The remaining corrections are of the order of a few 10^{-3} or less. The large statistical uncertainty of trigger efficiency correction is due to the limited amount of statistics in the control sample of the L1 logic. Contributions to the systematic error arise mainly from the uncertainty on the cut acceptance and on acceptance correction due to $K_{l2\gamma}$ decays.

Summary of R_K corrections		
	ΔR_K Correction	ΔR_K uncertainty
Background $K_{\mu 2}$	$+1.0013 \cdot 10^{-3}$	$\pm 0.110^{-3}$
Cut Acceptance	+1.116	$0.002\ _{(stat)}\ \pm 0.005\ _{(syst)}$
K_{e2} E/p Acceptance	+1.0277	$\pm 0.0041_{syst}$
Accidental losses	0.9976	$(\pm 1.3_{(stat)}\ \pm 2.3_{(syst)}) \cdot 10^{-3}$
$K_{\mu 2}$ LKr Acceptance	0.9997	$\pm 0.4 \cdot 10^{-4}$
Trigger Efficiency	+1.169	$\pm 0.008_{(stat)}\ \pm 0.002_{(syst)}$
Radiative Corrections	+1.063	$\pm 0.005_{(syst)}$
Total	**+1.424**	$\pm 0.008_{(stat)}\ \pm 0.008_{(syst)}$

Table 13.1: *Summary of corrections and uncertainties to R_K measurement. The largest statistical error comes from the uncertainty on the trigger efficiency. This is due to the limited amount of statistics, especially, in the control sample of the L1 trigger logic. The greatest contributions to the systematic error come from the uncertainty on the cut acceptance and on acceptance correction due to $K_{l2\gamma}$ decays. The uncertainty due to K_{e2} background subtraction is not reported here. The sources of error are completely independent and are added in quadrature.*

13.2 Measurement of R_K

The number of collected K_{e2} events, seen in Section 8.1.7, is:

$$4670 \pm 77 \ {}_{(stat)} \ {}^{+29}_{-8} \ {}_{(syst)}$$

585 of these events have been collected with a downscaling factor of 4 for the L2 trigger, all the others with with a downscaling factor of 2 (see Section 10.1). The downscaling of L1 trigger is 10.

The number of collected $K_{\mu 2}$ events is 619179.
These events have been collected with a downscaling factor of 10000.

The ratio between K_{e2} and $K_{\mu 2}$ collected events as a function of time can be seen in Fig. 13.1.

Summarizing the corrections presented in Table 13.1:

Ratio of K_{e2} and $K_{\mu 2}$ collected events	$(7.54 \pm 0.09_{(stat)} \ {}^{+0.03}_{-0.01(syst)}) \cdot 10^{-3}$
Downscaling Factor	$2.25 \cdot 10^{-3}$
Correction from Table 13.1	$(1.424 \pm 0.008_{(stat)} \ \pm 0.008_{(syst)})$

The value of R_K ratio measurement with 2003 statistics is:

$$R_K \ = \ (2.416 \pm 0.043_{(stat)} \ \pm 0.024_{(syst)}) \cdot 10^{-5}$$

to be compared with the theoretical prediction: $(2.472 \pm 0.001) \cdot 10^{-5}$.
The uncertainty of R_K ratio measurement is dominated by the statistical error.

R_K **measurement**	
Theoretical prediction	$(2.472 \pm 0.001) \cdot 10^{-5}$
World Average (PDG 2004)	$(2.45 \pm 0.11) \cdot 10^{-5}$
NA48 Measurement 2003 statistics	$(2.416 \pm 0.043_{(stat)} \ \pm 0.024_{(syst)}) \cdot 10^{-5}$

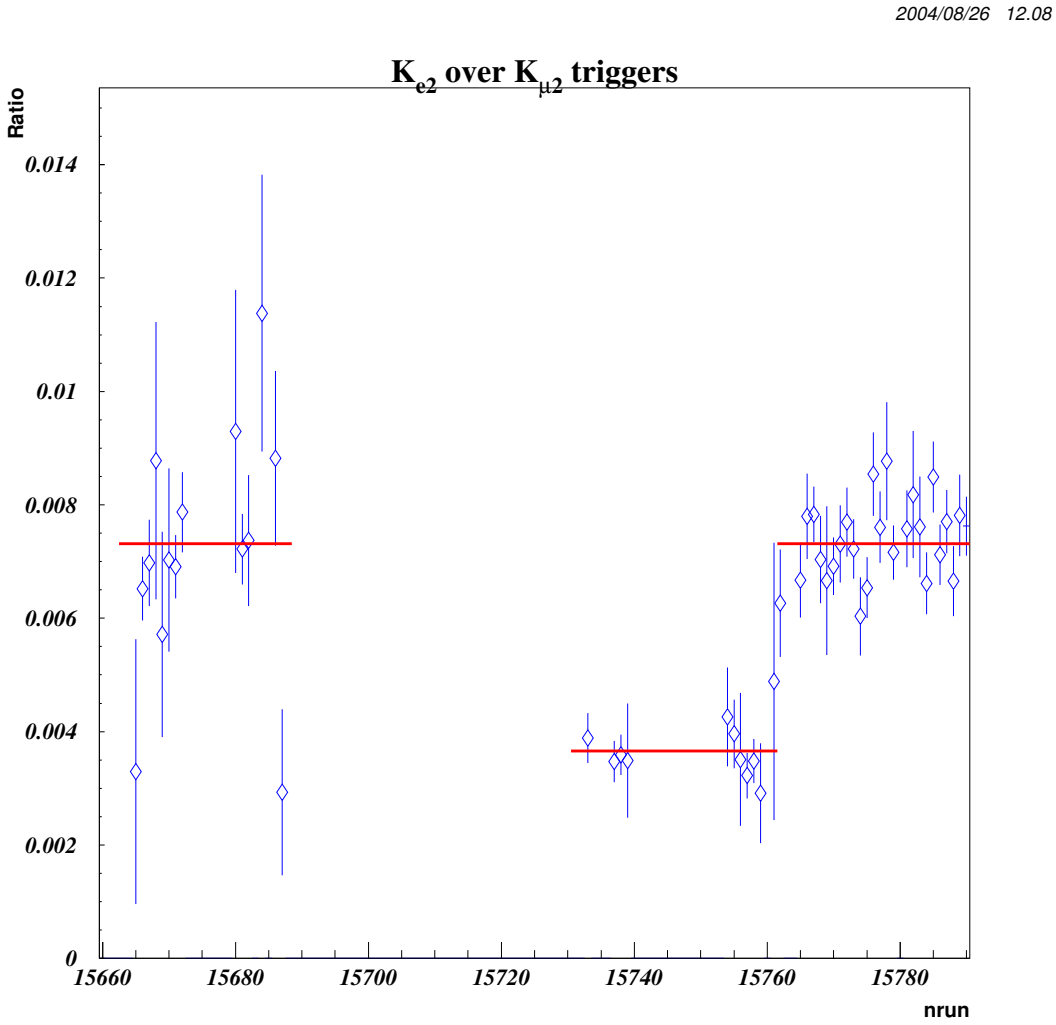

Figure 13.1: *Ratio between K_{e2} and $K_{\mu 2}$ collected trigger as function of time. It is clearly visible the change in trigger downscaling.*

13.3 Comparison between R_K measurement for positive and negative events

In case of no CP violation, the measurement of R_K measurement for positive and negative events must be consistent within errors and the ratio between R_{K^+} and R_{K^-} (A_{+-}), defined as:

$$A_{+-} = \frac{R_{K^+}}{R_{K^-}} = \frac{BR(K^+_{e2})}{BR(K^+_{\mu 2})} \frac{BR(K^-_{\mu 2})}{BR(K^-_{e2})} \tag{13.1}$$

must be consistent with 1.

The statistics collected in 2003 run is reported in Table 13.2. The ratio between K_{e2} and $K_{\mu 2}$ events of positive and negative charge as a function of time can be seen in Fig. 13.2 and Fig. 13.3.

Statistics collected in 2003		
	Positive charge	Negative charge
K_{e2}	3060 ± 50	1610 ± 50
$K_{\mu 2}$	398270	220909

Table 13.2: *The four statistical samples of the selected events.*

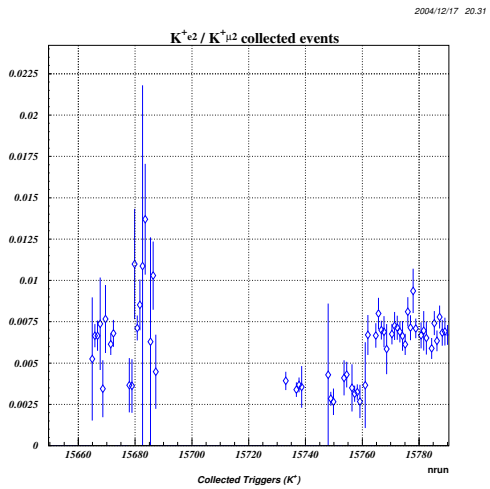

Figure 13.2: *Ratio between K_{e2} and $K_{\mu 2}$ collected events of positive charge as function of time.*

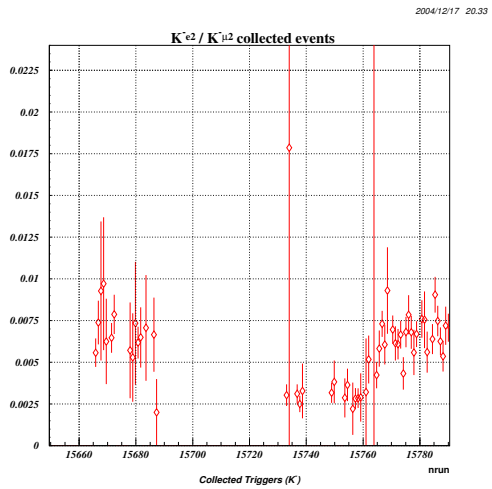

Figure 13.3: *Ratio between K_{e2} and $K_{\mu 2}$ collected events of negative charge as function of time.*

The correction to A_{+-} due to Acceptance and Trigger efficiency difference for events of positive and negative charge is shown in Table 13.3.

Summary of A_{+-} corrections		
	$\frac{\Delta A_{+-}}{A_{+-}}$ Correction	$\frac{\Delta A_{+-}}{A_{+-}}$ uncertainty
Acceptance	-0.0012	$\pm$0.0010
Trigger Efficiency	+0.001	$\pm$0.007
Total	**-0.0002**	**0.007**

Table 13.3: *Summary of corrections and uncertainties to A_{+-} measurement.*

Comparing the raw number of events in Table 13.2, it can be seen that $\frac{N(K^+_{e2})}{N(K^-_{e2})}$ is different from $\frac{N(K^+_{\mu 2})}{N(K^-_{\mu 2})}$ (see Table 13.4). $K_{\mu 2}$ Ratio is well in agreement with analogous measurements operated in $K \to 3\pi$ channels, while K_{e2} ratio is not, at the level of 2 standard deviations:

$$\frac{N(K^+ \to \pi^+\pi^-\pi^+)}{N(K^+ \to \pi^-\pi^-\pi^+)} = 1.796 \pm 0.001 \qquad [33]$$

$$\frac{N(K^+ \to \pi^+\pi^0\pi^0)}{N(K^+ \to \pi^-\pi^0\pi^0)} = 1.797 \pm 0.001 \qquad [34]$$

K^+ / K^- **Ratio**	
$\frac{N(K^+_{\mu 2})}{N(K^-_{\mu 2})}$	1.803 ± 0.003
$\frac{N(K^+_{e2})}{N(K^-_{e2})}$	1.89 ± 0.05

Table 13.4: *K^+_{l2} / K^-_{l2} Ratio employing the raw event numbers in Table 13.2.*

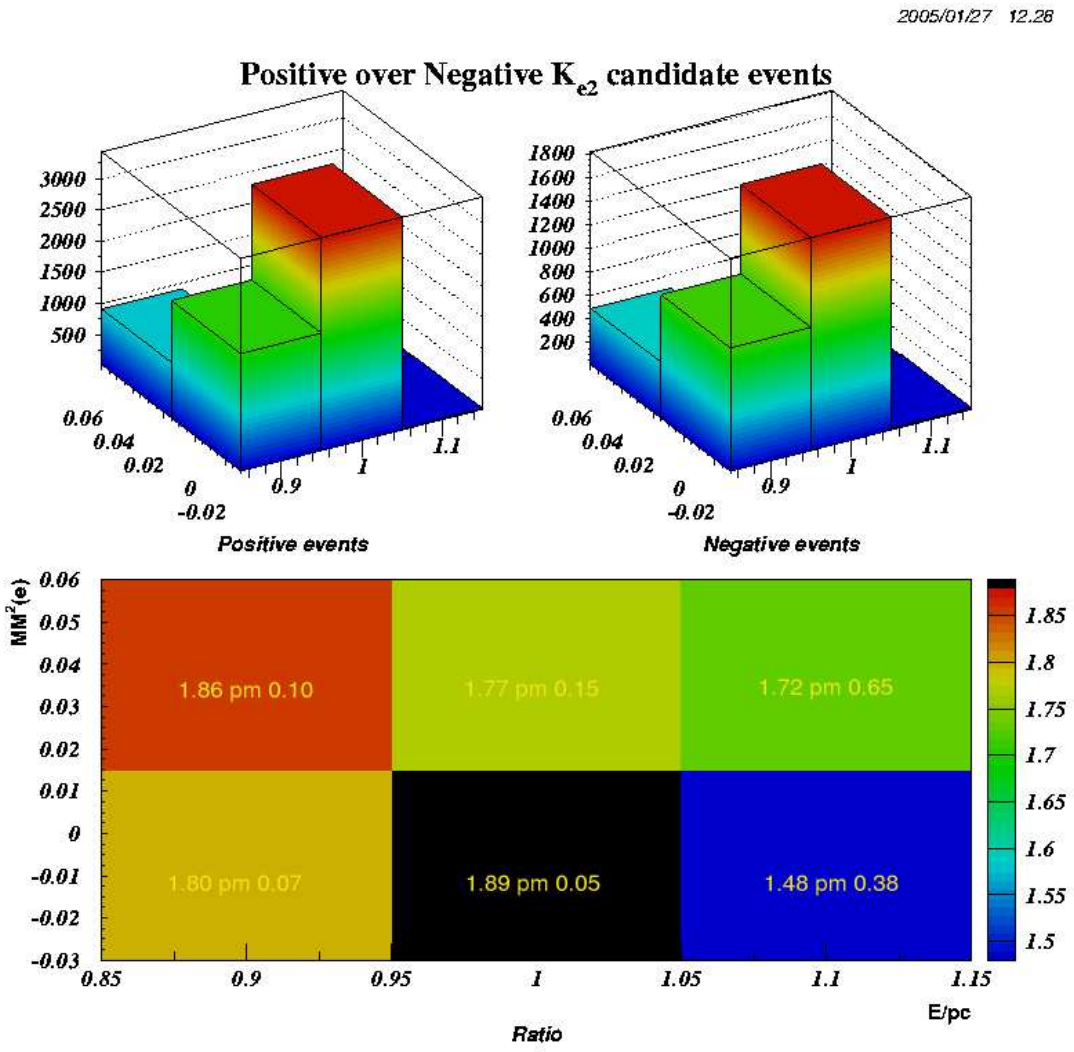

Figure 13.4: *Ratio of K^+ / K^- events in $MM^2(e)$ versus E/p plane. The maximum corresponds to the region of K_{e2} signal. The $K_{\mu 2}$ background occupies the left side of the plane, while K_{e3} background is contained in the top-middle bin.*

To check if the $N(K^+_{e2})$ / $N(K^-_{e2})$ Ratio obtained in Table 13.4 is due to instrumental effects, K^+ / K^- event ratio has been plotted in the $MM^2(e)$ versus E/p plane. It can be seen in Fig. 13.4 that K^+ / K^- event ratio maximum corresponds to K_{e2} signal region, while it is lower in $K_{\mu 2}$ and K_{e3} background regions. Nevertheless the statistics is not good enough to unequivocally conclude that there is an excess of K^+_{e2} over K^-_{e2} production.

Taking into consideration Acceptance and Trigger correction as in Table 13.3, the resulting measurement of A_{+-} is:

$$A_{+-} = 1.054 \pm 0.035$$

13.4 Conclusions

This thesis was devoted to the measurement of the R_K ratio with the statistics collected by NA48/2 in 2003 data taking. NA48/2 experiment has collected the largest sample of K^+ and K^- decays ever in the world, opening many challenging opportunities in Kaon experimental physics. The study of Kaon leptonic decays has been carried out in details in the present thesis.
The measurement of R_K, considering only 2003 statistics, has provided the result:

$$R_K \;=\; (2.416 \pm 0.043_{(stat)} \;\pm 0.024_{(syst)}) \cdot 10^{-5} \qquad NA48/2 \text{ (2003 } statistics)$$

with an accuracy improved by about a factor 2 compared with the PDG average of the previous measurements. Moreover NA48/2 performed the first comparison ever of the R_K measurement for K^+ and K^- leptonic decays:

$$A_{+-} \;=\; 1.054 \pm 0.035 \qquad NA48/2 \text{ (2003 } statistics)$$

Appendix A

K_{l2} Radiative Decays form factors

The present Appendix is intended as a reference for the implementation of the $K_{l2\gamma}$ radiative decays form factors into Monte Carlo simulation. The calculation presented here are taken from the Bijnens et al. article [32].
The matrix element of $K_{l2\gamma}$ Radiative Decays can be written as:

$$K^+(p) \to l^+(p_l)\nu_l(p_\nu)\gamma(q) \qquad [K_{l2\gamma}]$$
$$T = -iG_F e V_{us}^\star \epsilon_\mu^\star \left\{F_K L^\mu - H^{\mu\nu} l_\nu\right\}$$

where l stands for e or μ, and γ is a real photon with $q^2 = 0$ and with:
with

$$\begin{aligned} L^\mu &= m_l \bar{u}(p_\nu)(1+\gamma_5)\left(\frac{2p^\mu}{2pq} - \frac{2p_l^\mu + \not{q}\gamma^\mu}{2p_l q}\right) v(p_l) \\ l^\mu &= \bar{u}(p_\nu)\gamma^\mu(1-\gamma_5)v(p_l) \\ H^{\mu\nu} &= iV(W^2)\epsilon^{\mu\nu\alpha\beta}q_\alpha p_\beta - A(W^2)(qW g^{\mu\nu} - W^\mu q^\nu) \\ W^\mu &= (p-q)^\mu = (p_l + p_\nu)^\mu. \end{aligned}$$

ϵ_μ denotes the polarization vector of the photon with $q^\mu\epsilon_\mu = 0$. A and V stand for two Lorentz-invariant amplitudes which are related to the matrix element of the axial (vector) current.

The kinematics of (spin-averaged) $K_{l2\gamma}$ decays has two degrees of freedom, the chosen Lorentz invariant variables are:

$$x = 2pq/M_K^2 \ , \ y = 2pp_l/M_K^2 \ .$$

In the K rest frame, the variable x (y) is proportional to the photon (charged lepton) energy,

$$x = 2E_\gamma/M_K \ \ , \ \ y = 2E_l/M_K \ \ ,$$

The physical region of the Dalitz plot is:

$$\begin{aligned} 0 \leq \ & x \ & \leq 1 - r_l \\ 1 - x + \frac{r_l}{(1-x)} \leq \ & y \ & \leq 1 + r_l \end{aligned} \tag{A.1}$$

where

$$r_l = m_l^2/M_K^2 = \left\{ \begin{array}{l} 1.1 \cdot 10^{-6} (l = e) \\ 4.6 \cdot 10^{-2} (l = \mu) \end{array} \right. .$$

The partial decay rate is

$$d\Gamma = \frac{1}{2M_K(2\pi)^5} \sum_{spins} |T|^2 d_{LIPS}(p; p_l, p_\nu, q) \ .$$

The Dalitz plot density

$$\rho(x,y) = \frac{d^2\Gamma}{dxdy} = \frac{M_K}{256\pi^3} \sum_{spins} |T|^2$$

is a Lorentz-invariant function which contains V and A in the following form

$$\begin{aligned} \rho(x,y) &= \rho_{\rm IB}(x,y) + \rho_{\rm SD}(x,y) + \rho_{\rm INT}(x,y) \\ \rho_{\rm IB}(x,y) &= A_{\rm IB} f_{\rm IB}(x,y) \\ \rho_{\rm SD}(x,y) &= A_{\rm SD} M_K^2 \left[(V+A)^2 f_{\rm SD^+}(x,y) + (V-A)^2 f_{\rm SD^-}(x,y) \right] \\ \rho_{\rm INT}(x,y) &= A_{\rm INT} M_K \left[(V+A) f_{\rm INT^+}(x,y) + (V-A) f_{\rm INT^-}(x,y) \right] \ , \end{aligned} \tag{A.2}$$

where

$$\begin{aligned} f_{\rm IB}(x,y) &= \left[\frac{1-y+r_l}{x^2(x+y-1-r_l)} \right] \left[x^2 + 2(1-x)(1-r_l) - \frac{2xr_l(1-r_l)}{x+y-1-r_l} \right] \\ f_{\rm SD^+}(x,y) &= [x+y-1-r_l] \left[(x+y-1)(1-x) - r_l \right] \\ f_{\rm SD^-}(x,y) &= [1-y+r_l] \left[(1-x)(1-y) + r_l \right] \\ f_{\rm INT^+}(x,y) &= \left[\frac{1-y+r_l}{x(x+y-1-r_l)} \right] \left[(1-x)(1-x-y) + r_l \right] \\ f_{\rm INT^-}(x,y) &= \left[\frac{1-y+r_l}{x(x+y-1-r_l)} \right] \left[x^2 - (1-x)(1-x-y) - r_l \right] \end{aligned} \tag{A.3}$$

and

$$\begin{aligned} A_{\rm IB} &= 4r_l \left(\frac{F_K}{M_K}\right)^2 A_{\rm SD} \\ A_{\rm SD} &= \frac{G_F^2 |V_{us}|^2 \alpha}{32\pi^2} M_K^5 \\ A_{\rm INT} &= 4r_l \left(\frac{F_K}{M_K}\right) A_{\rm SD} \ . \end{aligned} \tag{A.4}$$

The subscripts IB, SD and INT stand respectively for the contribution from inner bremsstrahlung, from the structure-dependent part, and from the interference term between the IB and the SD parts in the amplitude.

The order of magnitude of the $\mathrm{SD}^\pm$ and $\mathrm{INT}^\pm$ contributions to the decay rate can be seen from the integrated rates

$$\Gamma_I = \int_{R_I} dxdy\rho_I(x,y) \ \ ; \ \ I = \mathrm{SD}^\pm, \mathrm{INT}^\pm, \mathrm{IB} \ \ ,$$

where $\rho_{SD} = \rho_{SD^+} + \rho_{SD^-}$ etc. For the region R_I we take the full phase space.

If V, A form factors are considered constants, the rates and for the corresponding branching ratios are:

$$\Gamma_I \ = \ A_{\rm SD} \left\{M_K(V \pm A)\right\}^{N_I} X_I \ \mathrm{BR}_I \ \doteq \ \Gamma_I/\Gamma_{\rm tot} = N \left\{M_K(V \pm A)\right\}^{N_I} X_I$$

with

$$N = A_{\rm SD}/\Gamma_{\rm tot} = 8.348 \cdot 10^{-2}.$$

The values for N_I and X_I are listed in Table A.1.

Table A.1: The quantities X_I, N_I. $\mathrm{SD}^\pm$ and $\mathrm{INT}^\pm$ are evaluated with full phase space.

	SD^+	SD^-	INT^+	INT^-	
X_I	$1.67 \cdot 10^{-2}$	$1.67 \cdot 10^{-2}$	$-8.22 \cdot 10^{-8}$	$3.67 \cdot 10^{-6}$	$K_{e2\gamma}$
X_I	$1.18 \cdot 10^{-2}$	$1.18 \cdot 10^{-2}$	$-1.78 \cdot 10^{-3}$	$1.23 \cdot 10^{-2}$	$K_{\mu 2\gamma}$
N_I	2	2	1	1	

To estimate Γ_I and BR_I, the form factors V, A values can be taken from Section 3.3 of Bijnens paper [32]:

$$M_K(V+A) \simeq -0.097 \ \ , \ \ M_K(V-A) \simeq -0.037 \ \ .$$

Bibliography

[1] R. Brown et al., *Nature* **163** (1949) 82.

[2] M. Gell-Mann, *Phys. Rev.* **92** (1953) 833.

[3] A. Pais, *Phys. Rev.* **86** (1952) 663.

[4] M. Gell-Mann and A. Pais, *Phys. Rev.* **97** (1955) 1387.

[5] K. Lande et al., *Phys. Rev.* **106** (1956) 1901.

[6] T.D. Lee and C.N. Yang, *Phys. Rev.* **104** (1956) 254.

[7] N. Cabibbo, *Phys. Rev. Lett.* **10** (1963) 531.

[8] J.H. Christenson, J.W. Cronin, V.L. Fitch and R. Turlay, *Phys. Rev. Lett.* **13** (1964) 138.

[9] G. Lüders *Kong. Dansk. Vid. Selskab, Mat-Fys. Medd.* **28**, 5 (1954)

[10] W. Pauli, *Nuovo Cimento* **6**, 204 (1957)

[11] J.R. Batley et al., *Phys. Lett. B* **54** (2002) 97.

[12] N. Cabibbo, *Phys. Rev. Lett.* **93** 121801 (2004); hep-ph/0405001

[13] M. Davier, LAL-98-68, Aug 1998. 25th SLAC Summer Institute on Particle Physics: Physics of Leptons (SSI 97)

[14] W. Loinaz et al., *hep-ph/0403306*

[15] Riazuddin, *hep-ph/0007146*

[16] K. S. McFarland et al., *Phys. Rev. D* **65**, 111103 (2002); hep-ex/0205080

[17] R. P. Feynman and M. Gell-Mann, *Phys. Rev.* **109**, (1958)

[18] T. Fazzini et al., *Phys.Rev.Lett* **1**, 247 (1958)

[19] Wu C.S. et al., *Phys. Rev* **105**, 1413 (1957).

[20] Particle Data Group, *Phys. Lett. B* **592** (2004) 1.

[21] F.Gilman, K.Kleinknecht and B.Renk in: K.Hagiwara *et al.*, *Phys.Rev. D* **66** (2002) 010001-113.

[22] W. J. Marciano, *Nucl. Phys. B* Proc. Suppl. **40**, 3 (1995)

[23] J. A. Thompson *hep-ex/0307053* (2003)

[24] A. Alosio et al., *hep-ex/0307016* (2003)

[25] A. R. Clark et al., *Phys. Rev. Lett.* **29** (1972), 1274.

[26] K. S. Heard et al., *Phys. Lett.* **55 B** (1975), 324.

[27] K. S. Heard et al., *Phys. Lett.* **60 B** (1976), 302.

[28] J.R. Batley et al., *CERN/SPSC 2000-003* (2000).

[29] Y. Giomataris et al., *NIM* **376 A** (1996), 29.

[30] M. Mota at al. A Flexible Multi-Channel High Resolution Time to Digital Converter ASIC. Nuclear science symposium, Lyon, France, October 2000.

[31] M. Finkemeier, *Phys. Lett. B* **387**, 391 (1996) ; hep-ph/9505434

[32] , J. Bijnens et al., *Nucl. Phys. B* **396**, 81 (1993)

[33] I. Mikulec, NA48 Weekly Meeting, January 25th 2005

[34] S. Balev, NA48 Weekly Meeting, January 25th 2005